

Development of Ultra-High Temperature Ceramic Composites by Sol-Gel Processing

Caen Khim Ang
BSc(Hons)



Submitted for the degree of the Doctor of Philosophy

Department of Materials Engineering
Future Manufacturing, New Horizons

Monash University
Clayton, Victoria
Australia

2013

Copyright Notices

Notice 1

Under the Copyright Act 1968, this thesis must be used only under the normal conditions of scholarly fair dealing. In particular no results or conclusions should be extracted from it, nor should it be copied or closely paraphrased in whole or in part without the written consent of the author. Proper written acknowledgement should be made for any assistance obtained from this thesis.

Notice 2

I certify that I have made all reasonable efforts to secure copyright permissions for third-party content included in this thesis and have not knowingly added copyright content to my work without the owner's permission.

Contents

List of Contents	i
Declaration	vi
Acknowledgements	vii
Summary	ix
1. Introduction	1
2. Literature Review	5
2.1 Ultra High Temperature Ceramics	5
2.2 Carbides and diborides	7
2.2.1 Refractory properties of carbides and diborides	8
2.2.2 Powder synthesis and morphology	9
2.2.3 Processing challenges	11
2.2.3.1 Sintering UHTC materials	12
2.2.3.2 Alloying and nanocements “hard metals”	18
2.2.3.3 Surface coatings	19
2.2.3.4 Summary	20
2.3 Sol-gel technology	21
2.3.1 Carbides by sol-gel	21
2.3.2 Carbon precursors	22
2.3.3 Oxide precursors	25
2.3.4 Morphology: nanopowders, fibers, coatings	29
2.3.5 Summary	30
2.4 UHTC composite materials	31
2.4.1 Rationale	31
2.4.2 Composite properties	32
2.4.3 Processing challenges	35
2.4.4 Nanodispersed ceramic materials	36
2.4.5 SPS Sintering (SPS)	39
2.4.5.1 Theory of SPS	39
2.4.5.2 Densification of UHTCs composites	40

2.4.6 Summary	42
2.5 Extreme environment testing	43
2.5.1 Extreme environments by hypersonic flight	43
2.5.2 Experimental testing conditions	45
2.5.3 Ground based testing	46
2.5.4 ZrB ₂ composites under simulated testing	48
2.5.5 Summary	49
2.6 Future of UHTCs	49
2.7 Scope of research	50
3. Experimental Methods	51
3.1 Synthesis and processing	51
3.1.1 Hafnium alkoxide synthesis for sol-gel	52
3.1.2 Zirconium oxide sol-gel	53
3.1.3 P123/PFA decomposition	54
3.1.4 Carbothermal reduction	54
3.1.5 Composite materials handling	55
3.1.5.1 Zirconium diboride	55
3.1.6 Zirconium diboride coated powders	56
3.1.7 Spark Plasma Sintering (Dr Sinter SPS-925)	58
3.1.8 Powder analysis	61
3.1.9 Sharp leading edge geometries	61
3.1.10 Composite surface preparation	62
3.1.11 Aerothermal tests: combustion zone and preparation	62
3.2 Characterization	63
3.2.1 NMR Spectroscopy	63
3.2.2 Thermogravimetry analysis (TGA)	63
3.2.3 TEM JEOL JEM2011LaB ₆ and JEM2100FEG	64
3.2.4 SEM JSM7001FEG	65
3.2.5 Raman Spectroscopy	66
3.2.6 Gas sorption	66
3.2.7 Density measurement	67
3.2.8 X-Ray Diffraction	68

3.2.9 Indentation	69
3.2.10 Flexural strength by 3-point bending	70
4. Hafnium carbide(HfC)	71
4.1 Synthesis of hafnium alkoxide	72
4.1.1 Organometallic synthesis	73
4.1.2 Analysis of hafnium n-butoxide	74
4.1.3 Conclusions of synthesis	75
4.2 Hafnia-carbon sol-gel	75
4.2.1 Condensation for gelation	76
4.2.2 Gelation to pyrolysis	77
4.3 Carbothermal reduction to HfC	78
4.3.1 Phase analysis	79
4.3.2 Carbon evolution and porosity	80
4.3.3 Microstructure and morphology analyses	88
4.3.4 Reaction of oxycarbides	90
4.3.5 Summary	93
4.4 Conclusions	93
4.5 Future work	94
5. Zirconium carbide (ZrC)	95
5.1 Stabilizing zirconium n-propoxide	95
5.2 Carbon by furfuryl alcohol polymerisation	96
5.2.1 Controlling the reaction of PFA to carbon	98
5.2.2 Control of solvent additions	98
5.2.3 Effect of acid catalyst	101
5.2.4 Summary	103
5.3 Development and evolution of nc-ZrC	103
5.3.1 Phase analysis	103
5.3.2 Carbon and crystallite interactions	104
5.3.3 Microstructure of carbon and ZrC	110
5.3.4 Microstructural evolution of nanoparticles	113
5.3.5 Conclusions	120

5.3.6 Future work	121
6. Composites of ZrB₂ by sol-gel ZrC	122
6.1 SPS sintering of ZrB ₂	122
6.1.1 Constants in SPS	122
6.1.2 Monolithic ZrB ₂ densification by SPS	126
6.1.3 Effect of heating rate	133
6.1.4 Effects of Die Size	137
6.1.5 Summary of SPS sintering of ZrB ₂	138
6.2 ZrB ₂ powder-gel composite	139
6.2.1 Carbon depleted powder-gel	139
6.2.2 Oxide film reduction	141
6.2.3 Carbon stoichiometry	143
6.2.4 Empirical calculations	147
6.2.5 Surface morphology	148
6.3 Densification of ZrB ₂ -nc-ZrC	152
6.3.1 Composites of ZrC in ZrB ₂	153
6.3.2 Conclusions of powder-gel densification	161
6.4 Conclusions of sol-gel ZrC composites	162
7. Materials for extreme environments	164
7.1 Microstructure and mechanical properties	164
7.1.1 Powder-gel and powder-mixed composites	165
7.1.2 Mechanical properties	167
7.1.2.1 Fracture toughness	167
7.1.2.2 Indentation hardness and strength	168
7.1.3 Summary	172
7.2 Aerothermal performance	172
7.2.1 Prediction, hypothesis and criteria	173
7.2.2 Oxidation response of ZrB ₂ at 3000°C	175
7.2.3 Z5O powder-gel (ZrB ₂ -nc-ZrO ₂)	180
7.2.4 Z5C14 powder-gel (ZrB ₂ -5%nc-ZrC)	182
7.2.5 Z5C16+ powder-gel (88ZrB ₂ -4ZrC-8C)	188

7.2.6 ZrB ₂ -ZrCp powder composite	190
7.2.7 Leading edge recessions and weight losses	195
7.3 Summary	198
8. Conclusions	199
8.1 Outcomes of research	199
8.2 Future work	201
8.3 Publications	202
8.4 Facility acknowledgements	202
9. References	203

Declaration

The following thesis contains no materials that have been accepted for the award of any other degree in any institution. To the best of my knowledge, it does not contain material previously published or written by any other persons, except where respectful and due reference is made in the text.

Caen Ang

April 2013

Acknowledgements

Since 2009, I have been honoured to receive generous support from numerous people, but also from unnamed and unrecognized persons that have contributed to the social system that allowed for the completion of this work. I would like to extend my appreciation.

Professor Yi-Bing Cheng, who I hold in the highest regard for his intuition, ideas, constructive thinking, and leadership. There was a shared belief in changing the world one small step at a time and a reinvigoration of ceramics interest at Monash. I wish to thank my two prominent collaborators, Tim Williams and Aaron Seeber, for their respective tutelage and fruitful discussions in electron microscopy and x-ray diffraction. Tim was consistently reminding me of limiting my boundaries of responsibility and focusing on the target. Aaron gave me the motivation to push out at the limits of what we can do – usually by creative invention.

I would like to thank all the staff and my colleagues at Materials Engineering, Chemical Engineering and the Monash Centre for Electron Microscopy. In particular, Huanting Wang, Don Rodrigo, Kun Wang, Ellen Lavoie and Silvio Mattievich for their experience and advice. Daniel Curtis for his innovation at the end; Bruce Dobney for his generosity at the start.

Underneath this is the Australian government, for the scholarships and the facilities at Monash, CSIRO and DSTO. It represents the commitment of this society to advancing knowledge and education, creating an aristocracy of initiative and ability. Despite its current state of flux, the Monash University Materials Engineering department provided ample opportunities to develop new skills, in return for enthusiasm and commitment. A special thanks to Chris Wood (DSTO) and Sonya Slater (DSTO) for their interest in high temperature materials.

To me, they were living inspirations, for all engineers dedicated to problem solving, alongside names such as Hyman J. Rickover and John W. Aaron.

I would like to thank my friends and family for their witness on this journey: EC, NM, NT, JN, VL, LS, SG, JN, ER, KK and KS, in addition to: KD, JB, RH, GR, IC and NC, who are no longer present. And finally, to Rowi: for her never-ending questions through this journey; yet always having an answer that was right.

The immediate future is created by our own acts and omissions, but the far future depends on edifying it to those who believe it evitable – or who have no vision at all. Living for the moment – can become foresight and intuition. Dreaming and prevarication – can transform into inspired action. I dedicate this thesis to those who choose to make a difference, in pursuit of excellence, for the necessity of posterity.

Caen Ang

Summary

A sol-gel route synthesized nanocrystalline hafnium carbide (HfC) and zirconium carbide (ZrC) for use in composite materials. The starting materials were zirconium and hafnium alkoxides and carbon was introduced by furfuryl alcohol. A block co-polymer surfactant homogenized the oxide and carbon components. Reduction to HfC and ZrC began at a low temperature of 1250°C and removal of the oxide phase was achieved at 1450°C. The carbide powder was nanocrystalline size less than 100nm. Production of HfC included a synthesis step that limited investigation of the sol-gel process. However, purchased alkoxides for zirconium allowed for detailed understanding of phase changes using X-ray Diffraction of the oxide and Raman Spectroscopy of carbon evolution. Morphology changes were observed using nitrogen gas sorption. Scanning and Transmission Electron Microscopy was used to image the carbide lattice, surface oxides and graphene-like carbons in the microstructure. While HfC synthesis demonstrated that shrinking core models apply, the ZrC results indicated that this type of nanoparticle carbothermal synthesis involved agglomeration and necking as a viable mode of mass transport in completing the carbothermal reduction. Understanding of this process allowed for the modest development of composites by sol-gel coating of powders. The sol-gel coating of ZrB₂ was successfully applied to coat ZrC nanoparticles on the powder. Detailed refinement of carbon content in the sol-gel coating was necessary reduce the surface oxide intrinsic to the ZrB₂ surface, while providing carbon for the sol-gel oxides. The sol-gel coating created a homogenous mix of ~200nm ZrC on the ZrB₂ surface after heat-treatment at 1450°C. Densification of the ZrB₂-5%ZrC powder was achieved by spark plasma sintering (SPS) at 1800°C, resulting in submicron sized ZrC particles at grain boundaries and triple points. The amount of carbon added to the sol-gel precursor dictated the porosity and thus some properties of the composites. Flexural strength of ~400MPa was obtained from the composites but no significant improvement of fracture toughness was observed. However, an improvement in hardness of about 20% was observed

over monolithic ZrB_2 . The oxidation performance of the composites was improved by the addition of a sacrificial carbide phase. Sharp leading edge samples were oxidized at $3000^\circ C$ and were compared to a traditional powder mixed composite. The finer and more homogenous distribution of ZrC caused gradual oxidation while maintaining leading edge stability. However, the powder mixed composite failed under the test. This illustrated the importance not only phase selection but also microstructural control. This indicated advantages in sol-gel processing of ceramic composites with improved densification, controlled grain size and improved properties.

1. Introduction

Ultra-High Temperature Ceramics (UHTC) are advanced inorganic materials that have melting points exceeding 3000°C. Advanced ceramics are used in specialized fields for their exclusive properties. Crystal structures of UHTCs are almost exclusively boron and carbon interstitials in a metal lattice with nearly full covalent bonding character. They are used in refractory applications where other materials cannot be used.¹⁻⁴

Their high temperature stability is also responsible for their resistance to processing by sintering. Sintering involves an external source of thermal energy supplied to the material at temperatures 50-80% of the material's melting point where solid-state diffusion is appreciable. The thermodynamic driving force is the reduction in the surface area, replacing all solid-vapour interfaces with solid-solid, from the morphology state of loose particles to one consolidated mass. This is a considerably expensive process. Methods to change this include manipulation of the sintering process by increasing the surface area of the particles and diffusion behaviour in the system. Nano-size particles possess a very high surface area. There have been over a dozen publications on nanocrystalline UHTCs produced from a solution or sol-gel process because the intimate mixing found in liquids allows for a low synthesis temperature while maintaining nano-size particles.⁵⁻⁷ These can be sintered at lower temperatures. The main disadvantage of sol-gel is the low yield from the mass-volume ratio of liquid processing. Thus sol-gel is often used for specialized morphologies, such as fibres, films and in particular, surface coatings where micron-size powder processing may be difficult.⁸⁻¹¹ Due to the high surface area from the small particle radii, nanoparticles can behave differently to their micron-size counterparts. The carbothermal reduction process has not been fully investigated in these nanomaterials. The nature of particle agglomeration, the behaviour the reaction and the effect of high surface area has been neglected. This is not only invaluable to understanding fundamental questions of surface catalytic activity and chemical reaction, but also to applied outcomes such as processing particle size and control of impurities. Current

instrumental analysis can investigate the evolution of the carbon reaction because these techniques were not previously available.

Poorly sintered ceramics usually results from particles unable to coalesce. This eventually yields ceramics with residual porosity. Avoiding this is important because ceramics are flaw sensitive. But using the nanoparticles directly is expensive. Integrating this sol-gel with conventional powders can overcome both disadvantages. Correctly using two phases in a composite convey advantages that are absent in a monolithic material by combining the advantages of matrix and reinforcement. But most UHTC composites are produced by mechanical mixing of nanoparticle reinforcement and matrix powder. This limits microstructural control and homogeneity of the two phases to well above the micron-level. Few publications have been reported of nanoparticle attachment or treatment of powder surfaces prior to sintering. None have been reported on UHTC materials.

It is possible that using a nano-UHTC phase would replace the coarser powder surface with a higher effective curvature and thus may increase the driving force for sintering. The dispersed minor phase could restrict the grain growth that accompanies the final stages of sintering. The reliance on the intergranular phase for consolidation could result in depressed sintering temperatures. The composites were densified via Spark Plasma Sintering (SPS). The thermal source is via Joule heating from electric resistance of the powder, which is more efficient than an external source of thermal energy. However, SPS is a technology that is relatively recent in ceramic processing and includes phenomena that are not well understood.

UHTC composites are of interest to extreme environment conditions. Past and current investigations of extreme environments have been consistent with testing methodology of materials for hypersonic flight.¹²⁻¹⁴ The most commonly reported composition is ZrB_2 -SiC when it was discovered that passivation by SiC oxidation occurs effectively up to a limit of 1800°C.¹⁵⁻¹⁷ Few studies have attempted materials testing at 3000°C. Furthermore, most powder-mixed composites have required between 33-50 mol% SiC. It is possible that small amounts ~ 5 mol% of

well chosen phase and well dispersed particles could result in superior performance due to a more homogenous passivating layer. Thus the opportunity exists to investigate not only more refractory compositions at new temperature regimes, but also the effects of small nanoparticle additions, thermal conductivity, melting point and microstructural homogeneity on the oxidation performance.

The general aims of this research included validating the hybrid powder sol-gel technology by demonstrating the ease of densification of the composite and improved properties in extreme environments. The specific aims of the project were:

- To determine whether HfC and ZrC can be produced with controlled nanoparticle size using sol-gel technology
- To understand the phase evolution and control the reaction mechanism of carbon and oxides of hafnium and zirconium at the nanoparticle level
- To determine whether it was possible to integrate these nanomaterials into composite processing via in-situ sol-gel synthesis
- To understand the microstructural evolution of the UHTC composites and their response to extreme oxidative environments.
- Adapt processing equipment such as the Lindberg tube furnace and the SPS to predictable outcomes

The structure of this thesis covers three processes: sol-gel synthesis (HfC and ZrC), coating and densification of ZrB_2 via SPS and oxidation testing of materials. Chapter 2 presents an overview of literature, introducing the challenges in producing UHTC materials, the sol-gel approach and the new field of extreme environment testing and evaluation of materials. Chapter 3 covers experimental techniques, particularly the synthesis of the chemical compounds required for the sol-gel process. Upgrades of the Lindberg furnace, calibration of the oxidation facility and modifications to SPS are included. Chapter 4 covers the early investigation into the synthesis of HfC nanoparticles, investigating reaction mechanisms, phase and microstructural evolution. Chapter 5 advances the control of the sol-gel synthesis to produce ZrC nanoparticles with control over

carbon yield and understanding of the agglomeration behaviour. These two chapters were prerequisites for Chapter 6, which investigates the coating of ZrC nanoparticles from an in-situ sol-gel process on the surface of ZrB₂. This chapter covers the surface treatment, control of carbon yield and densification of the ZrB₂-ZrC composite. Chapter 7 establishes the role of phase selection and microstructure in comparison to powder mixed composites. The correlation between microstructure, phase selection and materials properties under thermal oxidation conditions are discussed. Chapter 8 presents the conclusion of the research program and outlines subsequent ideas for future research and development.

2. Literature Review

A review of current literature is provided for background. It initially introduces ultra-high temperature ceramics and applications relevant to the final material. It also includes a brief history and parameters of their processing. Conventional processing techniques are covered first, followed by an introduction into sol-gel techniques. The limitations of composite processing are discussed, ending with the potential of sol-gel to participate in composite formation is illustrated by recent examples. Finally, a background and methodology for testing the “extreme environment” is reviewed before closing with the scope of the research program.

2.1 Ultra High Temperature Ceramics

Ultra-High Temperature Ceramics (UHTCs) are a class of materials that possess a melting point above 3000°C. These are usually transition metal carbides and borides that possess excellent thermomechanical properties and high thermal conductivity but are vulnerable to oxidation and thermal shock.¹⁸ Their properties make them candidates for extreme environment applications, such as exposure to high temperature, high energy plasma and radiation, aggressive oxidation and corrosion. A major interest in UHTCs appears to be in design of future aerospace structures such as in thermal barrier coatings for vectored thrust engines, sintered components such as intakes, nozzles, passive leading edges and chamber components that require materials for these environments.¹⁹⁻²³

UHTCs usually possess strong covalent bonds in their crystal lattice, which render very low atomic diffusivity even at high temperature. As a result, processing of UHTCs has several challenges that should be noted in terms of technical hurdles and capital costs. High temperature graphite, applied pressure systems, high vacuum and inert atmospheres are commonly required. However, industrialization has driven favourable powder processing routes. Thus there has been more focus on “terminal” sintering technology rather than developing “special powders”. This does not mean that powder composition, size, aspect ratio and impurities have been neglected. In fact, the rise of nanomaterials is likely to increase the awareness that control of processing at both ends is equally

important. Nevertheless, conventional powder ceramic composites usually infer purchase, mixing and milling the powder before consolidation. Monteverde *et al* succinctly cites the continuing challenges with conventional UHTCs: sintering temperature $\sim 2300^{\circ}\text{C}$ without pressure, porous microstructures, inhomogeneity, and large grain size for full density, all resulting in reduced strength and toughness.²¹ These are clearly defined limits that undermine the dominance of micron-size powder systems. This is especially true to UHTCs because their sintering temperature is so high before solid-state diffusion is appreciable. There are techniques that do not rely on activation of powder surfaces, such as liquid phase sintering. Despite high densities from these methods, refractory ceramics should be limited to solid-state reactions. This avoids intermetallics, glass phases, or components that form a liquid phase during sintering. These will likely repeat the same phase transitions during applications at high temperature. The common solution is to apply pressure on the powder to consolidate UHTCs. One of the best of these techniques is Spark Plasma Sintering (SPS). However, despite the purported advantages of new sintering technologies, these compositions of $\text{HfB}_2/\text{ZrB}_2$, HfC and often SiC still require carefully selected sintering aids such as Mo/Ta/Zr-Si_2 to encourage diffusion and even some attempts at including a chemical reaction.²⁴⁻²⁶ These are strategies to increase solid-state diffusion. However, these microstructures still report issues with formation of non-equilibrium phases, incomplete reactions, required sintering aids and closed porosity.²⁷⁻²⁸ Surprisingly little study has been done on modification of the surfaces of these powders.

The condition of the starting powder is often overlooked in the densification of challenging ceramics. Powders are often coarse of size in the order of microns and purchased directly from a vendor. UHTC bodies should ideally not contain thermally inferior phases unless they deliberately convey an advantage. In particular, impurities from grinding media and oxygen uptake are key impurities of powder preparation. When mixed with high aspect ratio whiskers and fibers – often added for toughening – the milling is further restricted to prevent damage to the fibre/whisker aspect ratio, thus reducing its ability to mix well.²⁵ The powder itself is rarely altered, and this limits the driving force for sintering. Typical coarse UHTC powders of $\text{ZrB}_2/\text{HfB}_2$ yield in the order of 70-80% of theoretical density at

2100-2200°C.²⁹ They are generally considered undensifiable without a diffusion sintering aid and applied pressure below 2000°C.³⁰⁻³¹ The most logical step is to change the powder size, which should increase the driving force for sintering. Finer powders have always been in the interest of coatings, cermets, metals refinement, strengthening and creep resistance since these processes and properties also depend on high surface area.³² It is reasonable to conclude that modification of how powders are fed into systems – such as nanoscale powders – is desired for production and fabrication.

Sol-gel has been a proven technique in producing nanometre-size UHTC powders at low temperature.³³⁻³⁴ The versatility of a liquid solution precursor allows for morphologies not available in powder techniques, such as submicron-thick coatings, continuous fibers and porous materials. It also offers an advantage in processing and sintering technologies. This is not to say that the terminal sintering step is irrelevant. Densification of UHTCs also requires a proven sintering technology. SPS is the technical successor to the Hot Press (HP). This used external resistance heating from passing electric current ~ 500A through graphite, SiC or MoSi₂ electrodes. Passing several thousand amperes through a sample in pulses is a different mechanism. The pulsing of high currents through the powders purportedly results in a localised plasma on the surface, which rapidly cleans oxide impurities and promotes higher surface activity.³⁵ With additives of SiC and Ta/MoSi₂, full density is achieved at temperatures and dwell times better than hot pressing ~ 1800°C.^{26, 36} However, there are some contradictions between different materials suggesting that despite generally better performance of SPS over hot pressing, further investigation is required. Furthermore, SPS is pressure assisted, which is expensive and impractical for complex shapes, which may be required in industries such as aerospace manufacturing. Thus innovation in powders and sintering strategies is still a part of competitive UHTC materials.

2.2 Carbides and diborides

This section reviews the properties of the carbides and diborides that are the primary UHTC materials. The various production methods will cover powder-

based synthesis in significant detail, highlighting challenges in sintering UHTCs, but also focusing on some related topics that benefit from nanopowders such as powder-based coatings, cermets and metals processing.

2.2.1 Refractory properties of carbides and diborides

A brief overview of the UHTC carbides (MC_{1-x}) and diborides (MB_2) is provided, where $M = Zr$ or Hf . These are the compositions that are directly relevant to this work. However, other UHTCs will also be included where the same challenges are present in processing. The focus will be on the carbides because most of the program is focused on their synthesis. These carbides are non-stoichiometric face-centred cubic crystal structures following an NaCl-type lattice with variation in solubility of carbon and oxygen.³⁷ Some properties of the carbides and diborides covered in this work are shown below in Table 2.1.³⁷⁻⁴⁰ Highly covalent bonding and the short bond distance gives metal carbides the highest melting points over the diborides, nitrides and oxides.

Table 2.1. Some crystallographic, mechanical and thermal properties of the Zr/Hf family of carbides and diborides.^{37, 40} Note the electrical resistivity of MC_{1-x} .

	ZrC	HfC	ZrB ₂	HfB ₂
Crystal structure	Cubic	Cubic	Hexagonal	Hexagonal
Lattice parameters (Å)	a = 4.697	a = 4.642	a = 3.169 c = 3.530	a = 3.142 c = 3.476
Composition	ZrC _{0.55-0.99}	HfC _{0.6-0.99}	Zr _x B _{2x}	Hf _x B _{2x}
Melting point (°C)	3420	3928	3246	3380
Density (g cm⁻³)	6.59	12.7	6.10	11.2
Young's modulus (GPa)	495	480	496	500
Vickers Hardness (GPa)	25.5	26.1	20.0	24.8
Electrical resistance (×10⁸ Ωm)	76.5	39	9.7	10.6

Carbides possess a slightly higher melting point due to the shorter metal-carbon bond, and a slightly lower elastic modulus shown in Table 2.1. Moving down the Periodic Table from Zr to Hf, the lattice parameters decrease due to smaller ionic radii and shorter bond distance, resulting in higher thermal stability. The disadvantage of carbides is the affinity for oxygen. As a result, their use is generally restricted to reducing or inert environments, such as molten metal crucibles, nuclear applications or transistors.⁴¹ More conductive UHTCs such as TiC and TiB₂ have applications such as anodes for Hall-Héroult aluminium production or in magnetic recording heads.^{5, 42} UHTC materials are candidates for the next generation (Gen IV) nuclear reactors, which rely on advanced materials as passive safety features. The low neutron capture cross-section, in addition to higher temperature chemical and mechanical stability, drives research into ZrC into replacing SiC in nuclear fuel coatings and claddings.⁴³⁻⁴⁴ CVD-based ZrCl₄ with a hydrocarbon source has produced practical deposition of ZrC coatings in the order of 35µm.⁴⁵ ZrC and ZrB₂ are also being tested as a future solar receiver material able to withstand focused visible light.⁴⁶ The diborides are more resistant to oxidation due to the formation of the protective but volatile boric oxide decomposition product at around 700°C, resulting in a parabolic oxidation behaviour.⁴⁷ This makes them the primary candidate for more thermally aggressive and oxidative environments. Their properties are similar to the carbides, apart from a higher electrical conductivity.

2.2.2 Powder synthesis and morphology

Carbides are produced from reduction of an oxide, hydride or metal form, which indicates the extent of the oxidation of the metal cation and extent of endotherm for chemical reduction. Kinetically, the diffusion of carbon has been recognized as centripetal, so the coarseness of the oxide and carbon sources dictate the required diffusion distance and can predict powder size.⁴⁸⁻⁴⁹ Thus large inhomogeneities occur with powdered graphite, and smaller and more uniform particles sizes are generally obtained from liquid or gas phase precursors of carbon. Nevertheless, the required reaction temperature for carbon self-diffusion into the oxide lattice is still in the order of 1600-2000°C.⁵⁰⁻⁵¹ The borides have similar endothermic requirements shown in Table 2.2. However, carbon is often the reductant used to remove oxygen from boron, which means that excess boron

is often needed to drive the reaction to prevent carbide formation.⁵² The boron carbide reduction is also a common technique, and direct borothermal reduction can also be used. Both carbide and boride synthesis are strongly endothermic and it can be seen that $\Delta G < 0$ with temperatures ranging from a minimum of 1500°C to 1700°C in Table 2.2.⁵²

Table 2.2. Reduction reactions used to synthesize zirconium diboride and changes in free energy as a function of temperature.⁵²

Reactions	Category	Example	($\Delta G_{\text{rxn}}^{\circ}$) (kJ)
(1)	Carbothermal	$\text{ZrO}_2(c) + \text{B}_2\text{O}_3(l) + 5\text{C}(g) \rightarrow \text{ZrB}_2(cr) + 5\text{CO}(g)$	$1431-0.803T$
(2)	Borothermal	$\text{ZrO}_2(c) + 4\text{B}(c) \rightarrow \text{ZrB}_2(c) + \text{B}_2\text{O}_2(g)$	$301-0.178T$
(3)	Boron Carbide	$7\text{ZrO}_2(c) + 5\text{B}_4\text{C}(c) \rightarrow 7\text{ZrB}_2(c) + 3\text{B}_2\text{O}_3(g) + 5\text{CO}(g)$	$1378-0.924T$
(4)	Combined	$2\text{ZrO}_2(c) + \text{B}_4\text{C}(c) + 3\text{C}(g) \rightarrow 2\text{ZrB}_2(c) + 4\text{CO}(g)$	$1134-0.668T$

As a result, reaction temperatures to produce carbides and borides are usually in the order of ~2000°C. To drive the reaction forward, deliberate equilibrium shift with excess reactant or removal of reaction product from the system are typical strategies. There are numerous wet chemical routes for carbides, but for borides to date only thermal decompositions of borohydrides ($-\text{BH}_4$) in the presence of the target metal chloride (MCl_4) have produced the target metal diboride (MB_2).⁵²⁻⁵³ These processes require special equipment such as autoclaves (high pressure versions are usually quartz lined) and high vacuum combustion chambers. Synthesis temperatures are in the order of 700°C because the enthalpy of formation is negative, extremely exothermic and the heat released can continue the reaction in a self-propagating high temperature synthesis (SHS) reaction yielding nanosize ZrB_2 .⁵⁴⁻⁵⁵ However, these are still emerging technologies whereas 100-200nm TiC and ZrC are able to be purchased.

The current ceramic industry is dominated by coarse powder from inexpensive and heavily automated processes. Specialized powders are usually synthesized by laboratories. A pertinent demonstration of the powder industry is a brief overview of powders of ZrC, TiC, ZrB_2 and TiB_2 , which are listed in Table 2.3 from product sheets. The diborides are listed first in Table 2.3, followed by the carbides. Higher “Grades” denoted by increasing letter have smaller particle size, but at the cost of higher oxygen content. This is detrimental for sintering and

refractory properties. It is unclear whether the oxygen impurity is oxide or oxycarbide since these impurities are detected by EDS.

Table 2.3. Ti/Zr carbides and diborides properties according to H.C. Starck.

Compound	Size μm , D 90%	Impurities (< wt%)			HC Starck PD Code
		C	O	Other	
TiB ₂ Grade G	30	0.6	0.6	2.3	PD-5237
ZrB ₂ Grade A	12	0.2	1.0	0.7	PD-5172
TiB ₂ Grade F	7	0.4	2.5	1.1	PD-5123
ZrB ₂ Grade B	6	0.2	1.5	0.7	PD-5172
ZrC Grade A	35	0.4	0.6	0.9	PD-4004
ZrC Grade B	12	1.5	0.6	0.9	PD-4004
ZrC Grade XF	7	0.4	2.0	0.9	PD-4004
TiC STD250	3	0.5	0.8	0.6	PD-5208
TiC HV250	3	0.2	0.5	0.6	PD-5156
TiC STD120	1.5	0.5	1.3	0.6	PD-5208
TiC HV120	1.5	0.2	1.0	0.6	PD-5156

The second point to note is that the diborides appear to have more impurities of metals (iron, nickel, etc) perhaps indicating a metal catalyst processing aid. A third factor is that extensive ball milling has also been known to cause undesired phase transformations and chemical reactions due the high surface area affecting catalytic activity and surface energy thermodynamics.⁵⁶ These can form new phases in the mixture, or result in a disproportionate amount of surface oxide film to the bulk non-oxide. Special grades are available that manipulate equilibrium and predominance reactions. The HV high vacuum materials allow the reaction to take place stoichiometrically with less carbon and lower temperature, at higher production cost. The B grade ZrC has a smaller particle size likely achieved by using a higher carbon content, which is another method of providing a driving force for the reaction, particularly if at equilibrium the reaction product is rapidly removed. As powders are the dominant feed source for ceramic materials, a review of the challenges in powders processing is appropriate.

2.2.3 Processing challenges

This section highlights the challenges of powder synthesis. It illustrates the need for increased research into special morphologies and strategies to change the nature of bulk ceramic consolidation, particularly given the difficulty of UHTC

materials. This section effectively covers the types of ceramics by phase volume; sintered materials are considered 100% ceramics, while the term “hard metals” or cemented carbides refers substantial composition of a metal binder. A small section will cover minor phase UHTC powder additions in metals processing and coatings. These all have a relevance in dispersed, high purity, nanosize powders, but the focus will be on sintering and ceramic nanocomposite formation.

2.2.3.1 Sintering UHTC materials

If the bulk structure needs to be constructed of a ceramic, the powder must be consolidated by sintering. It is generally recognized that densification of UHTCs to acceptable density can only be achieved by applied pressure, which limits final shapes and adds post-processing costs. Smaller particle/crystallite size, deagglomeration, and lower content of impurities would be of benefit UHTC processing, but there is a stronger emphasis on sintering or terminal processing technologies. Two types of structural ceramics are used in sintering technology. The first is the oxides of Si and Al (including mullite and zircon), which have operating temperatures up to ~1600°C. Zirconia furnaces can reach ~2000°C. These oxides are structural refractory materials for tube, ovens, rapid heating and muffle furnaces. UHTCs have generally required the second type of structural material, which is graphitized carbon. This immediately adds a variable in controlling these reactions, as carbon has substantial interstitial solubility in most UHTCs.^{1, 38} Thus low temperature synthesis has lower energy consumption and potentially has better control of the reaction, because carbide formation and sintering involves the transport of matter by solid-state diffusion. In carbides, this is the movement of the carbon atom and the diffusivity is extremely low; this is indicative of strong bonding and thus high melting point.⁵⁷⁻⁵⁸ But diffusion is also confined to the rules of conservation of mass, electroneutrality and follow the respective chemical formula. The system must include the partial pressure of the atmosphere, because this affects electroneutrality. A simple example would be the production or sintering of carbides in an atmosphere with CO, O₂ and CO₂. Atomic diffusion of C or O in the carbide lattice MC_{1-x} must include this atmosphere and is affected by processing conditions such as vacuum and inert gas, with thermodynamic affinity for oxide formation.⁵⁹⁻⁶⁰ This non-stoichiometry is derived from other causes as well. Dopants/solutes added to a system modify the

kinetics by following electroneutrality. For example, if a mixed Cr_3C_2 was added to ZrC , and the diffusion of Zr vacancies is the rate controlling mechanism, this addition increases the sintering rate. However, if the interstitial carbon vacancies are the controlling mechanism, then the sintering rate is reduced due to saturation of the sites. Furthermore, carbides are often non-stoichiometric due to the varying oxidation states and the affinity of oxygen for interstitial sites. Reaching equilibrium, for example, $\text{HfO}_{0.1}\text{C}_{0.8}$ in a specific particle could indicate that the substitution of oxygen for carbon cannot complete to $\text{HfC}_{0.99}$ because of a high oxygen partial pressure, insufficient carbon monoxide (to remove oxygen) or the temperature is too low for the kinetics of the oxygen removing reactions. Fig 2.1 illustrates typical challenges noted in Hot Pressing (HP) of HfB_2 and HfC .⁶¹

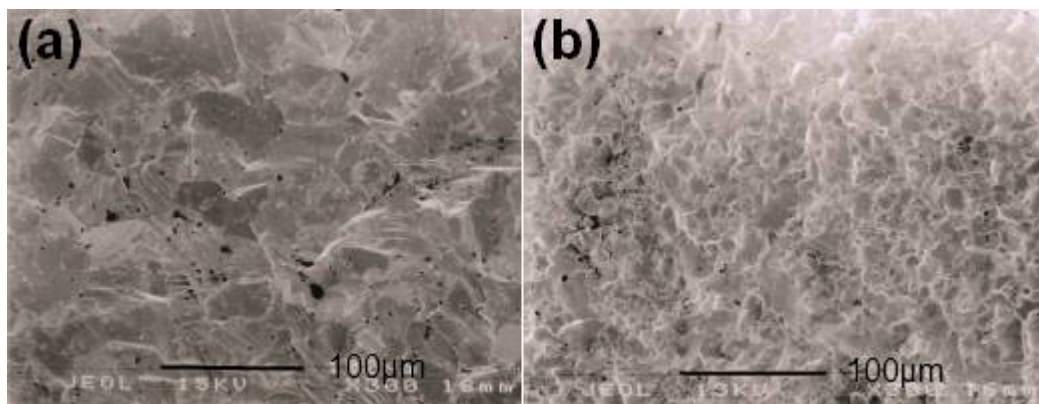


Fig 2.1. Typical Hot Pressed microstructures for **(a)** HfC sintered at $2500^\circ\text{C}/40\text{min}$ with large grains, pores and grain boundary glass **(b)** HfB_2 at $2160^\circ\text{C}/3\text{h}$ with grain boundary glass.⁶¹

Both samples did not reach full density, with 1% open porosity and 10% closed porosity.⁶¹ Without using applied stress, sintering to full densities in UHTCs becomes prohibitive and results in poor mechanical properties, well documented by Lanin et al.⁶² In providing more energy to the system, full densities at 3000°C resulted in decreased peak strength from 650MPa to 320MPa due to the increase in grain size to $30\mu\text{m}$ from $4\mu\text{m}$ at 2500°C .⁶³ This illustrates the difficulty in achieving appreciable diffusion and controlling it, as well as some complexities associated with processing ceramic powders.

The main factor for understanding powder sintering is that chemical potentials of concentration dictate that atoms move toward the concave surface.^{57, 64} This is important because all surfaces of powders are at curvature and the moving convex grain boundary is the movement of atoms, but the boundary migrates to the centre of the concavity. This is the same rule for pores if the surface is convex to the boundary. Note that electro-neutrality also dictates that each atom may also need to 'wait' for its counter-ion in order to maintain charge balance. Fig 2.2 explains the general concept of convex/concave surfaces (a) and the interaction of atoms in (b) grain boundaries and (c) pores.

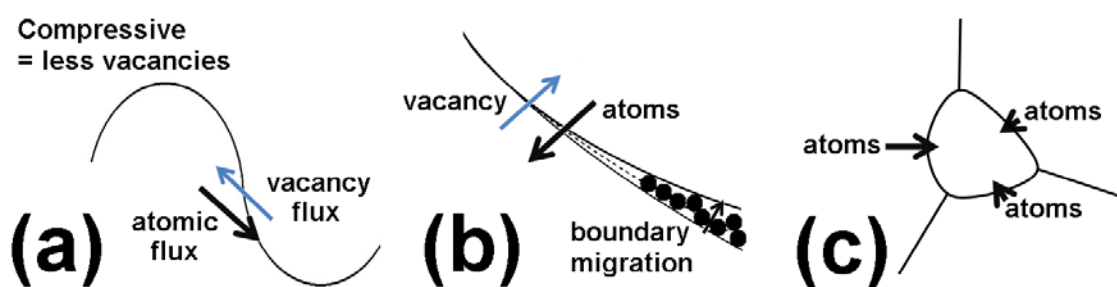


Fig 2.2. (a) Schematic showing aspects of curvature and atomic diffusion which apply to atoms moving in (b) grain boundary migration and (c) pore shrinkage.

Sintering involves the movement of atoms. In significant numbers, atoms form between particles in the objective of forming a smaller volume of higher density. With UHTCs the neck building between powder particles is particularly crucial. Because atoms move faster along the surface than in the lattice where they are restricted, surface diffusion can build necks between particles without reducing the actual volume occupied. This is known as a non-densifying mechanism and occurs preferentially at low temperatures. Studies have found that the dominant neck generating mechanism for Zr/TiB₂ systems appears to be a non-densifying vapour transport mechanism, which begins with surface mechanisms well before the densification temperature.⁶⁵ Eventually this stops the diffusion from the inside the neck and is responsible for porous microstructures. One method to overcome this limitation is an applied pressure, because this has no effect on the non-densifying mechanisms. Instead, it enhances the activity of the new grain boundary, forcing grain boundary sliding between the established necks. The other is a higher heating rate that can avoid the surface diffusion regime.

Another way to appreciate the contributions to sintering is to consider the basic thermodynamics. Starting at the initial stage of loose powder to final stage of consolidated bulk, it is best to list them by general order of magnitude. The contributions typically from largest to smallest in UHTCs are (1) chemical reaction, (2) externally applied pressure and (3) the reduction of surface area.⁶² The contributions from the work done by applied pressure in Hot Pressing (HP) where $p_a = 30$ MPa and a molar volume of $V_m = 12.2 \times 10^{-6}$ m³ (TiC, typical UHTC) can result in a work of 375J from (2.1):^{57, 64}

$$W = p_a V_m \quad (2.1)$$

However, this is irrespective of surface curvature due to particle size since molar volume is relatively constant. In comparison, the basic sintering model without applied pressure is the reduction in surface area. In (2.2), E_s represents a change (decrease) in specific surface energy from the volume of particles to a single body of the same volume:^{57, 64}

$$E_s = \frac{3\gamma_{sv}V_m}{a} \quad (2.2)$$

Where specific surface energy $\gamma_{sv} = 1$ Jm⁻² and particle diameter $a = 3$ μ m (typical powder sizes per Table 2.3) and E_s returns a value 12 Jmol⁻¹. Under the assumptions of UHTC processing with pressure assist, it can be seen that decrease in free surface energies are quite small as the value is rather low compared to the impressive contribution by applied pressure. However, HP is still challenged by UHTC materials as there is a pattern in UHTC requiring additives in quantities of 4-10% vol to improve kinetics, even addition of metals (Ni, Nb), to more innovative sintering using SiC.⁶⁶⁻⁶⁷ Table 2.3 also included 2-4 wt% oxide, carbon and other metallic contaminants. However, these encourage diffusion by creating chemical gradients of mobility, moving around solute and soluble atoms. As density increases, the overall surface curvature is reduced, the driving force is reduced and isolated pores remain at triple points such as Fig 2.5(c). But vapour

transport is still a problem at the last stage of densification, as it allows the grain boundary to move past the pore. Sufficient time must be allowed for the trapped gas to move along the grain boundary and exit. Particles such as SiC are often used to retard this migration to allow time for gas removal using these high diffusive paths.⁶⁸⁻⁶⁹ Otherwise, sintering must reduce the dwell time at high temperature because diffusion of the grain boundary can rapidly decrease the strength of the ceramic, noted previously.

One method to increase the driving force is to use a chemical reaction to facilitate diffusion. The typical values of the free energy of a chemical reaction can be expressed in (2.3) for values of absolute temperature $T = 2000\text{K}$ or more and an equilibrium constant K_{eq} defining the ratio of products over the reactants.⁶⁴

$$\Delta G^0 = -RT \ln K_{eq} \quad (2.3)$$

While this depends significantly on the reaction equilibrium, carbide/boride temperatures are likely quite large $\sim 2000\text{K}$ for reduction. The equilibrium constant is unknown, but is likely shifted to positive values because CO is always removed from the system. Nevertheless, output values from (2.3) range from 10^3 - 10^4 Jmol^{-1} for empirical values $1 < K_{eq} < 5$ indicative of typical yields in carbothermal reduction. This is impressively order of magnitude higher than applied pressure or surface curvature. But chemical reactions are rarely used due to difficulties in controlling the microstructure.⁶² Sintering additives can be considered a minor chemical reaction as it results in movement of vacancies, solutes and impurities. But there appears to be only some sporadic success with full reaction sintering. Using more raw precursors such as Zr and B after attrition milling densified ZrB_2 to 99% at 2100°C but applied pressure was still required.⁷⁰ But the same techniques have been used to densify Zr and C above 99% density as low as 1200°C using applied pressure.⁷¹ These disparities indicate there is much research required to understand how reactive sintering can be used, particularly when differences between the reaction and densification rates are not well understood.

However, if the reduction in surface area in (2.2) is inversely proportional to the driving force, reducing the particle size from 5 micron to 50nm results in a decrease in free surface energy of 1500Jmol^{-1} exceeding that of an externally applied pressure and comparable in magnitude to chemical reactions. This is an indication of the potential of nanoparticles in increasing the driving force for sintering. There is already some significant evidence of improved densification using pure nanoparticles without pressure. Sacks et al were able to densify their sol-gel derived 100nm ZrC powders to 98% density at $1900^\circ\text{C}/2\text{h}$ and 99% at $1950^\circ\text{C}/2\text{h}$, which suggests that the contribution from surface curvature is modest. This contrasts with results from Talmy et al, which reported 98% densification of 100nm TaC powders at a low 1500°C compared to their reportedly powder TaC failing to densify.⁷² For comparison, densification of micron size TaC has reportedly been in the region of 2300°C .⁷³ Nanopowders of HfC of 225nm were able to be fully sintered at 2400°C to 98.4% density with a grain size of about $4\mu\text{m}$ within 30 minute dwell time.⁷⁴ One unusual method of synthesis known as mechanochemical synthesis involves 25-50h high energy milling of ultrafine transition metals with toluene, able to form 7-10nm size carbides from room temperature and able to be sintered to full density at 1200°C .⁷⁵ However, some microstructures of these early monoliths were not released. Control of the densification process is extremely difficult with carbide and other nanopowders because: (1) Dispersion is difficult even with application of suspensions; (2) intra-agglomerate pores are more common than inter-agglomerate pores and (3) the larger particulate surface area requires applied pressures in excess of GPa to prepare greenbodies of nanopowders.⁷⁶⁻⁷⁹ The major challenge for ceramists is the high surface energy that means (4) grain growth is difficult to control both in size and uniformity if nanocomposites are to be obtained.⁷⁶⁻⁷⁹ The aforementioned densification of ZrC at 1200°C resulted in a $5\mu\text{m}$ grain size, indicating that the nanostructure had been lost.⁷⁵ These are challenges that must be overcome if nanostructured ceramics are the goal.

This section highlights some challenges in densification of UHTCs. The intrinsic problem is the low diffusivity of highly covalent atoms. Processing technology also involves slow heating that reduces the driving force for sintering before particle surfaces are activated. Any mechanisms that increase diffusion could be

useful, as long as the interaction between pore and grain boundary can be controlled. Using nanosize powders could be a key factor in driving densification. However, while densification appears more promising, the lack of consistent literature on processing UHTCs present a cautionary tale on the microstructural control of reactive sintering and highlights difficulties with nanopowders.

2.2.3.2 Alloying and nanocements or “hard metals”

Cemented carbides are usually a liquid-phase sintering process and dominate the tool industry of drilling and cutting operations. High temperature strength and hardness qualify UHTCs for this application. Failure mechanisms are spalling, abrasion, pullout of carbides or extrusion of the metal binder.⁵⁶ Nanostructured cemented systems have been investigated, showing improved physical, mechanical and tribological properties from smaller grain size and improved densification.⁸⁰⁻⁸³ The metal binder and ceramic carbide are mixed together with sintering additives and even rare-earth refractory precursors.⁸⁴ The compositions are usually tungsten carbide (WC), although there are reports of ZrC and TiC-based cermets.⁸⁵ Obtaining nanosize powders without the powder route is expensive, based on solution/sol-gel spray pyrolysis and CVD processes.⁸² As a result of the aforementioned challenges, these nanocemented carbides are only produced in research laboratories and even commercial level 100nm scale WC cemented tools have not been achieved.⁵⁶ The other major use for carbides – specifically the UHTC family – is grain refinement, dispersion and creep strengthening of metals. Substantial amounts of HfC, NbC, TiC, ZrC are found in the superalloys of W and Mo. Alloys based on Cu, Al, and Mg also use Ti, Mo and W is to produce a second quantity of hard carbides from the matrix atoms, with improved high temperature performance.⁸⁶ Less than 1.3% wt HfC reportedly doubles the elastic modulus and flexural strength of tungsten.⁸⁷ Even pure Mo with only 0.5 wt% HfC increases in yield strength at 800°C from 75MPa to 250MPa.⁸⁸ For nanopowders, less material can be used because of the higher surface area. More dispersion results in more particles and more respective strain fields that prevent dislocation motion and strengthen the material. The challenges in cements and alloying overlap with powder coating preparation, which addresses nanodispersion of UHTCs.

2.2.3.3 Surface coatings

Coatings can be deposited by several methods, but the powder-based coatings, despite their general coarseness compared to gas and liquid-phase techniques, dominate the industry due to their inexpensive processing and high mass deposition rate. While SiC is a major compound in powder coatings, UHTCs – TiC, ZrC, WC and vanadium carbide (VC) – are also used for wear, hardness, oxidation resistance and thermal barrier coatings.⁸⁹⁻⁹⁰ Like sintering, this is also dominated by versatile “terminal” technology for spraying the powder on the surface, and is often of cemented carbide composition.⁹¹ Cold and “warm spray” defined by temperature, plasma “hot” spray, detonation guns, diffusion bonding and simultaneous deposition under laser are some overlapping deposition techniques that use a powder feed.⁹²⁻⁹³ Powders can be especially coarse, particularly UHTCs. HfC and TaC have absurdly high melting points ($T_m \sim 4000^\circ\text{C}$) and correspondingly high oxide reduction temperatures, and vacuum spraying of these powders start with an unmilled powder size in the order of $50\mu\text{m}$, which challenges the required partial melt formation and densification.⁹⁴ A smaller final grain size is again advantageous for the aforementioned reasons of densification, but this requires smaller size powders.⁹⁵

Reduction in powder size results in higher ejection velocities, lowering gas and temperature requirements.⁹⁶ Detonation gun techniques have used typical cemented mixtures in nano-WC/Co to achieve much higher powder particle velocities $\sim 1\text{km/s}$ for higher density coatings shown in Fig 2.3(a).⁹⁷

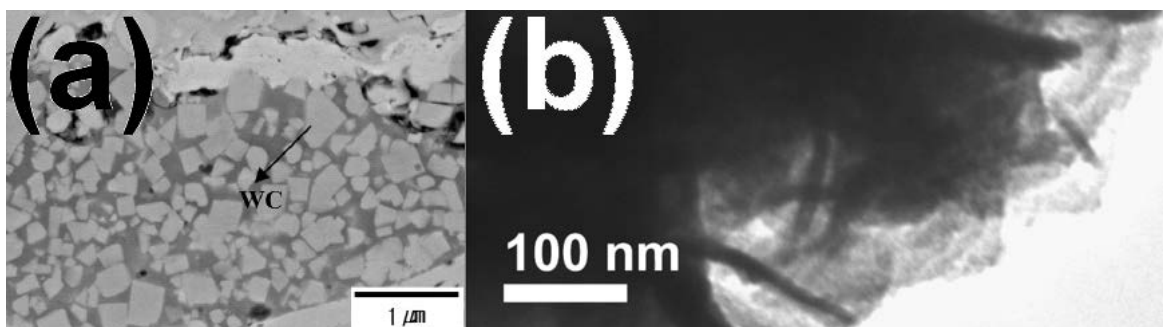


Fig 2.3. (a) Well dispersed nano-WC from low temperature plasma spray process
(b) TiB_2 plates derived from nano- TiO_2 from sol-gel laser deposition

“Hot” sprays suffer from decarburization of carbides due to the low oxidation resistance and only moderately inert atmospheres provided.^{89, 98} Nanoparticles have higher surface area and increased vulnerability to oxidation, causing a drive to use cold spray methods, relying on deformation interparticle bonding and particle-surface bonding.⁹⁶ The few nanopowders reported are generally derived from solution techniques due to their relatively inexpensive cost. Some carbide formation can be expected by using carbon rich atmospheres or mixing carbon with the powder feed. TiB/TiB₂ were synthesized in laser deposition methods using a TiO₂ sol-gel mixture in B₄C/C powder feed shown in Fig 2.3(b).⁹⁹ There is some interest in improving the powder feed for powder deposition coatings, but these are all subject to the same challenges mentioned in the sections on powder sintering. One aspect not explored is that under directed energy of some of these “hot” techniques, nanopowders should experience a depressed melting point due to the thermodynamic contribution of the surface energy to the stability of the particle. This can likely assist in mass transfer, preventing porosity, high density by better deformation on impact and offering improved solidification processing.

2.2.3.4 Summary

Ceramic micron-size powder is a permanent manufacturing line due to the versatility of its terminal sintering, deposition and forging technology. To change this, there must be a need for nanomaterials. Certainly using nanopowders over micron-powders would assist in producing superior materials, increase fundamental understanding of surfaces and applied research processes, as well as reducing energy consumption. These are excellent and desirable outcomes. But the key aspect is that the powder size means that nano-level features (e.g. micro and mesoporosity) are impossible to control and morphologies are limited. Currently the need for fibers, films, coatings, internal surfaces and better mechanical properties is driving interest in ceramic nanotechnology. Due to challenges in densification, UHTCs processing has already joined this group. While powders are useful for bulk processing, specialized requirements are satisfied by liquid and gas phase techniques. One such liquid technique is sol-gel or solution-based processing.

2.3 Sol-gel technology

The sol-gel or solution-based synthesis of UHTCs from organometallic liquid precursors is of increasing interest. Sol-gel uses chemical precursors in the form of a liquid phase to form polymeric and colloidal ceramics. The disadvantages of sol-gel – including low production yield, high cost of synthesis, batch processing and handling controls – are offset by advantages where specific morphology or microstructures are required. The solution-based techniques have been noted as low temperature sources for nanosize possibilities for sintering, coatings, nanocements and dispersion strengthening of UHTC-composed materials. This section will review sol-gel derived UHTC carbides as the focus of this research.

2.3.1 Carbides by sol-gel

The carbide sol-gel process is a simulacrum of the oxide-carbon powder processing. It uses a solution or 'sol' of the oxide precursor, mixed with a carbon precursor. Diborides have also been synthesized by adding a boron source in addition to carbon.⁴² Surfactants, precipitation and peptidization can stabilise the sol, which can then either be dried to 'gel' for porous monoliths, powders, cast on a substrate or drawn into fibers. The sources of the metal for the carbothermal reduction in gas phase can often be used for liquid phase processing. For example, $ZrCl_4$, a zirconium source for the zirconium oxide, is later reduced to ZrC in typical CVD processes.¹⁰⁰⁻¹⁰¹ The reaction still occurs at the nano-level because the diffusion distance for carbon to the neighbouring oxide is extremely short.

Synthesis of carbides through solution based synthesis was driven by early polymer-precursor SiC fiber technology from the 1970s that predates sol-gel SiC.¹⁰²⁻¹⁰⁴ The most common sol-gel process uses a metal alkoxide, often stabilised by a chelating agent, and the 'sol' performs a condensation reaction with a carbon source (that may also polymerize) to form a 'gel'. This results in polymeric or colloidal dispersions of oxide and carbon precursors. However, in titanium and zirconium, it is often simpler to precipitate or stabilize the oxide intermediate with carbon introduced in the form of a liquid prior to calcinations.¹⁰⁵ Absence of molecular networks can be considered solution rather than sol-gel processing, although the distinction is not emphasized. The result is a fine mix of oxide/carbon nanoparticles which can be reacted at relatively low temperature.

Sol-gel is a viable option for introducing high-aspect ratio or high surface area nanomaterials. The two key criteria are the selection of carbon and oxide sources.

2.3.2 Carbon precursors

There are several major criteria in selection of the appropriate carbon source. These depend on the complexity of the sol-gel process and the morphologies desired. For example, matching polymerisation rates are required to form Ti-Zr-O-C fibers, compared to a solution that merely requires mixing SiO_2 and C for nanopowder SiC. Solubility with the other components, boiling point of the carbon precursor when drying the mixture, polymerisation kinetics and decomposition ratio to carbon are key features in carbon sources.

Carbon sources often have poor solubility and boiling point outside the suitable range to maintain homogeneity with the other solution components during drying. This may lead to loss of the carbon source during evaporation, or conversely rapid evaporation of the solvent which may cause phase separation of the carbon precursor. The difficulty of integration is offset often when a particular morphology is desired. Using a pre-polymer carbon source to react with the oxide is one method of guaranteeing an interfacial reaction. Polyacrylonitrile (PAN) is a precursor for carbon fiber but has a relatively extensive preparation; but if mixed carefully with a stabilized titanium n-butoxide, the carbothermal reduction can be made to create TiC tubes shown in Fig 2.4.¹⁰⁶

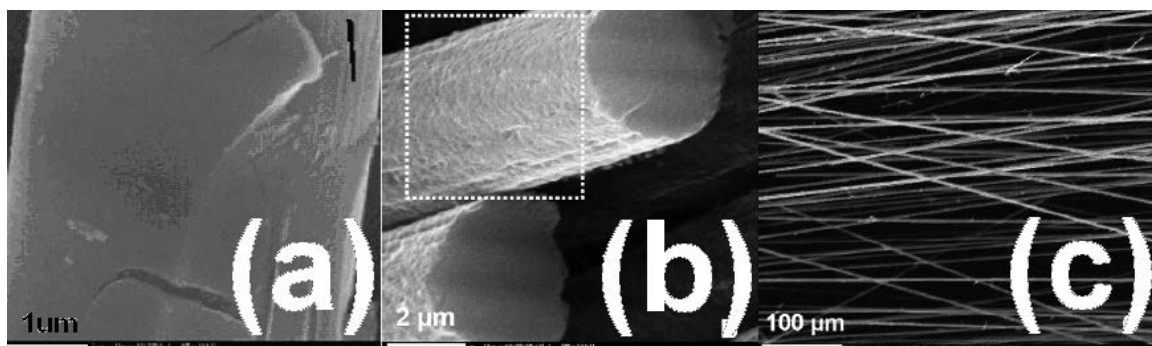


Fig 2.4. Example of (a) sol-gel coating of oxide on carbon resulting in (b) conversion at the surface (c) of multiple fibers in solution.¹⁰⁶

Other carbon precursors may have no solubility but are appealing because they are inexpensive. For example, soot and ash are usually nanoparticle and thus can form suspensions. Such a carbon source was used in the synthesis of TiC based on burned clarified butter – the mixture required pH control using ammonium nitrate, presumably to stabilize the colloids from expanding to micron size.⁵ Coal tar pitch, which decomposes to carbonaceous nanosize char, has been suitable to carbothermal reduction to synthesize SiC/C nanofibers at 1400°C and TiC at 1600°C.¹⁰⁷⁻¹⁰⁸

Carbides can also be produced by carbon black mixed with metal chloride precursors.¹⁰⁹ Some other unusual carbon sources are selected simply due to solubility. For example, polystyrene is a carbon source used because it dissolves in toluene, but would remain flocculated in water and ethanol based gels.¹¹⁰ The insoluble or particulate carbon precursors are generally high carbon yield and do not require a polymerisation step. Despite less solubility, they are inexpensive, simple, provide short diffusion distances to the oxide and good submicron level mixing. But sometimes more complex structures are required, which turn to biological carbon templates. An unusual example used a biomorphic carbon template of charred pinewood, mixed with stabilized alkoxides of Si, Ti and Zr to produce “biomorphic” carbides, deliberately utilizing the infiltrated 20µm pores as carbothermal reduction chambers shown in Fig 2.5.¹¹¹

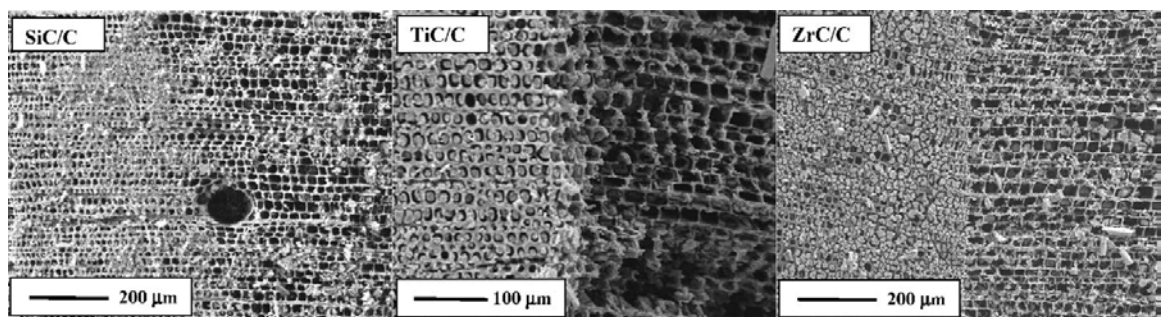


Fig 2.5. Template of charred pinewood to produce biomorphic carbides of Si/Ti/Zr.¹¹¹

In providing nanostructures unachievable by powder slurry infiltration, these biomorphic carbides have potential as membranes, filtration/separation and catalytic properties.¹¹²⁻¹¹⁴ However, most biological carbon sources are generally

used for good solubility, high yield and no polymerisation step. Examples include sucrose/saccharose, chitosan and cellulose. The higher molecular weight can limit their solubility, and high viscosity can prevent infiltration techniques. But these are superior to chars, ash and soot due to solubility. The drawback is that they require pyrolysis step to decompose to carbon. A methyl-cellulose mixed with a titania stabilized sol is capable of decomposing significant quantities of carbon to produce TiC.¹¹⁵ Saccharose is probably the most common biological carbon precursor. SiC nanowires and SiC/ZrC powders have been produced from a solvent of ethanol using saccharose as the carbon source.^{6, 116-117} Chitosan, a polysaccharide similar to cellulose, has been used as a carbon source to produce ZrC.¹¹⁸ Generally biological carbon sources are simple, having a high decomposition to carbon ratio per mole added. But the high polarity of hydroxide groups limits organic solubility. A similar limitation is on glucose and fructose. These biological carbon precursors can require water, which quickly alters the organic ambience, requiring the user to compensate for insolubility and phase separation. However, they are undemanding to handle and have minimal environmental impact.

As expected, the more toxic, artificial carbon sources are the most popular. One is the phenolic resin series, which has been the basis for sol-gel fibers, membranes, films and powders.¹¹⁹⁻¹²⁰ Often made from a condensation of formaldehyde and phenol with a $T_g \sim 90^\circ\text{C}$, their substantial solubility in organic solvents (for example, up to 50wt% in ethanol) makes it ideal for decomposing sufficient carbon for the reaction.^{7, 121} The condensation results in a predictable decomposition ratio, reporting char yields of about 40-60% wt C.¹²¹⁻¹²² Furfuryl alcohol is also a popular carbon source, due to its high solubility in ethanol, extremely low viscosity and known polymerization kinetics.¹²³ However, its disadvantage is that decomposition is heavily dependent on the level of crosslinking or alkylation of the resin, which can precipitate from solution when the molecular weight is too high or insufficient solvent is provided.¹²⁴ Yield of carbon can be varied depending on the level of alkylation, which is a key advantage of this monomer as a 'variable yield' carbon.¹²⁵ However, unlike phenolic resin, furfuryl alcohol networks form controllable mesoporous and

microporous oxide-carbon structures, making them ideal for selective membranes or catalytic surfaces where a template is important.¹²⁶⁻¹²⁷

The carbon source can also be derived from the process itself. Oxide sources are often stabilized by organic chelating agents, which are organic and decompose to carbon, provided the molecular weight is increased by crosslinking, condensation and esterification. Acetic acid, citric acid and ethylene glycol esterification can produce large polymers sufficient to decompose to carbon.⁴² Other molecules are so small, such as acetylacetonate "AcAc", that a 50:1 "AcAc":Zr molar ratio (250C/Zr) is required to produce ZrC indicating a 3/250 "retention" of possible carbon atoms.¹²⁸⁻¹²⁹ This inefficiency is offset by the simplicity, because it eliminates a component of the sol-gel process.

It can be seen that several carbon precursors exist for solution based reactions. The complexity of monomer to polymer reactions for producing carbon in these materials already shows a cautionary tale: high carbon yield is usually associated with an increase in complexity during processing. Selection of the carbon phase is a decision that is based on the requirements of the future microstructure.

2.3.3 Oxide precursors

The reduction of oxide to carbide is known as "shrinking core" or "contracting volume" by carbon diffusion; it is the morphology of oxides in the sol-gel that usually dictates the morphology.^{49, 74, 130} The major challenge for selecting oxide precursors is that these are organometallic synthesis reactions and the methodology is often brief and not published in detail in materials publications. This section briefly covers the selection criteria based on differences in oxide precursors for sol-gel.

The simplest oxide source is the chloride, which can transform to oxide at high temperature. The chlorides are still able to be substituted by the more stable oxygen species. Baca et al synthesized titanium carbides and diborides using $TiCl_4$ as the precursor at 1300°C, however, the experimental preparation suggests significant hydroxide stability using citric acid in low pH, which suggested condensation bridging of Ti-O took place.⁴² Another oxide source is

zirconium oxychloride, which is still in Zr^{4+} state, with two chlorides and one oxide occupying the co-ordination sites. Fig 2.6 shows two series of ZrC nanoparticles derived from carburization of $ZrOCl_2$. Yan et al (2012) used a zirconium oxychloride to produce nano-ZrC at $1550^{\circ}C$.¹³¹ Yan et al (2007) also reported using a similar method using oxychloride to produce nano-ZrC at $1400^{\circ}C$.⁷

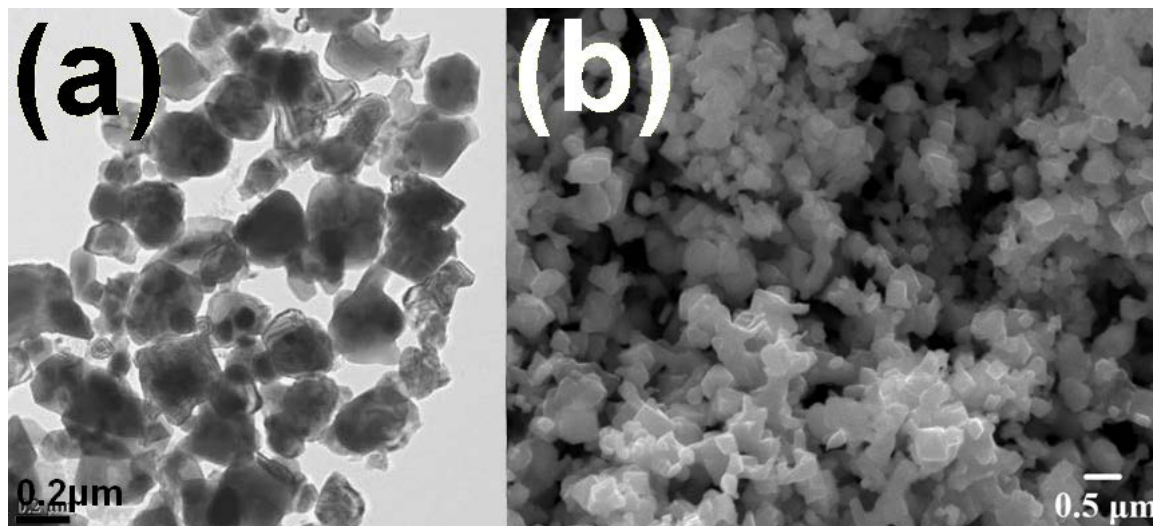


Fig 2.6. Nano-ZrC produced from the same oxide and carbon source, but different control over the sol-gel process showing (a) stabilized, 200nm (b) precipitated, 600nm.^{7, 131}

However, Yan et al (2007) achieved a smaller particle size of $\sim 200nm$ shown in Fig 2.6(a) over Yan et al (2012) in Fig 2.6(b) that reported $\sim 600nm$, with correspondingly lower carbothermal reduction temperature as expected due to smaller particle size that indicated shorter carbon diffusion distances.^{7, 131} Yan et al (2007) likely stabilized the hydroxide form by adding ammonium nitrate, so no proton accepting species was available whereas Yan et al (2012) likely lost the hydroxide stability and formed larger zirconia agglomerates.^{7, 131} Description of the experimental method suggested knowledgeable use of a drastic pH shift and possibly an electric double layer to stabilize colloids. This is an excellent example of the distinction between sol-gel and solution based processing in control over nanoparticles synthesis. Preiss et al further investigated pitch-based carbons with alkoxide, glycolate, peroxide and rutile particles in Fig 2.7.¹³² Briefly, this investigated the effects from different oxide “sizes”, which dictate the final ZrC size. The $5\mu m$ scale bar in Fig 2.7 indicates that (a) and (c) are well into submicron size, while (b) and (d) are distinguishable to micron size.¹³² The tracks

in Fig 2.7(a) appear to be from drying and cracking; textures within the “grains” show agglomerates of nanoparticles.¹³² In summary, most species form limited networks and thus form submicron precipitates. Due to their ability to form complete networks, the alkoxides are generally the most favourable oxide source, associated with polymeric gels that yield the smallest particle sizes.^{110, 117}

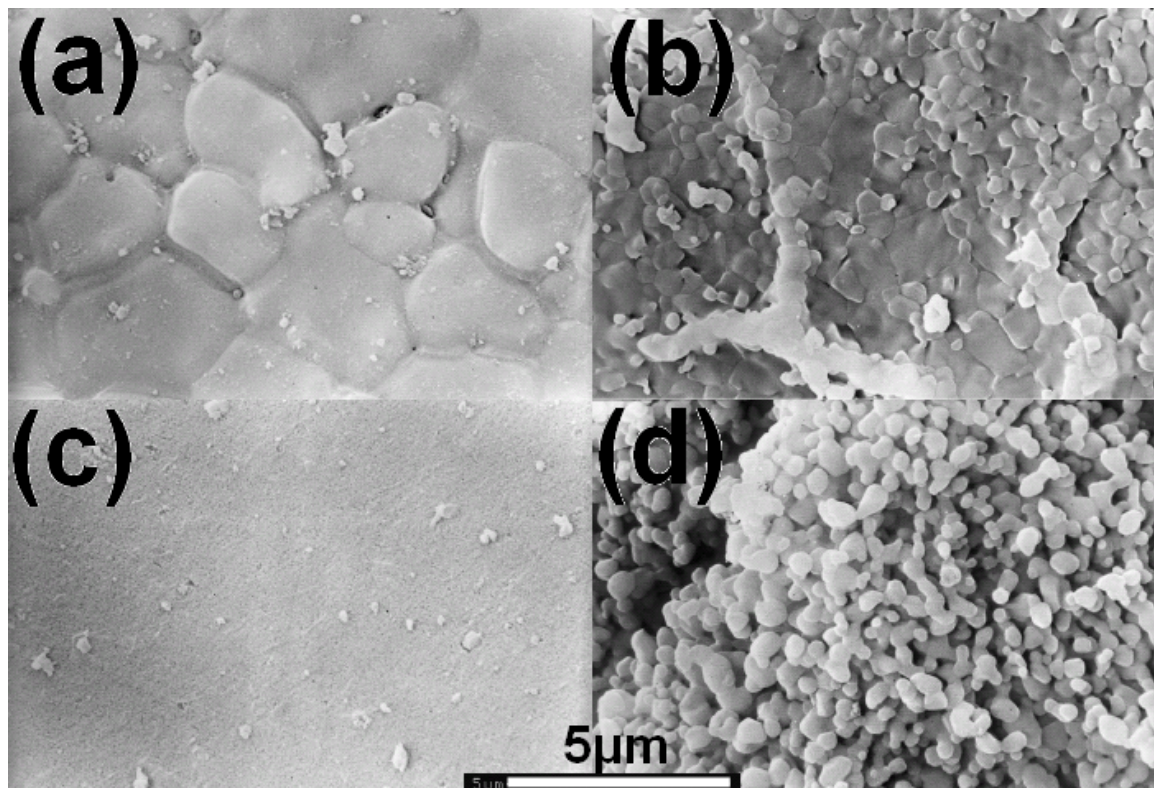


Fig 2.7. Sol-gel using coal tar carbon with oxide precursor in (a) alkoxide (b) glycolate (c) peroxide (d) rutile powders resulting in different particle sizes.

However, these are mostly Si-based for SiC. The decreasing ionic radius makes sensitivity to nucleophilic attack increase $\text{Si}^{4+} < \text{Ti}^{4+} < \text{Zr}^{4+} < \text{Hf}^{4+}$ down the periodic table. Thus most metal alkoxides are more difficult to handle, being moisture-sensitive and require chelating, usually with acetylacetonone “Acac” or similar structures such as acetic acid or citric acid, which can compete with water for a sufficient length of time to stabilize hydroxide form.^{106, 128-129} To date, hafnium alkoxides have needed extensive chelating or are conducted in air-sensitive Schlenk synthesis.¹²⁸⁻¹²⁹ A recent method to avoid this has been reported to use a chloride form of hafnium, but this was adjusted to an acidic pH in order to stabilize the hydroxide, in addition to a citric acid chelation.¹³³ Zirconium n-propoxide synthesis of carbides have all reported chelation.^{132, 134} A successful

chelating leaves the hydroxide as the primary form, and allows for the synthesis of a polymeric oxide, a prerequisite for a sol-gel with finer particle sizes.

The final oxides of solution-based processing are known as pre-ceramic polymers, which were a specialty of carbon composites but now used equally for ceramic nanomaterials. The first was for SiC production, known as polycarbosilanes or PCS, formula $(-\text{SiHMe}-\text{CH}_2)_n-$ although many variants exist.^{102-104, 135} This is a precursor that contains sufficient decomposable silicon and carbon in the molecular structure for heating direct to carbothermal reduction. It is generally used for fibers and carbon composites because the polymer has a T_g and thus a easily controllable viscosity. There is one reported zirconium structure able to decompose to zirconium metal, a carbon and boron source shown in Fig 2.8 and thus produce ZrB_2 and ZrC under the correct conditions.¹³⁶

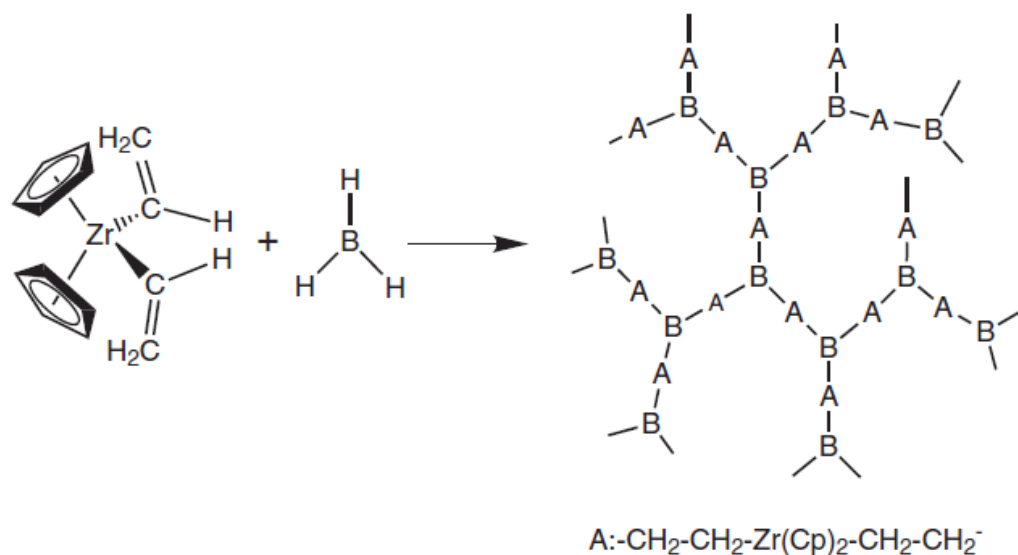


Fig 2.8. Preceramic polymer for Zr, B and C, able to produce a solution based ZrB_2 , ZrC and B_4C powder mixture.¹³⁶

In contrast, sol-gel requires empirical calibration to know when the viscosity is suitable for fiber spinning and is more complex, having more than four components in the mixture. Pre-ceramic polymers form fine particles on decomposition. Thus distributed SiC in ZrB_2 composites have used PCS as the precursor for SiC because it is liquid form and able to coat particles well before

sintering.¹³⁷ The reported microstructures are similar to the ideal materials outcome for this project. These would effectively be 2-in-1 (carbon + oxide) solutions and could replace solution-based nanopowders. However, these structures require dedicated organometallic chemistry, are expensive to purchase or simply do not exist and must be pre-synthesized.

It can be seen that the selection of the oxide source also involves a choice regarding the final microstructure. Sources that are more sensitive and difficult to handle are able to be processed with more control. But the coarse and less expensive sources – oxidized or chlorinated or crystallized (eg. rutile) – are cheaper, quicker to process and only require prevention of agglomeration. The choice of oxide precursor thus determines the desired range of diffusion during carbothermal reduction, ranging from 50nm up to 500nm. Thus the effective reaction distance between oxide and carbon depends on the level of meticulousness and goals of synthesis when selecting oxide and carbon sources.

2.3.4 Morphology: nanopowders, fibers, coatings

A dried oxide sol-gel with the decomposed carbon precursor results in calcination to nanopowders. The solution-based powder in forms of HfC, ZrC, TiC and SiC all result in submicron powder size, uniformity and purity being superior to that of conventional oxide/carbon powder mixtures.^{5-6, 115, 129} If a network of carbon/oxide is achieved, and the precursor can be mesoporous and even more finely mixed. For example, SiC precursor reported by Jin et al using phenolic resin as a carbon source reported their oxide/carbon precursor with a surface area of $112\text{m}^2\text{g}^{-1}$, and pore diameters of 10nm.¹²² The resulting nanopowders appear to be highly sinterable due to small size or surface properties as the pores could assist in reaction gas product removal.

Recent developments show that conventional powder methods can still produce crude nanoparticles. But the ability to produce fibers truly separates sol-gel with powder methods. Instead of precipitation or drying, the viscosity of the sol increases as solvent is removed, until it can be drawn from the solution and spun. Hasegawa et al reported the synthesis of the oxides of titania or silica followed by reduction using carbon from phenolic resin, which indicates that unless a suitable

carbon template is used, a polymeric gel is usually needed for fibers.^{119-120, 138} Typical dimensions of these carbides are reported as 20-100nm diameter and length <100µm but most are SiC rather than its Ti/Zr/Hf-based UHTCs despite some similarities in the methods in which they are synthesized.^{117, 139} Reports of rare ZrC, ZrB₂, TiC and TiB₂ solutions have used the chloride in CVD rather than solution-based methods.^{11, 140-141} Fiber research is less open than other literature as it is often a protected technology used in aerospace and defence research in armour for personnel and vehicles.

As noted, sol-gel nanocarbides can also be used in thin coatings below the thickness achievable by conventional micron powder spraying. Micron powder spraying is also limited if the substrate is porous (composite coating, carbon composites) where it cannot infiltrate. Spray conversion processes (SCP) are designed to stabilize a metal oxide sol (such as titania or tungsten) so that it is mixed homogeneously with a carbon source during the high temperature coating process. SCP has been developed and patented by McCandlish and Kear from Rutgers University, allowing carbothermal reduction of the composite powder to produce nanosize cemented carbide coatings.⁵⁶ Manocha et al used a silica/zirconia based gel to partially produce oxycarbide phases to increase the thermomechanical strength and oxidation resistance by surface coating on a carbon-carbon composite.¹⁴² Other methods of coating include using the oxide to produce interfacial carbide between the gel and substrate.¹⁰⁶ Gadiou et al also produced TiC/SiC coatings using a carbon fiber substrate.¹⁴³ Furthermore, sol-gel offers options for composite matrices. Xuetao et al impregnated carbon-carbon felts with a zirconium-based solution in order to produce a zirconium carbide-carbon composite.¹⁴⁴ These are all morphologies that highlight the advantages of the sol-gel process in processing options not available to powder methods.

2.3.5 Summary

The sol-gel or solution-based synthesis of UHTCs offers advantages in nanostructured materials where such properties are required. Nanomaterials are produced with ease from even simple solution processing. An important fact overlooked is that processing below 1600°C does not require a graphite furnace. The section has highlighted that while carbides and even diborides can be

produced by the sol-gel technique, the majority of the morphologies are in powder form. Sol-gel has advantages over conventional powder, such as fibers, infiltration and thin coatings. However, it requires organometallic synthesis, strategic selection of the carbon and oxide source and understanding of wet chemistry, coating/wetting and viscosity.

2.4 UHTC composite materials

Composite materials involve two or more phases chemically and physically distinct from one another into a single structure, in the hope of conveying improved properties. Additives or impurities that participate in densification processes are generally not considered composites, although these may nucleate sufficient desirable phases that improve the mechanical properties. For example, fibers may be included for toughness of a ceramic matrix in a composite, but a third phase may be added for reaction sintering for good bonding with the ceramic but weak interface bonding to the fiber. The composite is usually referred to by the two major phases. The control of particle size, viscous flow and fiber length may also be part of this processing. The increasing complexity of such materials highlights the advancing frontiers and requirements for new technologies, and stresses the need for understanding of the phenomena involved in these processes. Many multi-phase carbon and ceramic composites can be sintered from simple shapes with pressure assisted sintering. The close of this chapter covers the terminal sintering method known as SPS. But the technology is still not well understood, and UHTC composites still require strategic innovations to form the desired materials.

2.4.1 Rationale

The rationale for composite processing is to improve materials performance through the synergy of two different materials. This compensates or eliminates the disadvantages in both matrix and reinforcement. Toughening by composite design arguably began from Neolithic grass-reinforced mud brick dwellings, to the now common SiC fiber-reinforced defences on armoured vehicles. In a ceramic matrix, the obvious is the low reliability, which can be made more predictable under mechanical testing by making their response to strain more consistent. The second more pertinent property to extreme environment conditions is the

oxidation resistance of non-oxide ceramics, commonly by incorporating a phase in the microstructure that sacrificially oxidizes first and forms a stable passivation layer that prevents the substrate from oxidative attack. These synergies are typical of ceramic systems. However, there are several other rationales for composites – such as the inclusion of phases for magnetic or electrical functionality which are not covered here but can use the same processing technology. Composite materials can sometimes be easier to process because mixtures often allow for phases to form during processing, which encourages diffusion and thus densification. The distinction between additive and composite is usually whether the phase appears in substantive quantities to synergistically improve a desired performance property. Since many composites have a clearly defined methodology highlighting the purpose of the second phase, the literature reviewed here will focus more on composites designed to achieve the first two properties of oxidation resistance and toughening. This is an important distinction to note because many additives – particularly when matrix and reinforcement need to be UHTCs – likely degrade refractory performance.

2.4.2 Composite properties

The addition of a nanophase can improve oxidation, mechanical performance and densification. However, nanocomposite UHTCs are rare to find since both would have poor self-diffusion coefficients and likely have high sintering temperatures. Notable conventional UHTC composites include work by Goutier et al, who investigated composites based on ZrC, of which the easiest to densify being a (ZrC:ZrB₂) at 43:57 mol% eutectic composition.¹⁴⁵ Tsuchida et al appears to have investigated the entire composition from ZrC to ZrB₂ at 10wt% intervals using SHS powders of ZrB₂ and ZrC densified using SPS, which resulted in a mixture of carbide/boride grains in the microstructure.^{55, 146-147} These are conventional powder mixing, because UHTC fibers and nanomaterials are still emerging.¹⁴⁰

Probably the most common attempts to disperse nano-phases in UHTCs involve the ZrB₂ and nanosize-SiC combination. While not a true UHTC composite, nc-(nanocrystalline) SiC is not only used as a sintering additive for densification and microstructural refinement, but also for strengthening, toughening and oxidation

resistance in 10-30 vol% (33-50 mol%). Sintered microstructures show randomly dispersed SiC in ZrB_2 .¹⁴⁸⁻¹⁴⁹ The migration speed of SiC is slow and thus intragranular SiC represents retardation of the matrix grain boundary.¹⁴⁸⁻¹⁵⁰ The fracture mechanism of these composites compared to pure ZrB_2 is observed to become transgranular, and it is proposed that intergranular SiC, intragranular microcracking and crack deflection are responsible for the increase in toughness from 2.3-3.5 $MPa \cdot m^{1/2}$ to 6.4-6.7 $MPa \cdot m^{1/2}$.^{148-149, 151} However, densified ZrB_2 materials with or without SiC also report fracture toughness in this range. Values of 4.2-4.6 $MPa \cdot m^{1/2}$ are more realistic from additions of nc-SiC.¹⁵² Thus it can be concluded that the addition of nanoparticles add some boundary drag effects in controlling grain growth and increase in strength, while only providing minor improvements in fracture toughness. Since nc-SiC is known to be eventually enveloped by the moving ZrB_2 boundary, the location of the nc-SiC nanoparticles is critical and this can vary depending on the dispersion technique used. Fig 2.9 emphasizes that nanoparticle mixing leads to varying size agglomerates to form, along with unknown SiC particle-grain boundary relationships. Using typical micron-size SiC particles yields coarser but actually more predictable microstructures.¹⁵¹

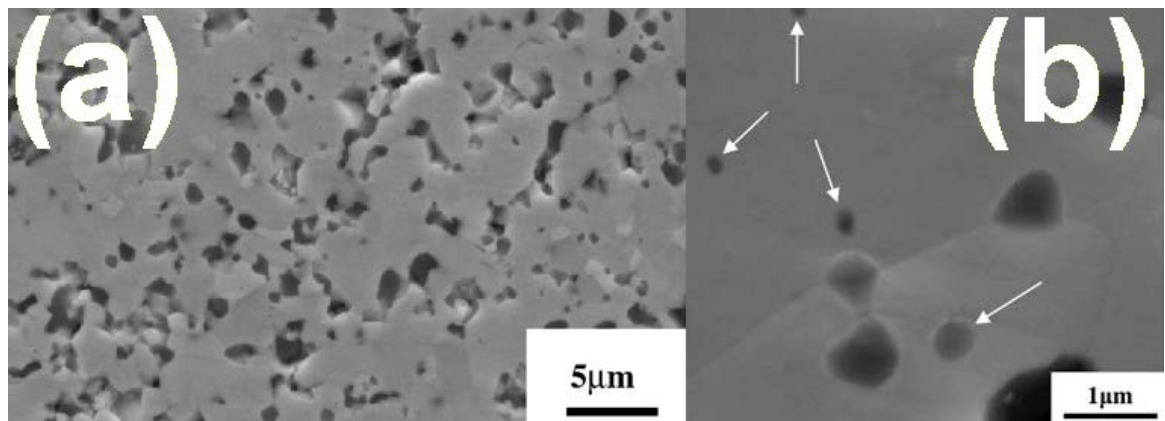


Fig. 2.9. Two examples of a conventional of nanocomposite design of ZrB_2 -SiC. Note the lack of control over dispersion of the dark SiC phase **(a)** agglomerated to 3 μm and **(b)** nano and agglomerated, intragranular and intergranular.¹⁴⁹⁻¹⁵⁰

The addition of whiskers (w-SiC) or fibers (f-SiC) are more consistent in toughening the ceramic material. An addition of 20% w-SiC into both TiB_2 , ZrB_2

and AlN increases fracture toughness to over $7 \text{ MPa}\cdot\text{m}^{1/2}$.¹⁵³ For increasing oxidation performance, the baseline data is that above 750°C , ZrB_2 oxidation is parabolic, and relies on liquid borica sealing of porous zirconia.⁴⁷ Zhang et al designed a composite with whiskers of w-SiC in ZrB_2 for several objectives: toughening to prevent catastrophic failure from superficial defects and oxidation resistance by the formation of liquid borosilicate glass, which under specific conditions allowed for crack healing behaviour as well.¹⁵⁴ Nanoparticle SiC is often used to add silica to the borica layer with less toughening under these conditions. The typical data from reported oxidation tests are weight loss of material, reduction in strength after testing and the thickness and visual density of the protective oxide layer. Monteverde et al hot pressed samples with 15% vol SiC particles to obtain a 15 micron oxide film protecting the underlying surface after 4 cycles of 5 minute exposure at 1600°C in a furnace.²¹ Below 1500°C , ZrB_2 -SiC oxidizes to ZrO_2 , B_2O_3 and SiO_2 , forming a borosilicate passivation layer until about 1800°C , when oxygen partial pressure is too low and the vapour pressure of borica increases.^{52, 61} This reliance on Si, B and O transport limits the ability of the surface to protect against further oxidation at higher temperatures, and active oxidation of SiC to $\text{SiO}(\text{g})$ becomes appreciable.¹⁵⁵ Without the borosilicate phase, the zirconia layer is reportedly porous.¹⁴ Typical additions of about 20-30 vol% SiC have an upper limit of protection to about 1800°C .¹⁷ The effect microstructure and dispersion are not compared as they are sintered from conventional processes, with approximately the same homogeneity. Currently, there are two strategies for improving oxidation performance past 1500°C : use the high temperatures present in the system to densify the oxide or use a third phase that modifies the surface oxide. Replacing SiC with LaB_6 additions to both ZrC and ZrB_2 have found improvement in densification at higher temperatures.¹⁵⁶⁻¹⁵⁷ With a ZrB_2 matrix, oxidized ZrC and SiC appears to yield a eutectic composition and oxidized ZrB_2 - LaB_6 yields a $\text{Zr}_2\text{La}_2\text{O}_7$, or glassy lanthana species at zirconia grain boundaries to densify surfaces at elevated temperatures.^{154, 158-159} These appear to be promising systems for temperatures above 2000°C , but have yet to attempt nanomaterial coating or dispersion to investigate the homogeneity of oxide layer formation.

2.4.3 Processing challenges

The high aspect ratio of whiskers and fibers allow for toughening of ceramics if mixed well. Milling time of whiskers is usually less than 12 hours. For example, ZrB₂-20%-w-SiC composites were milled for 12 hours using zirconia balls in ethanol.¹⁵⁴ A similar composition of 10-30% vol w-SiC reported only 10 hours milling time, and a warning to restrict ball milling speed of 200rpm.¹⁵³ If harder balls are used, such as WC or SiC, the parameters are reduced further. For example, Yang et al added fibers to ZrB₂ in a 20% vol ratio to WC balls and attrition milled for only 6h.¹⁶⁰ Sciti et al reported 24h milling of 20 vol% SiC fibers without improvement in fracture toughness of the ZrB₂ matrix, although this was attributed to strong interface bonding rather than fiber damage.¹⁶¹ However, the fiber length is shown in microstructures to be substantially shorter in Fig 2.10.

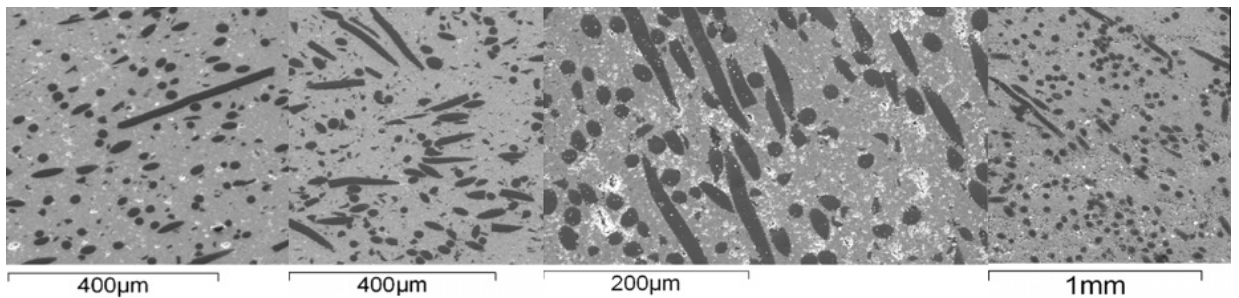


Fig 2.10. Final microstructures of milled 1mm fibers, showing at least 50% reductions in length after processing.¹⁶¹⁻¹⁶²

To put in perspective, ZrB₂ with a fracture toughness of $\sim 4 \text{ MPa}\cdot\text{m}^{1/2}$ from HV_{1kg} indent corresponds to a 40µm micron crack from the indentation. Thus there is a clear trend of reducing milling time in order to prevent cutting of the fibers. Similar work using w-SiC and f-SiC in 10 and 20 vol% in ZrB₂ composites reported that the initial length of 1mm was cut to about 400 micron after processing.¹⁶² For nanopowders, severe milling methods – such as attrition or vibration milling – are more effective, although generally ultrasonic treatment followed by milling is used, presumably to encourage adhesion to the micron-size powder surface.¹⁴⁹⁻¹⁵⁰ These challenges in preparing nanocomposite powders still do not account for diffusion additives. Typical additions are MSi₂ (M = metal) and Y₃Al₅O₁₂ as additives, but these react with surface boric acid and zirconia found in ZrB₂ systems, along with the highly active nanophase or fiber surface.^{24, 26, 153, 163} More impure systems yield impurities of metals such as Zr and Ni in cation-exchange

reactions.⁶⁶ If these are added, the only solution is a reaction sintering to remove these phases; for example, perform a boro-carbothermal reduction of TaSi_2 to react and form nanoparticle TaB_2 and a SiC phase. Otherwise these yield intermetallics and glassy phases that assist in densification, but compromise high temperature performance.¹⁴⁰

The ideal answer for well dispersed composites is to electrically or chemically disperse the second phase onto the micron-powder surface and maintaining that mixture during greenbody formation. This synergistically keeps the advantage of making bulk structures that is too expensive for monolithic nanomaterials. The typical approach to nanoparticles is to mix them, and there are far less restraints compared to fibers and whiskers. Milling causes oxygen uptake and impurities from the milling media noted in Table 2.3, but because nanoparticles have a higher surface area, their susceptibility to oxidation and higher catalytic activity probably results in more disproportionate and rapid formation of surface oxide films. This could also be substituted for electrical or chemical dispersion. Sol-gel powder coatings are already found in some nanocomposite ceramic systems.

2.4.4 Nanodispersed ceramic materials

Powder coatings by liquid-based methods offer the advantages of using conventional powder processes with one added step of an easy pre-treatment. This treatment can be relatively simple, yet avoids the issues involved in milling operations. Fig 2.11(a) and (b) shows two examples.

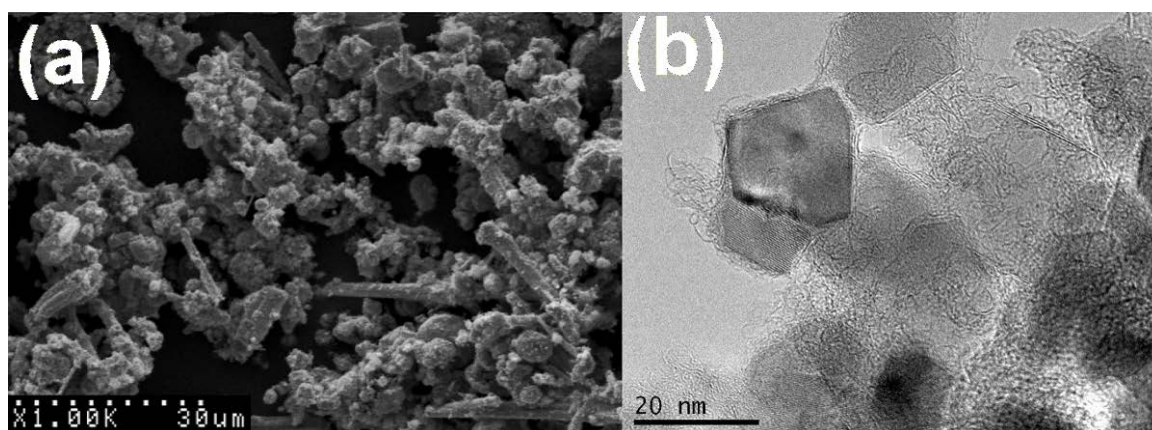


Fig 2.11. (a) SLS mixed ZrB_2 - ZrC fiber-powder (b) Mixed TiC - SiC sol-gel powder, but no densification has been reported.¹⁶⁴⁻¹⁶⁵

The first is a Solid-Liquid-Solid (SLS) synthesis method, which yields mixed ZrB_2 -whiskers in ZrC that can proceed to terminal sintering without modification.¹⁶⁴ Fig 2.11(b) demonstrates mixed Si-O-Ti nanopowders in carbon that reduce to SiC and TiC at nanometer level homogeneity by 1450°C.¹⁶⁵ Mixed liquid precursors have been used to create suspensions of SiC nanoparticles in ZrB_2 and SiC in C/ B_4C in alkali ethanol-based solution, but no sintering or microstructures have been reported.^{78, 166} Apart from these examples, solution based UHTC nanocomposite coatings have not been explored. But they have been documented in oxide systems where the nanoparticles have proven difficult to disperse and are listed in Table 2.4. The term parent phase often refers to the micron size powder, while the second or minor phase refers to the nanoparticle precursor. The use of nanoparticles has been reported to increase surface activity, retard grain growth thus preventing coarsening and coalesce in favour of the minor phase rather than the matrix.¹⁵⁰

Table 2.4. Examples of ceramic nanocomposites studied using powder-solution coating or powder-gel method.

Author	System	Purpose
Huang et al ¹⁶⁷	Al_2TiO_5 , sol-gel coated Al_2O_3 & SiO_2 mullite precursor	Prevent large Al_2TiO_5 agglomerates, mixed mechanically & presumed colloidal sol, nanocomposite
M.-C. Wu et al ¹⁶⁸	$BaNd_2Ti_4O_{20}$, solution-based CuO	Nanocrystalline sintering aid Adsorption on powder & dried
Zhu et al ¹⁶⁹	ZrB_2 , solution-based C/C precursor, phenolic based	Sintering aid, surface activity, not nanocomposite
Zhu et al ¹⁷⁰	ZrB_2 , C/SiC precursor as polycarbosilane	Sintering aid, surface activity, not nanocomposite
Gao et al ¹⁷¹	Si_3N_4 - SiC, solution based yttrium nitrate	Sintering additive, minimum composition (10%), colloidal sol, nanocomposite ceramic
Kawano et al ¹⁷²	β -sialon (z=2)/ Si_3N_4 , solution based TiO_2	Minimum phase composition required (25%), colloidal sol, nanocomposite ceramic
Tatli et al ¹⁷³	Si_3N_4 , solution-based MgO	Higher densities, colloidal sol, nanocomposite ceramic

Tatli et al demonstrated that higher density can be reached for coated systems.¹⁷³ Some of the above examples in Table 2.4 have used a precipitation and drying technique where nanocrystals have adsorbed to the parent particle surface.¹⁶⁸ Interestingly, large phase volumes have been observed for some systems, which appears to mean that the densification involves both phases.¹⁷¹⁻¹⁷² While the densification of the minor or nanoparticle phase will result in lower sintering temperature, this would cause microstructures similar to Fig 2.9 of nc-SiC coalescence to micron size intergranular particles. A coated powder based method has been attempted on WC-based cermets where 1%, 5% and 10% nano-WC was solution milled.¹⁷⁴ The general morphology is shown in Fig 2.12 below.

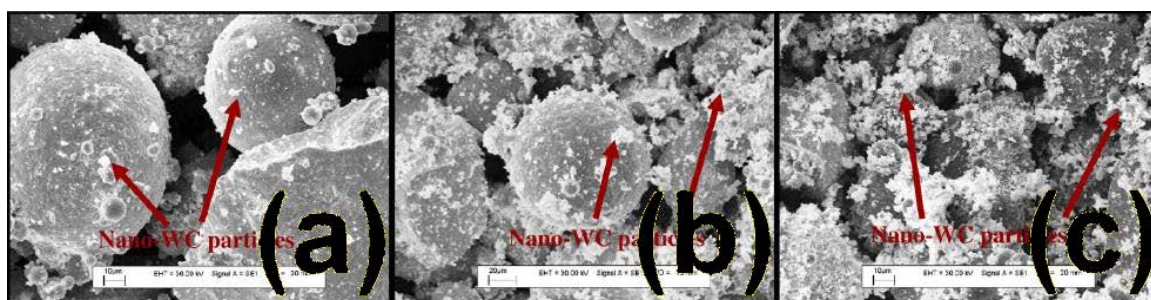


Fig 2.12. Powder feed of Ni-Tung60 alloy with (a) 1% (b) 5% and (c) 10% nano-WC by weight pre-laser deposition.¹⁷⁴

This is actually a pertinent example of applying nanosize particles to micron size feeds. It changes the nature of the densification between surfaces due to surface diffusion operating preferentially on the nanoparticles and fills pores that would otherwise require liquid or other impurities to assist greenbody formation or densification. An analogous mechanism in UHTCs is a study by Zhu et al, coating ZrB_2 with phenolic resin. Recognising that the zirconia layer was already a surface film impurity, reduction of this to ZrC provided sufficient surface activity to perform a remarkable low temperature densification by pressureless sintering at 1900°C .¹⁶⁹ Despite the likely presence of some ZrC, this was technically a sintering additive. The most refractory solution-based precursor that is well mixed with the UHTC powder is the production of ZrB_2 -SiC via the polycarbosilane ($-(SiHMe-CH_2)_n-$) preceramic polymer using shearing and blending before

sintering.¹³⁷ It is clear that a gap exists for a well dispersed solution-based dual-UHTC composite.

2.4.5 Spark Plasma Sintering (SPS)

A brief review of SPS is included since this is the technology used for the densification of ZrB_2 . Also known as Pulsed Electrical Current Sintering (PECS) or Field Assisted Sintering (FAS), this involves higher pressures than Hot Pressing (HP), with a pulsed current passed directly through the compacted powder instead of external heating. A more efficient densification technology, it has been promising for densification of more challenging covalent materials of carbon, boron and UHTCs.

2.4.5.1 Theory of SPS

Two high strength graphite dies compact a powder in a graphite collar, and a DC pulse passed into the die under an applied pressure. A schematic by Groza et al is attached below in Fig 2.13.

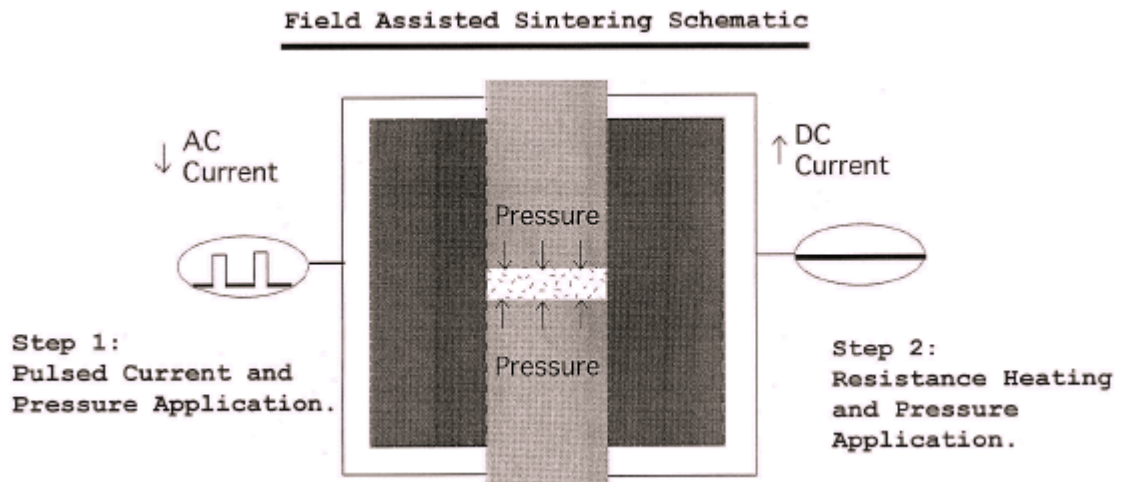


Fig 2.13. SPS schematic reproduced from Groza et al.¹⁷⁵

The maximum applied pressure is dictated by the die material. Maximum pressures are in the order of ~ 100 MPa, while Inconel and WC dies approach 300MPa. Sintering temperatures up to 2400°C and heating rates at hundreds of degrees per minute reduces processing time to less than half an hour because the isothermal hold is usually in minutes. This ensures less contributions from

non-densifying mechanisms and development of metastable phases along the ramp or grain growth.¹⁷⁶ The purported physical effects of SPS is noted by Tokita et al: spark plasma, spark impact pressure, Joule heating and electrical diffusion.¹⁷⁷ The proposed mechanisms between particles is shown in Fig 2.14 as the electric current is pulsed. The path of conductivity follows three sequences: (1) small contact area, resulting in a voltage drop, high resistance and Joule effect; (2) conduction through the surface film (or vaporization and exit by vacuum); (3) arcing between particles in the gap between particles can cause evaporation and causing matter transport to form necks.¹⁷⁵

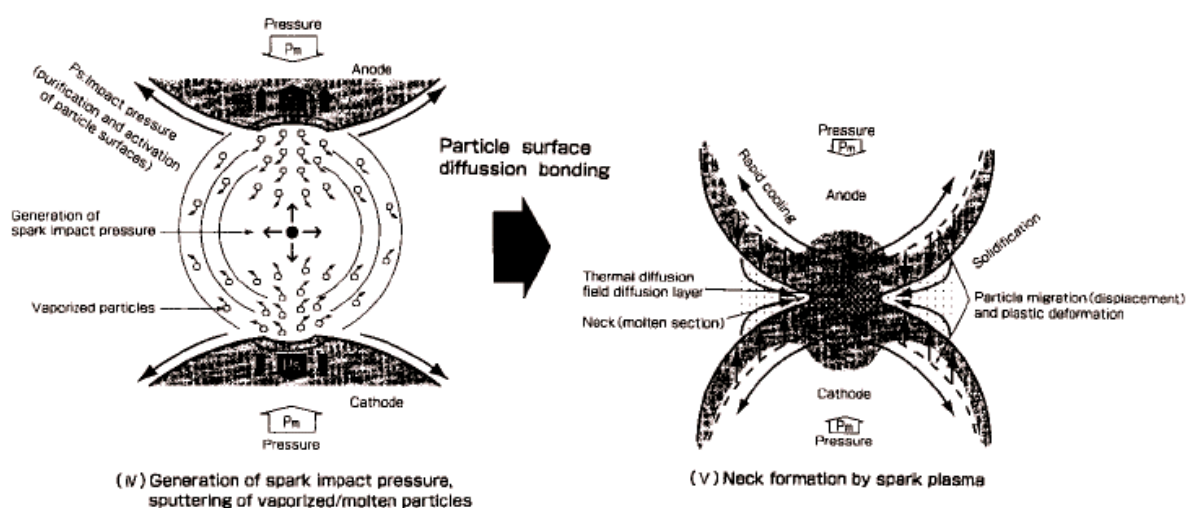


Fig 2.14. Proposal of plasma and breakdown of surface oxide phenomenon resulting in intimate particle-particle contact reproduced from Tokita et al ¹⁷⁷.

The spark plasma and impact pressure effectively creates a sputtering phenomenon, which eliminates adsorptive gas and purges surface impurities.¹⁷⁷⁻¹⁷⁸ Reviewing the basics of densification, the electrical field results in increased diffusion of ions (often referred to as electromigration).¹⁷⁹ Secondly, surface non-densifying mechanisms are likely less favourable under these conditions, because necks do not rely on the surface/volume diffusion growth of necks and evaporation-condensation, which are reductions in surface curvature but are non-densifying.¹⁸⁰⁻¹⁸¹ Contact is provided by “spark plasma pressure” and surface purging in Fig 2.14. Application of high pressure and faster heating rates (above 500°C/min) have been shown to completely suppress grain growth.¹⁸² Due to early powder contact, the fast heating rate moves immediately to the grain boundary source diffusion mechanisms that are densifying processes. This

effectively skips the start and intermediate stages of sintering.¹⁸³⁻¹⁸⁴ These promised effects have been successfully transferred to UHTC densification.

2.4.5.2 Densification of UHTC composites

A myriad of publications now use SPS, showing improvement in densification over HP.^{30, 185-186} These still report use of sintering additives.²⁸ Strategies for sintering are still used. Returning to basics, using a chemical reaction and particle surface curvature have been demonstrated on several UHTC systems such as B_4C -WC, TiB_2 - B_4C and HfB_2 -SiC from base metal and B precursors sintered to over 95% density at 1700°C.¹⁸⁷⁻¹⁸⁹ This includes increasing the surface curvature by nanoparticles or adding fibers.^{68, 162, 170, 190} Mechanically activated self-propagating high temperature synthesis currently has the best dispersed and small uniform size powders for UHTCs and these have repeatedly been sintered to high densities in ZrB_2 -SiC, ZrC- ZrB_2 and HfC-Hf B_2 .^{36, 54, 147, 189, 191-193} Thus it is difficult to report any conclusions apart from the fact that SPS is more efficient than HP technology, requiring a lower temperature and faster processing time.

But there are difficulties in determining SPS temperature distributions. The first problem is the difference between the surface measured temperature and core, which can approach 200°C higher than expected at 1300°C, because the pyrometer which controls the input current is reading the surface of the die shown in Fig 2.15.¹⁹⁴

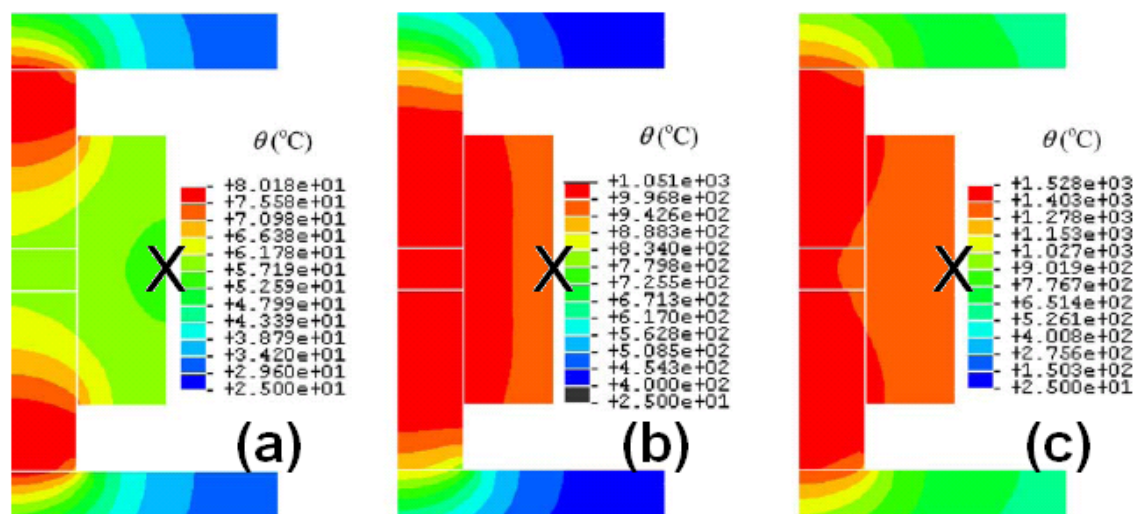


Fig 2.15. SPS die cross-section showing only right half. Comparison of internal temperature distribution where only the surface of the die is (a) 56°C (b) 983°C and (c) 1309°C measured by optical pyrometer at point X.¹⁹⁴

It is evident that in conductive samples, the temperature gradient is less severe through the die than in insulators, where the majority of the current passes through the graphite collar.^{215; 265; 266} How this affects the sintering performance has not been extensively characterised. But SPS consistently reports hundreds of degrees lower processing temperatures than HP. The second issue is that while using insulation reduces heat losses, current draw and radial temperature gradients, the effect of current on densification is unable to be measured except by crude methods such as not insulating the die and forcing current draw.¹⁹⁵ For the UHTCs such as ZrB_2 and HfB_2 , the activation of particle surface and removal of surface oxides are one of the key performance criterion for SPS not found in HP. The effect of surface oxides is to reduce densifying mechanisms, likely through early evaporation-condensation mechanisms and as a result coarsening is a consistently reported phenomenon for preventing densification.

As noted, the charge transfer between particles requires conduction to occur by electrical/thermal breakdown of the insulating oxide, discharge or arcing.³⁵ While tunnelling can occur through the surface oxide, the arcing phenomenon is accommodated by vaporization of the surface, and charge transfer is inferred to produce intermittent plasma.^{35, 177, 196} Because small capacitors are effectively created at each particle contact, the result is either breakdown of the film or evaporation by the ionized gas.^{175, 178, 194} Direct particle-particle bonding occurs and vapour discharge should be detected. This is unreported in literature. Oxide films on ZrB_2 were conventionally countered by reaction sintering with mixing with carbon, but this has not been investigated to confirm that a plasma effect does indeed replace this standard strategy.^{169, 197} Powders are already wrapped in graphite foil prior to sintering in SPS. Thus there are several fundamental issues to understand about SPS. The plasma phenomenon is not easily investigated. Transposing one sample size to another requires a different densification temperature. Furthermore, since all reported literature records pyrometer surface temperatures, it is possible that the higher internal processing temperature is

responsible for superior performance over HP. Without controls, densification of two different size samples need calibration. These inferences – such as the plasma, surface oxide purging and spark pressure - of the SPS should be carefully examined given that the technology is not well understood.

2.4.6 Summary

Composite materials clearly offer advantages for improved materials performance. However, the difficulty in dispersing the second phase is still a challenge. Nanomaterials offer advantages in low volume additions if dispersed well, but few publications have investigated other methods of dispersion apart from mechanical mixing. The difficulty in densification of carbon and UHTC materials has driven innovation. This is demonstrated by gas and liquid phase surface pre-treatments, co-suspensions and precipitation, as well as the crossover of precursors between densifying carbon and ceramic composites. The future offers more innovative preparation of starting materials over ostentatious sintering technology, returning synthesis and colloidal chemistry to ceramic processing. Despite minimizing parameters in using SPS, results are not comparable to pressureless sintering due to heating rate, applied pressure and pulsed current. This adds a last thought to any applied research outcomes: it is important to remember that applied pressure was used because it was required or necessary, but not because it was desired. This is important to applied research outcomes, such as extreme environment materials that require complex shapes.

2.5 Extreme environment testing

The term “extreme environments” have generally been associated with high energy physics such as radiation, corrosion or high temperature processes. It is interesting to note that conditions for endo-atmospheric hypersonic flight actually include all three processes. Other examples include use of TiB_2 for electrodes in aluminium production, ZrB_2 and ZrC solar receivers and carbon-carbide plasma-facing structures in fusion reactor systems.^{46, 198-199} What makes these processes extreme is that they push the boundaries of survivability of the material. This section highlights the most common testing regimes that UHTCs are subjected to validate their brazen name. The extreme environment that tests the ZrB_2 composites in this thesis is commonly associated with hypersonic flight. But the

derived principles, experimental setup and methodology of results can apply to other extreme environment testing.

2.5.1 Extreme environments by hypersonic flight

Hypersonic velocity is a term for speeds where “sonic barrier” linear theory fails and temperature effects on fluids become critical.²⁰⁰ It is known as the “thermal barrier” because insufficient time is provided to free-stream gas molecules moving out of the flight path and a shock-compressed zone forms.²⁰¹ Temperatures in this zone exceed 10000K and Fig 2.16 shows the surface temperatures of a typical spherical re-entry body under this exposure.²⁰²⁻²⁰³

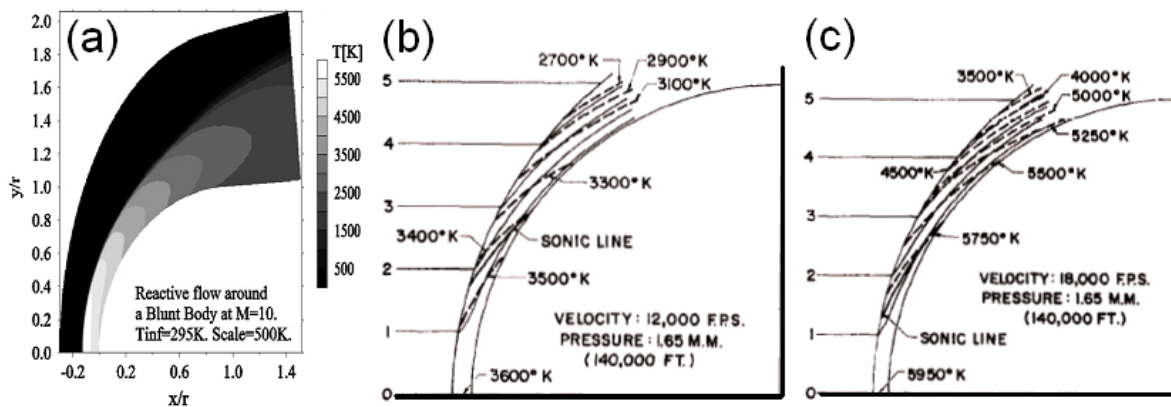


Fig 2.16. Typical temperatures of 3000°C at (a) Mach 10 (170,000ft) and (b) Mach 12 and (c) Mach 18 caused by convective heating.²⁰³⁻²⁰⁴

Heating is caused by dissociation of the molecules within a close fitting sheath around the vehicle, exposing the surface to radiative/convective heat transfer. The counterintuitive solution by Eggers & Allen et al was to use high drag shapes instead, forcing a detached bow-shaped zone that kept the radiative plasma sheath at a stand-off distance from the vehicle.²⁰⁵⁻²⁰⁶ Thus the frustrum “truncated cone” shape became the common geometry to re-entry accelerators: ballistic missiles, interplanetary capsules and the Space Shuttle Orbiter.²⁰⁷⁻²⁰⁸ However, their aerodynamic properties such as lift-to-drag ratio are poor and are unsuitable for sustained cruise due to higher propulsion requirements, limiting time to abort, manoeuvrability and cross-range.²⁰⁹ Future vehicles with sharper and more

aerodynamic profiles require new materials because the ablation at the sharp edge are beyond the limit of C/C and SiC/C composites.²⁰

The term ablation describes the high temperature wear-corrosion process caused by external surface pressure, skin friction and radiative heating.²¹⁰ Semi-passive ablator systems were originally designed to use direct sublimation of surface char that endothermically consumed energy in exchange for mass lost, with coolant carrying away some of the heat. Failure in these ablative carbon-composite systems was the spallation and ejecting of solid chunks, because the system was not exchanging mass for the absorption of energy that dissipated the heat.²¹¹⁻²¹⁴ In the case of ceramic composite, design criteria are different. Sharp leading edges are fully passive, relying on high thermal conductivity to maintain a negative heat flux over most of the downstream surface where absorbed energy is re-radiated.²¹⁵ The char is a layer or film that prevents further oxidation of the underlying surface and may even behave as crack-healing phase.¹⁵³⁻¹⁵⁴ Oxidation results in gas products, and these should be permitted to leave the surface during the early oxide layer formation, but oxidation and gas evolution should decrease as it densifies because bubbles can increase the diffusivity of oxygen through the layer.⁴⁶ This could occur by sintering or by a sufficiently high viscosity of liquid oxide. As maintaining leading edge geometry is the primary objective, mass loss and temperature distribution are delicate kinetics. Thermodynamically, radiative and convective heating is balanced by conductive and re-radiative cooling. These concepts were first tested in the 1990s by NASA.

2.5.2 Experimental conditions

The most notable experiment in ceramics for extreme environment conditions for ZrB₂ materials is briefly covered here. These were known as the SHARP (Slender Hypervelocity Aero-thermodynamic Research Probe) tests in a collaboration between NASA Ames, Sandia National Laboratory and the US military.^{209, 216-217} A deactivated warhead of a Minuteman III Mark 12 MIRV used a frustrum sphere-cone of ablative carbon-carbon and phenolic carbon.^{209, 216-217} In May 1997, SHARP B1 substituted this nose cap with one of HfB₂-SiC for the tip of the re-entry vehicle in Fig 2.17, with re-entry data monitored via instruments before impact. SHARP B2 occurred in September 28, 2000, using four retractable

1-inch strakes composed of UHTC materials, designed to be recovered.⁴⁴⁻⁴⁵ The strakes were 20 degree leading edges of $\text{HfB}_2\text{-SiC}$, $\text{ZrB}_2\text{-SiC}$ and $\text{ZrB}_2\text{/C/SiC}$. Fig 2.17 (b) & (c) denote the B2 design. SHARP B2 samples were exposed to the re-entry environment from an altitude of 700km, then retracted in pairs that corresponded to their predicted single use (before ablation) and multi-use (after ablation) temperature limits at two different altitudes of 47.9km and 43.3km respectively. Unretracted flight time corresponded to less than two minutes exposure at a predicted $\sim 3000^\circ\text{C}$. SHARP B2 can be considered the first experimental testing of sharp UHTC structures, setting the standard for testing conditions – up to 3000°C , $\sim 20^\circ$ edges, few minutes exposure and the techniques for thermal oxidation microstructure analysis.

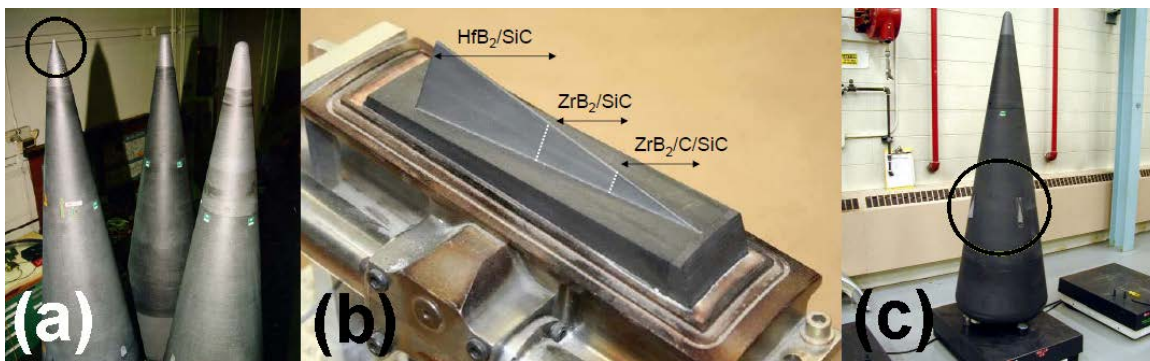


Fig 2.17. (a) SHARP B1 $\text{HfB}_2\text{-SiC}$ substituted tapered nose on leftmost Mk12 re-entry vehicle (circled) (b) SHARP B2 UHTC strakes of sintered UHTC composites (c) mounted in retractable positions (circled)^{209, 216-217}

Results indicated the large thermal stresses were due to an unexpectedly large temperature gradient. The results of B2 suggested that fracture toughness, strength and reliability (Weibull modulus) were lower than expected due to poor processing. Released micrographs indicated agglomerate inhomogeneity in the hundreds of microns. This was an impetus that led to a new effort in UHTC materials.

2.5.3 Ground based testing

Most reported literature uses ground facilities, coupled with modelling and comparison to rare and expensive flights. Testing for aerothermal properties in UHTCs may eventually be standardized, as in other high temperature industries.

A good example is the construction of carbon-carbide rocket nozzles in Fig 2.18, where after consolidation and inspection, the actual testing can be through direct firing and characterisation, under the exact operational conditions.²¹⁸⁻²¹⁹ Thus most UHTC testing is indicative, a guide or a screening process. Heat flux values for hypersonic flight range from 500 to 2000Wcm⁻³ and are certainly reproducible.²²⁰ However, the exact conditions are harder to recreate, since the heat flux is derived from convective dissociated gas flow, recombination reactions under non-equilibrium non-ideal gas and radiative transfer from a plasma sheath.

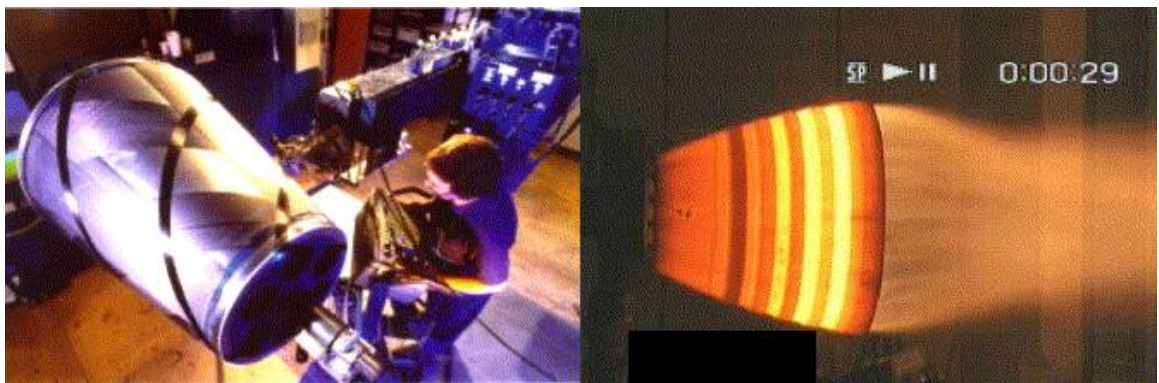


Fig 2.18. Testing of Vulcain C/SiC nozzle by Astrium (formerly DASA).²¹⁹

This body of physics is known as “aerothermodynamics” although simpler thermal testing is often referred to as “aerothermal”.^{22, 221} The most simple is furnace oxidation up to 2000°C (zirconia furnace) with specimens aggravated by whether air flow is injected. More aggressive environments require combustion sources. Oxyacetylene combustion is capable of reaching temperatures of 3500K, although 3000°C is common as a ballpark figure.²²²⁻²²⁵ Note that combustion gas species are ionized but unsuitable for simulation of hypersonic flight conditions – the incandescent blue zone is dissociated acetylene in C₂/H₂/O₂, with a reducing zone of CO, H₂ and ionized protons.²²⁶ The envelope is a mixture of unburnt hydrogen, soot, CO, CO₂ and water vapour.²²⁷ The predicted behaviour under oxyacetylene combustion is likely to be a low-shear environment where heat transfer occurs to the surface and scale simply absorbs energy, melts or vaporizes.^{144, 224-225, 228} Laser ablation also reaches the required heat fluxes with a simpler temperature envelope. All the above testing facilities only yield static weight losses, limited microstructural characterisation and cannot reproduce flight

conditions. These are actually testing the cooling mechanisms; conduction away from the tip and re-radiation. Probably the most accurate testing environment is the arc-jet or plasma torch, providing heat fluxes similar to that of oxyacetylene.²¹⁰ The testing gas can be selected (e.g. 80-20 N₂/O₂, or even other planetary atmospheres) but more importantly the gas is dissociated in O[·]/O^{2·} rather than O₂.^{210, 221, 229-230} A high-shear aerothermodynamic flow can act on liquid layers, which can expose the underlying material so failure propagates downstream according to actual conditions.²³¹⁻²³⁴ SHARP B1 and B2 results were correlated with ground based arc-jet facilities.^{209, 216-217} It is noted by Bertin and Cummings at USAF that plasma wind tunnel arc-jets are run under conditions careful not to damage the facility, with reported conditions less severe than oxyacetylene.^{14, 52, 207, 235-237} Thermogravimetry (TG) instruments are also confined to low temperatures (furnace is alumina <1500°C, Pt thermocouple) due to sensitivity to damage. Current literature indicates that responses under arc-jet appear to be similar to results found in furnace and combustion flame tests.^{14, 52} However, oxyacetylene combustion is inexpensive, well understood and is actually a mainstay of ablation testing of many materials due to its relatively similar composition to rocket exhaust. It yields aggressive conditions that are a broadly acceptable standard for extreme environment materials to survive.

2.5.4 ZrB₂ composites under simulated testing

Diborides are the leading candidates for thermal oxidative environments. HfB₂ and ZrB₂ were already known to form porous ZrO₂ scales, improved by additions of SiC that passively oxidizes up to 1500°C to form a protective borosilicate glass between zirconia pores.²³⁸⁻²⁴⁰ Note that 10-30% vol SiC calculates to 33-50 mol% SiC per ZrB₂ molecule, indicating a significant catalytic activity required for formation of the protective scale. However, recent research at Defence Science & Technology Laboratories (DSTL) & Loughborough (UK) in late 2012 at 3000°C confirmed the presumption that the addition of SiC would have performed less effectively than even the control ZrB₂ because SiC is in an active oxidation regime.²²³ By 2100°C, silica is usually removed and the system must rely on molten or densified zirconia.^{228, 241-242} To date only a half dozen reported publications have tested at ~ 3000°C and most are carbon-composites.²⁴²⁻²⁴⁵ In order to replace borosilicate in the porous zirconia for surface passivation above

2000°C, a third phase must act as an “oxide layer additive” – either assisting in densification of ZrO₂ or promoting eutectic liquid formation. Modelling based on nuclear core meltdown or “corium” scenarios indicated zirconia still has high viscosity ~ 3000°C.²⁴⁶⁻²⁴⁷ Both additives are now being explored in recent composites using quantities of a tertiary phase, such as LaB₆, La₂O₃ and WCW_xB_y.^{158-159, 248} These could prevent oxide detachment by stabilizing the zirconia transformation and some of these compositions reported no oxide layer detachment even after thermal cycling.²⁴⁹ Another example would be samples of ZrB₂-LaB₆ composition exposed at 2400°C for 10 minutes, which resulted in a 500µm oxide layer comprising of a solid solution La₂Zr₂O₇ glass yielding only 0.2% mass loss.¹⁵⁹ However, these were conventional powder mixing. Most have focused 1D oxidation studies due to the ease of analysing semi-infinite solid diffusion, testing has not reached 3000°C for ceramic composites and few sharp leading edge tests are in open literature.^{221, 250-251} An example by Monteverde et al compared properties such as thermal conductivity on materials survival and leading edge stability.²⁵¹ The results indicated that survivability relies on the majority (85%) of the surface experiencing a negative heat flux (energy re-radiated away).^{221, 251} Empirical sharp leading edge tests followed by modelling are important in understanding how UHTCs can maintain leading edge stability.

2.5.5 Summary

In summary, the properties of diborides and carbides are known from persistent thermodynamic and solidification studies.^{1, 38-39} The properties derived from mechanical testing have well defined ASTM standards. However, evaluating UHTC performance in extreme environments is still emerging. Most of these investigations are based on the boundary conditions associated with hypersonic flight operations. Because real flight testing is expensive, most results are simulated using oxyacetylene combustion, furnaces and arc-jets. Caution should be taken due to lack of standards to compare testing methodology, particularly since analysis may be limited to only the cooling (conductive/re-radiative) component. Few true UHTC compositions have been made, few have been tested at 3000°C and none have investigated effect of microstructure on the homogeneity of the passivation oxide layer.

2.6 Future of UHTCs

The result of literature analysis suggests that there are several processing gaps available for exploration. The return of synthesis chemistry allows for advanced nanomaterials to be studied, with the advantage of liquid phase processing. This research field thus has gaps identified as follows (1) while the sol-gel processing of nanocrystalline carbides has been studied in conventional terms of yield, powder size and phase, very little understanding of the agglomeration and evolution of carbon has been studied; (2) as a result of this, there is very little understanding of how to uniformly disperse phases in a powder mixture, especially in nano-to-submicrometer scales; (3) this also means that very few UHTC composites have been produced using non-mechanical mixing. (4) The effect of extreme environment of 3000°C on materials has not been well explored in open literature, particularly on ceramics; (5) control via sol-gel processing allows for investigation into the effect of small phase additions and effect of microstructural homogeneity on the formation of the protective oxide layer. But these effects have not been fully explored in the stability of 2D leading edge geometry. These five aspects are investigated in the following four chapters.

2.7 Scope of research

The present fundamental research program proposed the synthesis of HfC and ZrC nanoparticles via a sol-gel process. The first two years focused on the sol-gel process to control future composite processing. Both had an excellent foundation of processing parameters in literature. The HfC process had substantial focus on chemical synthesis of the hafnium alkoxide, while the ZrC nanoparticles will focused more on particle interactions and controlling carbon yield. This carbon yield was critical for processing ZrB₂ composites. Key analytical techniques were TEM and SEM for morphology, and XRD and TGA to determine stoichiometry and compositions. Collaboration with MCEM and CSIRO facilities was crucial. The final year developed composites of ZrB₂-5% mol ZrC using a unique powder-gel hybrid process sintered by SPS, within sufficient skill to control densities between sample sizes. The goal was to understand the role of the gel nanoparticle coating on the sinterability of the powder. Included were control ZrB₂ and composites mixed with the sol-gel nanosize ZrC as a comparison. Two

sample configurations were used for mechanical and oxidation testing. Rectangular specimens were required for three-point bending to obtain flexural strength and modulus. Sharp leading edge specimens were prepared for oxidation testing using SHARP B2 methodology; 20° leading edge cut for testing at 3000°C for 10s and 180s exposure to combustion flame, with crucial collaboration with DSTO. These oxidized samples were examined by SEM, optical microscopy and EDXS analysis to understand the roles of microstructure, phase selection, phase properties and oxidation behaviour at this relatively new temperature regime that defines UHTC composites.

3. Experimental Method

3.1 Synthesis and processing

The synthesis of carbides via sol-gel involved several steps common to both HfC, ZrC and later coated ZrC on Cf/ZrB₂. Chronologically, this involved handling of raw materials, sol-gel wet chemistry, processing equipment and modifications - particularly a Lindberg ST 54233 furnace and the SPS Syntex™ SPS-925.

3.1.1 Hafnium alkoxide synthesis for sol-gel

To synthesize hafnium n-butoxide Hf(OC₄H₉)₄, hafnium (IV) chloride 98% (Sigma-Aldrich) under argon was transferred to a Schlenk flask with Suba-Seal® (Sigma-Aldrich) attachments under a N₂/vacuum 4-port manifold without further precautions. A systematic flowchart of the process is shown below in Fig. 3.1.

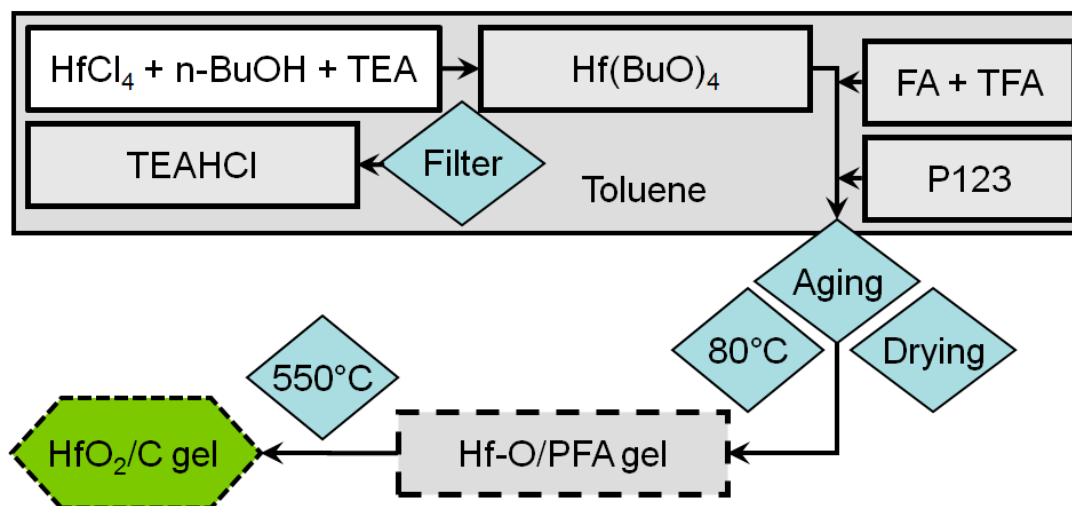


Fig 3.1. Sol-gel synthesis with pre-requisite alkoxide synthesis. The envelope under the solvent toluene represents the air-sensitive portion of the synthesis, where the gel could not be opened or inspected.

The solution was stirred in a 1:5 molar ratio of n-butanol or n-BuOH 99.8% (Sigma-Aldrich) with toluene 99.8% (Sigma-Aldrich) as a mutual solvent. The solution rapidly changed from yellow to violet within 30 minutes. In alkoxide syntheses from metal chlorides, the chloride leaving group is generally encouraged by ammonia directly introduced to the solution.²⁵² To avoid use of ammonia gas, triethylamine or TEA $\geq 99.5\%$ (Sigma-Aldrich) was used to drive

the equilibrium forward, causing a withdrawal of the violet colour and the formation of a white triethylamine hydrochloride (TEAHCl), which was removed by an inline filter. Evaporation of excess solvent resulted in a yellow viscous liquid characteristic of alkoxides based upon an extensive hafnium alkoxide preparations by Bradley *et al* that included instructions on preparation of other alko- groups (R = Me, Et, i-Pr, t-Bu).²⁵³ Calibration of the gel point was guided from detailed work by Larbot *et al* using acetic acid and ethanol to control the water hydrolysis rate.²⁵⁴ Gels were synthesized as oxides, followed by oxides with P123 (PEG-PPG-PEG or Pluronic® P-123) (Sigma-Aldrich), followed by oxides with P123 and carbon. Incubation at 80°C in a laboratory oven resulted in transparent amber gels within 18 hours, which became opaque after 24 hours. The oxide gel could then be inverted without flow and formed the basis for the gel point. Surfactant P123 was then added to the alkoxide gelation process at a 1:20 P123:Hf molar ratio with no observable differences in gelation time. For the carbon component, detailed data was provided on temperature and concentration variables for furfuryl alcohol (FA) 98% (Sigma-Aldrich) polymerisation using trifluoroacetic acid ReagentPlus® 99% (Sigma-Aldrich) as the catalyst.¹²⁵ The pre-polymerized furfuryl alcohol in this work was designed in a 6:1 FA:Hf ratio and was incubated at 60°C for 3h before being added to the P123/hafnium alkoxide solution, effectively resulting in an 27 hour acid-catalysed polymerisation.

3.1.2 Zirconium oxide sol-gel

The block co-polymer surfactant P123 was first dissolved in 99.7% ethanol. Acetylacetone (ReagentPlus® ≥99% Sigma-Aldrich) or “AcAc” was added next in order to prevent the alkoxide addition from immediately undergoing hydrolysis by water. Failure to do so can induce a rapid condensation reaction, producing a zirconia gel, precipitate or suspension. To this solution, zirconium n-propoxide (ZNP) (Sigma-Aldrich) 70% wt in 1-propanol was added to bring the ratios of P123/etOH/AcAc/ZNP in solution to 0.05/40/1/1. The carbon source furfuryl alcohol 98% (Sigma-Aldrich) (FA) was added in a 1/2 ZNP/FA molar ratio. Acid-catalysed cationic polymerisation to polyfurfuryl alcohol (PFA) used 33% HCl (10.82M by titration). This retained C/Zr ratio was fixed at a HCl/Zr ratio of 1. The flowchart shown in Fig 3.2, which demonstrates this process can be conducted without an air-sensitive Schlenk envelope.

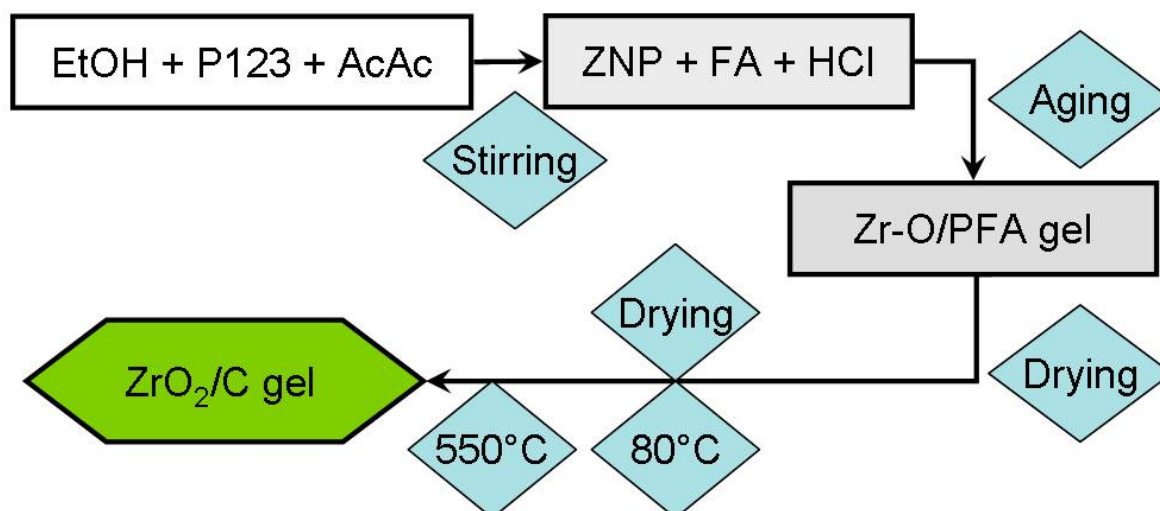


Fig 3.2. Schematic synthesis of sol-gel zirconia-carbon precursor.

The gel point was empirically calibrated by simple oven gelation studies by Larbot *et al*, although water was directly introduced via the acid catalyst for FA polymerisation.²⁵⁴ Solutions were aged for 72h and dried for 24h at room temperature and then at 80°C for 24h to remove ethanol.

3.1.3 P123/PFA decomposition

The samples were placed in the hot zone with an aluminium hook and the quartz tube was plugged at one end to a relief bubbler. The gel was transferred to this alumina crucible, weighed and pyrolyzed at 550°C/5h in a Ceramic Engineering Ltd (Sydney) furnace with a BTC-4300 controller, which repeated every time the furnace was switched on/off. The flowing gas was N₂ at a rate of 120mL/min to remove the surfactant P123 and prevent excessive carbon oxidation.

3.1.4 Carbothermal reduction

To produce carbides, the pyrolyzed gel product was placed in an alumina crucible and fired up to a maximum temperature 1450°C for 2h or 5h under flowing Ar at 120mL/min in a Lindberg 54233 Single Tube furnace. The Eurotherm controller was set to ramp at 2°C/min. The vacuum was monitored by a Dynavac TM-8. In 2011, discovery of SiC/SiO₂/mullite contamination ended a costly six month hiatus before the furnace was overhauled. Fig 3.3(a) and (b) display the furnace before and after the overhaul.



Fig 3.3 (a) Lindberg 54233 ST furnace used for HfC synthesis in 2009. **(b)** New configuration from 2012 for ZrC and ZrB₂ projects.

Carbothermal reduction was now possible without buffering the atmosphere. Filters were added and the leak points were calibrated from the maximum vacuum pressure. Plutone® piping runs from regulator to gate valve, with Inficon® Pirani CC-3 and Bourdon gauges to better control vacuum.

3.1.5 Composite materials handling

Once the sol-gel process was linear from alkoxide (80°C), oxide (550°C) and carbide (1450°C), the ceramic nanopowders were used in composite synthesis.

3.1.5.1 Zirconium diboride

Zirconium diboride was purchased in quantities of 250g from ABCR, the distributor of H.C.Starck. The Grade B formula contained 96-97% ZrB₂, with 0.2-2.5% impurities of HfB₂ and 0.1-1% impurity of Fe in the elemental composition shown below in Table 3.1:

Table 3.1. Impurities listed in ZrB₂ powder from ABCR (HC Starck)

Impurity	Mass fraction (µg/g) or (ppm)
Carbon	0.2 % max
Oxygen	1.5 % max
Nitrogen	0.25% max

Iron	0.1% max
Hafnium	0.2% min

The ZrB_2 powder was of reported purity 97% (up to 2.5% HfB_2) with a particle size of 3-5 micron as verified by SEM imaging. This indicated that the powder was milled due to the high oxygen uptake (refer to Table 2.3).

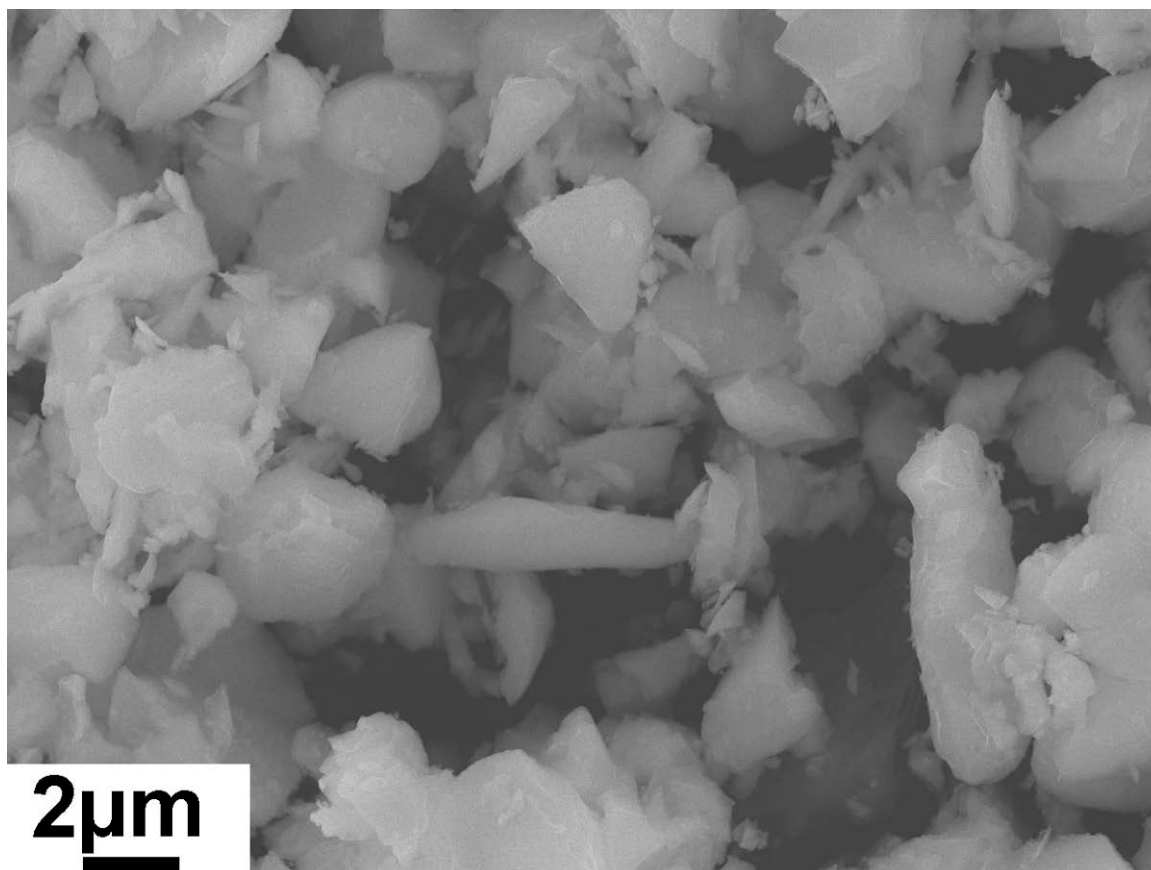


Fig 3.4. ZrB_2 powder as purchased and viewed by SEI without conductive coating. Note lack of contrast, which may occur from surface oxide layer charging.

3.1.6 Zirconium diboride coated powders

The modified powders were prepared by modification of the zirconia sol-gel process in new laboratories in 2010. Fig 3.5 shows the modified process. However, the furfuryl alcohol ($C_5H_6O_2$) 98% (Sigma-Aldrich) (FA) was added at an FA/Zr molar ratio at a minimum 4:1. Solutions were aged for 72h at room temperature. When this was completed, the solutions were transferred to open containers and the ZrB_2 powder was added during stirring.

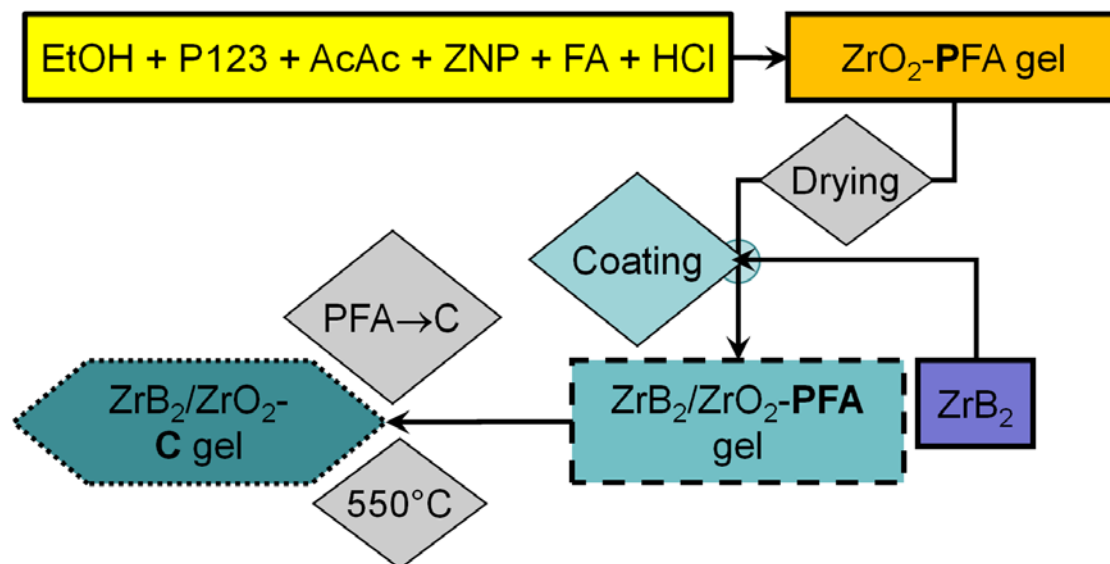


Fig 3.5. Schematic of sol-gel zirconia-carbon precursor coated on ZrB₂ powders.

Coating the sol on the ZrB₂ powder should take place while the powder is immersed, as it is extremely adhesive to any surface. The ZrB₂ powder was added at a 95% molar ratio based on the designed ZrC yield, fixed at 5 mol% or 4.59wt% ZrC in the composite. This yield assumed the full conversion of ZNP to ZrC. For convenience, the gel portion which becomes ZrC will be referred to as 4.6wt% ZrC and referred to in wt% where possible. Alcohol drying resulted in rapid gelation of the powder-gel composite, at which point no mechanical stirring is possible. The settling of powder in the gel appears to occur less in glass over plastic and inhomogeneity can occur from drying of the gel around the edge. Further drying occurred at 80°C for 24h to completely remove ethanol. The gel often formed a grey greenbody. This powder-gel cast in the container often shrank and maintained greenbody cohesion during furnace transfers. The powder-gel cast was mixed with acetone and crushed by an agate pestle and mortar and dispersed ultrasonically where necessary. The dried powder was pyrolyzed under nitrogen flowing at 120mL/min at 5°C/min to 550°C for 5h to decompose the surfactant and remove residual monomer FA. After pyrolysis, the powders were again dispersed by agate pestle and mortar to break up coated ZrB₂-5% gel (ZrO₂/xC) agglomerates. After carbothermal reduction, the powder shrank into a greenbody and had to be dispersed again to break up agglomerates. The synthesis laboratory and its relatively simple equipment is shown in Fig 3.6.



Fig 3.6. Basic laboratory equipment for powder-gel process

From left to right, these are a standard laboratory oven, stirrer plate, Schott bottle, agate pestle and mortar, Keiq sieves and solvents. Powders were sieved to 50-100 μ m by Keiq Sieves (Keison International Ltd). No milling was used in order to minimize oxygen uptake.

3.1.7 Spark Plasma Sintering (Dr Sinter SPS-925)

Ceramic specimens were prepared by Spark Plasma Sintering using the Dr Sinter SPS Syntex 925 (Fuji Electronic Industrial Co., Ltd), a technology that is also known by its technical name Pulsed Electric Current Sintering (PECS). A photograph of the setup was attached in Fig 3.7(a). Two graphite cylindrical punches compressed powder in a graphite collar. Graphite foil lined the inner collar and the punches such that the powder was wrapped in carbon. Graphite spacers of increasing size resulted in contact with upper and lower electrodes, completing the circuit. Powder mass was 2.3g for 10mm samples while 30mm samples were 24.0g. Parameters such as chamber pressure, specimen displacement and displacement rate were monitored using the software.

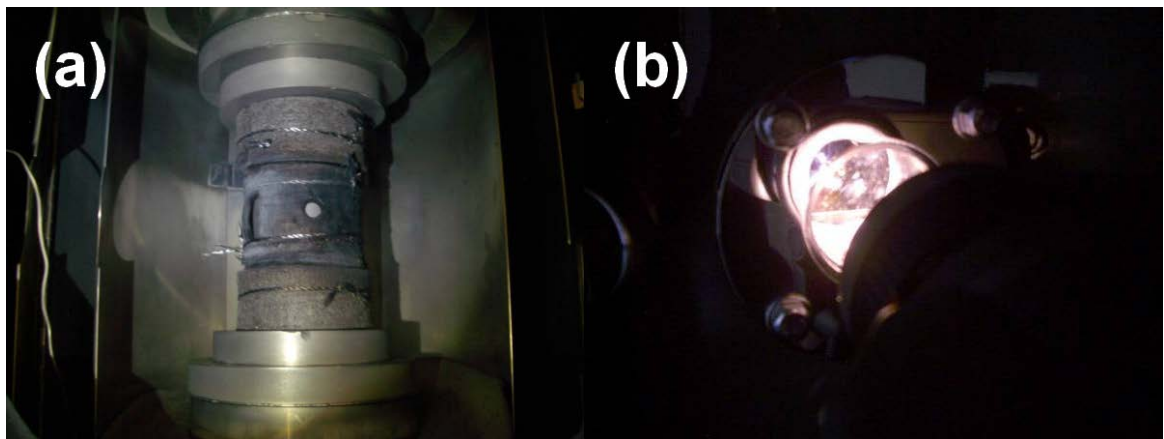


Fig 3.7. (a) Setup in the chamber of the SPS Syntex® SPS-925 for a 30mm die, with a viewing port on the left for the pyrometer **(b)** Pyrometer dependence on chamber window to view infrared emissions from the carbon wrapped die.

Applied pressure was kept constant by manual hydraulic control. The temperature was controlled using an optical pyrometer focused on the die surface. Pyrometer position was set slightly above the target area because of the shrinkage caused by densification. The pyrometer LOS must be fixed as shown in Fig 3.7(b) to constantly view the surface of the graphite die. Interference in the pyrometer LOS will result in the SPS current trajectory spike above the positive feedback loop of the program. Incidents included residue on the quartz viewing window, or pyrometer focus on the carbon felt insulation rather than the die. Close monitoring of the die surface (shown in Fig 3.8) or current draw is required.

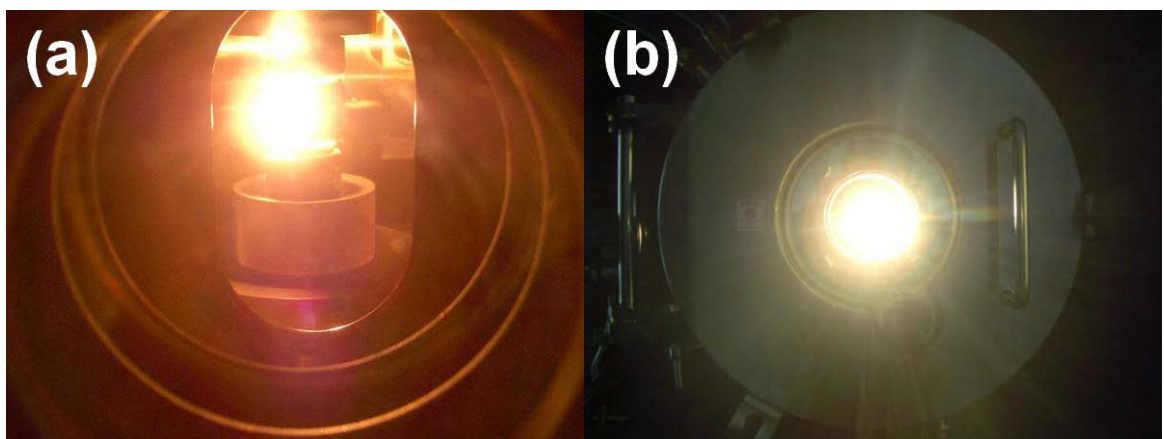


Fig 3.8. (a) Normal operation SPS-925 where only the central graphite die was heated to incandescence. **(b)** Failure of pyrometer LOS resulting in overheating

The SPS is sensitive to damage. Failure to shutdown can result in melted die cores requiring replacement, volatilization of materials and damage to the steel electrodes. Maximum temperatures were up to 2000°C and held for 5 min at a maximum applied pressure of 40MPa and modest heating rate of 100°C/min and a default 12:2 (on:off) pulse rate. As sample size increased, larger dies had a lower aspect ratio and relative surface area. The increase in thermal mass meant that cooling relied more on conductive heat transfer via the stainless steel electrodes over radiative cooling. Deformation of the cooling jackets adjacent to the electrodes resulted after several large B₄C samples were produced, resulting in restricted operations until Inconel™ plates arrived. The second modification was additional thermocouples at the upper and lower electrodes shown in Fig 3.9.



Fig 3.9. Lower and upper steel electrodes of the SPS Syntex® SPS-925 showing the ring of felt/steel denoting the attachment of K-type thermocouples.

These features and modifications indicated that the 925-series is a research-level machine attached to a disproportionate industrial generator. Maximum pressure and temperature are not simultaneously/frequently usable. The uncertainty added to the intention to eventually transfer sintering across to pressureless techniques, thus minimum parameters were used in this research program. This also resulted in fewer interruptions since the limits of the SPS were not being pushed.

3.1.8 Powder analysis

Powder preparation for XRD, SEM, TEM, Raman spectroscopy all used an agate pestle and mortar. Harder HfC, ZrB₂ and ZrC samples were ground with a boron

carbide pestle head/mortar located at CSIRO where necessary. For TEM dispersion of powder in acetone/ethanol in Pyrex® bottles was by ultrasonic treatment for up to 5 minutes to achieve suspension.

3.1.9 Sharp leading edge geometries

The test samples were cut from a Struers Secutom-10 using a 10-inch steel diamond coated blade of diameter 0.25mm, running at 3500rpm at a rate from 0.005mm/s. The 30mm diameter discs of thickness 5mm were marked with 1mm marker, yield two wedges. Cutting was stable until proximity of the approaching free surface on the other end resulted in an uncontrolled fracture. The leading edge was more important and was cut first. When it reached the opposite side a brittle fracture notch often occurred shown in Fig 3.10. This defect was nipped off or plane ground. The coupon was then reversed to cut from the tip at the other end. Both wedges had angles of 20°, with the longest wedge 29mm and the secondary wedge 24mm. Both were cut to an edge radius of below 100µm.

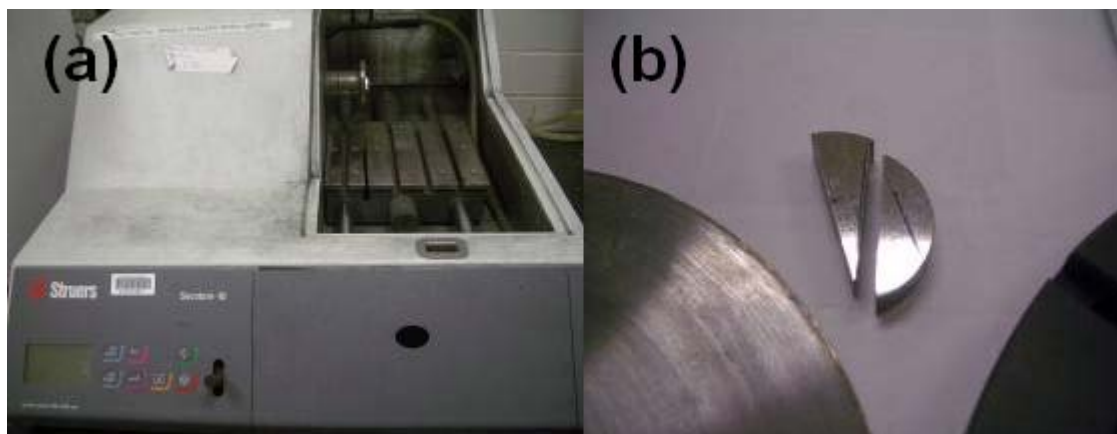


Fig 3.10. (a) Secutom-10 **(b)** 30mm sample bisect and leading edge cutting.

3.1.10 Composite surface polishing

The sintered samples were demoulded with a uniaxial press. The resulting expelled cylinder was comprised of the two graphite punches sandwiching the ceramic sample. Plane grinding began with Magnetic Disk (MD) diamond plates MD-Piano 220 and Piano 1200 for fine grinding. A sample was sent to Struers, which followed the diboride method found online. Most samples were adapted from the Struers diboride sequence from Piano 1200, to P2500 and P4000 SiC. The adapted method involved water lubrication only, use of composite submicron

debris and rapidly sheared SiC particles from the paper at 50N/sample. This resulted in a surprising mirror finish. But more importantly, P4000 SiC could not abrade the ZrC/HfC nanoparticles. Intergranular particles and grain boundaries were topologically uneven to about $< 2\mu\text{m}$ and easier to identify in SEM.

3.1.11 Aerothermal tests: combustion zone and preparation

The experiments on the leading edge geometries were conducted at the Defense Science & Technology Organisation (DSTO). The High temperature Oxidation Materials Evaluation Rig (HoMER) in Fig 3.11 at DSTO is shown.

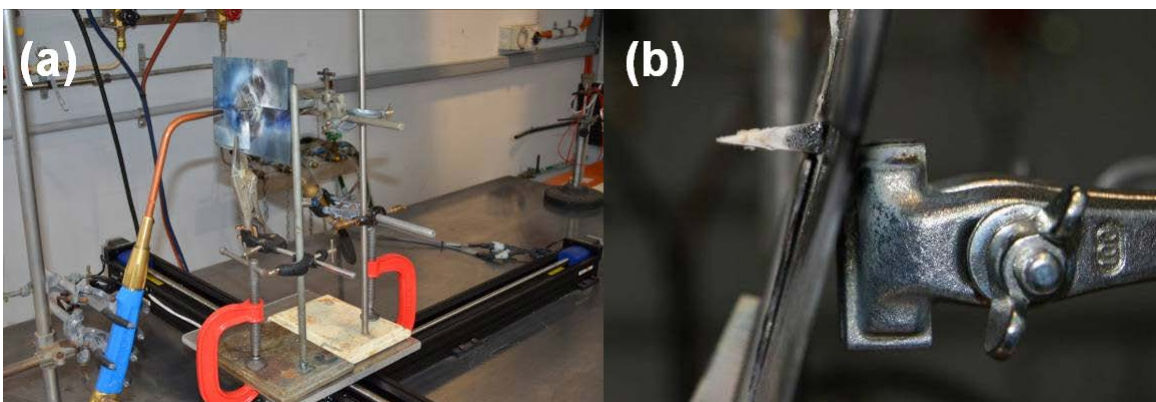


Fig 3.11. HoMER setup showing (a) specimen position, stage control and gas manifold, with (b) oxidized sample after oxyacetylene ablation.

Before design of flight vehicles, innovative ground based facilities were designed to screen suitable materials. A general guide to oxyacetylene testing can be sourced from scientific literature. A more distinct guide can be found in ASTM E285-08 “The Standard Test Method for Oxyacetylene Ablation Testing of Thermal Insulation Materials” but as noted by Corral et al, the combustion gases represent rocket motor exhaust rather than aerodynamic heating.²⁵⁵⁻²⁵⁶ Furthermore, reports of artefacts during furnace and oxyacetylene combustion have been reported, including Al and Ca impurities that are not expected in a hypersonic flight envelope.²⁵⁷ The oxygen regulator pressure was at 300kPa and acetylene at 150kPa. The step down pressure was 150kPa and 100-120kPa respectively with the nozzle size fixed at ID 12mm. Calibration with a two colour pyrometer and 10mV heat flux gauge in April 2012 used two overlapping wavelengths from 700nm to 1150nm in the IR region fixed to a 2mm diameter

spot at increasing distance from the nozzle. Fig 3.12 showed the change in heat flux as distance from the nozzle tip is increased.

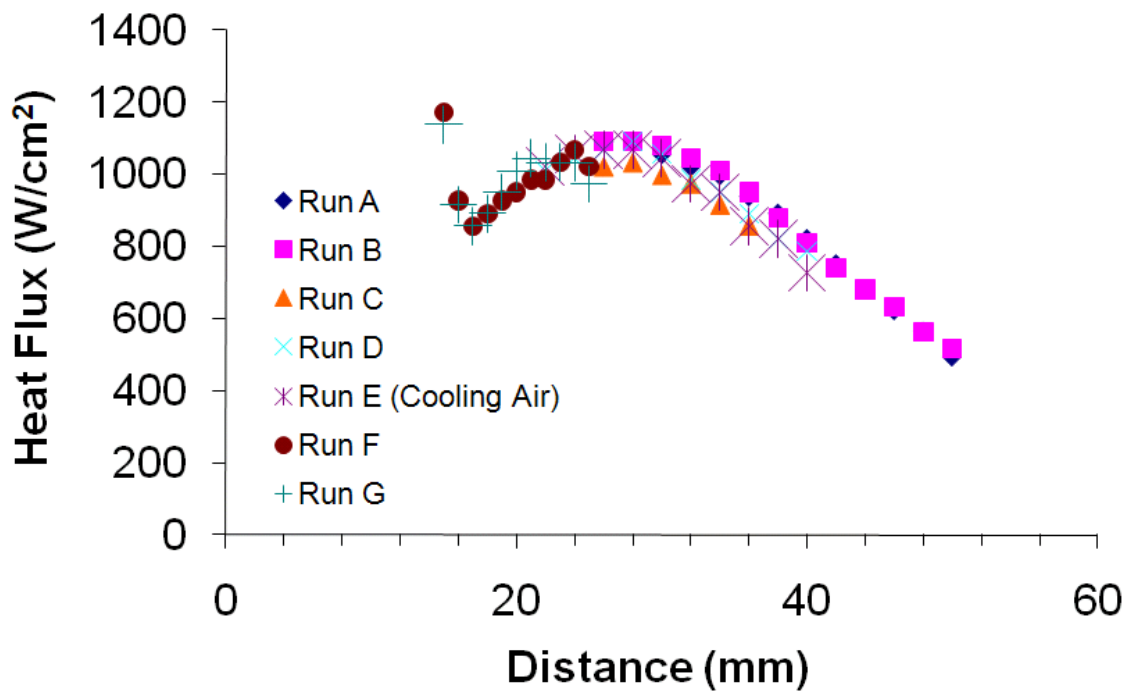


Fig 3.12. Heat flux to specimen distance on HoMER (courtesy of DSTO).

The peak heat flux of $\sim 1000 \text{Wcm}^{-2}$ (10MWm^{-2}) was found at a 26-30mm distance, corresponding to a peak temperature of 3400°C and yielding 2mm window. Fig 3.11 showed that the sample was fixed to a stainless steel clamp, and shielded by an air cooled Mo-alloy overlapping plate preventing the combustion gas from reaching the stage, specimen holder and control systems. This calibration was required to maintain heat flux intensity because the stage control is fixed during the test. Thus as the materials melt, recession of the leading edge results in a lower heat flux. As a result, testing is only accurate to a recession of $2000\mu\text{m}$. Samples cooled rapidly from 3000°C and within a minute were removed and transferred tip-up to pre-weighed polyethylene 5mL containers. They were cold mounted in epoxy resin to preserve a presumably brittle microstructure. They were then cut along the long axis in order to observe the cross-section of the microstructure. The thermal conductivity and distance from the flame tip created different boundary conditions, which was responsible for the different phases that developed along the tip and surfaces. These were analysed by optical

microscopy, SEM/EDS and XRD to determine the evolution of these compositions.

3.2 Characterization

3.2.1 NMR Spectroscopy

Both ^{13}C and ^1H NMR spectroscopy analysis of the synthesized alkoxide were first mixed in an Ar-glove box with CDCl_2 and n-butanol as a reference marker. The spectrometer was Bruker Avance400 (9.4T) with a 5mm broadband inverse probe with Z-gradients and a 5mm quad-switchable probe/4mm multinuclear solid state probe. The frequency for ^1H was at 400.1MHz and ^{13}C at 100.6MHz. Peter Nichols is the supervisor of the NMR facility in the School of Chemistry and he personally operated the spectrometer.

3.2.2 Thermogravity analysis (TGA)

TGA was conducted on a Perkin Elmer Jade TG/DTA 6300 shown in Fig 3.13.



Fig 3.13 Jade TG/DTA 6300 by Perkin Elmer for thermogravity analysis.

Mass loss was the primary determination of PFA decomposition and thus the amount of carbon yield in gel samples. After initialization, taring and crucible weight calibration, samples were fired in air to remove carbon at 3°C/min up to 800°C for 1 hour where weight loss stopped, indicating all carbon was oxidized. An accurate stoichiometric calculation was based on the oxidation of carbon. The remaining material is an oxide and thus the wt% C in the pyrolyzed gel was determined. This instrument was capable of differential thermal analysis (DTA) but this feature was not extensively used. The software was Pyris™ Manager 8.000172 by PerkinElmer Inc. Crucibles came in 20mg (short) and 160mg (tall) for different sample quantities. It should be noted that due to damage to the LED balancing system and electric motor in 2011, a consistent 0.3% wt error was found in the same samples.

3.2.3 TEM

Most of the ZrC and HfC bright field images were analysed at the Monash Centre for Electron Microscopy (MCEM) using the JOEL JEM2011 TEM. These are shown below in Fig 3.14.

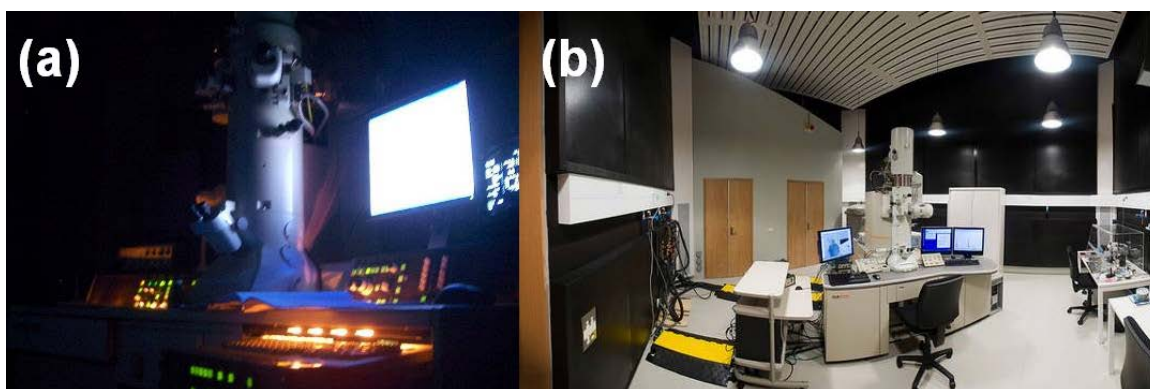


Fig 3.14. (a) JEOL JEM2011LaB6 operation **(b)** JEOLJEM2100F idle in wide angle capture. STEM and HAADF controls on attached table

Running at 200kV and a LaB₆ element at 103mA, it contained a high resolution objective lens pole piece and used an Oxford Instruments Si(Li) X-ray detector with UTW and an Inca X-ray analysis system. Bright field imaging used a Gatan 894 UltraScan 1000 CCD camera (2000 x 2000). Preparation passed through both a Gatan 900 liquid N₂ stage and a Gatan 655 turbo pumping station for the

single-tilt holders. Powders were prepared by suspension and pipette deposition on EMGrid® Agar S147-H holey carbon grids. Collaborated work, particularly for publications, was conducted by Tim Williams at MCEM, who operated the JEM2100F, which had the advantages of a FEG with true “point EDXS” and possessed STEM capability. It had a high resolution pole piece and piezoelectric stage allowing for minute adjustments and an oil free pumping system. The bright field detector used a Gatan UltraScan 1000 (2000p x 2000p) CCD camera but the STEM mode used the Gatan BF/ADF STEM detectors with a JEOL BF/HAADF STEM detector for analysis by Z-atomic contrast. The EDXS was performed with a JEOL 50 mm² Si(Li) EDX detector for line and mapping of elements. Software was Gatan Digital Micrograph with (*.DM3) Windows™ plug-in. Most TEM images were multibeam high resolution images as the aperture needed to be manually selected and aligned for complete bright field or dark field.

3.2.4 SEM

SEM was conducted at MCEM. Powder samples were mounted with carbon tape on provided aluminium stubs; these were coated using a Cressington 208HR SC (Sputter Coater) if necessary, followed by imaging using a JEOL JSM7001F in Fig 3.15. Ceramic samples were conductive except the oxide/carbon gels.

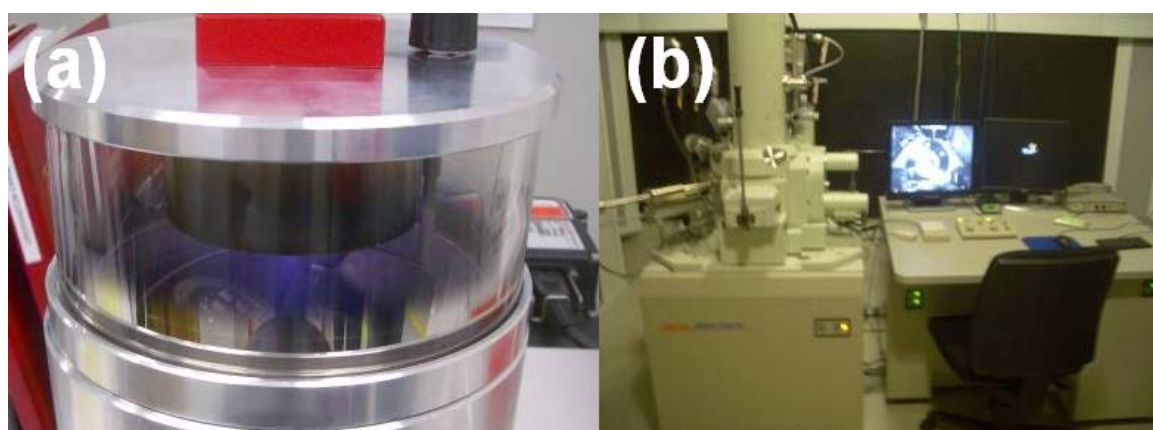


Fig 3.15. (a) Cressington 208HR sample coating (b) JEOL JSM 7001F SEM.

The JEOL JSM 7001FEG as it possessed 5-axis stage and an IR camera to monitor the loading procedure. The advantages of a field emission gun allowed for nanometer spot size for SEI imaging. It also had a retractable BSE detector and the EDXS system used a Bruker 10 mm² Si drift detector. Bruker® INCA™

software was later replaced by AZTEC™ in March 2012. In EDS mode this was used to characterize phases developed during materials aerothermal testing and qualify elements in composites, particularly where highly porous or damaged samples were cold mounted. Most images were viewed in Backscattered Electron Mode such that the phases were more easily distinguishable due to the "channeling effect". Sometimes it was possible to polish flat the samples that contained hard ZrC or even ZrO₂ nanoparticles present on the grain boundary. The BSE coefficient depended heavily on the orientation of crystallographic planes and thus electrons were "channeled" into a material if the beam was close to a major zone axis with fewer electrons backscattered. This resulted in a correspondingly lower BSE coefficient (dark contrast). Away from zones, the BSE coefficient was be higher (bright contrast). These are seen mostly in Section 6. Samples that were not polished flat due to hard secondary phase particles were directly topologically viewed in SEI.

3.2.5 Raman Spectroscopy

Raman Spectroscopy was conducted using a Reinshaw Invia. An extremely versatile technique due to the ease of sample preparation (powders are placed on a glass slide), the instrument used a low power of 5-10% of 300mW laser power at 533nm calibrated with a Si standard, spectra were collected over a range of 1000-3500cm⁻¹ which allowed for identification of D, G, 2D and D+D' peaks present in graphene and graphite. The resolution was not pressed for the limit of identifying peak shoulders as the evolution study was only interested in the ordering of carbon.

3.2.6 Gas sorption

The Micrometrics VacPrep 061 and TriStar II 3020 shown in Fig 3.16 were used for surface analysis of the product after 550°C/5h when the surfactant had been removed. It was also used to characterize the evolution of surface properties as the gel was treated up to 1450°C. A ~0.4g specimen of the sample was placed in the sample tube and analytically weighed. These specimens were evacuated to remove trapped gas and moisture by the VacPrep 061 250°C/8 hours. This resulted in a weight loss from solvent or moisture removal.

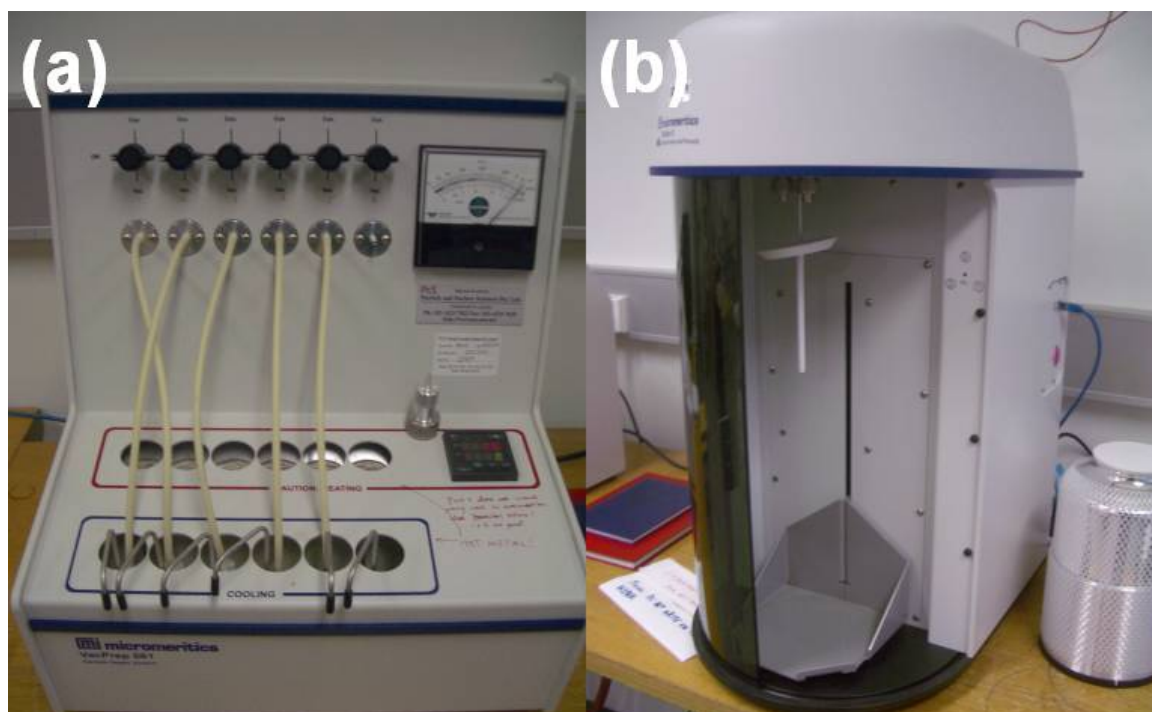


Fig 3.16 (a) Micromeritics VacPrep 061 with 5 operational ports sample degassing. **(b)** Micromeritics TriStar 3020 with a dewar of liquid N_2 to the right, which sits on the elevator before the samples are lowered into the bath.

The sample tube was transferred to TriStar 3020 analysis port with inserted filler rods and isothermal jackets attached. The TriStar software controlled the operation; the user selected for instructions, in particular the free space, P_0 and selected pressures to measure BET. With an unknown sample density, nanoparticle size calculations were relative. Like all vacuum-gas exchange systems, the TriStar experienced some leaking problems, but these were resolved by cleaning the o-rings. The seals were also much smaller, making this task much simpler with only three leak surfaces.

3.2.7 Density measurement

Density was conducted using the Archimedes principle on 10mm and 30mm SPS samples. Samples were bisected before being weighed using an analytical balance ($\pm 0.0001g$). Porosity is effectively the volume that is not occupied by the total bulk volume V_{bulk} . In the Archimedes technique, a fluid is used to measure this porosity. The sample is weighed (W_{air}) followed by immersion in a fluid of known density to fill the pore volume. This immersion often uses a vacuum infiltration in order to ensure all open pores are saturated. This weight (W_{sat}) is

usually the highest value. The sample is then weighed while submerged in the saturating fluid (W_{sub}). This step is crucial as it accounts for the closed pores which are not infiltrated. Thus the volume of the pores, the volume occupied by the matrix and the bulk volume can be expressed by the three equations (3.1 to 3.3):

$$V_{\text{pores}} = \frac{W_{\text{sat}} - W_{\text{air}}}{\rho_{\text{fluid}}} \quad (3.1)$$

$$V_{\text{matrix}} = \frac{W_{\text{air}} - W_{\text{sub}}}{\rho_{\text{fluid}}} \quad (3.2)$$

$$V_{\text{bulk}} = \frac{W_{\text{sat}} - W_{\text{sub}}}{\rho_{\text{fluid}}} \quad (3.3)$$

The volume of the open pores and the volume of the matrix add to the volume of the bulk. Thus the density of the sample can be calculated from the theoretical density. This used a simple rule of mixtures. To account for solid-solution, the densities were further refined by results of quantitative Rietveld analysis. The density of residual carbon could not be determined as noted in the report.

3.2.8 X-Ray Diffraction

Bulk powders (>0.4g) were transferred into aluminium socketed slides and pressed flat using polycarbonate discs. The X-ray goniometer was a Phillips 1300 X-Ray Diffractometer operating under CuK_α radiation (40kV, 25mA). The limitations of this system, along with aging software Trace v6, allowed for only identification of phases; the scans only allowed a fixed step size 0.02° between $10-80^\circ$ at $2^\circ/\text{min}$. Conventional lattice parameters were still obtained using Cohen's method and least squares method after fitting with to Pseudo-Voight function with GBC® Trace v6. Identification of phases used the ICDD database. Rietveld analysis was performed using a Bruker D8 Advance X-ray Diffractometer operating under CuK_α radiation (40kV, 40mA) equipped with a LynxEye detector was employed to obtain the XRD patterns. The samples were scanned over the

2θ range 10° to 130° with a step size of 0.005° and an equivalent variable count time (VCT) as shown in Table 3.2

Table 3.2 VCT Scan Parameters Used.

Scan Range ($^\circ 2\theta$)	Scan Speed (seconds per step)
15.0→25.895	2.6
25.9→45.595	8.2
45.6→61.495	17.3
61.5→78.195	39.8
78.2→130.0	82.6

Quantitative Rietveld analyses were performed on the data using the Bruker TOPAS™ V4.2 program. Background signal was described using a Chebyshev polynomial linear interpolation function. Cell parameters, vertical sample displacement, peak full width at half maximum and scale factor were all refined. Crystallite size was determined via the volume-weighted column height method, with instrumental broadening being modelled from the NIST 660b LaB6 standard using a Thompson-Cox-Hastings pseudo-Voigt function. Please note that quantitative results are based on the identified crystalline phases only. A refined lattice parameter was performed at the PDF beamline at the Australian Synchrotron at an X-ray energy of 15KeV with samples placed in 0.3mm capillary. Samples were scanned for 10mins from $16-96^\circ 2\theta$ values with data analysed using Bruker TOPAS™ V4.2 (Bruker AXS).

3.2.9 Indentation

A brief investigation of hardness and fracture toughness were measured using a Duramin A300 indenter, set at HV_{1kg} 1168 objective. The machine is shown below in Fig 3.17. The ECOS software automatically identifies corners and indentation widths (2a) allowing for rapid input of hardness values following the classical DPH/HV test developed in 1921 at Vickers Ltd (currently ASTM E92). Hardness was later compared to flexural strength or empirically correlated to strength by conversion tables suggested by Brooks et al.²⁵⁸⁻²⁵⁹

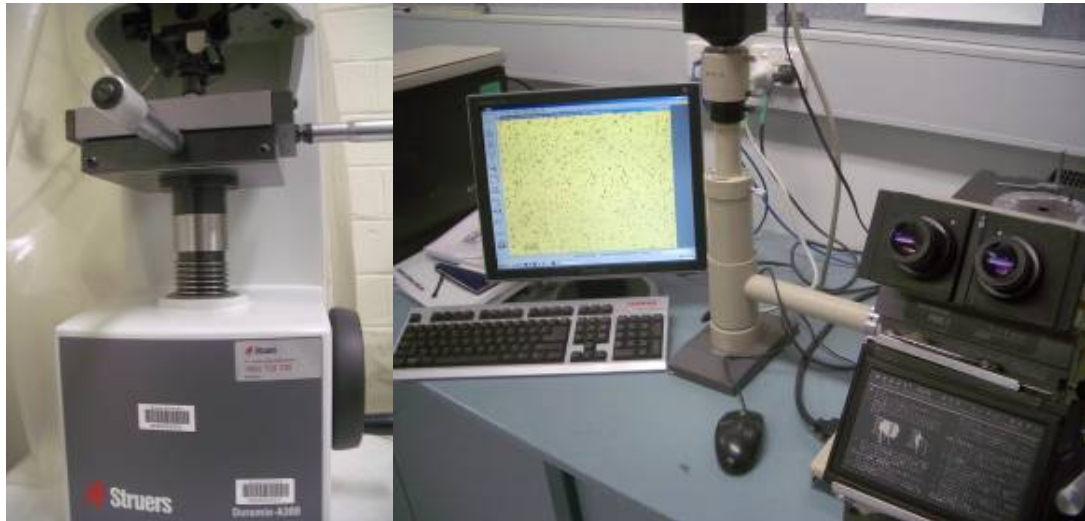


Fig 3.17. Duramin A300 indenter and inverted microscope for surface imaging.

However, optical microscopy using Spot Advanced® and a CCD camera was required for the fracture toughness. The Anstis equation is commonly used for ceramic specimens and is shown below:²⁶⁰

$$K_{DCM} = 0.016 \left(\frac{E}{H} \right)^{1/2} \frac{P}{c_I^{3/2}}$$

Due to the lower predictability of ceramic hardness and fracture toughness a minimum of 10 measurements were taken. Values for (2c) were gathered from the ECOS data. Hardness was directly measured, but elastic modulus was sourced from literature from a similar composite as 517 GPa, although this varies from 500 to 540GPa.²⁶¹

3.2.10 Flexural strength by 3-point bending

While the emphasis was on high temperature refractory performance, the flexural modulus and strength at room temperature was briefly investigated. Samples of 23mm x 3mm x 5mm bars were cut with 0.25mm diamond saw from the 30mm samples from the SPS after polishing. The edges were lightly chamfered but could not completely remove edge chafing, shown in the setup in Fig 3.18. The method was adapted from literature of similar ZrB₂ specimens, which closely adapted ASTM C1161 for ceramic materials in 3-point loading.

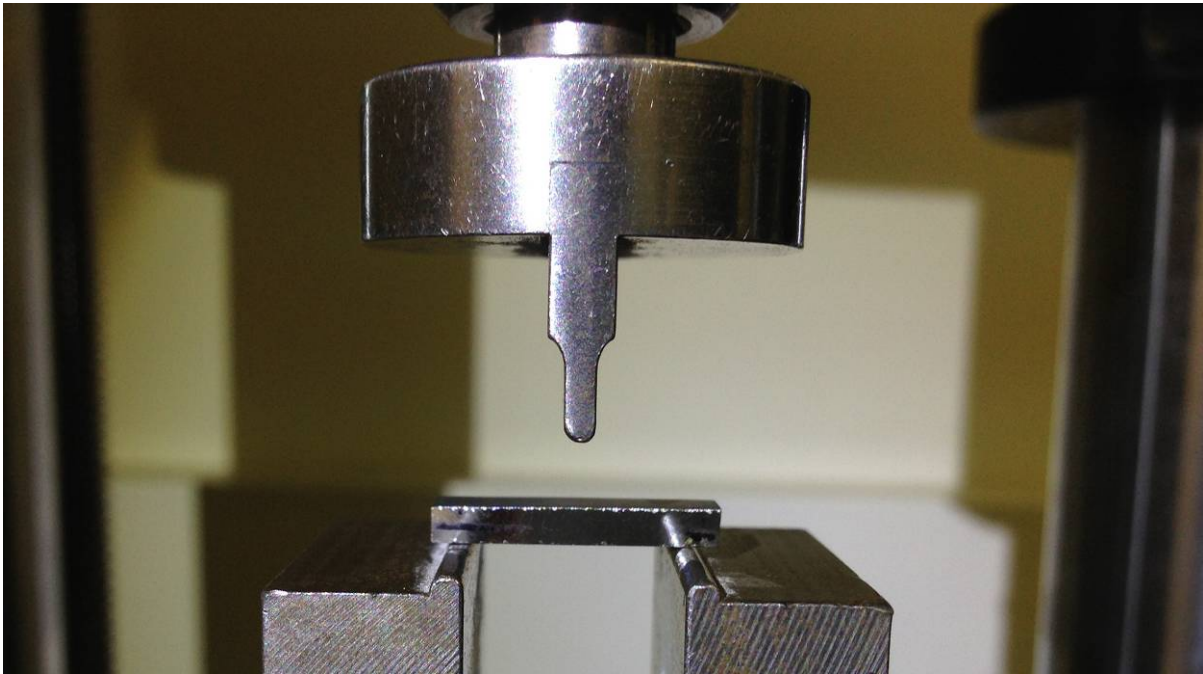


Fig 3.18. Instron 4505 with 3 point-loading 10kN cell on ZrB_2 composite bar at ambient temperature over an 18mm span.

Using a screw-driven Instron 4505 running software Merlin®, the crosshead speed was 0.2mm/min and a minimum of 3 samples were run for the two compositions: control ZrB_2 and the composite gel-modified ZrB_2 using a 10kN load cell over a 20mm span. Flexural modulus and strength were quoted as modulus and strength as the samples were assumed homogenous.

4. Hafnium carbide

This chapter focused on developing a sol-gel method to synthesize nanocrystalline (nc-) or nanopowder hafnium carbide (HfC). This early work was committed to modest objectives since it was initiated as an undergraduate program in 2008 and addressed the simple question of whether it was possible to adapt a similar work that produced SiC and TiC.^{123, 165} At the time, only a single work documented production nc-HfC, using a phenolic resin and acetylacetone as a carbon source.¹²⁹ With permission of the Monash Graduate School, early sections of this chapter (4.1 and 4.2) included brief synthesis and characterization from the Honours program as background for the reader. It should be noted that the undergraduate program only achieved the synthesis of sol-gel precursor and did not succeed in production of HfC. The success in the PhD project was due to samples that possessed sufficient carbon and able to synthesize HfC. The first question addressed was whether it was possible to synthesize the hafnium alkoxide precursor and in adequate quantity and purity. The second hurdle involved its integration into a sol-gel mixture without degradation or precipitation. These two technical hurdles were overcome during the undergraduate project. In the PhD program, sufficient carbon was present in the gel, and the effect of pyrolysis and carbothermal reduction was investigated. The goals of these two processes were to understand the nanoparticle evolution and investigate the microstructural evolution. Technical success was gauged by the stabilization of the alkoxide and the ability to control the polyfurfuryl alcohol (PFA) decomposition to produce sufficient carbon for the reaction. Success gave the ability to control the oxide crystallization in the gel and the subsequent formation of HfC both in high purity and nanocrystalline form. These three parts form the three major sections of this work. A further benefit would be derived from the ability to disperse the nanopowder, making it ideal for sintering studies.

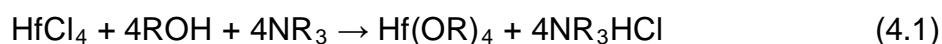
4.1 Synthesis of hafnium alkoxide

There was general agreement in the sol-gel methodology from the alkoxides Si, Ti and Zr from previous work.^{123, 165, 262-265} However, there was a significant difference with hafnium systems. Hafnium-based compounds are more expensive,

more unstable and the purchased chloride needed to be transformed to alkoxide first. Thus the project actually depended on successful synthesis of the hafnium alkoxide precursor before integrating into the standard sol-gel methodology. A gel is a stable formation of networked oxide “ether” condensation bridges between the hafnium ions. An unsuccessful synthesis resulted in oxide formation by self-condensation, which resulted in precipitated oxide powders. This would negate the nano-level mixing immediately. Therefore, observations coupled with limited instrumental analysis were an adequate gauge of success.

4.1.1 Organometallic synthesis

Chlorides are among the most thermodynamically stable anions for metals. The chloride anions needed to be removed for an oxygen because the goal of synthesis was the percolation of a $(\text{Hf-O})_x$ repeat unit. The developed reaction to replace the chloride group with an alkoxide proceeded according to equation 4.1;



where R represents an alkyl chain. Mixing the chloride and alcohol results in incomplete replacement due to an equilibrium and the addition of a base such as ammonia forced the deprotonated alcohol (RO^-) to behave as a nucleophile to remove the chloride from the system.²⁶⁶ This is because the conjugate acid is highly polar and formed a precipitate in an organic medium.²⁵³ But the alkoxide is a poor leaving group and is vulnerable to hydrolysis by water.²⁵² The synthesis was conducted in a Schlenk line. Hafnium (IV) chloride was transferred in a glove box to a Schlenk flask, dissolved in excess n-butanol observed in Fig 4.1.



Fig 4.1. Dissolution steps of hafnium chloride in n-butanol. Colour changes are due to ligand and coordination changes.

This was stirred at room temperature using N₂/vacuum 4-port Schlenk manifold shown in Fig 4.2. Reagents were injected through Suba-Seal™ under positive N₂. HfCl₄ powders that were pure and unhydrated yielded brilliant colour variations from yellow, orange, red, burgundy and purple that suggested changes in structure and cation-ligand co-ordination displayed in Fig 4.1.

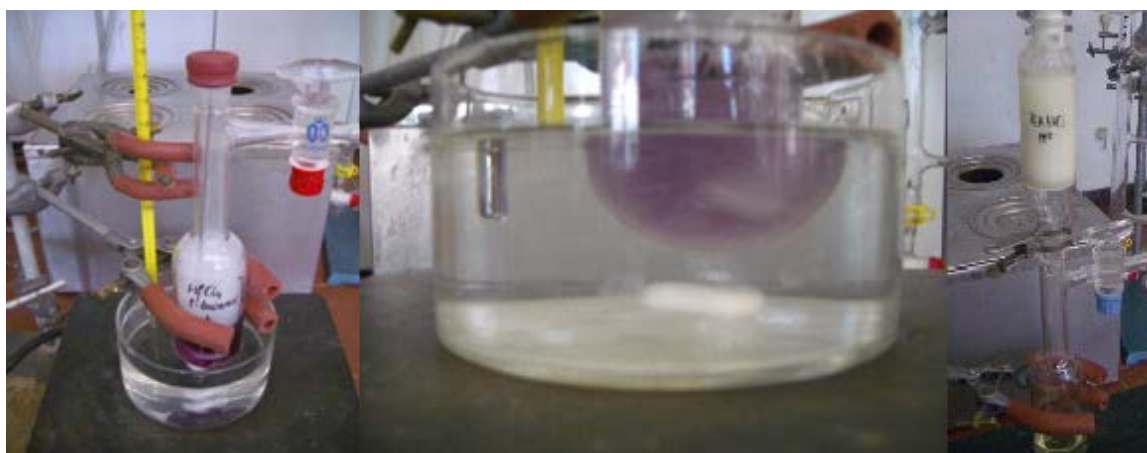


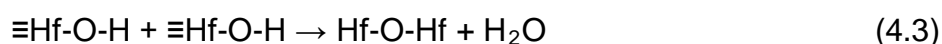
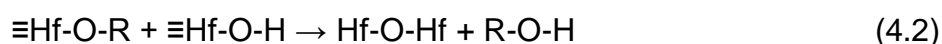
Fig 4.2. HfCl₄ in n-butanol after triethylamine injection through Schlenk Suba-Seal™. Precipitate forms and is removed by inline filter and the alkoxide is collected (right).

Completion of the reaction used an liquid organic base rather than ammonia gas added to the hafnium chloroalkoxide to complete the substitution, yielding a precipitate able to be filtered (Fig 4.2, far right) out from the non-polar solvent toluene.²⁵² The expected yield of the precipitate of 11 attempts of synthesis was 97.7±2.9%, which suggested complete chloride removal. However, this did not indicate which anions have substituted on the coordination positions available on Hf⁴⁺. At least two of these needed to have oxygen species for the sol-gel reaction to proceed.

4.1.2 Analysis of hafnium n-butoxide

The filtrate collected in Fig 4.1 was slightly opaque and became darker and viscous as toluene was evaporated. The extracted product was a yellow liquid characteristic of alkoxides.²⁵⁴ Previous literature on a hafnium ethoxide in ethanol/air showed some stability, indicating that the ligand exchange reaction can inhibit hydrolysis and credible NMR spectra can be obtained if water content

can be lowered to prevent it from acting as a catalyst.²⁶⁶ It was expected that a hafnium ion in close proximity to an alkyl chain would cause some electron deshielding – lower applied field required for resonance would be expected, and a positive chemical shift would be observed on the alkoxide protons. Briefly, the ¹H-NMR for the assumed hafnium *n*-butoxide in butanol showed a definitive chemical shift, which may have been caused by the previously described mechanism at 4ppm from 3.8ppm for the C₁ (closest carbon position to Hf⁴⁺, which suggested a stable structure of shifted butanol and residual un-shifted butanol in a solvent of toluene. Presumably the shifted butanol represented the butoxide attached to Hf⁴⁺. The ¹³C-NMR yielded more critical information on the impurity of the alkoxide since the position of the carbons relative to one another could be gauged. The spectra yielded a myriad of inequivalent carbons representing a mixed alkoxide, suggesting the Hf-O-R groups were instead a mixture of residual chlorides, -OEt, -OBu and -OH. No post-synthesis (ammonia-hexane mixture) purification occurred, leaving terminal -Cl impurities, while water contributed to the other impurities.²⁶⁷ But both Hf-O-R and Hf-OH could be used for the condensation reaction (4.2) and (4.3) for the sol-gel process;



This indicated that the precursor was suitable for the sol-gel condensation reaction despite being marginally impure, but control of composition would be challenging because the molecular weight was not fixed.

4.1.3 Conclusions of synthesis

A hafnium containing alkoxide was produced, particularly from the evidence of the ¹H-NMR. It contained other leaving groups likely -OH and -Cl and was only able to be produced in small quantities.

4.2 Hafnia-carbon sol-gel

The alkoxide was needed to be added to the sol-gel mixture. The major hurdle was whether the alkoxide could be added to a mixture to form a stable solution without precipitation. This followed the general formula used by Wang et al and

Zhong et al in TiC/SiC synthesis duplicated with Hf in Table 4.1 below.^{123-124, 165, 262-264} Note that stoichiometric control was difficult because the amount of toluene and alkoxide were unknown in the filtrate.

Table 4.1. Components of HfO₂/C sol-gel mixture

Component	Molar Ratio (M _{Hf} =1)	Role
P123	0.05	Surfactant for oxide/resin solubility
Toluene	excess	Solvent
Ethanol	40	Esterification to produce water
Acetic acid	about 1	Chelating of alkoxide for stability
Hafnium alkoxide	1	Hafnium oxide source
Furfuryl alcohol	6	Carbon source, monomer
TFAc acid	2	Catalyst for furfuryl alcohol

Larbot *et al* used acetic acid to chelate and partially prevent the condensation by forming a chelate bidentate “lock” of AcCOO⁻ on Hf⁴⁺ that protected two sites from attack by water.^{254, 268} This might give time for two hydroxides from two different hafnium ions to form an ether (Hf-O-Hf) bridge. Adding ethanol in the solution began hydrolysis because some alcohol ligand substitution occurred, releasing acetic acid. Ethanol and acetic acid formed a small amount of ethyl acetate and water per mole of the reaction. This small amount of water performed a nucleophilic attack on the protected hafnium alkoxides. Limited displacement of ligands by the produced water caused a slow condensation, which released more water from equations (4.2) and (4.3). Thus if water was being produced, it could only occur if the oxide network was being formed. The trigger was the injection of acetic acid and ethanol.

4.2.1 Condensation for gelation

The method of using acetic acid (AcCOOH) was adapted from Larbot *et al* using two chelate bidentate “locks” on the Hf atom.^{254, 268} This is shown schematically in Fig 4.3 below, showing how two sites are “reserved” and prevent a structure of four hydroxides collapsing from Hf(OH)₄ to HfO₂. However, many of the reagents were wet (particularly ethanol) and vacuum was poor.

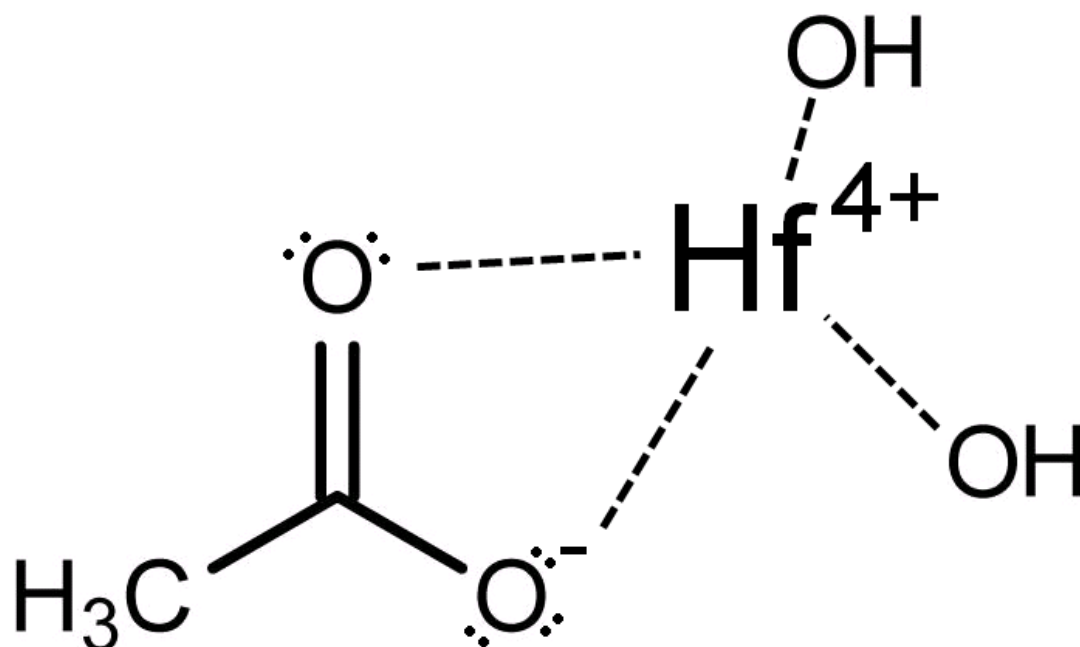


Fig 4.3. Example structure of an acetic acid chelated Hf^{4+} with two hydroxides.

The most stable AcCOO^-/Hf molar ratio h was found to be about a half that required by Larbot's method ($h = 0.9-1.3$). This suggested that water contamination provided the other half of hydrolysis, but preserved at least 0.9-1.3 sites per Hf^{4+} ion. The stepwise addition of glacial acetic acid up to a molar ratio of $h = 1.1$ was followed by incubation under N_2 for 24 hours at 80°C . Two calibration gels were processed. The first was an alkoxide gel shown in Fig 4.4.



Fig. 4.4: Amorphous hafnium oxide sol-gel after gelation.

At six hours a transparent gel was produced and able to be inverted after 18 hours without flow. The second calibration gel P123 was added to the hafnium alkoxide gel with no change in gelation time. P123 was used as a surfactant to prevent micron-level phase separation between PFA and the oxide network.^{123-124, 165, 262-264} This indicated that P123 did not interfere with the hafnium oxide sol-gel process. Finally, the gel was run with all components in Table 4.1. The only observed change was the addition of furfuryl alcohol (FA), which made a dark solution characteristic of its polymerisation.¹²⁷ This was stirred at 60°C for 3h until the solution became black. The PFA solution was transferred to the main sol-gel flask, which resulted in black gels. It was added at a designed molar ratio of C/Hf=6 for equation (4.4):



where 3C represented the minimum stoichiometry of solid-state carbothermal reduction. However, a mistake in the calculation actually resulted in two series of gels: some with a maximum of 6C and the other with a maximum of 30C based on all the carbon atoms in the polyfurfuryl alcohol (PFA) resin.

4.2.2 Gelation to pyrolysis

All solution compositions were incubated under N₂ atmosphere at 80°C. The carbon gels were dark and impossible to judge by visual observation except by surface finish. After drying at 120°C/24h with no observed shrinkage, these gels were pyrolyzed at 550°C/5h in N₂ to remove the surfactant polymer. They did not collapse to powder, indicating the presence of a three-dimensional structure. In fact, they appeared like brittle glassy pieces. Gels with poor FA to PFA polymerisation were transparent amber, while high PFA decomposition gels yielded reflective pieces with the appearance of polished obsidian. The darkness of the gel was indicative of how much carbon was present in the gel.

4.3 Carbothermal reduction to HfC

The process of forming HfC from the gel required sufficient carbon to complete the oxide reduction from equation (4.4). The sol-gel process described above created an interpenetrating network of polymer oxide and carbon from

decomposed PFA. This resulted in an intimate mixing of oxide and carbon. In a twist, the error in the stoichiometry calculation of PFA resulted in a set of samples possessing an oversupplied amount of carbon for the reduction reaction. This was the primary research of the doctoral program. This section analysed the phase evolution, carbon and crystallite microstructures and reaction mechanism in the sol-gel process and covered the transitions from the gel to HfC.

4.3.1 Phase analysis

The pyrolyzed HfO₂/C gels with a high carbon ratio were examined after 550°C treatment by XRD in Fig 4.5.

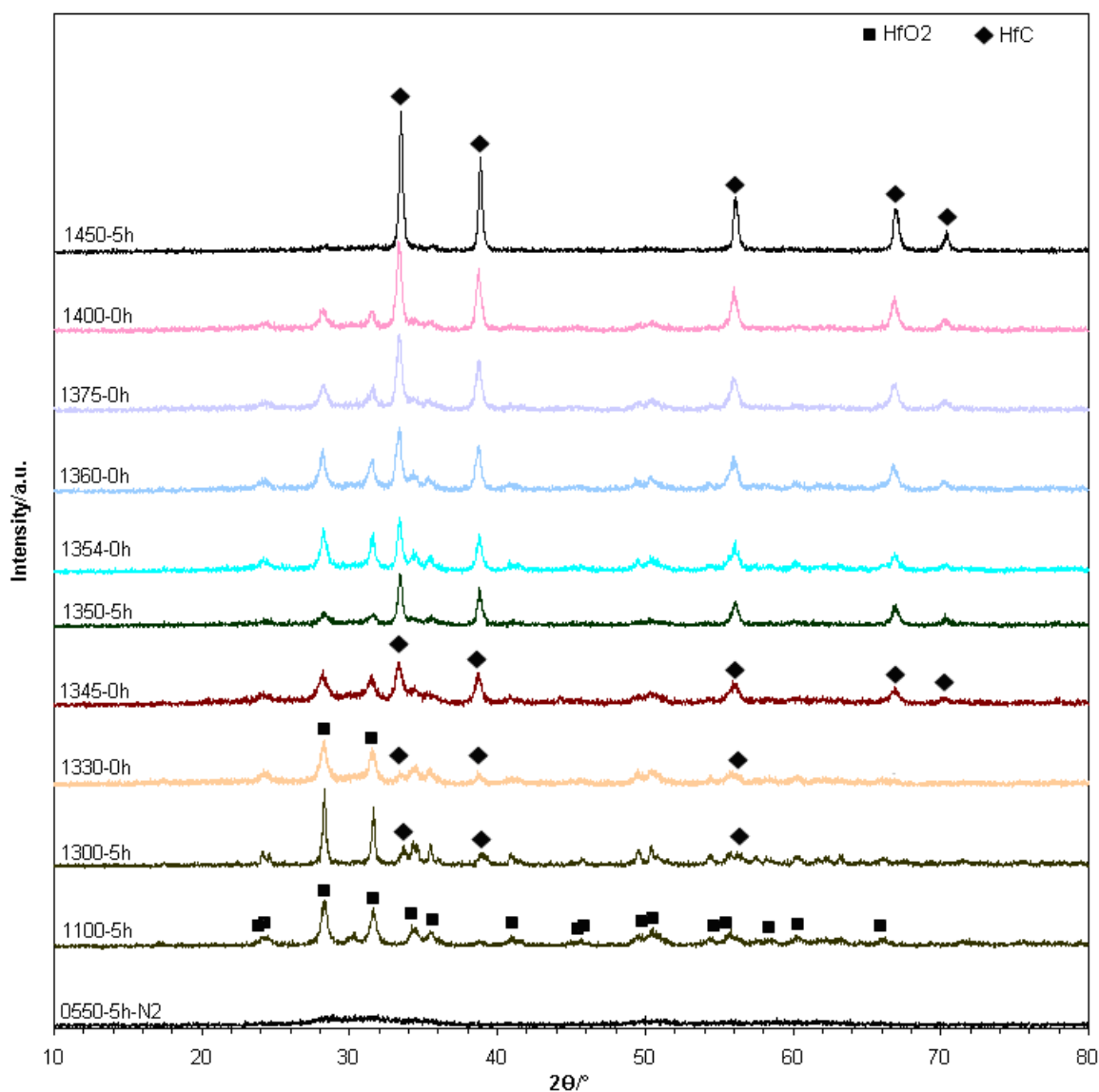


Fig 4.5. XRD evolution of the sol-gel precursor, demonstrating an amorphous gel at 550°C, followed by oxide crystallisation and transformation to carbide.

Fig. 4.5 showed both 5h isotherms at selected temperature and the point isotherms (no holding time) that attempted to halt the reaction at specific yield ratios of oxide and carbide. The gel was amorphous, with crystalline phases developing only after further heat treatment. Until 1100°C only *m*-HfO₂ was displayed in the spectra, but between 1330°C and 1375°C most of this oxide transformed into *c*-HfC. The residual oxide was removed by 1450°C, but the lattice parameter of the cubic phase was still 4.633±0.001Å from conventional x-ray diffraction and 4.6330±0.0001Å from the synchrotron PDF beamline. This was lower than the reported stoichiometric value (4.641Å) for cubic hafnium carbide from JCPDS card No. 65-2906, which was attributed to dissolved oxygen in the interstitial sites of the hafnium carbide lattice.²⁶⁹⁻²⁷⁰ The lattice parameter corresponds to approximately ~HfC_{0.8}, which was highly substituted given the relatively low reaction temperature.^{39, 271} The reaction rate could be inferred from a carbothermal study of TiC by Koc *et al* of “converted fraction” that used isothermal treatments from 900°C to 1400°C using three reaction stages (I, II and III).^{105, 272} Stage I was the formation of suboxides, Stage II indicated the oxycarbide formation and Stage III was the purification of oxycarbide, which was reported to be between 1000°C and 1400°C.²⁷³⁻²⁷⁵ The equivalent “Stages II” and “III”, if applied to the current sol-gel HfC system, appear to occur over a window of 150°C between 1300°C and 1450°C. This indicated that the kinetics of the reaction occurred very quickly. But it could not complete the last ~10% removal of the dissolved oxygen. These were investigated in later sections.

4.3.2 Carbon evolution and porosity

The excessive FA stoichiometry in the design ratio suggested that carbon was oversupplied. TGA confirmed that carbon oxidation (a weight loss process) began at 400°C and was removed by 600°C. By weight loss this corresponded to the 550°C precursor having 38 wt% C, or 11:1 C:HfO₂ molar ratio in Fig 4.6(a). From equation (4.4) that suggests only 3C is required, a significant quantity of carbon must have remained unconsumed. The 1450°C HfC sample presumably contained a carbon-carbide mixture. Fig 4.6(b) demonstrated the TG curve of the 1450°C sample in air showing the initial carbide oxidation (a weight gain process). The oxide was formed at just under 500°C and carbon oxidation is complete by 650°C. The weight change from the oxidation of pure HfC would result in a weight

gain to HfO_2 , or 105% of the original weight. The overall weight loss means that carbon remained in the HfC sample, and its oxidation resulted in a weight loss that was larger than the weight gain of HfC to HfO_2 . For example, $\text{HfC} + 2\text{C}$ oxidizes to HfO_2 and loses CO, which by weight per mole calculated to 224g ($200.11\text{g} + 2 \times 12.01\text{g}$) initially and 210.5g as the final weight. This would be 94% of the initial weight. In this sample it was higher, at 86% of the initial weight, which demonstrated the original sample at 1450°C was $\text{HfC} + 2.75\text{C}$.

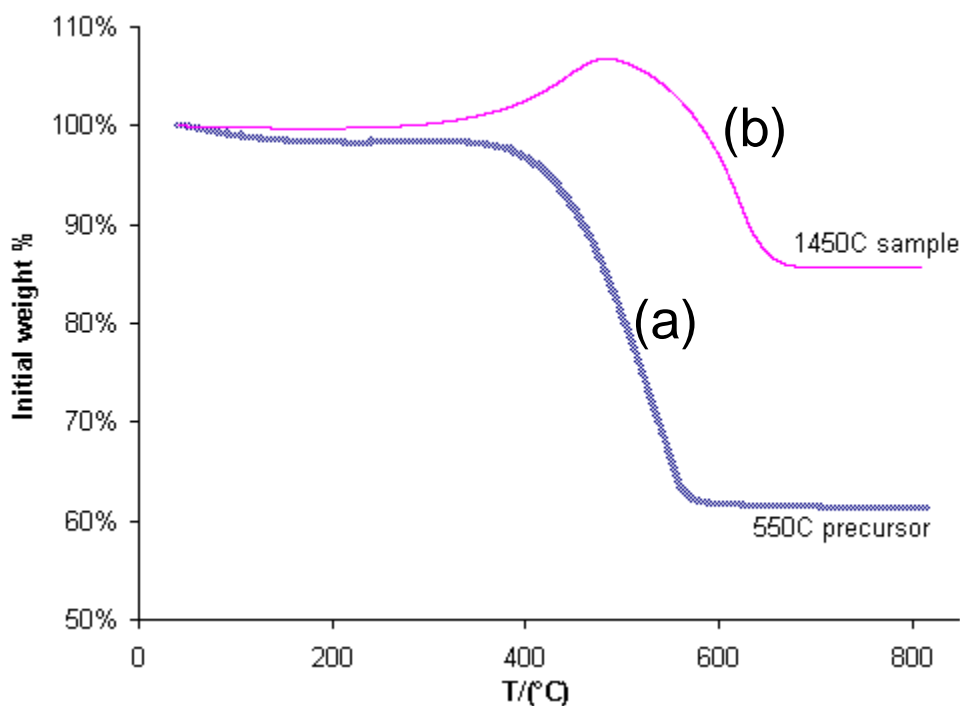


Fig 4.6. (a) TGA on pyrolyzed gel $\text{HfO}_2\text{-C}$ after 550°C showing carbon oxidation only and (b) after 1450°C treatment showing oxidation of HfC to HfO_2 (a weight gain process) and residual carbon oxidation (a weight loss process).

This indicated the carbothermal reduction used $\sim 8\text{C}/\text{Hf}$ to complete the reaction, and was consistent with the earlier problems of the furnace atmosphere previously discussed. This sample is referred to as Hf11C. The surface properties of the gel were investigated. However, there was a large contribution of carbon to the gas sorption surface area of pyrolyzed gels. Previous gels with $1.7\text{C}/\text{Hf}$ from poor PFA polymerisation yielded low BET surface areas $\sim 20\text{ m}^2\text{g}^{-1}$. The carbon rich precursor referred to as Hf11C yielded a BET surface area of $159\text{ m}^2\text{g}^{-1}$ after

pyrolysis at 550°C. This indicated the high contribution by the microporous carbon region after PFA decomposition. After transformation to hafnium carbide at 1450°C it was presumed that residual carbon of 2.75C/Hf still contributed to the final BET surface area of 35.5 m²g⁻¹. Fig 4.7 showed the gas absorption hysteresis of gels after pyrolysis and after conversion to HfC. Closure of the hysteresis at $P/P_0 \sim 0.4$ indicates the presence of micropores. The hysteresis closes due to the tensile strength failure corresponding to the collapse of the N₂ meniscus.

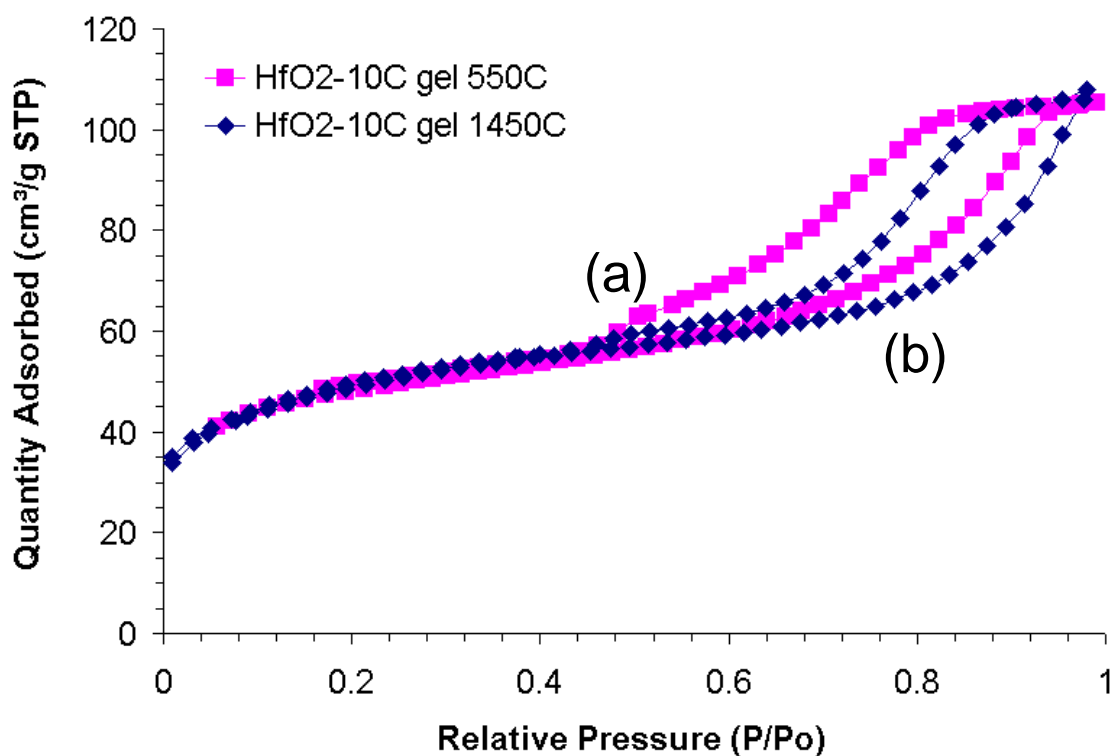


Fig 4.7. Nitrogen adsorption-desorption isotherms of the gel (C/Hf=11) pyrolyzed at 550°C **(a)** and the sample after heating at 1450°C **(b)**, both indicating a mesoporous profile and presence of micropores.

In analysis of Fig 4.7(a), it can be seen that the lack of closure at the start of the hysteresis of the 550°C sample indicated a larger presence of micropores, and this was likely explained from the PFA decomposition that resulted in microporous carbon.^{126-127, 276-278} The converted HfC-C sample has less microporous carbon due to a later closure of the meniscus in Fig 4.7(b). The larger values of P/P_0 indicated the mesopore and macropore condensation. Both samples have microporous carbon and other pores sizes. Therefore it was likely

that the general structure of the gel had not significantly changed during the reaction because the majority of the pores and interparticle gaps were still filled with carbon and other pore sizes. Thus both 550°C and 1450°C microstructures were simply particles embedded in a carbon matrix. Fig. 4.8 shows the measurement of pore volumes at different pore size contributions of the samples heated at 550°C and 1450°C.

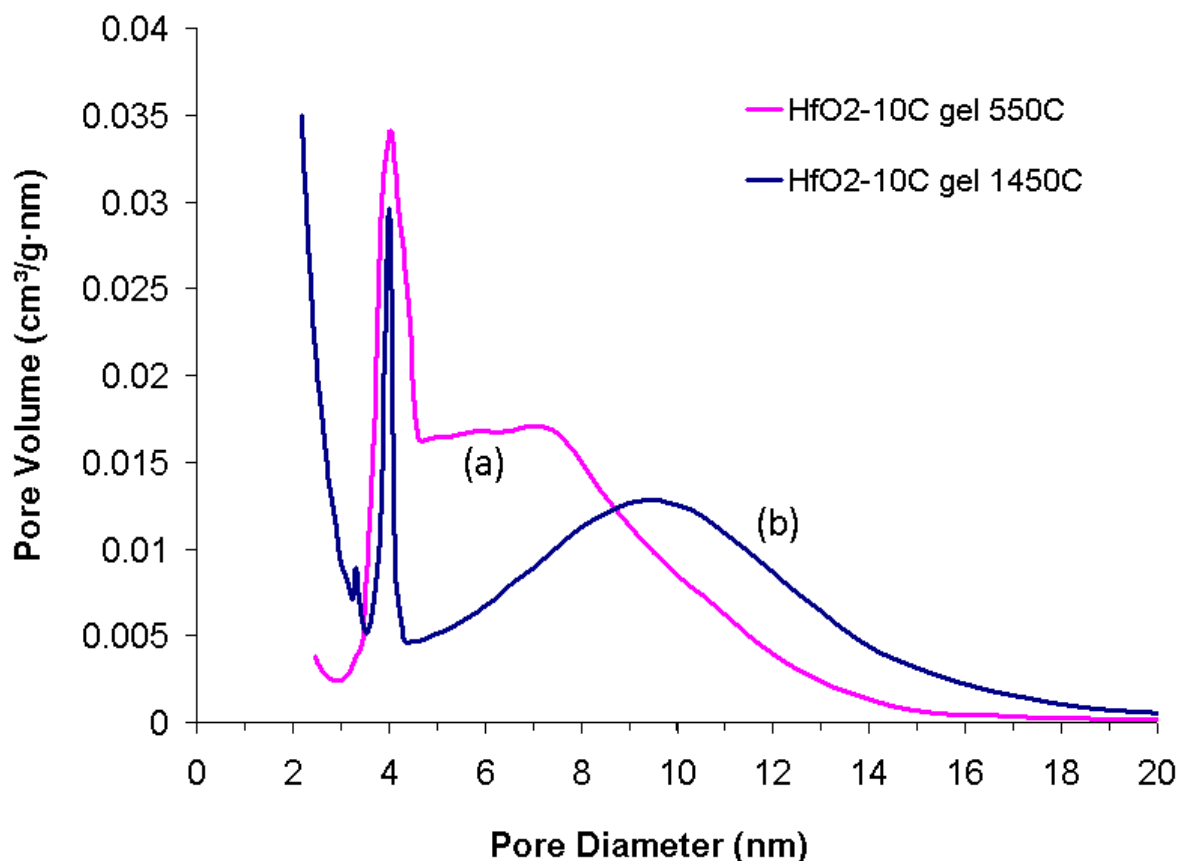


Fig 4.8. Nitrogen pore volume from size contributions of **(a)** pyrolyzed gel at 550°C and the sample **(b)** after heating at 1450°C.

This illustrates further differences before and after conversion from HfO₂/11C to HfC-3C. Logically, more microporous carbon should be present from the data in Fig 4.7(a) because the sample at 1450°C would represent depletion of 80% of the carbon that was required to form HfC. The second difference was that the 550°C HfO₂/C gel had a difference in mesopore sizes to the HfC-C sample. The gel plateaus earlier than the HfC-C sample, which indicated that the mesopores were likely smaller and thus completely filled much earlier than the gel. This consumption of carbon between particles as an evolution of microstructure was

supported by the pore size distribution of Fig 4.8. Smaller mesopores are observed in the 550°C gel matching the analysis of Fig 4.7. The 550°C pyrolyzed sample in Fig 4.8(a) showed a relatively narrow 4nm pore distribution and broader pore sizes that ranged up to 8nm. Later TEM bright field images confirmed the pores between particles. At 1450°C relatively larger pores with a broad size distribution from 6-14nm are displayed. From the XRD, transformation to HfC occurred, and the TGA shows that 80% of the carbon was consumed. The consumption of the carbon in the carbothermal reduction likely resulted in channels or gaps being opened between HfC particles, allowing the depression of local partial pressure of [CO] or [CO₂] from the reaction assisted by the flowing argon. It was also possible that formation of HfC resulted in some necking between nanoparticles to create random pores. Gaps between particles have increased as a result of loss of carbon between crystallites. Thus the interpretation of Hf11C in Fig 4.8(b) at 1450°C was the presence of microporous carbon between HfC nanoparticles, with pores widened by the consumption of carbon between particles. This caused a shift in the pore distribution toward larger size pores. A brief note on presence of the peak at 4nm; this was currently assigned to the artefact known as the tensile strain effect (TSE), rather than the presence of many 4nm pores.²⁷⁹ Multiple theories and methods exist for calculation of pore size distribution. The pore structure in this material due to P123 percolation was likely interconnected, and the modelling system correctly interpreted the pores open at more than one end; or more correctly, open at multiple ends. Since pore volume was measured indirectly from the supernatant gas, the pressure at which it desorbs could be from multiple causes as the meniscus gradually recedes, depending on the wetting angle, pore size and structure and relative pressure of the analysis gas. The meniscus defines the boundary between the vapour and liquid. However, if the pore system is well interconnected this reportedly and consistently results in the rapid collapse of the meniscus, causing a forced closure of the hysteresis that is interpreted (by software analysis of the desorption branch of Fig 4.7) as the presence of a pore at ~3.8nm.²⁷⁹ While understanding of this effect was limited, verification by TEM provided accurate support for this reported issue, and the 4nm pore was verified by TEM for the 550°C pyrolyzed precursor. However, at 1450°C, considering the chemical reaction of carbon to diffuse distances of ~100nm, the presence a fixed

4nm pore system in Fig 4.8(b) does not seem plausible and was assigned to TSE. This circumvented the complexity and limitation of the gas sorption techniques. Further TEM was conducted to examine the microstructural changes of the gel. Fig 4.9(a) and (b) at two magnifications indicated the early crystallisation of oxide in the 550°C sample. These show a crystalline phase contrary to the amorphous XRD spectra in the 550°C sample in Fig 4.5. These nanocrystalline oxides may be the initial nuclei of *m*-HfO₂, embedded in an amorphous carbon matrix and may only be partially crystalline.

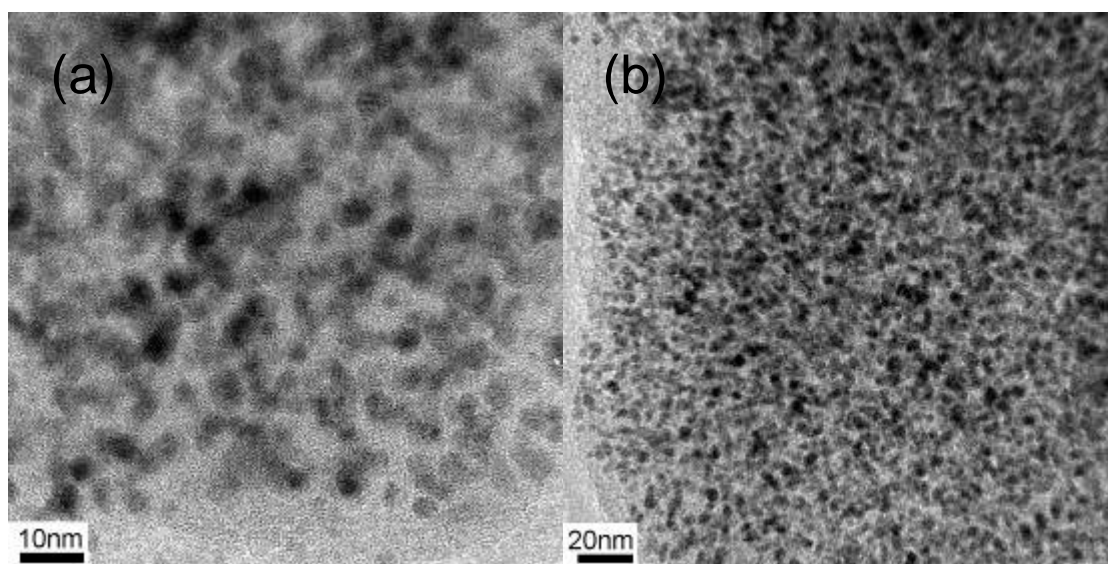


Fig. 4.9. Bright field TEM images of pyrolyzed gel (550°C/5h), indicating (a) the early crystallisation of HfO₂ and (b) its homogeneity in the carbon matrix.

The homogeneity of the mix of HfO₂ and carbon at the nano scale highlighted the significant advantage of the sol-gel process compared to the conventional powder mixing. The TEM images in Fig 4.9 also showed that the pores between particles match the pore distributions in Fig 4.8. Pores of 6-8nm represented the gaps between particles, but and some of the gaps shrink to about 3-4nm. However, the channels could also be microporous because the “walls” of the channel that are not compromised of particles are carbon. The actual network type was difficult to gauge based on the limited data, but the most likely explanation was a mesoporous network with microporous carbon walls. This was verified later by the carbon matrix “wrapping” oxide crystallites. The interaction of carbon and the crystallites was shown in Fig 4.10. It showed high and low

magnifications of the microstructure at 1330°C. Fig 4.10(a) confirmed a substantial assembly of the carbon microstructure from its initial amorphous state to a graphene-like structure. As 1330°C contains predominantly HfO_2 as a crystalline phase from the XRD it is assumed that Fig 4.10 was images of oxide particles. Fig 4.10 (b) indicated that before conversion to HfC, significant agglomeration and coalescence of nanoparticles occurred, from 4nm size at 550°C to 40nm size by 1330°C.

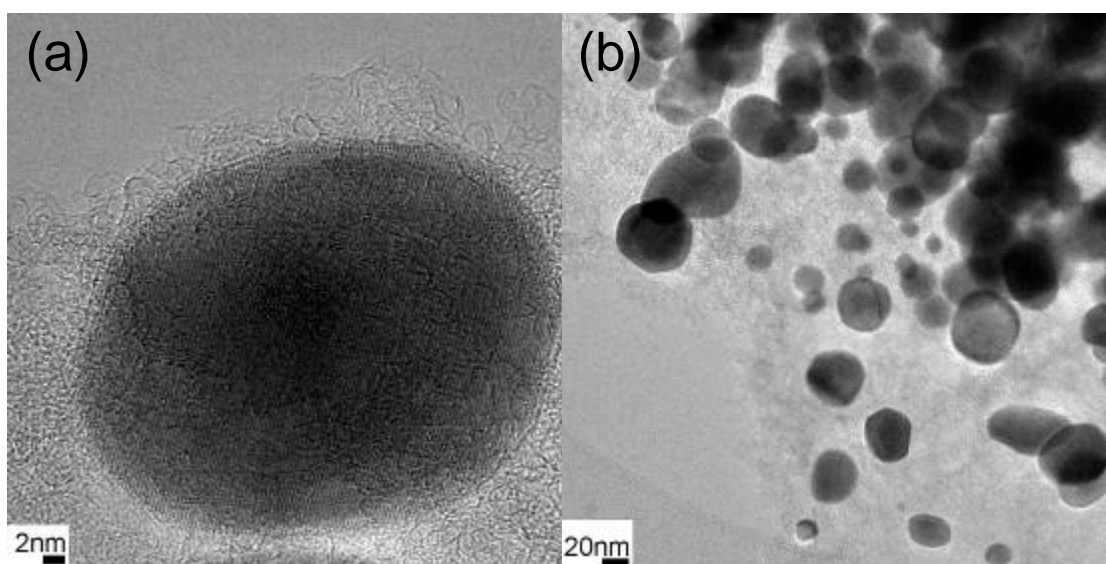


Fig. 4.10. (a) High resolution TEM microstructure of an oxide crystallite at 1330°C/0h, with development of carbon microstructures to graphene-like structures **(b)** Uniform oxide crystallites at 1330°C.

The gas absorption hysteresis in Fig 4.7 indicated that a mesoporous structure was maintained throughout the crystallisation of $m\text{-HfO}_2$ and transformation to HfC. A reasonable description for this nanocomposite evolution is that it begins as a carbon-oxide ($\text{HfO}_2 + 11\text{C}$) and ends as a carbon-carbide ($\text{HfC} + 3\text{C}$) composite. The carbon played a significant role in the reaction. Fig 4.11 shows the Raman spectra for key reaction temperatures. It shows that amorphous carbon, containing sp^3 bonds appeared to be dominant in the 550°C powder and even through the start of the carbothermal reduction at 1330°C. This suggested that during the carbothermal reduction, carbon was amorphous. Only after substantial conversion to HfC does the carbon begin to assemble and order itself.

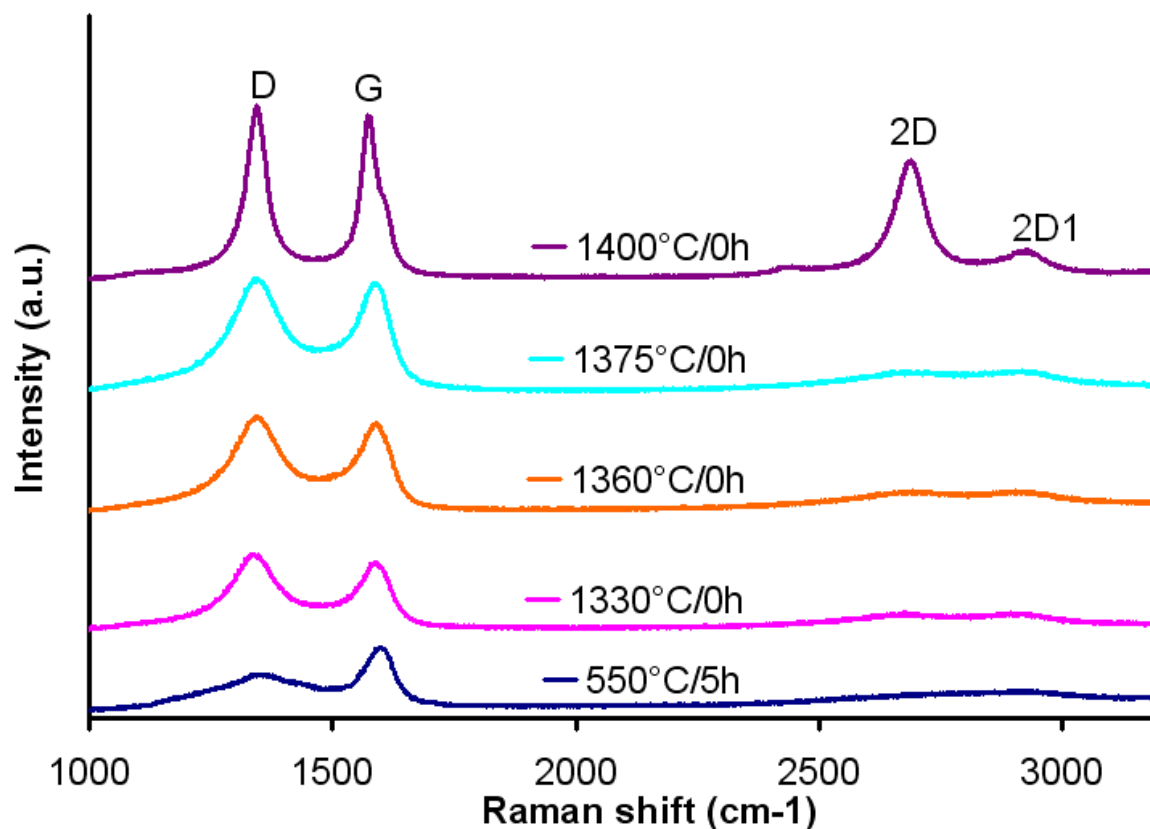


Fig. 4.11. Raman spectroscopy showing the 1350cm^{-1} D and 1600cm^{-1} G peaks developing from amorphous sp³ carbon. Note the peak 2730cm^{-1} is pronounced only at 1400°C .

The 1400°C the D-G peak ratios identified at 1350cm^{-1} and 1600cm^{-1} demonstrated the characteristic of graphite as suggested by Ferrari *et al*, but the position of the 2D peak showed that the 2D1 peak (at 2930cm^{-1}) may qualify as graphene.²⁸⁰⁻²⁸¹ The presence of three discernable peaks at 2444cm^{-1} , 2D at 2700cm^{-1} and 2D1 at 2935cm^{-1} form the morphology of Raman spectra for graphene.²⁸⁰⁻²⁸¹ However, the 2D shift for graphene begins at 2640cm^{-1} and increases in wavenumber as the number of layers increases; the position of 2700cm^{-1} for the 1400°C sample actually denotes more than 10+ layers.²⁸⁰⁻²⁸¹ The evolution of the D/G ratio from 0.4 to 1.1, supported by the discernable 2D and the unmarked D+D' at 2930cm^{-1} also proved gradual ordering of the carbon network from amorphous carbon to graphite beginning at 1330°C .²⁸² Thus smaller 1-3 layers found in TEM images may be graphene, but for accurate terminology were referred to as “graphene-like” in this work. This graphene-like carbon displayed in the TEM appeared to assemble and order itself only when a

significant quantity of the oxide was consumed. This indicates that the conversion HfC was part of the graphitization process. Therefore the early carbothermal reduction microstructure in Fig 4.10 suggested that over 1330°C to 1400°C short and extensive graphene-like sheets are possible microstructures, appearing as ‘strings’ in a TEM bright field image. Carbon was thus present in significant quantities, with its own porous structure and evolution, and arranged centripetally around oxide crystallites.

4.3.3 Microstructure and morphology analyses

The carbothermal reaction was likely to be a solid state diffusion mechanism. Carbon is the diffusing species in carbothermal reduction of oxides and diffusion couple studies.⁵⁷ It implied from the Raman spectra that carbon was amorphous during the reaction, as well as changing its own microstructure to graphite. However, this solid-state diffusion was demonstrated by TEM/EDS studies of powders with the reaction halted at between 1330°C and 1360°C in order to interfere with the diffusion kinetics in Fig 4.12.

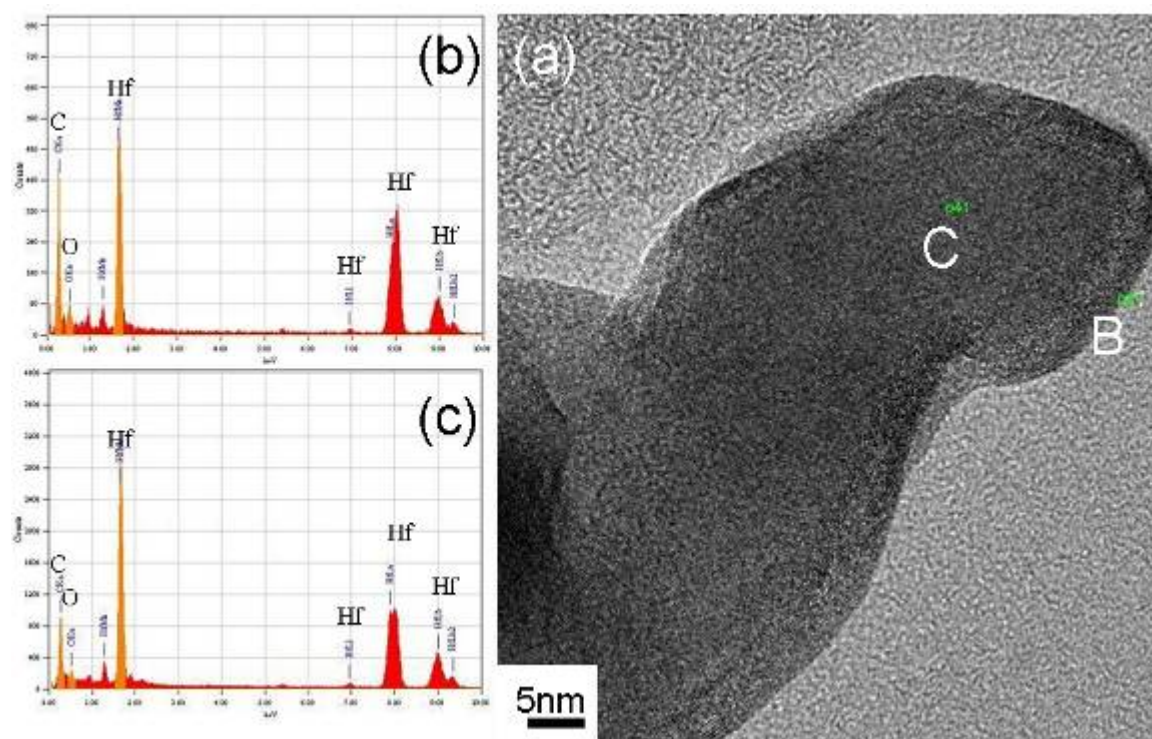


Fig. 4.12. (a) TEM image of the sample fired at 1354°C/0min. (b) EDXS spectrum for the edge marked B. (c) EDXS spectrum of the core region of the particle marked C. Not the consistent Hf signal intensities, but different C/O signal.

Fig 4.12 shows a HfO_xC_y particle in the sample heated at 1354°C for 0 min and then cooled down to room temperature. EDS spot quantification was conducted at outer surface of the crystal (B) and the centre of the HfO_xC_y particle (C). Point EDXS maps carefully obtained from the particle (note the matching Hf intensities) indicated that the carbon concentration in the fringe is significantly higher than that in the core. This clearly confirmed the theory proposed by Maitre & Lefort *et al* on the zirconia-carbon reaction in 1997; their “contracting volume” or “centripetal diffusion” idea suggested that carbon centripetally diffuses into the surface of the particle, forming an intermediate oxycarbide by removing the first oxygen, before displacing the second oxygen.⁴⁹ This result was also observed in another HfO_2 to HfC reaction of small $\sim 225\text{nm}$ nanopowders.⁷⁴ This validated the sol-gel process because it created the ideal morphology of carbon surrounding the oxide crystallites, with short diffusion distances. The SEM microstructure of Hf11C obtained at 1450°C in Fig 4.13 appeared more as a composite than dispersed powder due to the graphene-like carbon matrix. The SEM in Fig 4.13 showed particles in dense matrix, which according to the TGA and TEM analyses must be carbon.

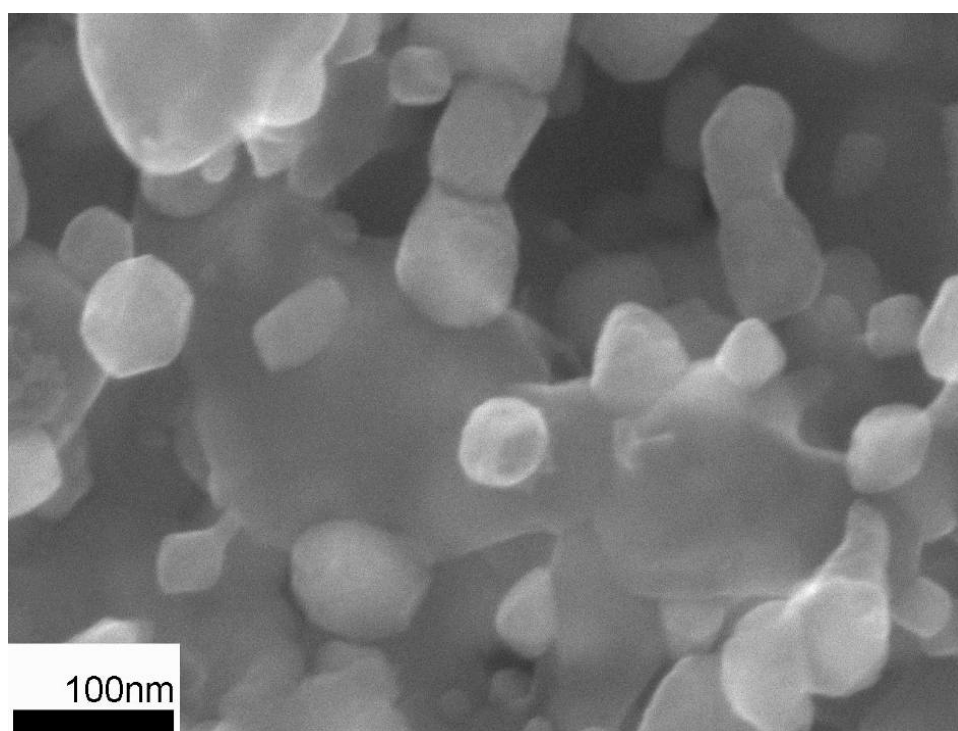


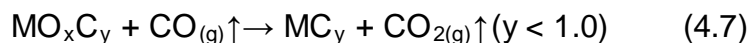
Fig 4.13. SEI imaging at 1450°C demonstrating uniform morphology of the carbide nanoparticles in the matrix

However, this was also verified by the volume fractions, given that the molar ratio of C to HfC is 3 to 1, correlating to a volume fraction of about 50-50 of the SEM image. This suggests that it was possible to use a sol-gel mixture to make nanocrystalline hafnium carbide, but the amount of residual carbon needed to be controlled in order to disperse the powder for use. Both Raman and TEM analyses pointed to evidence that graphitization occurred after the carbothermal reduction and if hafnia reacted with amorphous carbon well before graphitization occurred, this may explain the relatively low carbothermal reduction temperature as well. It is known that amorphous carbons – including carbon black, resins and pitch – possess a higher surface area and reactivity than graphite.⁷² Carbon possesses rather poor diffusion in its covalent structures, and surface diffusion is more effective than lattice diffusion. It would be of interest to note by Raman spectroscopy whether graphitization has occurred in other sol-gel carbide synthesis. If graphitization has occurred before or during carbothermal reduction, then the short atomic diffusion distance across a nanoparticle is responsible for the low temperature reduction consistently reported. If graphitization has not occurred, it suggested that a key aspect of low temperature carbothermal reactions is more due to amorphous carbon. It would have a higher diffusivity than graphite due to the activation energy required to move C through a 3D carbon lattice. One aspect of the “contracting volume” theory should be that no changes in crystallite volume would occur. The various TEM images of crystallites in Hf11C before the carbothermal reduction at 1330°C and after 1450°C support that this mechanism dominated since all grains in these samples are at about 40-60nm size. This suggested that carbon mobility, not oxide mobility, was the rate controlling step of the reaction, which correlated with carbon being the diffusion species of the reaction.⁵⁷

4.3.4 Reaction of oxycarbides

The hafnium carbide produced at 1450°C likely contained substantial dissolved oxygen. These are known as oxycarbides, and were a well known intermediate because carbides are usually non-stoichiometric with impurities of oxygen when there are difficulties with processing. The oxycarbide purification – displacement

of oxygen by carbon and usually at temperatures 1600-1800°C – was generally agreed to occur via both $C_{(s)}$ or $CO_{(g)}$ in reactions of the following steps^{49, 130, 273}:



The reaction between HfO_2 nanoparticles and carbon in this work offered some explanation for the difficulty in conventional carbothermal reductions. First, many reactions do not start with amorphous carbon. It was known that graphite was a carbon source with less reactivity than amorphous or nano-carbon.⁷² This sol-gel reaction observed graphite (10+ layer) structures at 1400°C, despite the fact that PFA was always considered by literature as a non-graphitizing carbon.²⁸³⁻²⁸⁴ This definition of “non-graphitizing” relied on the concept that akylation formed sterically hindering structures that need to be removed before the graphene sheets can align. However, the data in this research indicated that the temperature of about 1330°C, transformation from oxide to carbide became thermodynamically favourable or the diffusion of carbon appreciable. Simultaneously, carbon started to order, form structures that make diffusion less favourable and likely increasing diffusion distances by phase separation.

The second visual evidence of the challenges in carbothermal reduction was the microstructure displayed in Fig 4.14(a) that showed the carbon-carbide at 1450°C. It can be seen that each crystallite boundary was wrapped in 2-3 graphene-like layers (marked O) and an intermediate amorphous layer (marked X). The diffusion is centripetal. While the first stage of carbothermal reduction was regarded to be a solid state reaction, it was known that the reaction product must leave the crystallite as a gas (either $CO_{(g)}$ or $O_{2(g)}$). If the carbon layering was part of equations 4.5 and 4.6, then under a centripetal mechanism it was possible these layers were truly the in-situ microstructure, representing $C_{(s)}$ centripetally diffusing into the crystal. But if this were true, such a structure would likely hinder gas exit for equations 4.5 and 4.6 since $CO_{(g)}$ was also a reaction product. This reaction relies upon gas transport and thus conditions are more likely to approach equilibrium. This would conveniently explain the reaction being unable to

complete. This would mean that reactions 4.5-4.7 would be initially rapid, and then slowed as the carbon layers build up. The chemical driving force is also reduced, as well as the gradient in atomic flux of carbon.

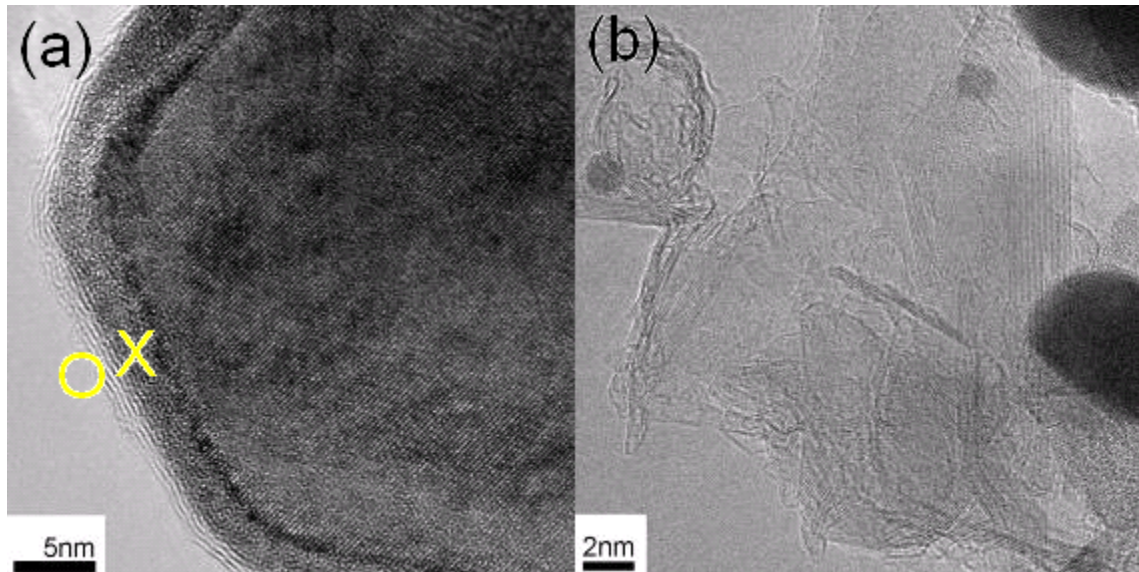


Fig.4.14. (a) Amorphous layer (marked X) and layered carbon (marked O) on an hafnium carbide crystallite formed at 1450°C **(b)** High aspect ratio carbon microstructures unattached to crystallites.

This was supported by the decreasing change in peak intensity of converted HfC in the XRD spectra as temperature increased. This correlated with 'converted fraction' studies by Koc et al that suggested that the second oxygen removal from oxycarbide was more difficult than the first.^{105, 272} This would explain the higher temperature treatments required to complete the purification in HfC and other carbides^{74, 128}. Once the graphitization occurs on the surface, transport of carbon to displace oxygen in the lattice was reduced. Thus two mechanisms shown in the Raman spectroscopy and the TEM images suggested why carbothermal reduction was usually at ~2000°C. First is that carbon begins to lose mobility by forming graphite, and second was that the centripetal model could force equilibrium of the reaction by bottlenecking the reaction gas exit, or reactive gas entrance. It is also possible the intermediate amorphous layer may be a partially crystalline surface. The carbon displayed in Fig 4.14(b) may simply be layers that attached to any available surface on cooling because their formations during high

temperature reactions had a prohibitively high surface energy. It was also possible that the graphene-like coating was a discontinuity created by a boundary, caused by a phase. For example, non-oxide materials form a thin surface film that can be oxygen rich during processing. To use this powder – such as for sintering – the excess carbon was clearly a problem as HfC registers a molar ratio of 3C residual. Certainly some interparticle carbon layers were beneficial because both carbon and particle have similar oxidation sensitivity. It likely made agglomeration and necking mechanisms between particles difficult, homogenized the reaction mixture and constrained the crystallites, and prevented necking between nanoparticles.^{115, 285-286} Evidence suggested that sintering and necking occurred between particles when higher temperatures were applied to purify the carbide.²⁸⁷ However, Talmy et al determined that only a residual ~0.3C (to TaC) was necessary for sintering to full density, attributed to removal of surface oxides by carbothermal reduction.⁷²

4.3.5 Summary

Sol-gel processing in the hafnium-oxygen-carbon system was used to produce nanocrystalline hafnium carbide of ~100nm size at 1450°C. The understanding of this system and the reactions involved were improved. It has been found that because the precursor was a templated hafnia gel structure with impregnated carbon derived from PFA, this insured an intimate and homogenous mixture at the nano scale that was not achievable by conventional powder mixing. The precursor was highly porous and crystallisation created an ideal reaction system for centripetal diffusion. The monoclinic HfO₂ phase was removed at 1450°C. The oxide crystallites were prevented from agglomerating due to the PFA derived carbon matrix. Carbon layering with graphene-like assembly was observed from residual carbon. The assembly of carbon appeared to occur only after the carbothermal reduction indicating that carbothermal reduction of oxides with amorphous carbon could be an intrinsic aspect of sol-gel processing.

4.4 Conclusions

This program demonstrated that it was possible to produce nanocrystalline HfC of ~100nm. The difficulty with this technique was that the hafnium oxide precursor is hygroscopic. While it was not possible to effectively synthesize large quantities

for other research (such as the amounts required for sintering) it was possible to manufacture sufficient quantities for a fundamental study. The synthesized alkoxide was successfully integrated into a sol-gel technique and produced a homogenous mixture of nc-HfO₂ and carbon. It became mesoporous after 550°C decomposition of PFA into carbon and the nc-HfO₂ reacted with amorphous carbon to produce HfC starting from 1300°C. The reaction was via carbon diffusion from the surface of HfO₂ inwards. It was clear that the homogenous nano-scale mixing, the high surface area nanoparticles, and the mesoporous structure derived from the sol-gel process allowed for a substantial reduction in the carbothermal reaction temperature. Carbon coatings were found wrapped on the surface of HfC, which consisted of a graphene-like outlayer and an amorphous intermediate layer. The carbon coating could prevent coarsening.

4.5 Future work

Several factors were identified for future improvement. The alkoxide was not stable for handling in air and focus on synthesis prevented control of PFA decomposition to carbon. Understanding of the evolution of the gel was also limited due to the sheer amount of carbon in the system. Excessive carbon prevented analysis in gas sorption techniques – it neglected the crystallite morphology because of the extensive volume occupied by microporous and mesoporous carbon. Advanced techniques such as Rietveld analysis was not used due to carbon microabsorption and carbon unable to be quantified. TEM imaging and diffraction was also hindered. Controlling carbon concentration in the compositions allowed for control of the carbothermal reaction microstructure and the ability to integrate nanoparticle dispersion techniques in powder processing. Future work would focus on the understanding and control of the PFA-PFA decomposition as a pre-requisite to synthesis. Given that carbon began to be consumed above 1330°C, the surface area should rapidly drop and grain growth should significantly increase for both carbon and carbide phases. A reduced amount of carbon would be more ideal to investigate particle evolution, since carbon contributed much of the gas absorption surface area. Lower residual carbon would be useful for applied processing (sintering or coating) research.

5. Zirconium carbide (ZrC)

This chapter attempted to advance the control of a sol-gel method to synthesize nanocrystalline zirconium carbide (ZrC). Armed with the experience of HfC, the objectives of this chapter are elevated. However, the same types of hurdles were still present. Due to the complexity of moisture/air-sensitive synthesis, a suitable zirconium alkoxide precursor was sourced. This allowed for time devoted in investigation of controlling the PFA decomposition, instead of alkoxide synthesis and purification. The first challenge was to successfully stabilize the air-sensitive alkoxide and develop a formula to allow the sol-gel process to work without inert N₂/Ar atmosphere. Stabilizing the alkoxide was a necessary part of mixing P123 and FA in the sol-gel. This would simplify subsequent ceramic processing. The major hurdle was to control of the PFA decomposition to carbon that was notably absent in the HfC program. This was a key issue because it was known that as the gel eventually transformed to ZrC, residual carbon would hinder instrumental analysis of the carbothermal reduction and prevent densification. The last hurdle was to achieve the correct phase and microstructure of the nanoparticles. Technical success in this chapter was indicated by a level of understanding of this system that was sufficient to make structural ceramics for extreme environments the subsequent research program.

5.1 Stabilizing zirconium n-propoxide

The initial work involved the addition of components to the sol-gel suspension. This repeated previous methods by Wang et al in synthesis of SiC.^{123, 262-263} The major difference with HfC program aside from a different metal alkoxide was the stabilization of the alkoxide in air, which was the first investigation. Using acetylacetone or “AcAc” was adapted from literature techniques by Dolle and Sacks et al.^{6, 129} Recall that the ratio of AcCOO⁻/Hf using acetic acid chelating in the previous HfC program was $h = 1$. The minimum ratio h to stabilize Zr⁴⁺ ion from water additions was also AcAc/Zr = 1, confirmed by literature as a ratio usable for stabilizing alkoxides.^{6, 288} There were some observations during this early sol-gel stage to note. The AcAc was added before the alkoxide in order to prevent the alkoxide addition from immediately undergoing hydrolysis by trace

water. It appeared that the competition for the Zr^{4+} co-ordination ligand was a dynamic equilibrium, inferred by the reversibility of the reaction. For example, during early stages, a successful recovery of a precipitated solution could be made by excessive addition of AcAc. Competition for the co-ordination site between “AcAc” dual carbonyl groups ($2 \times \delta^-$), polar water (δ^- on oxygen) and propanol existed as long as the coordination number of Zr^{4+} remained the same. A slight yellow colour upon alkoxide addition was indicative of a ligand replacement. Instability or chelation failure caused a rapid self-condensation reaction that quickly yielded white material, presumably hydrated zirconia. Thus the solutions were impervious to uncontrolled hydrolysis and air sensitive controls were unnecessary. The default formula settled on the ratios shown in Table 5.1:

Table 5.1: Default values used for the sol-gel mixture to form ZrC.

Component	Molar ratio	Role
P123	0.05	Surfactant for oxide/resin solubility
Ethanol	40	Eluent
Acetylacetone	1	Chelating of alkoxide for stability
Zirconium n-propoxide	1	Zirconium oxide source (ZNP)
Furfuryl alcohol	2	Carbon source, monomer
Hydrochloric acid	<1.25	Catalyst for furfuryl alcohol, water source

The AcAc chelation simplified the process immensely. Hydrochloric acid (which contained 66% water) was able to be used as the acid catalyst instead of trifluoroacetic acid. Ethanol (fully miscible with water) was used as a safer solvent than toluene. Thus carbon content via PFA decomposition was the only remaining variable. The carbon content was required for ZrC synthesis. Therefore the goal of the first part of this research was to empirically ensure that carbon content by PFA decomposition could be controlled.

5.2 Carbon by furfuryl alcohol polymerisation

The reaction of furfuryl alcohol (FA) monomer to polyfurfuryl alcohol (PFA) polymer regulated the quantity of carbon. This was crucial for the carbothermal

reduction of the oxide. In the HfC process, an excess of FA polymerisation was used to ensure sufficient carbon remained after pyrolysis to react with HfO_2 . This left residual carbon. In the ZrC system, this nanopowder was intended for sintering, and the presence of residual carbon needed to be controlled. Excess carbon resulted in powder that could not be sintered. But the powder also needed sufficient carbon for the reduction reaction in (5.1) simplified to:



Thus the production of ZrC was completely dependent on the availability of solid carbon from PFA decomposition, which depended on the FA-PFA reaction. This could be gauged by the opacity of the gel shown under white light in Fig 5.1; heavily crosslinked PFA gels were dark.



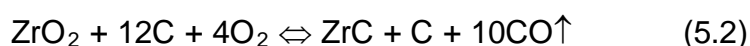
Fig 5.1. Heavily crosslinked PFA gels and examination for PFA precipitates under transmitted light.

The first plan required the control of furfuryl alcohol crosslinking to empirically determine and predict how much PFA decomposed carbon was in the gels.

5.2.1 Controlling the reaction of PFA to carbon

At the surfactant burnout temperature, PFA decomposed to carbon. However, FA monomers are constantly lost during wet chemistry and certainly evaporated during the surfactant burn out. Dimers and certainly oligomers are larger and may be trapped and decompose rather than evaporate through the pores from the gel. During 550°C treatment under flowing N_2 , the larger PFA crosslinked molecules decomposed to carbon, and the ratio of C to ZrO_2 in the gel was fixed for (5.1). Therefore, gel required enough PFA crosslinking to leave sufficient carbon after

550°C for the stoichiometric 3C to ZrO₂ ratio. However, this ratio was usually higher. During the HfC program over much of 2009, the furnace had major difficulties due to oxygen contamination, thus required ~8C/Hf molar ratio. This was likely due to the presence of oxygen or other species that reduced the efficiency of the reaction. An example could be equation (5.2) where only 3 of 12 moles of C are used in the reaction but the furnace conditions are poor and so an excess of carbon is added:



Note that ZrC can be produced from (5.2), but left residual carbon. The initial heating trajectory consumed oxygen and removed it from the furnace, leaving the 3C ratio to react with ZrO₂ in an oxygen-free environment at the isotherm. The ZrC forms and cools in an inert atmosphere. But if the furnace conditions can be made predictable, then an optimum carbon ratio can be determined. When the furnace was rebuilt in 2012, this requirement dropped to a more acceptable ~4C ratio from tests with gels with known carbon content. Once the reaction was empirically predictable, gels could be designed to yield specific carbon ratios, such that the reaction could complete and leave a tailored amount of carbon. To understand the empirical PFA decomposition to carbon, several processing variables needed to be investigated to determine their effects on the polymerization of FA.

5.2.2 Control of solvent additions

The first variable investigated was the effect of solvent additions. It was expected that ethanol had no effect on the FA to PFA reaction. This was because the cationic condensation only produces water. However, while literature values for solvent/oxide ratios range at about 40/1, washing, transfer and decanting obviously changes these values.^{268, 289} Furthermore, it was necessary to determine whether a 40/1 etOH/Zr ratio was sufficient to dissolve or suspend the amount of PFA that was being produced. As FA polymerized to PFA, they were much larger and longer branches of molecules that were effectively resin-like or can be considered rubber-like molecules. At sufficiently high molecular weights, these could no longer be supported the solvent and precipitate from the solution.

Thirdly, it needed to be confirmed that the loss of solvent did not alter the polymerization process.

A series of gels were designed with ratios from Table 5.1. Briefly, the block copolymer surfactant P123 (Sigma-Aldrich) was dissolved in 99.7% ethanol and acetylacetone (ReagentPlus® ≥99% Sigma-Aldrich) or “AcAc” was added next in order to prevent the alkoxide addition from immediately undergoing hydrolysis by water. To this solution, zirconium n-propoxide (ZNP) (Sigma-Aldrich) 70% wt in 1-propanol was added to bring the ratios of P123/etOH/AcAc/ZNP in solution to 0.05/40/1/1. The carbon source furfuryl alcohol 98% (Sigma-Aldrich) (FA) was added in a 1/2 ZNP/FA molar ratio. Acid-catalysed cationic polymerisation to polyfurfuryl alcohol (PFA) used 33% HCl (10.82M by titration) at a 1.25HCl/Zr ratio. But the solvent ratio was boosted from 40 to 80, 120 and 160 in four separate gels and incubated for a standard 72h. Fig 5.2 shows the effect of solvent on the carbon content of the gel at 550°C.

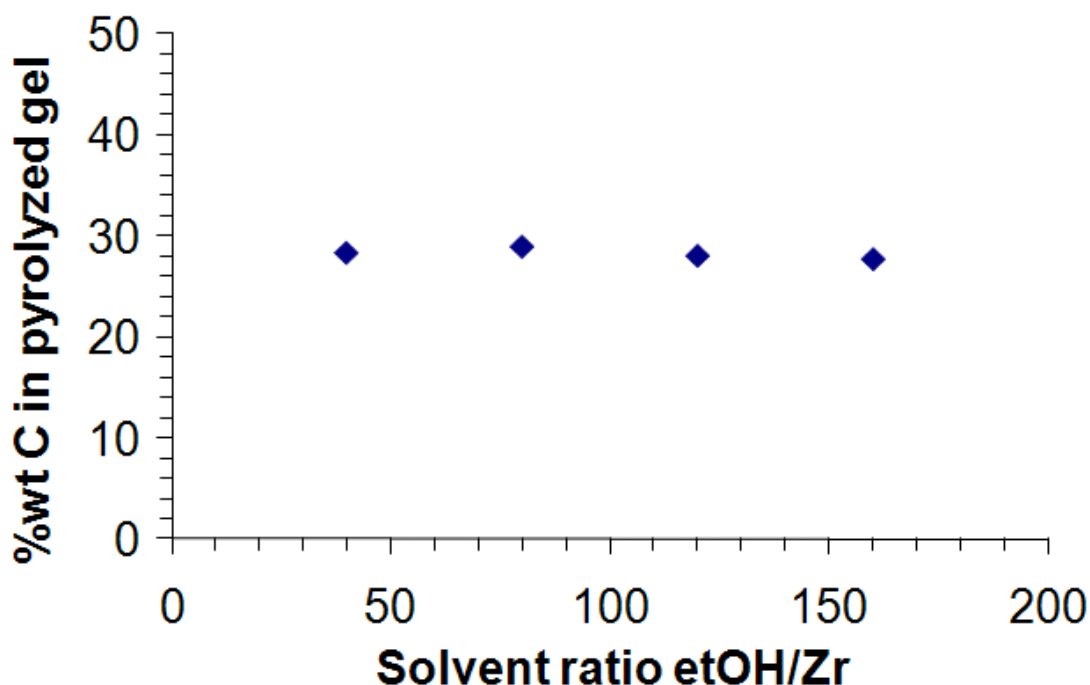


Fig 5.2. Effect of solvent ratio on the FA polymerization and PFA decomposition

These were dried and pyrolyzed at 550°C to decompose the PFA to carbon. The carbon rich gels were subject to a TGA treatment in air. Since carbon burns off as carbon monoxide or carbon dioxide, the residual material is zirconia. Thus the

carbon to zirconia weight ratio or % wt carbon of the total gel mass from components ($\text{ZrO}_2 + \text{C}$) in the gel can be determined. It can be seen here that the effect of solvent was negligible and such operations of rinsing, evaporation and transfer did not affect PFA formation. This suggested that ethanol was a spectator in the solution and did not significantly participate in any reactions of furfuryl alcohol. Furthermore, no precipitation of black resin showed that a 40/1 etOH/Zr ratio was sufficient to maintain PFA solubility.

5.2.3 Effect of acid catalyst

The effect of acid catalyst was determined in order to select an appropriate level of polymerization and crosslinking, which was the key to determining how much carbon was present after pyrolysis. Discussion of the molecular chemistry of PFA crosslinking was not strictly necessary for covering its molecular structure, particularly since the organic solvent simplifies the structure of the polymer.¹²⁵ The most pertinent feature for this discussion was that PFA decomposition to carbon is determined by the amount of alkylation or crosslinks in the molecular network. Another approach to this notion was that a threshold size of oligomer determines evaporation or decomposition to carbon. The alkylation often reaches a maximum of ~65%, resulting in an equivalent percentage of carbon retained after decomposition.^{123, 262-263} The remaining 35% are lost as oligomers that are small enough to evaporate or escape the gel at 550°C. In simple terms, only two-thirds of the carbon atoms are retained at maximum polymerization. These values are compatible with ratios for phenolic resins and pitch-based carbon sources.^{7, 121} Logically, the most effective way to control the PFA decomposition was to ensure that the added furfuryl alcohol always reached full polymerization. In other words, the PFA decomposition was far more predictable by full polymerization of a small amount, than to partially polymerize a large amount. Logically partial reactions yield widely distributed oligomer sizes, whereas full polymerisation was biased toward heavier and more completely crosslinked molecules. Fig 5.3 showed the carbon content in the gels as increasing amounts of acid catalyst were added to a fixed amount of furfuryl alcohol. The compositions of all the components match the values in Table 5.1, except the acid values from 0.25 to 1.25 HCl/Zr. Fig 5.3 shows that when given a fixed

polymerization time of 72h, the amount of acid catalyst added eventually reached plateau to maximum carbon content.

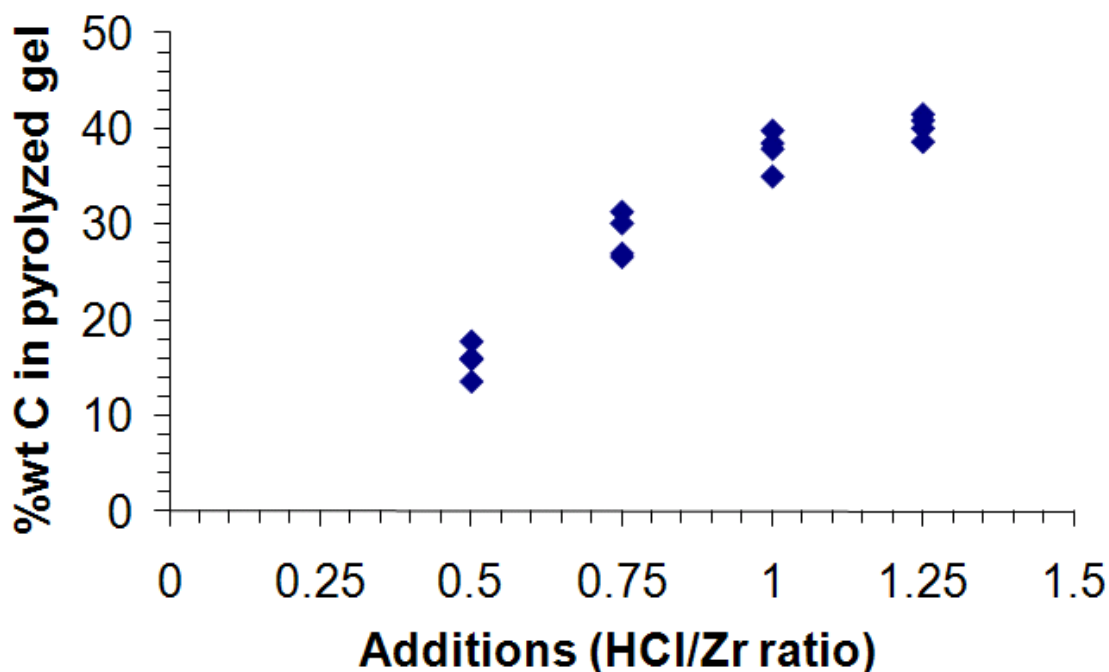


Fig 5.3. Effect of acid catalyst ratio on the PFA decomposition caused by PFA condensation at 23°C.

At higher values of acid, no further increase in carbon content in the gel was possible. This polymerization rate may become irrelevant since high temperature or large acid additions can reach the maximum alkylation rapidly. This was probably because water was a reaction product, thus polymerisation slows dynamically as it approaches equilibrium and the sol becomes saturated with water. Thus complete crosslinking between all available alkylation sites could not be reached due to steric hindrance from adjacent oligomers.¹²⁵ This insensitivity at values higher than $\text{HCl/Zr} = 1.25$ meant that it was possible to control the carbon ratio simply by changing the initial amount of furfuryl alcohol and driving the reaction to its maximum carbon retention. The only limiting factor was solvent that prevented PFA from coagulating. But the solvent ratio could be increased without affecting the FA-PFA reaction or carbon content in the gel. These sets of experiments also yielded the error in PFA decomposed carbon is $\pm 1.1\text{wt}\% \text{ C}$, not including the TGA error. This was the limit of duplication, because conditions varied in furnaces, losses of FA monomers and different losses during drying.

5.2.4 Summary

The most convenient variable to control the amount of PFA decomposition was the amount of acid catalyst. In order to offer a more consistent decomposition, the acid catalyst was added in ratios sufficient to reach the maximum PFA decomposition. This resulted in typical errors: temperature variations, solvent washing/transfer and mis-timing of aging negligible to the carbon yield from PFA decomposition. The error in the PFA decomposition to carbon was accepted at $\pm 1.5\text{wt}\%$ C. This included the TGA error $\pm 0.3\text{wt}\%$ C. This error was accepted as part of the sol-gel process. This allowed for the development of a study in forming nanocrystalline ZrC with an appropriate amount of carbon to investigate the reaction evolution from oxide to carbide.

5.3 Development and evolution of nc-ZrC

The gel for this series of experiments was selected as the Table 5.1 default, because it yielded a 4C/Zr ratio after pyrolysis at 550°C . This resulted in a gel with sufficient carbon for reduction to ZrC, but with only small amounts of residual carbon. This allowed for in depth investigation into particle microstructure and phase evolution by XRD, TEM and gas sorption. The process is shown schematically in Fig 5.6. As noted, the key aspects of synthesis were the stability of the AcAc chelated zirconium ion.

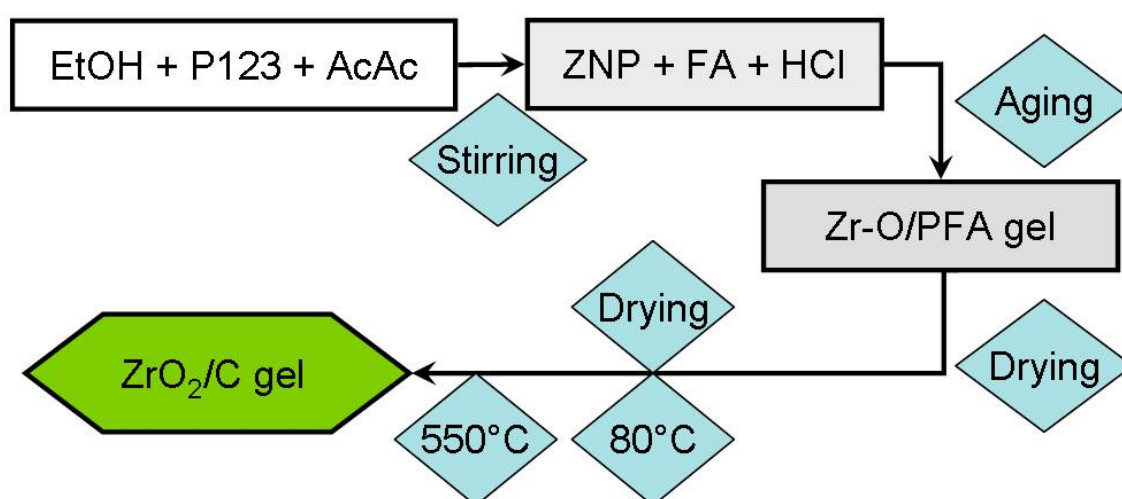
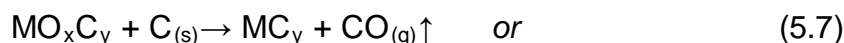
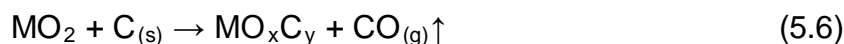


Fig 5.6. Schematic of the sol-gel technique to produce ZrO₂-C gels.

This allowed water to be introduced via the acid catalyst for FA polymerisation, which was controlled by the carbon content after pyrolysis. Solutions were dried for 24h at STP and at 80°C for 24h to remove ethanol resulting in black shiny gels. The dried gels were pyrolyzed in a flowing nitrogen furnace at 550°C for 5h under a flow of 120mL/min in order to remove the surfactant and yield carbon from PFA decomposition and these gels were a shiny but brittle glass-like substance.

5.3.1 Phase analysis

The 550°C treatment decomposed the PFA to carbon and the ZNP to zirconia, resulting in a carbon-zirconia gel. The phase evolution was shown by XRD in Fig 5.7 as the precursor was heated from 550°C to 1450°C. Initially tetragonal zirconia was observed, with relatively sharper peaks from crystallite growth as temperature was increased. Between 1000°C and 1400°C a phase of monoclinic oxide was observed. This was likely formed on cooling, where the lower surface energy caused crystallite growth could no longer prevent the phase transformation. By 1450°C, the tetragonal oxide was completely removed from the spectrum and only a cubic phase remained. The phase at 1450°C was identified as cubic zirconium carbide, with a lattice parameter of 4.695±0.001Å from conventional diffraction using Monash facilities and 4.6950±0.0001Å from synchrotron-derived data. This indicated a near complete conversion with little dissolved oxygen remaining in the lattice since 4.698Å is the reported cell parameter for oxygen-free ZrC_{1-x} .^{129, 290} Carbides with dissolved oxygen are known as oxycarbides. Further reduction occurs by the displacement of oxygen by carbon into this intermediate, requires higher temperatures <1600-1800°C and is known to occur via both $C_{(s)}$ or $CO_{(g)}$ in the following half-reactions:^{49, 105, 130, 273}



Note that the removal of oxygen from the oxycarbide lattice can occur even after the oxide phase is removed. Thus it is possible to fully remove the oxide from the system and appear to have pure metal carbide at equation 5.6, but this would

actually be an oxycarbide in form MO_xC_y . The progress of the reaction after oxide removal can be monitored by oxygen solubility in the oxycarbide and this has been a consistent standard since the 1970s.^{271, 291}

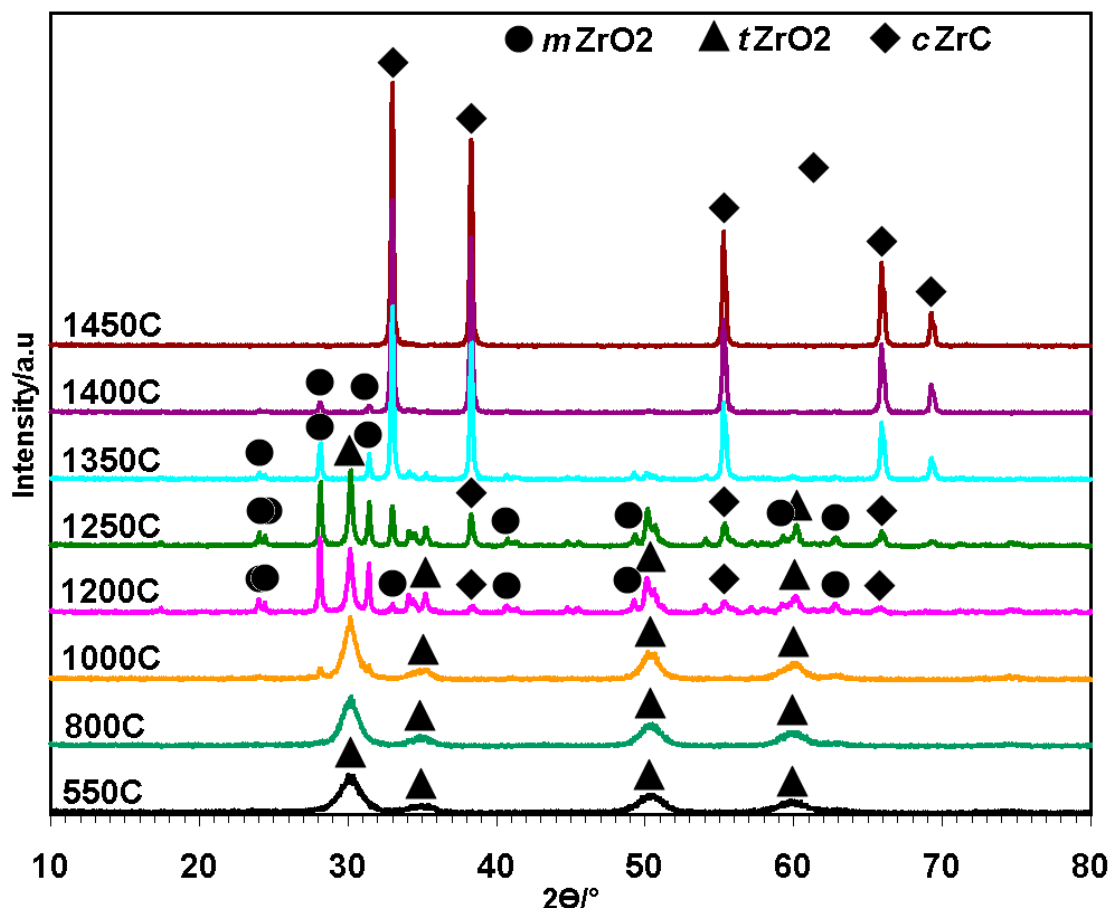


Fig 5.7. XRD patterns of sol-gel precursor, showing oxide to carbide transformation.

From the lattice parameter derived from this ZrC, the sol-gel derived reaction included both the reduction of zirconia and the removal of oxygen from the oxycarbide. Compared to the HfC work, the reaction evolution was very similar and thus the nanoparticles in close proximity to carbon was considered responsible for the low temperature conversion of ZrO_2 to ZrC, but this was investigated further by TEM and Raman spectroscopy.

5.3.2 Carbon and crystallite interactions

The role of carbon determined much of the carbothermal reduction behaviour. Carbon content, microstructure and phase analysis were of prime importance.

Firstly, the amount of carbon was controlled by the acid catalyst during the synthesis to vary the decomposition stoichiometry for the carbothermal reduction. The half equations from Reactions 1-3 (where M=Zr) were often simplified to reaction (5.9);



which sufficed for basic compositional analysis due to the high purity of the carbide. TGA spectra in Fig 5.8(a) showed that the zirconia-carbon gel had a weight loss of 43.3 wt%, corresponding to 4C/Zr ratio. Even with furnace upgrades this was more than sufficient for carbothermal reduction. A 0.5C/Zr ratio remained after the reaction, indicating the reaction occurred with 3.5C/Zr.

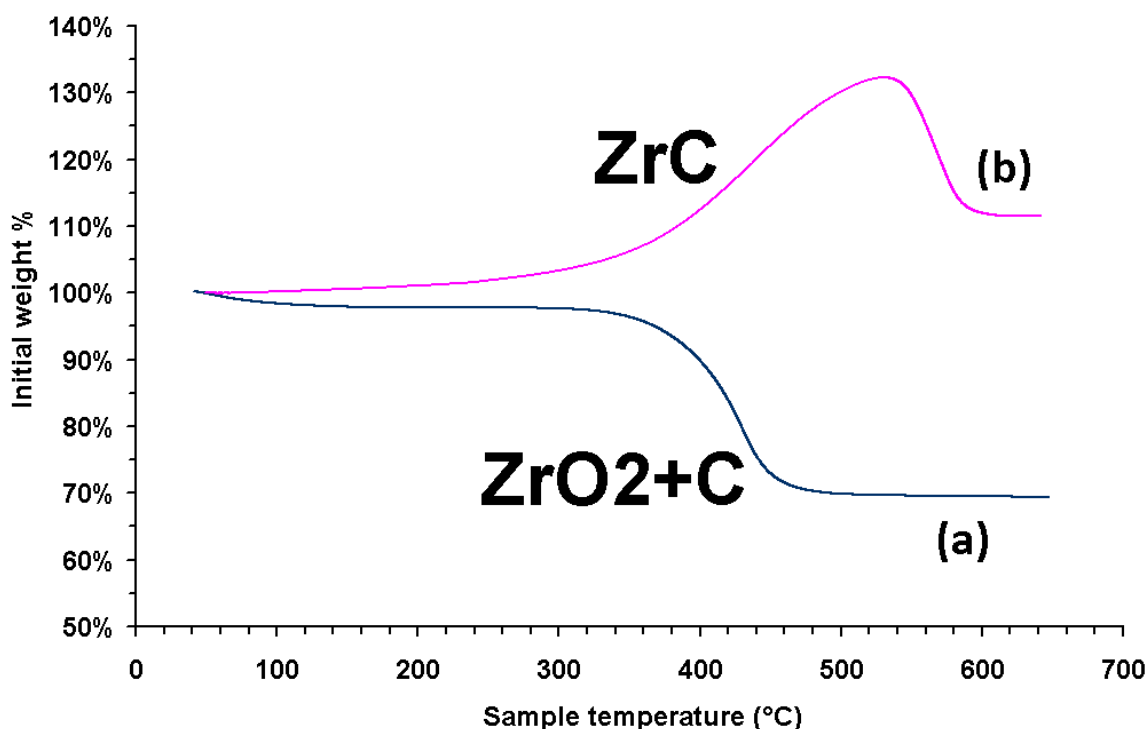


Fig 5.8. (a) TGA on post-550°C zirconia-carbon gel showing carbon oxidation only and (b) 1450°C ZrC product oxidized to ZrO_2 (weight gain) and oxidation of residual carbon (weight loss).

This was displayed in Fig 5.8(b) for the carbide oxidation, as the weight loss includes the oxidation of excess carbon. There are several possibilities to explain this 3.5C/Zr requirement for the reaction, including variables such as the oxygen

and [CO] partial pressure in the furnace. First, there could be residual oxygen during treatment and this was consumed by the excess carbon as a buffer. Second, it could be the loss of reactant [CO] through gas flow or the [CO] lost during oxycarbide reduction in the reactions of (5.7) and (5.8). These would all demand a slightly higher C/Zr requirement than the stoichiometric 3/1 ratio. Note that over the entire course of the study, the required carbon ratio never fell below 3.5C/Zr, which was indicative of a significant leak and aging of equipment. Comparative results in literature report ratios even closer to the 3/1 described by (5.9) indicating relatively superior seals and purging equipment.^{6, 128-129}

The microstructure of the early carbon and oxide was analysed via TEM and electron diffraction. Fig 5.9 showed the 550°C microstructure that suggested significant porosity with 5nm oxide crystallites embedded in carbon. It appears that carbon was still amorphous. The pattern of linked chains of crystallites in the TEM image suggests imprinting left by zirconia networks or the structure formed by surfactant. This is consistent with reported work on the HfC program, and by Zhong *et al* and Wang *et al* that noted the effects of the block co-polymer surfactant when removed by the 550°C decomposition, leaving in a carbon matrix with oxide crystallites separated by pores.^{123, 165} Because the focus was on the particle evolution during carbothermal reduction, analysis of the pore structure of the 550°C pyrolyzed gel is covered later. Carbon evolution was examined by Raman spectroscopy shown with key samples in Fig 5.10 as temperature was increased. This was one of the more reliable ways to determine the ordering of the amorphous carbon as temperature was increased because carbon microstructures severely interfered with the transmission beam in the bright field imaging of HfC-C. Much like XRD, Raman Spectroscopy included the entire sample, rather than a specific region. However, some challenges were encountered mainly due to signal-noise from less carbon. The first two peaks were assigned D and G, corresponding to vibration of sp^2 -hybridized bonds in carbon – breathing motions of sp^2 bonds caused by structural defects are responsible for the D peak, whereas the G peak was related to sp^2 stretching of chains and rings of the Brillouin zone centre E_{2g} vibration mode.²⁹² Their relative intensity, size and positions give information of the degree of order in the carbon network.²⁹³

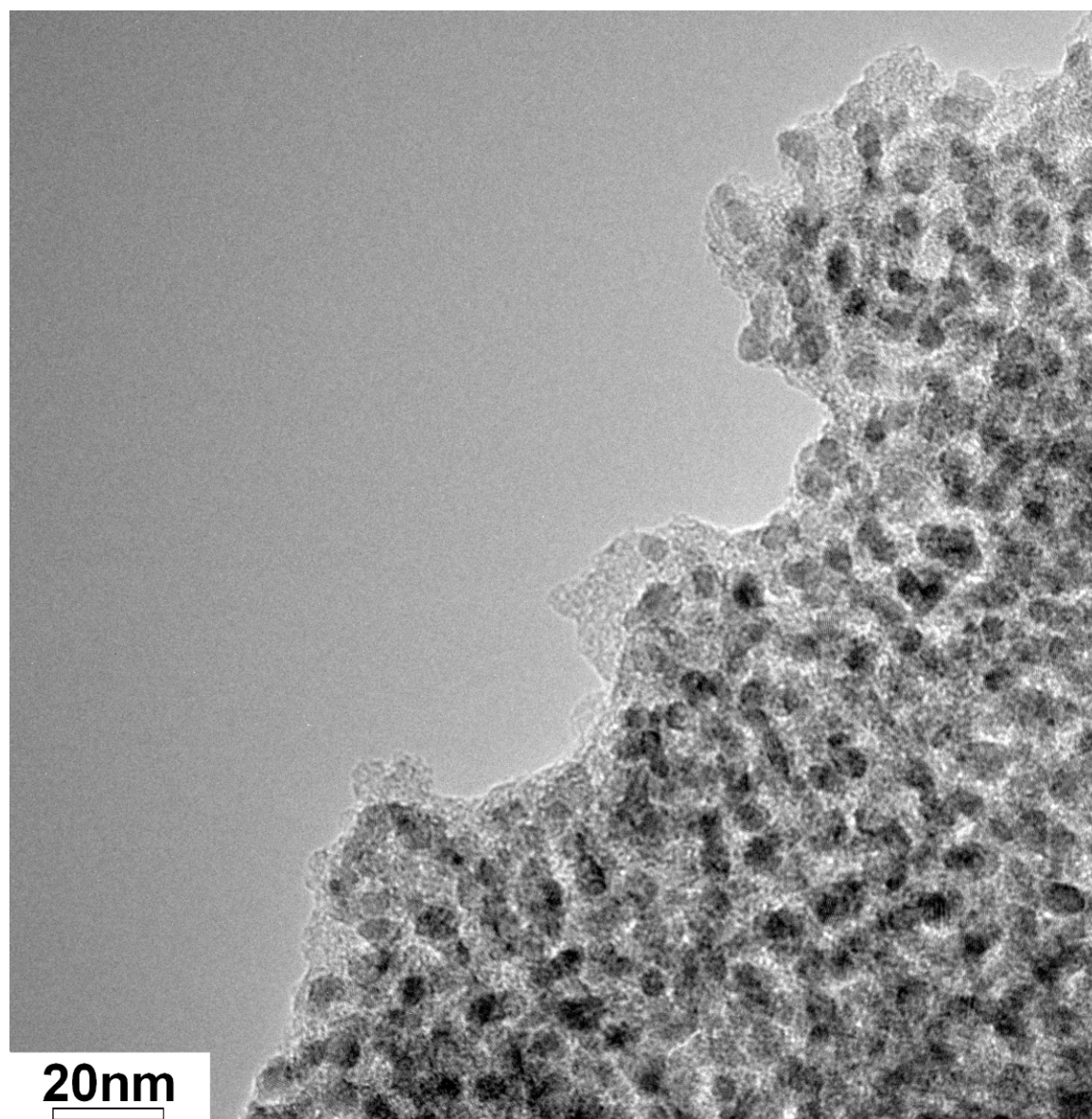


Fig. 5.9. TEM image of the nanocrystalline zirconia-carbon from pyrolyzed gel after surfactant burnout and PFA decomposition at 550°C.

The second set of peaks assigned 2D and D+D' are signatures for graphene and defect ends of the carbon network. It appears that the assigned D peak is weak at 550°C and becomes progressively sharper at its value of 1332 cm^{-1} without significant shift by 1400°C. The G peak initially begins at 1589 cm^{-1} and shifts to 1577 cm^{-1} by 1400°C. From 1200°C, the presence of a D+D' peak at 2930 cm^{-1} suggests sample edge defects of carbon. According to Ferrari *et al*, an asymmetrical shape of the 2D peak at 2670 cm^{-1} suggest that less than ~5 layers of carbon have assembled and this was supported by the fact that the size of the 2D relative to G was also too small to be single layer graphene.^{280, 294}

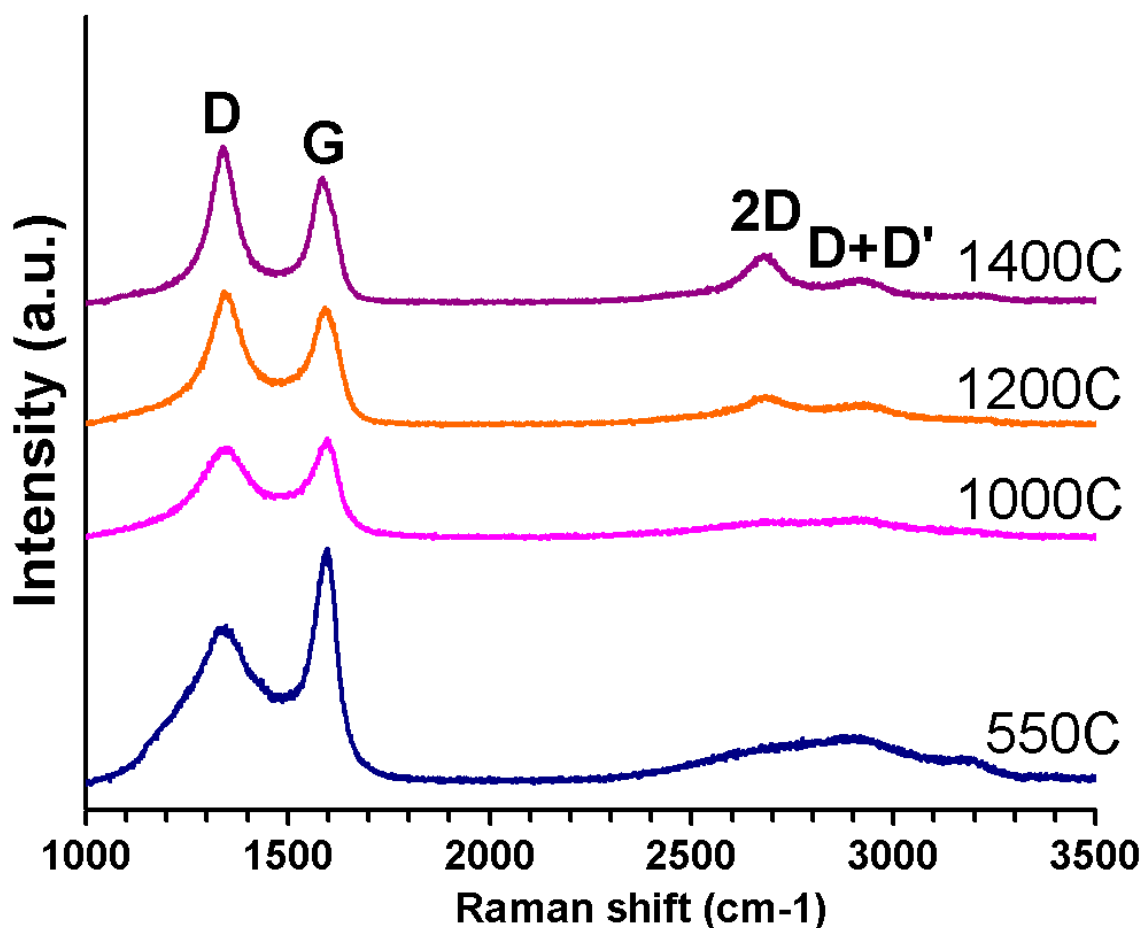


Fig 5.10. Raman spectra of $\text{ZrO}_2\text{-C}$ gel and subsequent carbonization. Note the 2D and D+D' peaks are seen only above the 1200°C (carbothermal reduction)

However, the evolution of the D/G ratio from 0.72 to 1.24, supported by the discernable 2D/D+D' peaks was sufficient to suggest increased ordering of the carbon network. This led to the conclusion that the carbon in the zirconia-gel was amorphous at 550°C. It gradually assembled until carbon was several (but less than ~5) layers thick. For graphite to be identified by Raman Spectroscopy, a 2D_{1A} shoulder (at 2670 cm⁻¹) was needed but the signal intensity here was weak, the amount of carbon is low and the reaction temperature was relatively low for graphite to be formed.²⁸² Nevertheless, this indicated that the reaction up to 1450°C involved the ordering of carbon to graphite as expected. It is likely that the Raman signatures for graphene are more evident over graphite in ZrC-C because less carbon resulted in less stacking of the graphene layers compared to previous HfC-C results.

5.3.3 Microstructure of carbon and ZrC

The microstructure of both carbon and ZrC was analysed using HR TEM. This was conducted on a 1450°C treated sample shown in Fig 5.11.

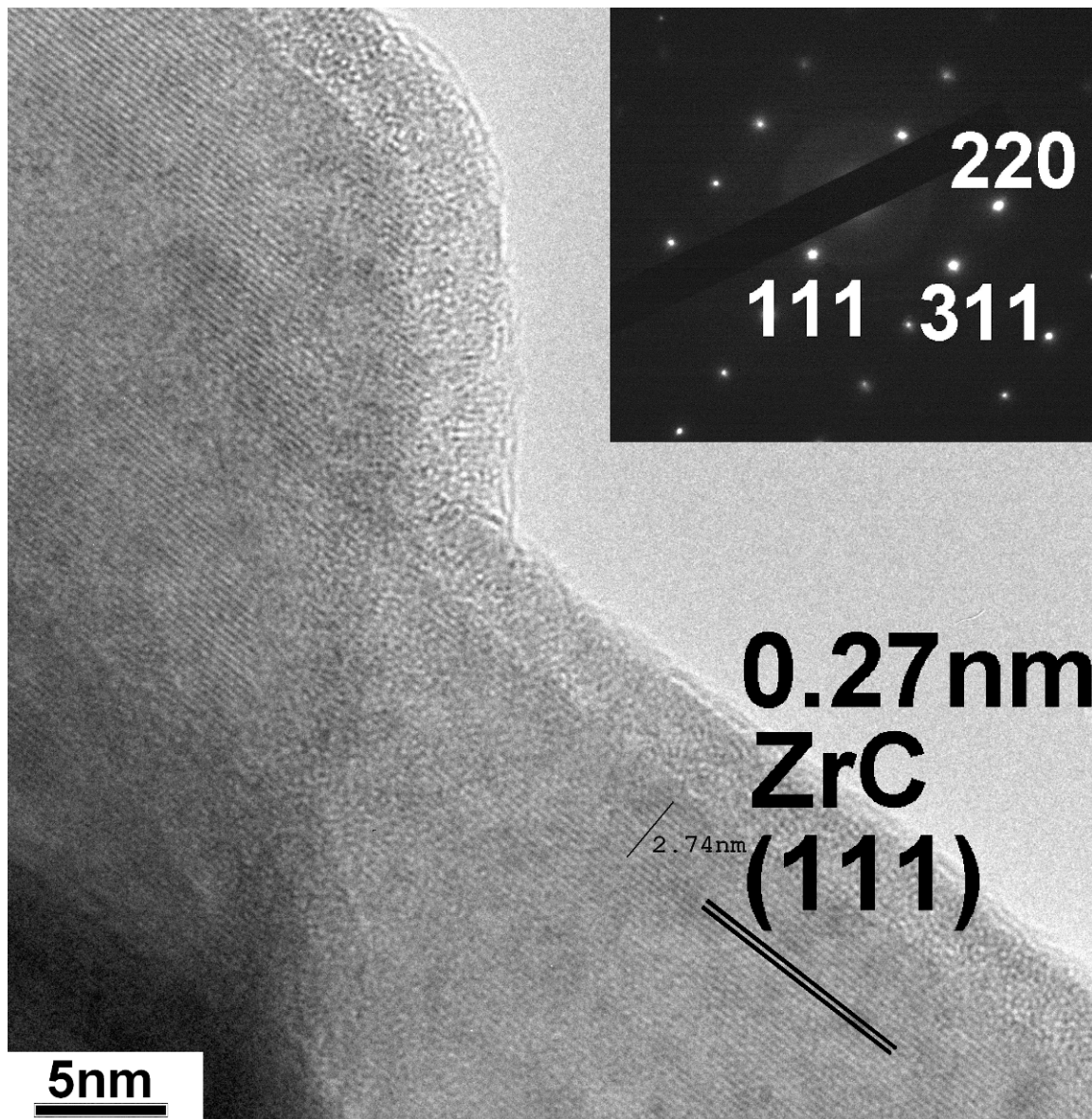


Fig 5.11. TEM bright field image of 1450°C ZrC (111) planes from [112] zone axis with SAED in the upper right inset. A disordered intermediate region and graphene-like layers can be seen on the surface.

The measured d-spacing corresponded to the interplanar spacing ZrC_{111} , matching the observed XRD lattice parameters for zirconium carbide. Some epitaxy was observed between the graphene-like structures, which appears to show the layers visible on the (111) on all carbide surfaces. The Raman analysis also matches observations in HR TEM that showed carbon to be triple-layer

graphene-like structures. The carbon was thus pre-graphitic as most of the regions demonstrated either disordered single “graphene-like” layers up to the maximum ~5 layers suggested by the Raman 2D peak. Most TEM images of 1450°C samples displayed a microstructure of three distinct regions: ZrC “core” crystalline regions, a disordered surface region and “graphene-like” carbon wrap. It should be noted that the crystallites at 1450°C are not all associated with a disordered region – a carbide crystallite edge was observed with 2-3 layers of carbon and no disordered region in Fig 5.12(a). Size did not appear to be relevant to the number or thickness of these carbon layers. The disordered surface was examined to determine its composition since it was defined by an interface, which could be attributed to a phase boundary. This was not possible in the HfC system due to excess carbon. Both Fig 5.11 and Fig 5.12(b) were examples of the three noted microstructure zones.

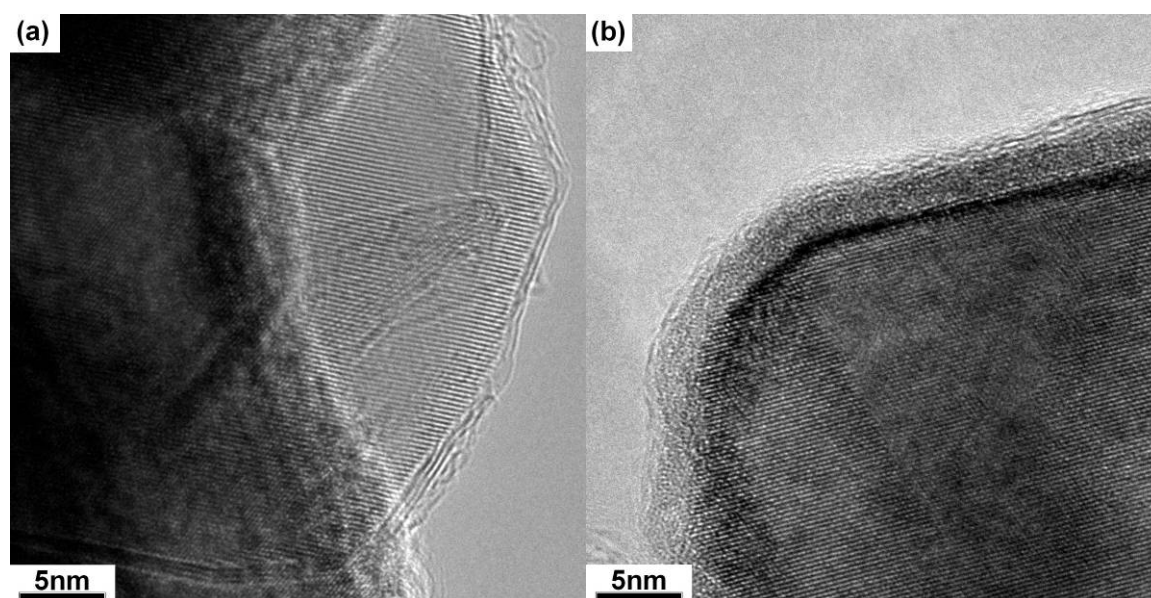


Fig 5.12. HR TEM images of the carbide/carbon at 1450°C (a) without a disordered zone (b) including a disordered zone.

Bright field imaging near the zone axis clearly showed discontinuity of the lattice fringes from the core into the disordered region. Graphene-like carbons are observed immediately adjacent to this region (Fig 5.11 and 5.12(b)). Investigation of this disordered region used STEM / EDS, supported with high angle annular dark field (HAADF) STEM imaging that reveals Z-atomic contrast. The STEM / EDS line scan in Fig 5.13 clearly demonstrates a Zr, O and C gradient even at

the beginning of the disordered region, suggesting this intermediate region contains substantial Zr well into crystal of depth $\sim 5\text{nm}$.

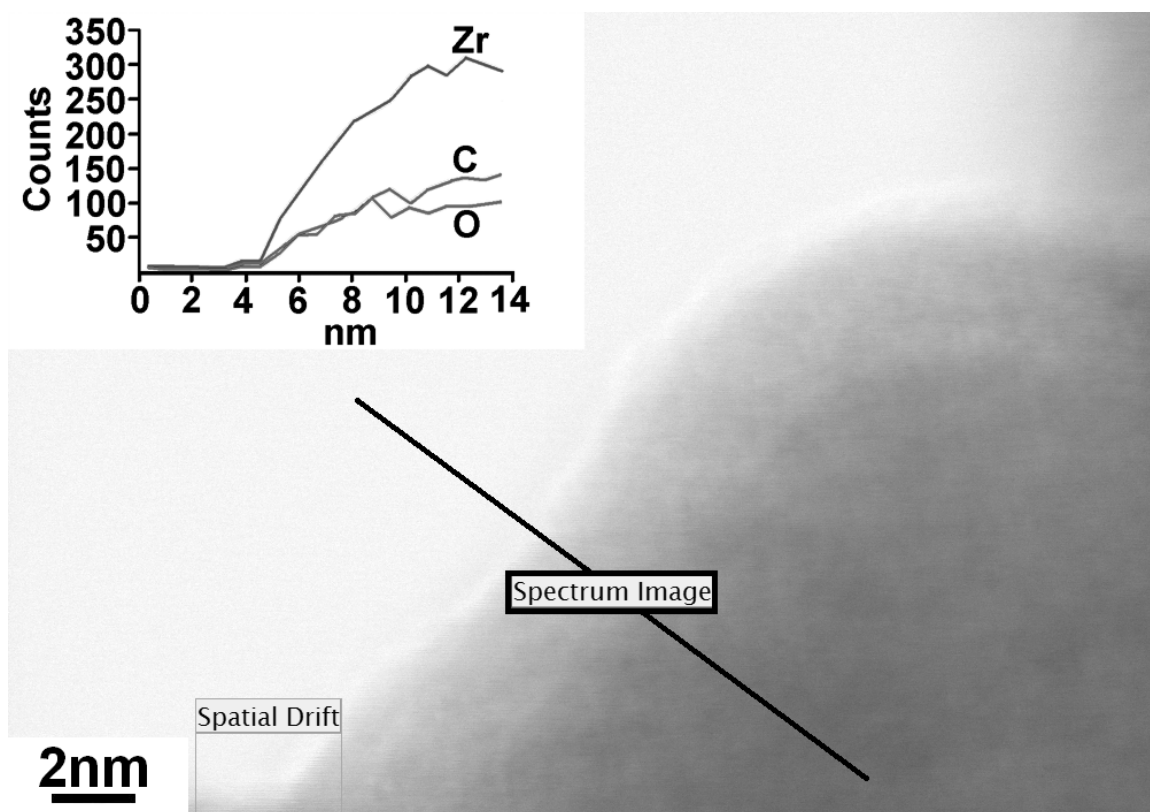


Fig 5.13. Bright field STEM image and line scan on semi-infinite region from the surface of ZrC.

However, this gradient could be the result of a smaller interaction volume since edge-core emission differences cannot be dismissed. From EDS, Zr is clearly present in this disordered surface region. These observations are supported by the HAADF imaging in Fig 5.14 (a) and (b). The brighter regions represent higher atomic number contrast. Fig 5.14(a) possesses a clear lattice fringe meeting the carbon wrap with no disordered zone. Fig 5.14 (b) demonstrates the intermediate disordered zone. This higher atomic number present in the disordered region indicates Zr is present in this intermediate zone. This indicates the intermediate region is well defined of 2-3nm depth. Interestingly, the 2-3nm disordered layer contains Zr and must likely contain carbon given that it is between ZrC and C. But lattice fringe discontinuities – contrast between clean and amorphous-like surfaces in Fig 5.12 – suggest that this region is different in some way. The most

likely explanation for this the typical surface oxide layer found on non-oxide materials after processing.⁷⁶

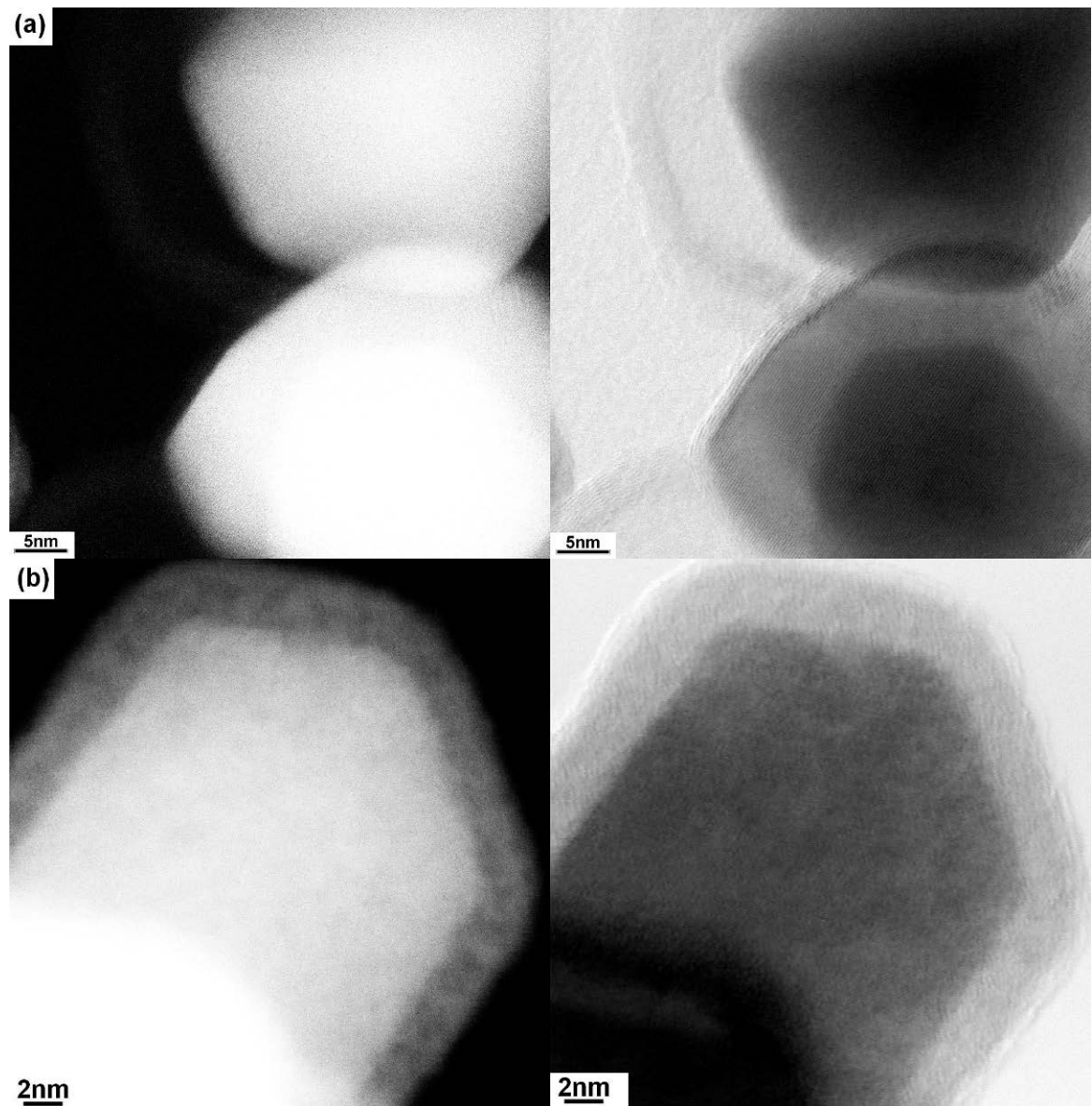


Fig 5.14. (a) STEM HAADF and bright field of 1450°C particles. (a) Shows clean particles with graphene-like formations. (b) STEM HAADF of another crystallite indicates Zr rich layer and surface carbon in graphene-like structures

Given that zirconium was also in this surface layer, it may be a thin oxycarbide or possibly an oxide, as moisture was unlikely under TEM ultra-high vacuum. It should be highlighted that given the large surface area of nanoparticles, even a thin oxygen-containing layer could represent a disproportionate impurity. The carbide and carbon have similar sensitivity to oxidation as the TG curve cannot

distinguish two separate oxidation peaks. Thus a slight excess of carbon such as the microstructure in Fig 5.12(a) and again in Fig 5.14(a) was probably beneficial in protecting the underlying surface.

5.3.4 Microstructural evolution of nanoparticles

A surface in-situ reaction microstructure would be difficult to capture using microscopy. Prevailing theory for carbothermal reduction had been reported since 1997; according to the “contracting volume” theory by Maitre & Lefort *et al* this reaction occurred by carbon diffusion into the oxide.⁴⁹ Thus the surface carbide should form first because of the proximity of carbon at the surface and relative carbon depletion in the centre means the core is the last to achieve stoichiometric ZrC. This was verified in the previous HfC research results. But homogenization of carbon could occur extremely quickly due to the short diffusion distance from the surface to the core. A different set of techniques must be employed to study the change in morphology of the particles. XRD and gas sorption are ideal techniques that are not dependent on sample features or extensive preparation.

It was likely that the reaction took place very quickly and such a gradient may not be obvious over a short diffusion distance. There was evidence of crystallographic changes occurring in preparation for carbothermal reduction. Fig 5.15 demonstrates a change in lattice parameter of both tetragonal and monoclinic oxide phases with a lengthening of the *c*-axis. This may be indicative of suboxide formation and carbon-oxygen displacement until sufficient to cause a phase change to cubic oxycarbide. Similar phenomenon was observed in suboxide phases in titania before the transformation to TiC because oxidation state of Ti^{4+} was decreasing.^{105, 273, 275} However, the mass transport of the oxides during the carbothermal reduction were much more significant in characterising the behaviour during the reaction. The presence of monoclinic oxides in the X-ray diffraction patterns from Fig 5.7 inferred that another mechanism for this solid-state reaction may be through the formation of agglomerates rather than simply centripetal diffusion of carbon into the oxide. The monoclinic phase must be attributed to t-ZrO₂ aggregates necked and sintered into large particles. These are then transformed on cooling.

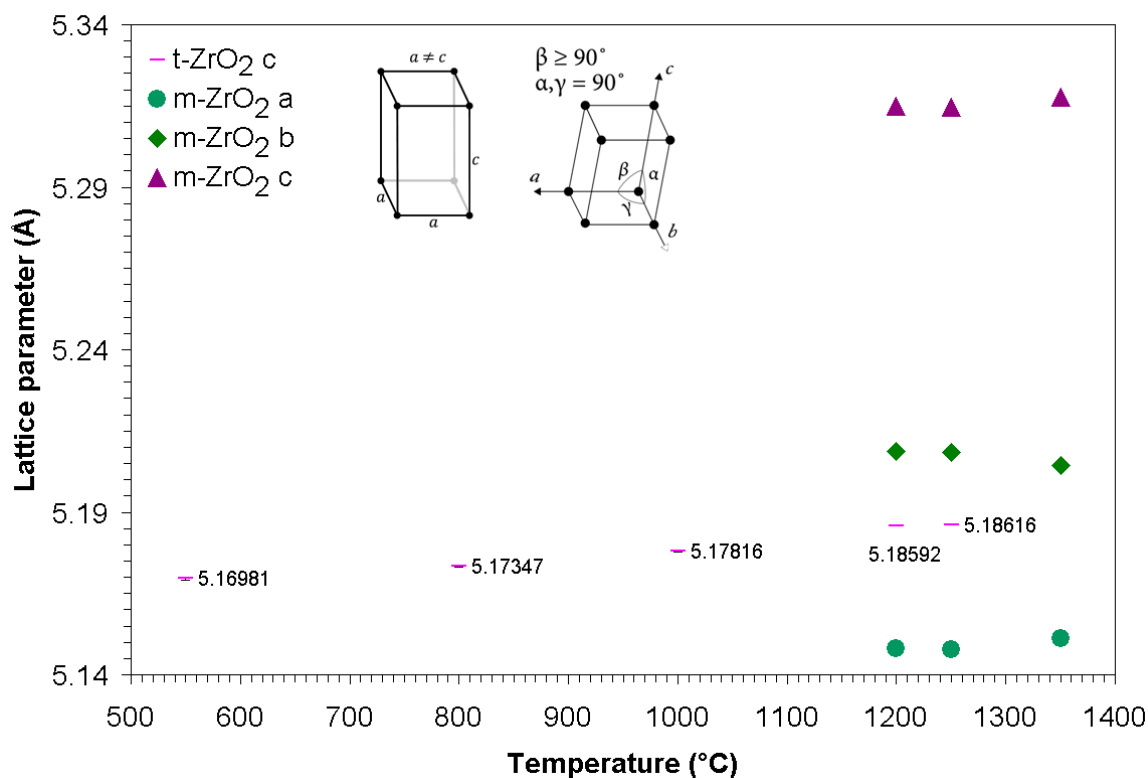


Fig 5.15. Observed lattice parameter expansion in c-axis of t-ZrO₂ during carbothermal reduction and in m-ZrO₂ formed on cooling.

It was also likely that regardless of which stage the reaction was at, there must be a driving force to reduce the surface area. The first observation of agglomeration was crystallite sizes shown in Fig 5.16. Both 550°C and 1450°C XRD crystallite size data matches observations in TEM images. It can be observed that as the zirconia-carbon gel was heated, the 20nm size t-ZrO₂ overlaps in the same reaction sample as the 55-80nm crystallite size for c-ZrC. Further proof is that the c-ZrC, once transformed, *does not* increase in size. If “contracting volume” was operating by itself, oxide and carbide sizes would be identical. The logical interpretation of Fig 5.16 was that 2-3 tetragonal oxides (with carbon wrapped or in close proximity) coalesce to form a larger carbide particle from the reaction. The second inference of agglomeration was the residual monoclinic oxides, and their respective average crystallite sizes. These were observed at lower temperatures where carbothermal reduction was incomplete. Carbon was required to remove oxygen from the oxide. To consume more carbon, the agglomeration of t-ZrO₂ was favourable as each oxide had its own epitaxial carbon.

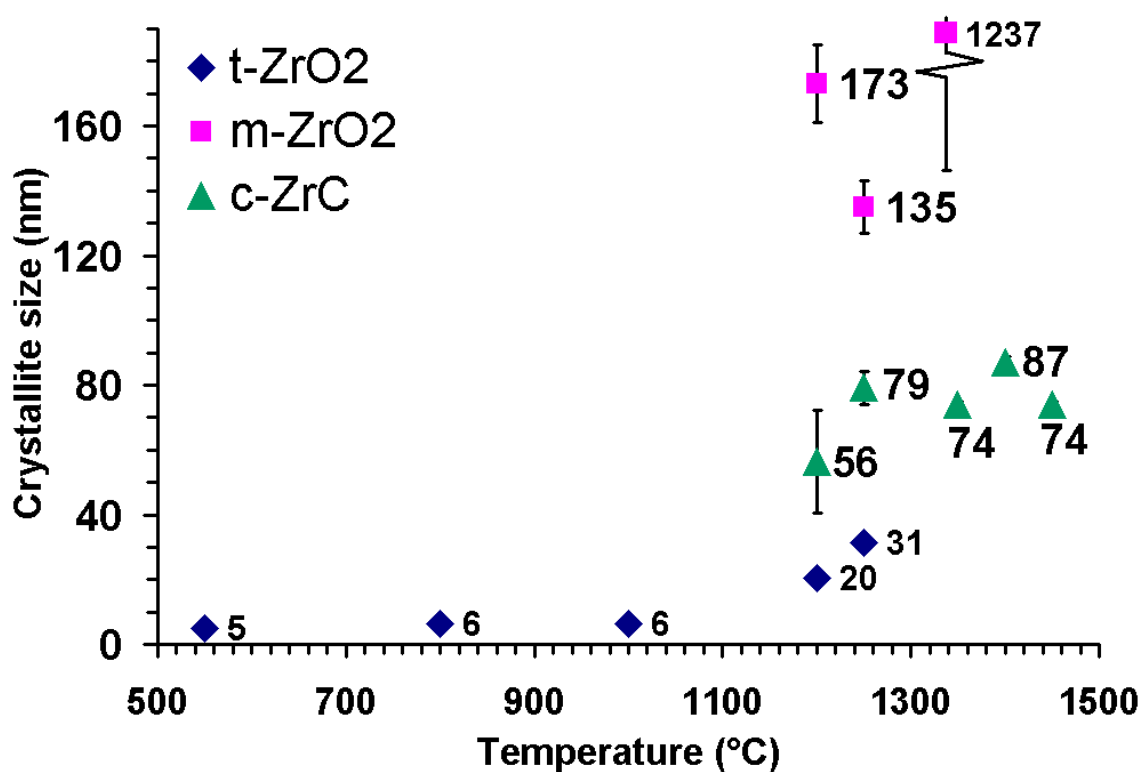


Fig 5.16. ZrO₂-C gel crystallite sizes after Rietveld analysis. Standard deviations are shown.

However, because carbon can only be found with a nearby oxide, this would result in an unfavourable sequence of agglomeration, as further carbon was required to reduce the attached oxide. A large agglomerate of oxide unable to transform might form larger agglomerates, in order to acquire additional carbon for the transformation, but this would add further oxide particles. When the isotherm ends (at too low a temperature for carbothermal reduction), these larger oxides are thus displayed as monoclinic oxides on cooling, from 100nm up to 1 micron in size and are unable to transform to carbides at 1350°C. Further evidence of an agglomeration for mass transport was the change in BET, Langmuir and single point surface area(s) determined by nitrogen sorption analysis shown in Fig. 5.17. Nitrogen sorption is a common technique for characterisation of nanoporous carbon and carbons derived from oxide sol-gel processes.²⁹⁵⁻²⁹⁶ Initially the zirconia-carbon gel at 550°C (displayed in Fig. 5.9) can be considered a dense material, with interparticle carbons

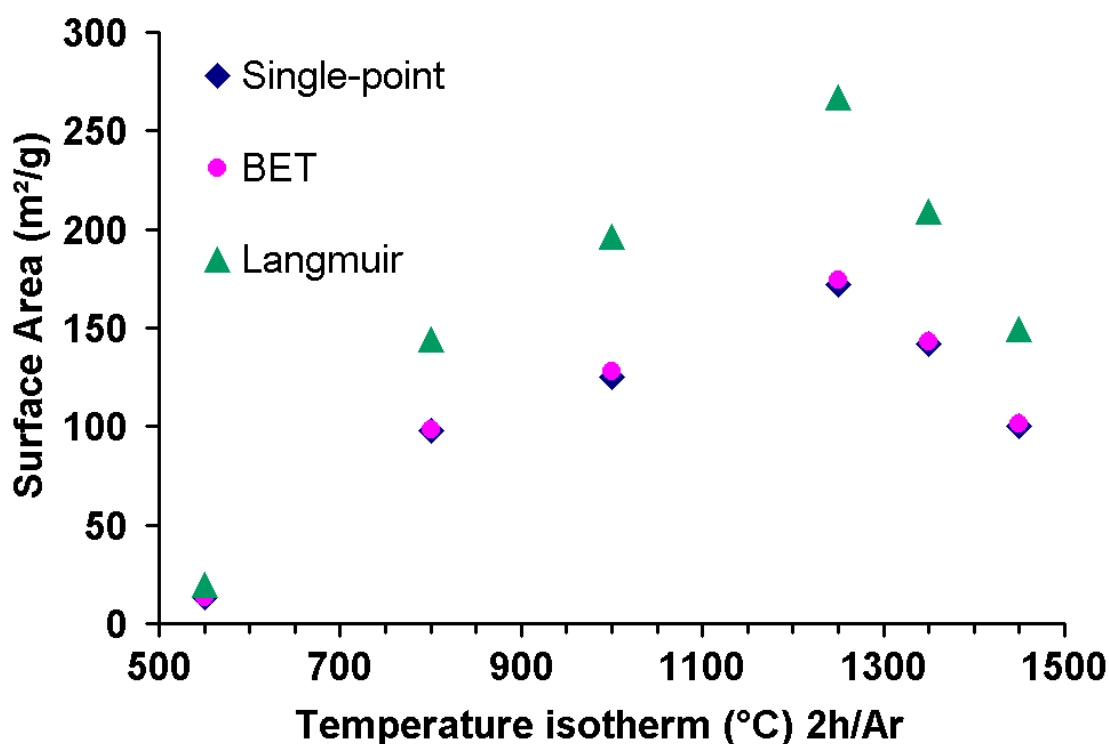


Fig. 5.17. Change in surface areas from gas sorption of ZrO_2 -C gel after heat treatment.

. Gas sorption can resolve the pores from PFA-derived carbon because they are still in micropore-mesopore range after surfactant burn out at 550°C .^{123, 165} Heat treatment resulted in gradual consumption of interparticle carbon or ordering of carbon between the oxides. Surface area increased as more pores are created, connected and more particle surfaces were revealed or become better defined, since the first carbon consumed would be near the carbon-zirconia interface, and this reaches its highest value at 1250°C . A schematic of this can be seen in Fig. 5.18. The decreased surface area at above 1250°C was due to the increase in particle size, which could be explained by the agglomeration and necking of carbide crystallites. The apparent surface was now decreased by neck formation, which gradually reduces the surface area of carbide particles. Thus peak surface area was observed during the carbothermal reduction, where interparticle carbon was rapidly consumed by the reaction, but necking has not yet begun between the particles. In reference to surface areas in Fig 5.17, it should be noted that low temperature zirconia-carbon gels demonstrate Type III isotherms, and BET surface area in Fig 5.17 at these temperatures should be taken with caution.

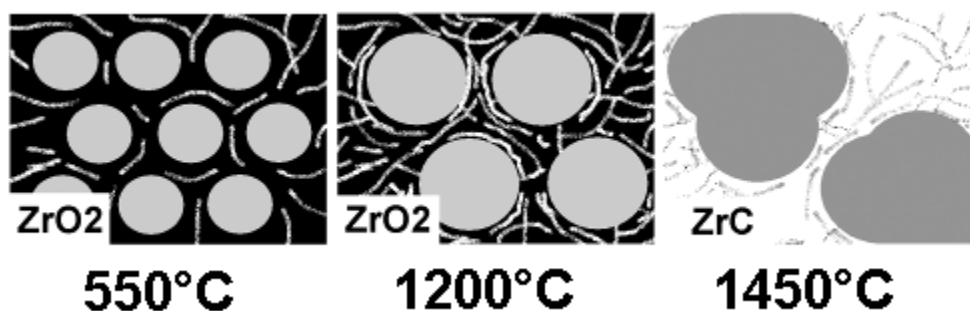


Fig. 5.18. Reaction schematic of $\text{ZrO}_2\text{-C}$; ZrO_2 and regions of carbon between particles opening, followed by ZrC formation and particle contact.

The Langmuir surface area was also provided because PFA decomposition often yields microporous carbons, particularly below carbothermal reduction temperature.²⁶⁵ A linear isotherm profile is shown in Fig 5.19.

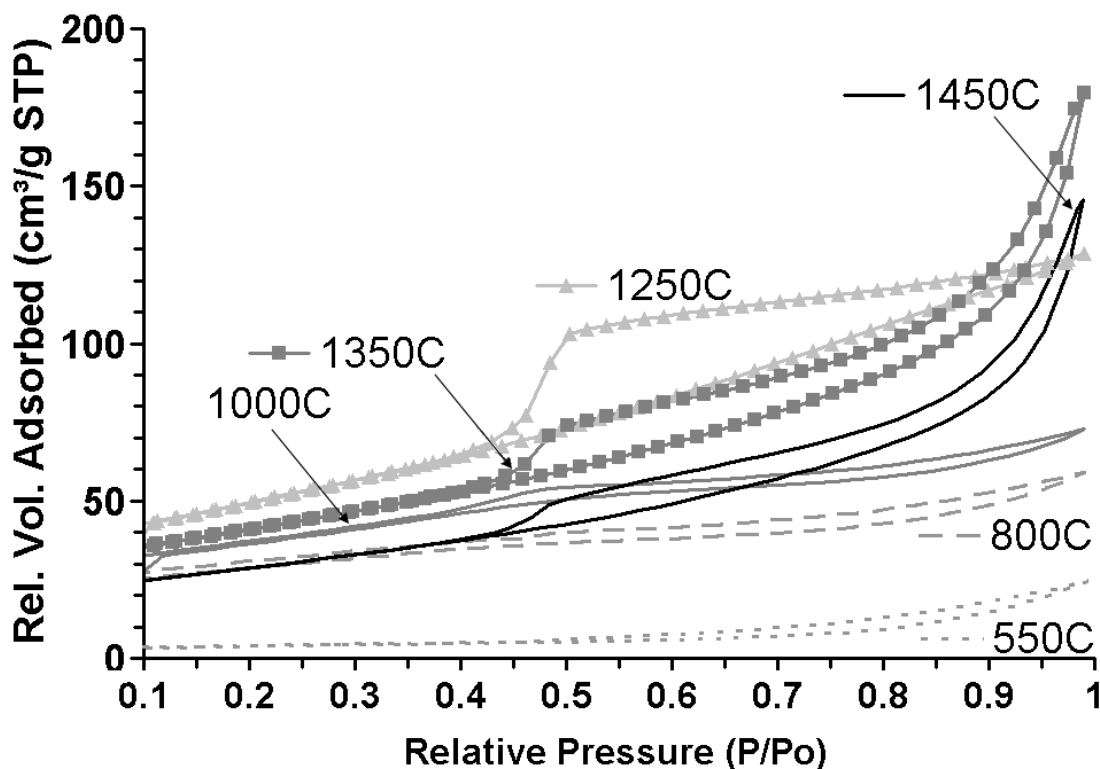


Fig 5.19. N_2 sorption linear isotherm profiles for $\text{ZrO}_2\text{-C}$ treated up to 1450°C.

It can be observed that desorption relative volume increased dramatically during the reaction temperature at 1250°C. A classical Type IV isotherm, the increase in gradient at lower relative pressures $P/P_0 \sim 0.42$ from 1250°C indicated the highest presence of micropores or very small mesopores. These likely developed

from the ordering of carbon in the microstructure. As the reaction approached 1200°C to 1350°C, interparticle carbon was rapidly consumed and the pores become larger – the mesopore volume was at its maximum. This dramatic change was supported by the TGA showing a carbon composition would drop from the initial 4C to 0.5C/Zr, as it is consumed to form ZrC. The gaps formerly occupied by carbon close again, likely due to ZrC agglomeration from high surface energy.

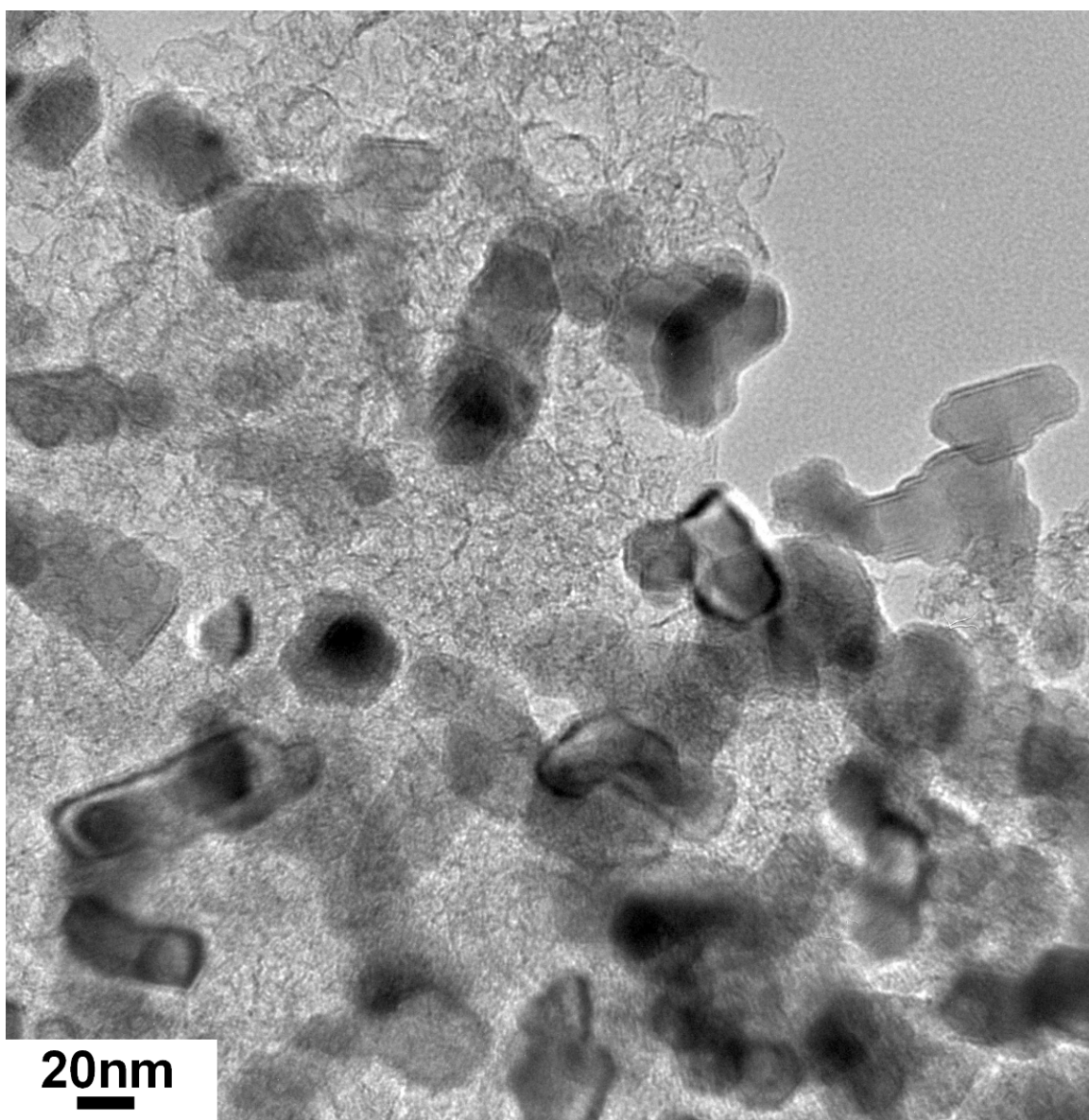


Fig 5.20. TEM image of ZrO₂-C gel treated at 1450°C to form ZrC

Nevertheless, spacing between crystallites were now much broader and non-uniform compared to the initial gel product, matching the high macropore

contribution to the gas sorption isotherm in Fig 5.19. Thus mesopores at 1250°C were replaced by macropores, shown in the rise in desorption-adsorption quantities at higher relative pressures from 1350-1450°C indicative of larger pores and voids. This surface area analysis was supported by TEM imaging. The formation of ZrC resulted in some particle contact as shown in the TEM images. However, the majority of the gaps by 1450°C are easily within the macropore size. The non-equiaxed crystallite geometries in Fig 5.20 at 1450°C of ZrC were unlikely to be from growth morphologies, and are likely to have occurred through previous necking from the oxide reaction. The temperature was also too low for carbide growth or necking.

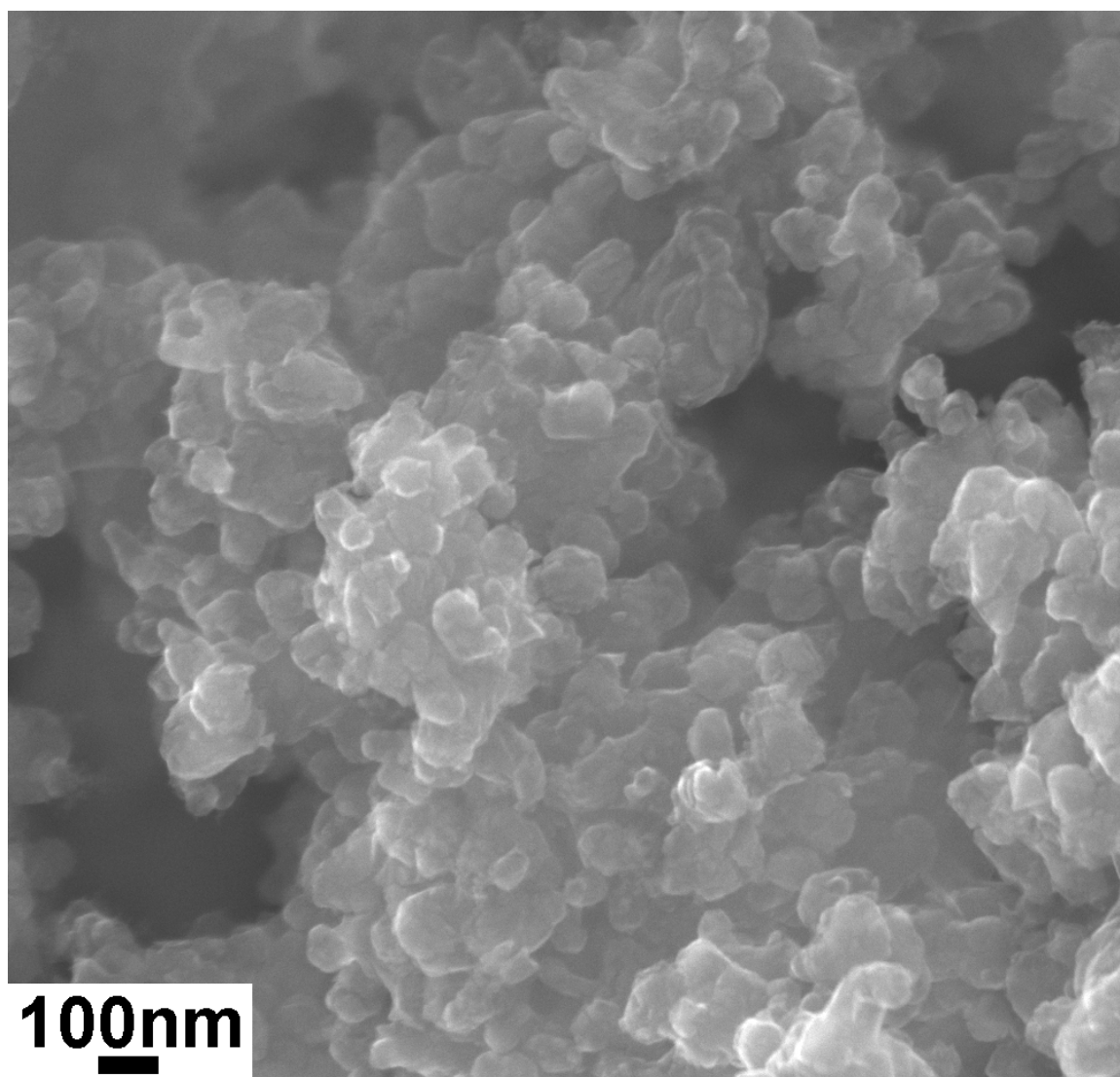


Fig. 5.21. SEM micrograph of ZrC nanopowder after 1450°C/2h formed from ZrO₂-C gel.

Therefore contact might result from particles sticking together to reduce surface energy. There was also evidence that bonded carbon layers can act as bridges between carbide particles given that these ZrC formations each possess layers of graphene-like carbons¹⁶⁵. The TEM and SEM images of the distribution of carbides in Fig. 5.20 and Fig. 5.21 supported both XRD and gas absorption interpretations for this agglomeration reaction. Given the pre-reaction oxide crystallite size was about 20nm, the minimum agglomeration factor was likely in the order of three oxides per transformed carbide. Reaction kinetics between adjacent oxide and carbons likely occurred very quickly since the longest diffusion distance was in the order of ~20nm. However, it should be noted that powders are heated, cooled and analysed. It was entirely possible that two processes are sequential and centripetal diffusion occurred first and the carbides coalescence. The “contracting volume” oxide- to-carbide model was valid but it was unlikely this model was useful as a mechanism to predict final particle size particularly given the increasing interest in carbide nanoparticle synthesis. The evidence indicated that homogenization occurred through agglomeration of entire crystallites and thus direct particle contact from nanoparticles was certainly a more descriptive mass transfer mechanism for understanding this reaction. This work illustrated that the sol-gel nanoparticles undergo substantial microstructural evolution, which was critical for understanding processing when integrated into composite preparation.

5.3.5 Conclusions

The sol-gel process was produced nanosize ZrC via a surfactant templating of organic zirconia and furfuryl alcohol based resin. Careful sequencing of added components in the sol and understanding basic organometallic chemistry can simplify to the point of handling in air. Successful control of PFA decomposition was possible when the appropriate variables are selected. Control of carbon was clearly more viable by understanding of the acid catalyst and its effect on the yield of carbon from PFA. Controlled carbon ratios allowed for a detailed study of the reaction mechanism via gas absorption, XRD and electron microscopy and while allowing for higher compositions of carbon if necessary. This highlighted the third challenge of whether sufficient understanding was acquired to process this ZrC for composites. The intimate mixing of the 4nm zirconia particles with carbon,

which also prevented oxide agglomeration, allowed for a low temperature carbothermal reduction. The microstructure makes it likely that particle agglomeration must occur to complete the mass transfer given the evidence of oxide agglomeration. For the use of nanocarbitides, the contracting volume approach may require revision to predict particle sizes.

5.3.6 Future work

There were limits on the use of ZrC nanopowder. Layering from graphene-like carbon occurred on the surface of the carbides, despite the PFA derived carbon being non-graphitizing. The amorphous region between the crystallite and layered carbon was determined to be a surface oxide layer present in all non-oxide materials not kept in an inert atmosphere. But most important of all was that there was no control over the agglomeration size except by oversupply of carbon, or a method to disperse the graphene bonding. Therefore, this powder would still need significant improvement for monolithic sintering. Some of the difficulties of nanopowder densification can be found in a review article by Mukhopadhyay et al.⁷⁶ However, it was never the intention of this project to densify the nanopowder directly. The key findings were the surface energy behaviour of the nanoparticles, their agglomeration if mixed with carbon, the lattice parameter and particle size during the reaction.²⁹¹ These were all key points in understanding how to seed ZrC on the surface curvature of a powder.

6. Composites of ZrB₂ by sol-gel ZrC

Research in nanosize HfC and ZrC via sol-gel processes was critical in understanding the phase evolution and agglomeration behaviour of nanoparticles. This was necessary to understand dispersion of nc-ZrC in a ZrB₂ composite, because the intended goal was to seed the surface of ZrB₂ by creating a gel-coated powder, which is referred as powder-gel in the subsequent discussion, and subsequently transform it into a powder with attached nanosize ZrC. The first section of this chapter investigated the densification process in SPS to explore the sintering of monolithic ZrB₂ as a control in comparison to the subsequent composites. Synthesis of the powder gel explored four distinct steps. The first was the powder-gel without sufficient carbon for the transformation to ZrC. This investigated how the surface oxide film found on the ZrB₂ powder would interact with a gel oxide source. The second experiment investigated the amount of carbon required to suppress oxide formation, and this involved the production of gels rich in PFA. Finally, the morphology and microstructure of the powder was investigated to characterise the nanoparticles formed on the surface of ZrB₂ and its formation mechanism compared to monolithic ZrC gels. The chapter closed with the densification of the powder-gel in comparison to control ZrB₂ powders.

6.1 SPS sintering of ZrB₂

Some early investigation into the controls and constants in SPS were conducted to better understand the processing technology. Two key processes to control were the effect of heating rate and die size. Densification of ZrB₂ established a baseline for the effect of the addition of nanoparticles.

6.1.1 Constants in SPS

There was certainly an interest in understanding this relatively new sintering technology. However, only the phenomenon affecting the differences in processing between composite and control will be the focus of this section. The densification phenomenon of SPS were critical processing parameters because of the number of samples under different sample sizes, compositions and other research projects funnelled through this instrument. In Fig 6.1, a microstructure

ZrB_2 was displayed after heating to 1900°C at $100^\circ\text{C}/\text{min}$ at 40MPa in a 10mm sample. The most pertinent feature was that the material on the top surface in (a) is more dense than the centre regions in (b). This indicated that porosity in the centre was not removed. Given that nearly full densities are achievable, the most likely mechanism was that closed pore volume occurred, and well before grain boundary contact could take place in the centre.

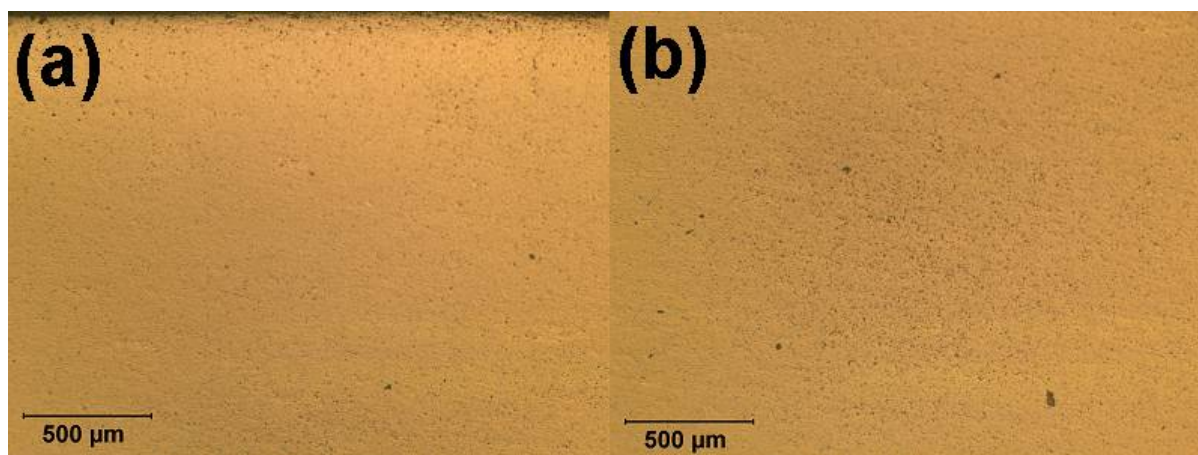


Fig 6.1. Optical micrograph cross-section of ZrB_2 10mm sample denser than bulk. Sample was sintered to 1900°C (a) top surface and (b) sample centre (2mm from surface).

The best explanation for closed pore volume was based on the current path, temperature of sample and the graphite foil. While SPS was designed to pulse current directly into a sample this may not occur in practice.^{177, 196} The DC current approached through the spacers, and concentrated to a higher current density along the 10mm diameter punch. Wrapped in carbon felt, the punch offered three paths that are considered separately. (1) The current passed directly through the sample (2) The current passed through the graphite foil. (3) The current passed through the collar and punches. These are shown in Fig 6.2. However, it was likely that all three paths are available and when a parallel circuit model is considered, resistivity determines the amount of voltage and current in each path. Graphite is an electrical conductor. The ZrB_2 powder, possessing a surface oxide layer, was likely the path of the highest resistance. Kirchhoff's current and Ohm's law then segregate the current according to resistance. Thus, it was logical that

most of the current initially passed through the graphite collar. The first stage can be considered to be no more than highly efficient hot pressing, with more electrical activity on the surface of the greenbody. As densification occurred and surface oxides were removed by carbothermal reduction, the electrical conductivity of the compact improved. However, the close pore volume resulting from better surface densification prevented central pore removal and limited the maximum densification.

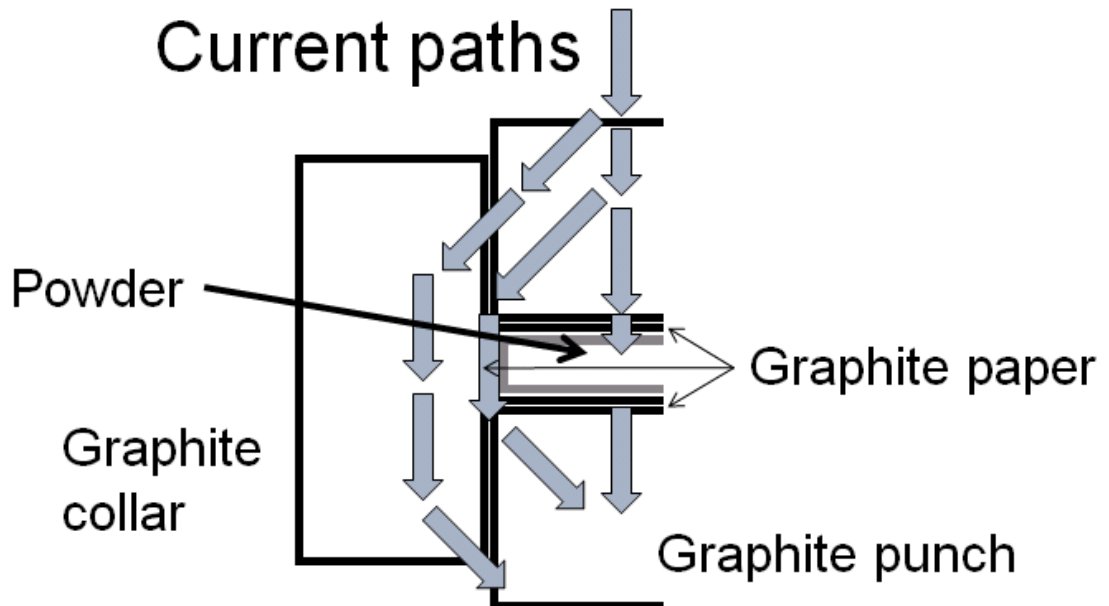


Fig 6.2. Available current paths in SPS sintering of SPS-925 with ZrB_2 on example 30mm die configuration.

Carbothermal reduction was likely because the sample was wrapped in graphite foil 0.1mm thick. As reported by Zhu and Mishra et al, carbon reduction of the surface oxide caused increased surface activity thus a chemical driving force for densification.^{169, 191, 197, 297} It was known that carbon is the diffusing species in carbothermal reduction.⁵⁷ ZrB_2 samples all possessed porous cores and closed surfaces, which may have been from reaction with surface carbon. However, the later composites already had carbon from decomposed PFA by the gel processing. Ironically, these composites (designed for full densification) actually resulted in surface porosity, because the surface had excess carbon because of the 0.1mm of graphite foil. The role of electric current on diffusion was not studied in this research program. However, there was evidence that current did pass

through the sample, consistent with the “spark plasma” from causing expelled oxides reported in literature.¹⁹⁶ A substantial amount of oxide was removed from the powder by the furnace. The surface spacers adjacent to the graphite die were shown in Fig 6.3, showing the thin white film found immediately after sintering.

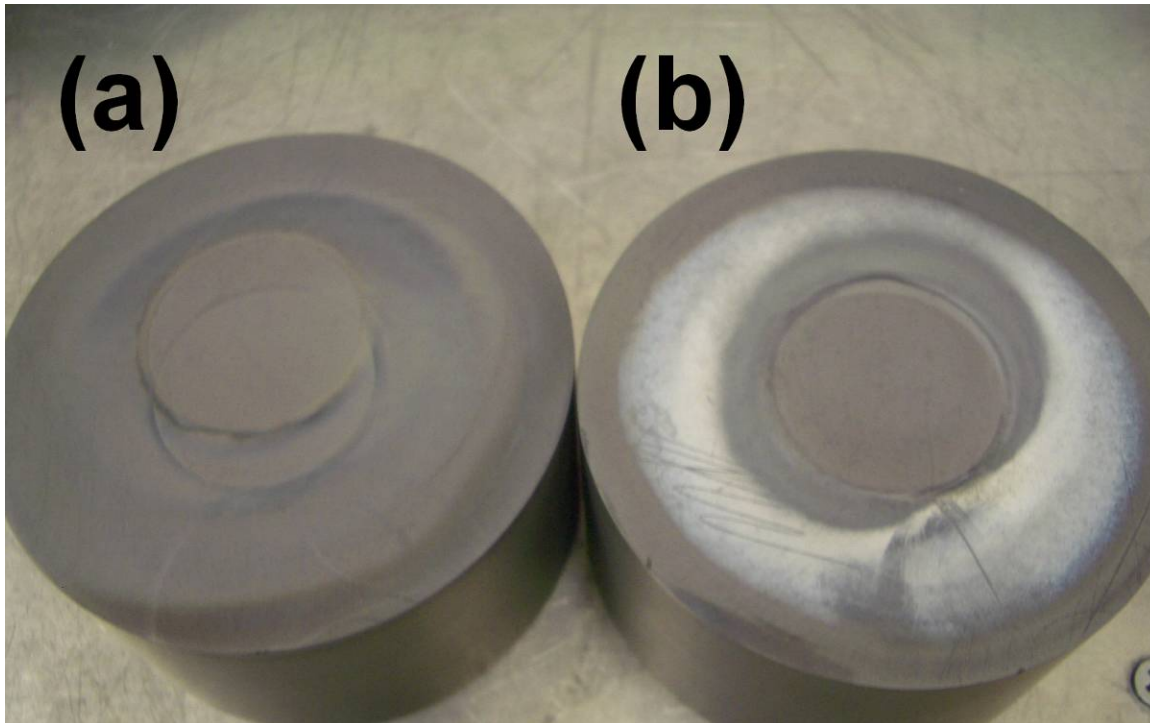


Fig 6.3. (a) Upper punch with mostly ejected gas **(b)** Ejection oxide from 100mm spacer on lower punch. The upper punch always had less oxide deposited.

EDS analysis confirms this film was rich in Zr and occasionally B was detected. This was likely to be zirconia and boria from ZrB_2 surface film. The deposition was resistant to scratching and needed to be removed by abrasives or scalpel. High vacuum performance (4-6Pa) was suitable for vapour deposition by high velocity gas phase. This could be caused by high temperatures since the vapour pressure would be quite high, particularly for boria. Interestingly the oxides were ejected down in preference to the direction of pulsed current rather than vaporizing up. The volatilization of insulating surface films is a well discussed phenomenon of SPS.¹⁷⁸ Thus it is possible that oxides were physically removed by a violent vaporization associated with the SPS removal of oxide films by the plasma on the powder surface. Another related SPS effect inferring a spark plasma was sparking, shown by a die collapse during sintering due to mechanical

failure of the die. This resulted in melted graphite-carbon surfaces, implying the presence of a spark discharge. Vacuum is an excellent dielectric. But if sufficient gas or ionized molecules were in the vicinity, this was sufficient to yield a conductive path for a spark discharge. However, this gas could be produced both by high temperature volatilization of components as well as the ionized plasma.

These aforementioned phenomena needed to be kept in consideration. Certainly SPS dies in operation were surrounded by significant ionized or high energy gas particles. But this is not necessarily the result of spark plasma in the sample powder. The major conclusions from these phenomena were that the effect of close pore volume was minor on larger 30mm dies, which were more homogenous because the outer 1mm could be discarded. However, carbon and SPS removal of surface oxides were two factors that had to be considered, because they decreased the required amount of carbon from PFA decomposition, and suggested reaction sintering occurred on the surface of the powder compact.

6.1.2 SPS Densification of monolithic ZrB₂

A brief investigation into the densification of ZrB₂ was investigated as a control for the composite. The heating rate was fixed at 100°C/min at 40MPa applied pressure. Images in Fig 6.4 from (a) to (d) showed the microstructures after 5 minute holds at 1600°C-1900°C, resulting in relative density from 72 % to 93% respectively. In Fig 6.4(a), the darker regions denote pores or mounting resin as the contrast was increased to highlight powder particles. Charging is observed on edge vertices likely from retained surface oxides. Since the powder size was known to be 4-5µm from Fig 3.4, the grain size had not significantly increased, and necking was beginning even at this temperature. Some necks that formed had the appearance of non-densifying surface diffusion mechanisms rather than viscous or impinging surfaces, since some have high radius of curvature and protrude significantly from the parent surface. Most possess the partial surface “spark plasma” pressure, which could generate this morphology.¹⁷⁶ In Fig 6.4(b), the intermediate stage of densification had begun and most have grain boundary contact, showing shorter pore channels and broad necks on all particles, highly contrasted with the mounting resin. Note that most of the pore channels were already closed at 1700°C, which indicated the speed of the SPS moving quickly

to the final stage of sintering. Fig 6.4(c) and (d) represent the final sintering stage; pores are closed off and isolated, and some grain growth has initiated.

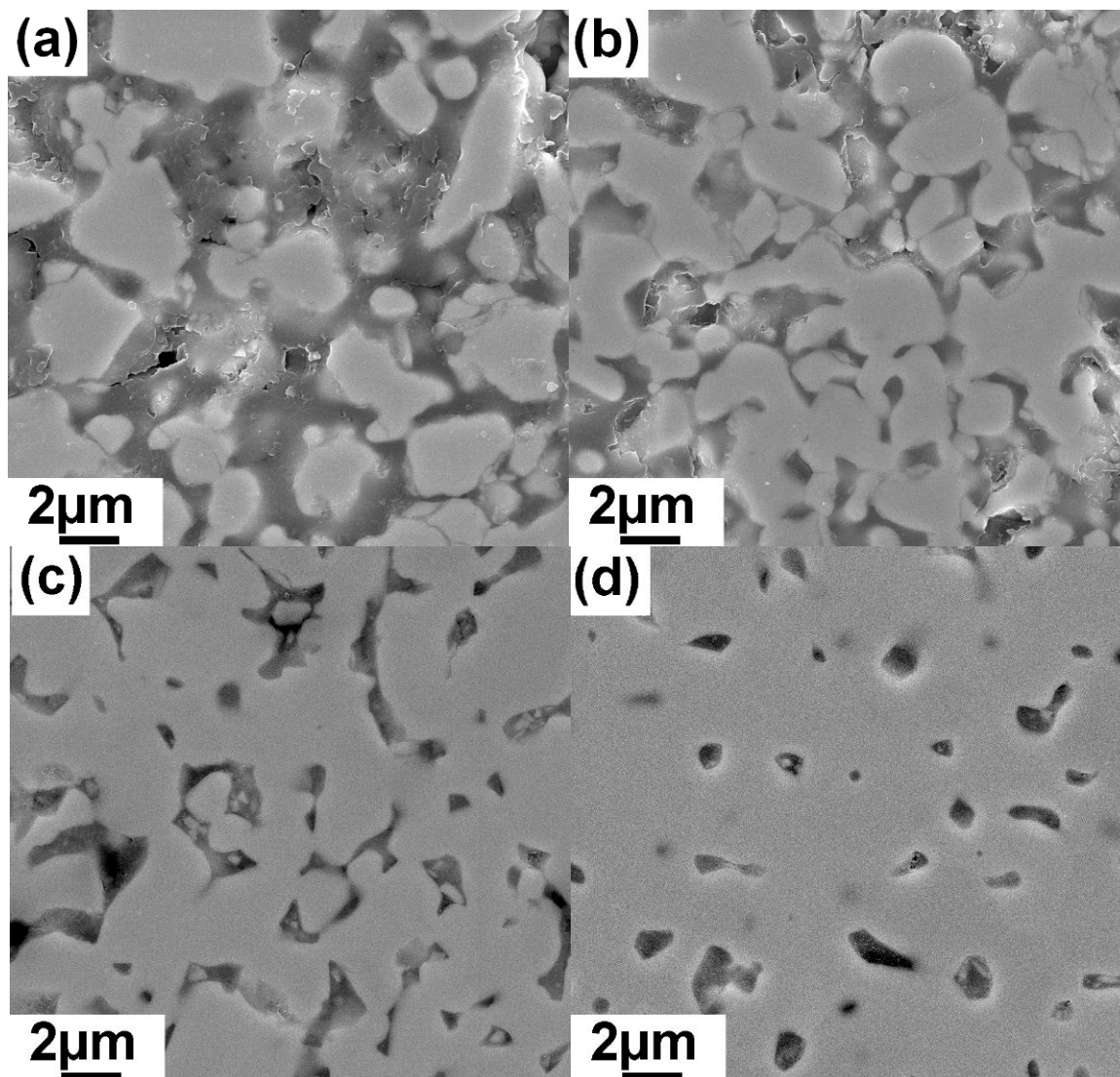


Fig 6.4. SEM BSE of densified ZrB_2 at 100°C/min, 40MPa applied pressure at (a) 1600°C (b) 1700°C (c) 1800°C (d) 1900°C for 5 min.

These results are expected; it was well known that SPS provides the advantage of skipping the early and intermediate stages of diffusion. But once high density was reached, the phenomena associated with SPS – such as accelerated diffusion – becomes a problem. Closed pore volume at 1900°C and possible surface reaction sintering ensured the situation where typical high densities have a cost in grain growth. This was not only likely at the holding temperature, but also the purported increased kinetics from electric current through the sample

probably resulted in accelerated grain boundary movement (covered later). But to continue the densification trajectory, the sample was heated to 2000°C. The microstructure is shown in Fig 6.5, showing early inhomogeneous grain sizes (3µm to 30µm), trapped intragranular pores from pore-boundary breakaway and the intergranular pores with curved shape that indicate a pore drag. For example, grain A in Fig 6.5 was no longer growing uniformly, consuming smaller grains in a classical Ostwald ripening.

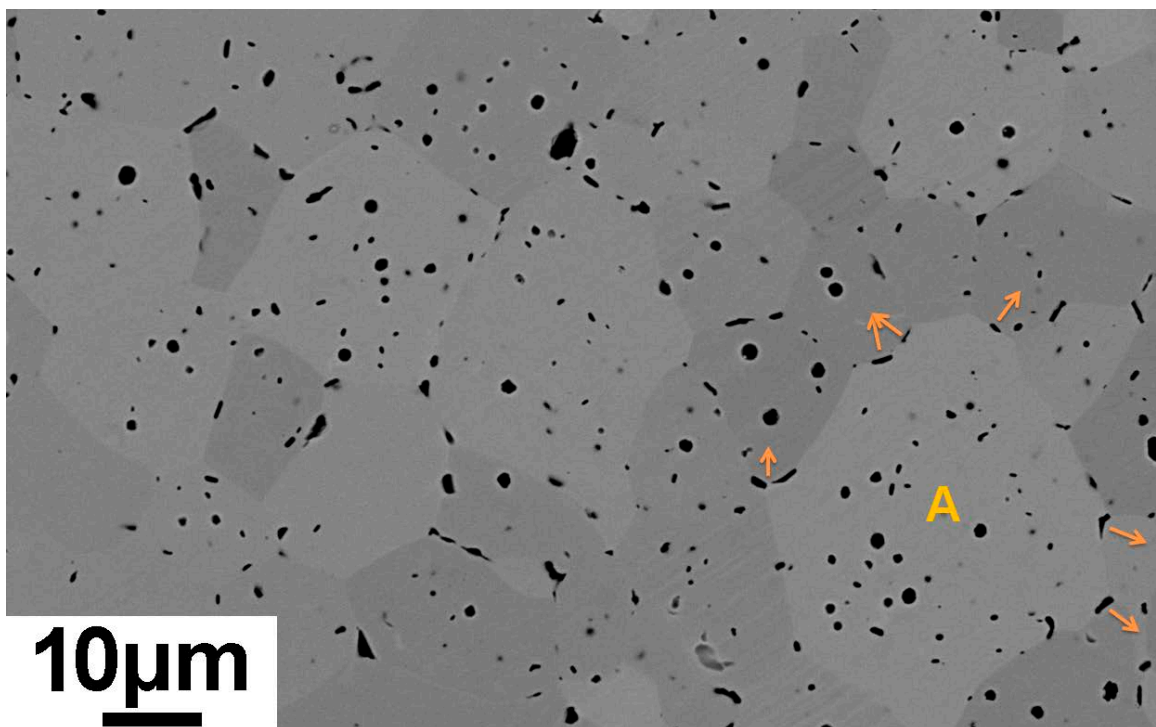


Fig 6.5. BSE microstructure of ZrB_2 at 2000°C/5 minutes at 40MPa

The arrows around grain A were a guide to the direction of grain boundary migration. This was determined by the leading surface of the pore adjacent to the arrow becoming less curved than the trailing end, which was caused by the force of the grain boundary of A moving under its own curvature. This last stage of grain growth was well documented when sintering ZrB_2 without additives. There are two causes of coarsening discussed here, although conclusions are difficult to draw from the limited data. The first cause of coarsening was reportedly surface diffusion through oxygen contamination - grain growth caused by a high ratio of surface diffusivity versus grain boundary diffusion.²⁹⁸⁻²⁹⁹ Work by Baik et al assumed that because densification was controlled by grain boundary diffusion,

the grain-size density relationship with increasing oxygen contamination follows accelerated vapour phase transport kinetics in diboride materials.²⁹⁸⁻²⁹⁹ It was tested by doubling the oxygen impurity, that resulted in an order of magnitude larger grain size during the final pore removal process at ~95% relative density.²⁹⁸ Oxygen infers two oxide species; the early volatilization of bororia and the higher thermal stability of zirconia, both requiring carbon reduction to remove or nullify.^{169, 197, 297} This contamination contributed to a higher surface diffusion coefficient, since the activation energies are much lower. Thus the small grain size of Fig 6.4 is indicative that oxide contamination was not an issue to coarsening, because an oxide removal process did occur (Fig 6.3). Some negligible, unquantified oxide remained. The most definitive proof was by direct observation of the oxygen rich layer, cited in SEM work by Mishra et al on ZrB_2 at 1800°C/30min without C additions, indicating a layer of significant 500µm thickness.¹⁹⁷ This same microstructure could only be observed in Fig 6.6 from TEM of the surface of a pore in the microstructure sintered at 1900°C from sample in Fig 6.4(d).

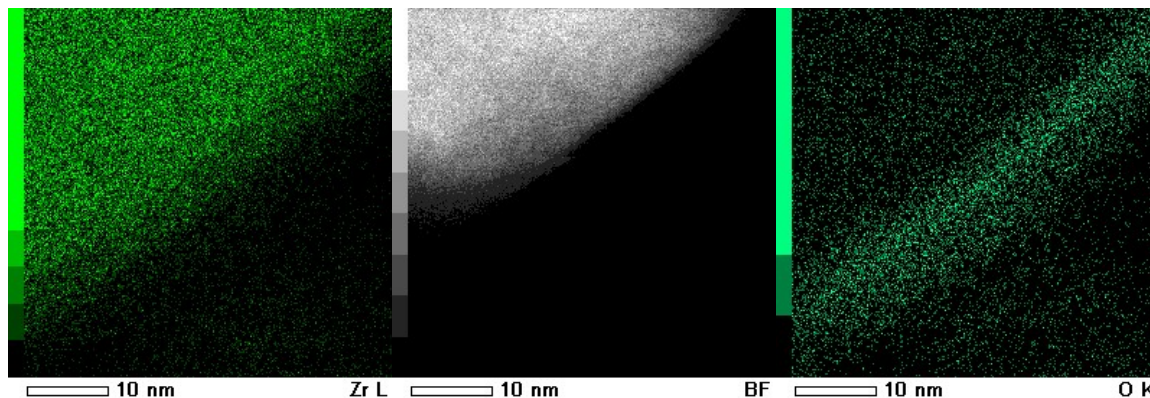


Fig 6.6. Oxides on sintered ZrB_2 at 1900°C indicating a residual 10nm oxide layer.

Because water and oxygen are unlikely contaminants in TEM vacuum, this demonstrated that an oxide surface is still present on some porous regions. No oxides were observed on the clean grain boundaries, which inferred that pore regions contain the residual oxide content. At this stage, the SPS sintering behaviour up to 1900°C can be described by removal of oxides, allow grain boundary contact (or spark plasma pressure), but migrating the oxides to the

pores, which then show inability to halt ZrB₂ boundary migration in Fig 6.5. The high aspect ratio of intergranular pores at the perimeter of grain A in Fig 6.5 did correlate with literature that reported mechanisms of accelerated vapour transport and surface diffusion mechanisms in ZrB₂ consistent with residual oxides.^{65, 300}

Yan et al identified in ceramics that grain size becomes much larger as the density increases, following the pattern of grain growth being controlled by surface diffusion, while grain boundary diffusion dictates density.^{298, 301-302} Coarsening still occurred despite significant oxide removal. Because the oxide contribution to coarsening was small, this raises another cause of coarsening as the SPS process itself, which is discussed in a later section.

The density-grain size relationship still follows the classical Avrami curve to maximum density as grain size increased rapidly. Grains were 3µm at 1900°C/93% density in Fig 6.4(d), but were 10µm to 20µm at 2000°C/96% density in Fig 6.5. This rapid consolidation to 90% density by SPS suggested that it can actually separate densification and non-densifying mechanisms by fast heating rate. However, the final stage of sintering appears to be similar in HP.^{65, 300} The densities achievable were comparable to the lower heating rates of HP, except the final grain size was an order of magnitude less, from 50µm to 5µm.²⁹⁸⁻²⁹⁹ The same issue occurred at about 93-95% relative density – grain growth at the cost of density and removal of pores. In summary, the smaller grain size does indicate that SPS had an advantage (for example, over hot pressing) in preventing coarsening by oxide removal, but is still able to coarsen a microstructure via another mechanism discussed later.

Unfortunately the oxide removal cannot be attributed directly to the spark plasma effect, because the sample was wrapped in graphite foil, and coincidentally demonstrated distinct chamber pressure changes associated with chemical reaction. This indicated that a process occurred to produce gas, shown in Fig 6.7. This highlighted the temperatures and an approximate yield of gas evolution, and it likely involved a thermodynamic change in state because it was specific to temperatures 1300°C and 1600°C. With only ZrB₂, ZrO₂ and C in the system, this left few possibilities. But the free energy change for ZrC formation at 1300°C

makes it very likely that a reduction of surface film (nanocrystalline oxides) was more likely to explain a burst of gas such as CO .^{7, 60, 131, 303} The rise in chamber pressure at 1600°C was probably more indicative of carbothermal reduction than the process that occurred at 1300°C.

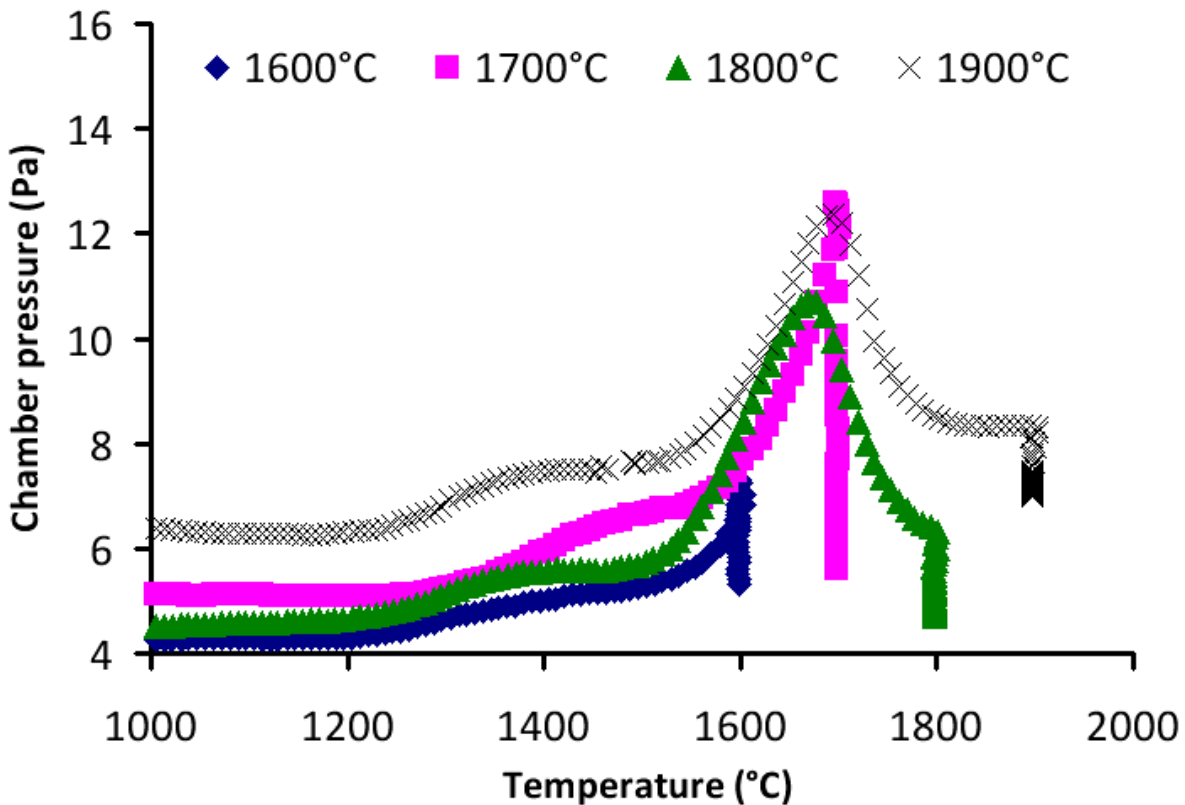


Fig 6.7. Change in chamber pressure during densification of ZrB_2 at 40MPa at 100°C/min.

One supporting reason for a chemical reaction was the enhancement of the densification rate. SPS volatilization of the surface boron was a plausible mechanism, but could not cause the rise in chamber pressure since it would have damaged the Pirani gauge.¹⁷⁸ It was also dismissed because the oxide purging simply sputtered on the adjacent spacers and would not contribute to the sintering trajectory. Fig 6.8 showed the change in displacement or densification rate during the sintering of ZrB_2 . Because the 10mm collar was effectively a cylinder of fixed circumference, displacement represents the shrinkage inherent in densification. There are two concepts that must be distinguished here; reaction rate and densification rate. The trajectories of their rates can be very different and must be carefully interpreted. The chamber pressure in Fig 6.7 is dynamic, representing the rotary vacuum pump removal of the gas. This is a substantial

delay, which likely denoted that the peak chamber pressure at 1700°C indicated that the peak of the reaction occurred at ~1600°C. In the minute to remove the gas, gas evolution from the sample may have ceased. However, the densification assistance from the chemical reaction may occur more or less instantaneously. The rise in chamber pressure at 1650°C in Fig 6.7 was associated with a small rise in densification rate at 1600°C. Holding between 1600°C and 1700°C showed that the reaction can be used to increase densification. Densification also occurred at 1800°C-1900°C, which is not associated with any gas producing reaction. The microstructures in Fig 6.4 suggest this is the actual surface activation of densification mechanisms intrinsic to ZrB₂. However, the earlier reaction sintering process cannot be neglected and is a key feature of sintering contributions discussed later in composites.

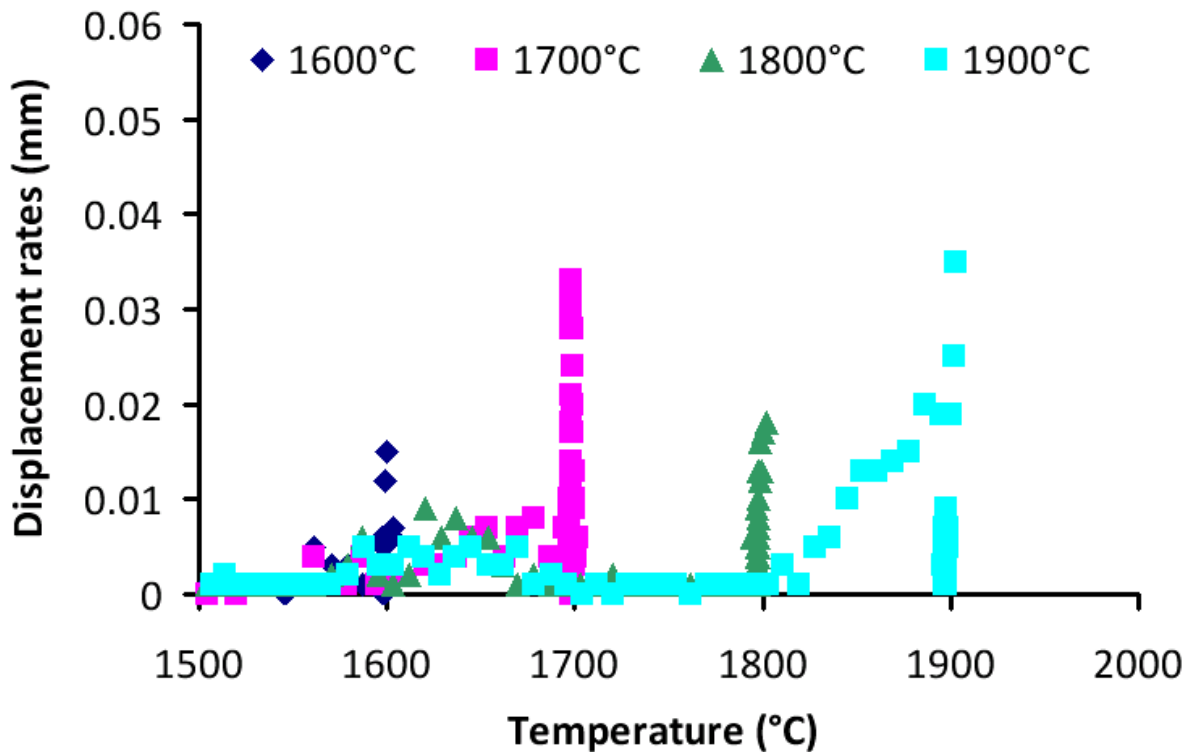


Fig 6.8. Densification rates of 10mm ZrB₂ samples, showing increased rates just below 1700°C and 1900°C.

Holding at 1700°C resulted in the trajectories of both the reaction (by centripetal lattice diffusion) and grain boundary diffusion to occur together since densification rate increased.^{48-49, 130} This correlated with the large number of broader necks at

the 1700°C microstructure in Fig 6.4(b) that suggested this temperature involved significant coalescence of ZrB₂ grains by lattice or grain boundary mechanisms.

Thus there were two stages of densification of ZrB₂ in SPS: first was the limited reaction sintering of surface oxides that resulted in a sudden increase in the densification trajectory. The second stage was the activation of the ZrB₂ grain boundary coalescence and diffusion once contact between powders were achieved at ~1800°C. This was the mechanism that provided the majority of the densification, emphatically shown by the displacement rates of the 1900°C sample in Fig 6.8. These results indicated that the initial low temperature sintering rate was increased by carbothermal reduction. The fall in densification rate at 1900°C also indicated that the final stage was still limited by pore removal, which was in agreement with earlier analysis. This caused coarsening, which was covered in the subsequent section.

6.1.3 Effect of heating rate

The effect of heating rate was examined for the primary reason that scaling up of samples to 30mm in size was required for mechanical and oxidation testing. The current draw increased quickly from 3% to 19% of the SPS power system from the 10mm die to the 30mm die during blind heating at 100°C/min, resulting in different temperature distributions. However, a second reason was to understand the grain boundary diffusion, particularly at the 1900°C isotherm. This was likely the other reason that grain growth occurred, since most oxides were removed. A third reason was to investigate if a fast heating rate was necessary, as it would make comparisons to any pressureless sintering difficult.

Fig 6.9 demonstrates the displacement rates when ZrB₂ is heated under 40MPa pressure to 1900°C at different heating rates. The reactive sintering can be observed at all heating rates ~ 1650°C. It can be observed that at lower heating rates, the increased densification rate corresponded to the temperatures at 1650°C and 1800°C respectively. Higher heating rates caused higher displacement changes at 1650°C. This indicates that it was caused by kinetics, and suggested that it affected the carbothermal reduction, which in turn affected

densification rate. Note that an early boost in densification rate resulted in a lower densification rate later because the driving force had been reduced.

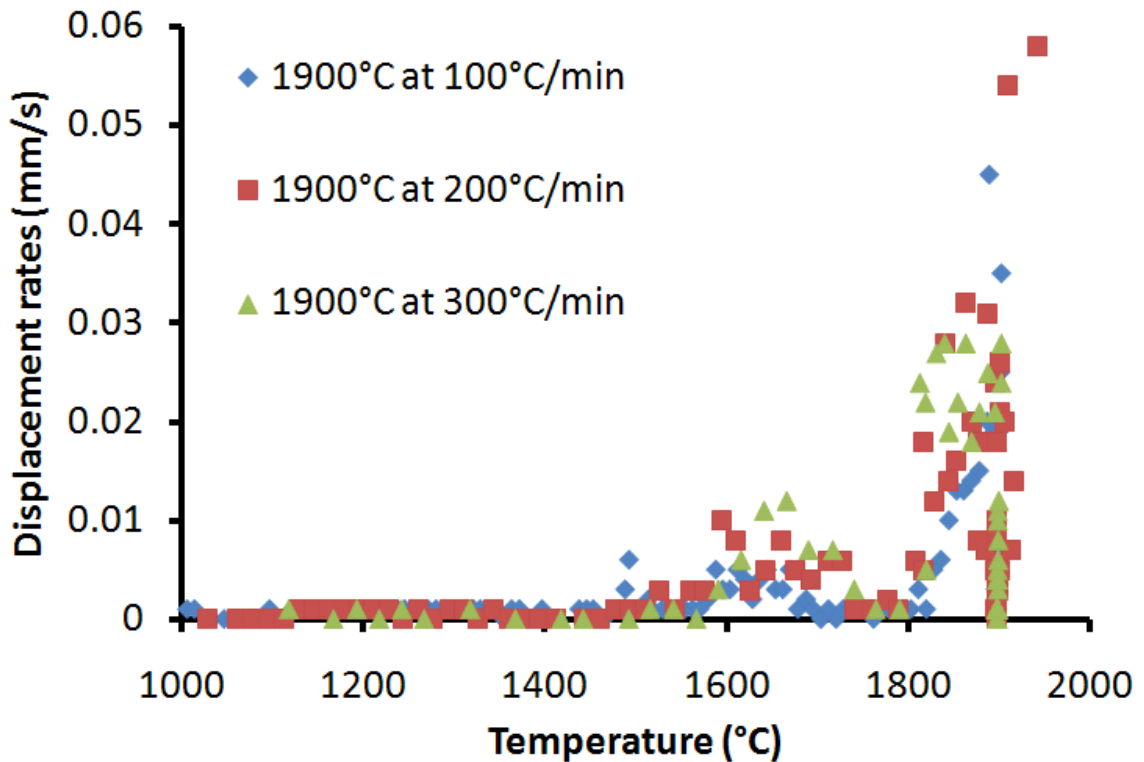


Fig 6.9. Densification rate at 100°C-300°C/min up to 1900°C

The displacement rate at 300°C/min at 1900°C was the lowest likely because more densification had occurred earlier. At 100°C/min, the driving force for sintering at 1900°C is higher because the second derivative of the displacement rate was higher for the 100°C/min sample. This implied the possibility that the densification at 1600°C affected the densification at 1900°C and that the two contributions could be interchangeable. This was explored later in the composite ZrB_2 -ZrC. The displacement curves are shown in Fig 6.10. No differences were observed in the displacement during temperature change, although the sample heated at 100°C/min did appear to densify more slowly. However, this could be because the heating rate was limited to deceleration at 1 minute integers, at half multiples of the previous step. The 300°C/min sample was slowed to 200°C-100°C/min increments, for example at 1600°C the heating rate was slowed to 200°C/min to 1800°C, then stepped to 1900°C for 1min before holding for 5 minutes. This prevented overshooting. The 200°C/min run was slowed at 130°C-

70°C/min in the final two minutes. The 100°C slowed to rates comparable to HP, at 70°C-30°C/min approaching the 1900°C plateau.

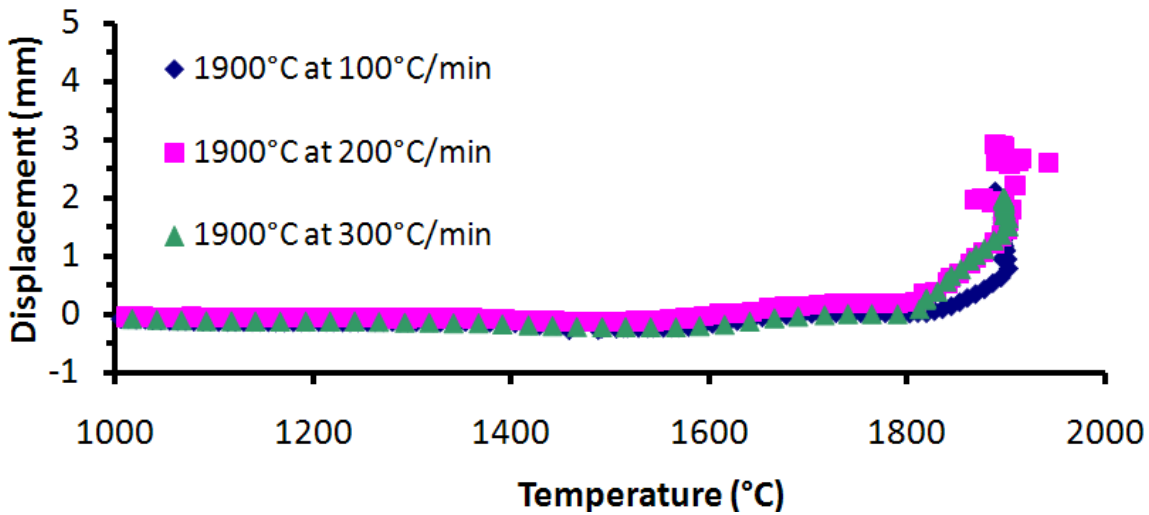


Fig 6.10. Displacement over the temperature programs up to 1900°C

This could have the effect of reducing grain boundary diffusion mechanisms since the other two are still heating at a faster rate. The rise in chamber pressure in Fig 6.11 shows that there was a rise in gaseous products at 1600°C and 1800°C.

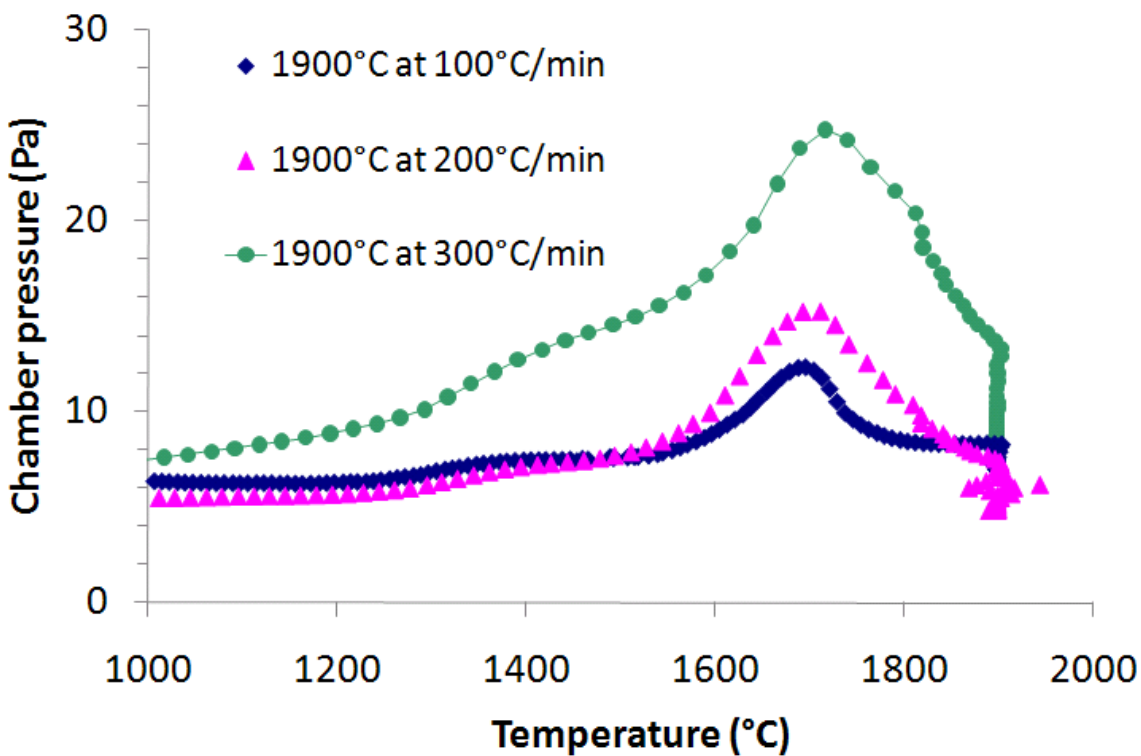


Fig 6.11. Chamber pressures over the temperature programs up to 1900°C

This supported earlier analysis of carbothermal reduction producing gas from the sample. As heating rate increased, more gas was observed in the sample from a lower temperature. This indicates that a superior heating rate resulted in a greater surface reaction, and may have corresponded to a higher densification due to the faster purging of the oxide on the powder and activation of surfaces. It was known that the driving force reduces over time as solid-vapour interfaces were replaced with solid-solid. A high heating rate resulted in a higher kinetic energy for the carbothermal reduction and thus more energy for diffusion mechanisms. This likely purged the powder surfaces better, reducing the problematic non-densifying surface diffusion and evaporation-condensation mechanism. The effect of heating rate on the microstructure was profound, because the relative density achievable was 96% to 99% and finally 99.7% from 100°C/min, 200°C/min and 300°C/min respectively. But the grain size was different, shown in Fig 6.12.

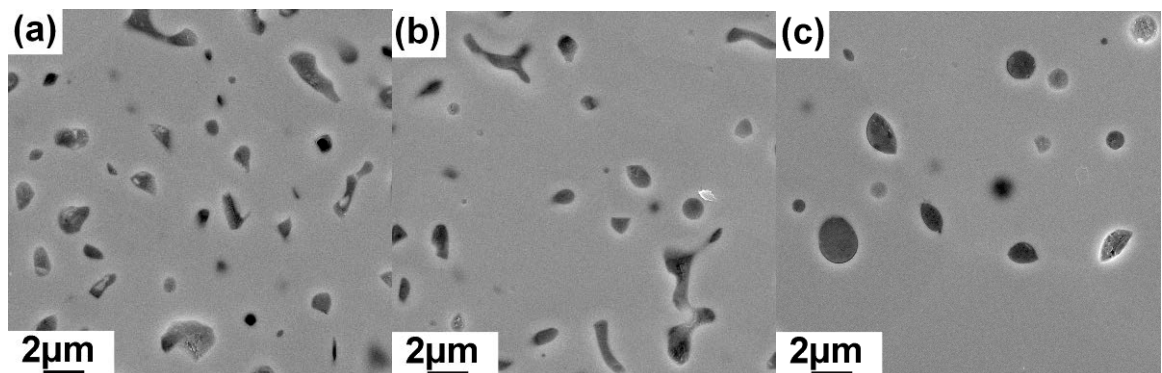


Fig 6.12. BSE microstructures at (a) 100, (b) 200 and (c) 300°C/min to 1900°C

It appeared that the effect of heating rate was to give a lead to the kinetics of grain boundary and lattice diffusion once contact was achieved between powder surfaces. This addressed an earlier question of what another cause of coarsening might be: the intrinsically high heating rate of SPS, which is increased by increasing current draw and thus more diffusion. The first cause of coarsening by oxide contamination can be dismissed even further, because Fig 6.11 implied more carbothermal reduction occurs as the heating rate is increased. Thus the SPS operation was responsible for coarsening. Higher heating rates were not ideal. The first underlying fact to remember was that reliance on applied pressure and heating rate made it less likely to be pressurelessly sintered. In larger

samples, increasing carbon insulation was needed and higher heating rates become prohibitively difficult due to the current density required in larger dies. This can be a variable when upscaling because the same temperature can require different amounts of current. Upscaling is simpler in pressureless sintering. Thirdly, the grain growth was difficult to control and yielded decreasing benefits in density. At high heating rates, densification and grain growth were less distinguishable and appear to occur together. Fig 6.12 showed last stage of densification with a significant number of smaller pores that exert drag on the 1900°C samples, shown by the convex bias against the grain boundary migration direction, particularly at 300°C/min in Fig 6.12(c). However, the heating rate encouraged boundary mobility and diffusion. These pores appeared to reach an equilibrium micron size and the microstructure at 300°C/min shows that grain boundary retardation was not occurring because these were already intragranular. The grain size was also larger since only 3 grains are inferred in the same magnification in Fig 6.12(c) whereas more grains are visible at 100°C/min and 200°C/min in Fig 6.12(a) and (b). The presence of the grain boundary can be inferred by the leading edge of the pore from the trailing edge, particularly in Fig 3(c). The high heating rate suggested that all mass transport mechanisms were accelerated; pores quickly reform in low-aspect ratio shapes, and grain boundary migration is rapid. This investigation resulted in a decision to restrict the heating rate to 100°C/min to allow the nc-ZrC in the composite a better chance to exert sufficient drag on the ZrB₂ migration.

6.1.4 Effects of Die Size

The effect of die size was investigated to gain an empirical relationship between different die sizes. Fig 6.13 showed the densities of 10mm samples compared to 30mm samples at the same recorded pyrometer temperature. For a 10mm die, the die wall is 10mm thick, which separates the ceramic sample and the die surface detected by the pyrometer. For a 30mm die, the die wall thickness becomes 40mm. Thus the surface temperature detected by the pyrometer becomes less accurate for larger samples, as the real temperature in the sample is likely higher. Relative density was chosen as the parameter of choice since it was a bulk property and a more predictable. Samples were heated at 100°C/min to their respective 5-min densification isotherms in both 10mm and 30mm dies.

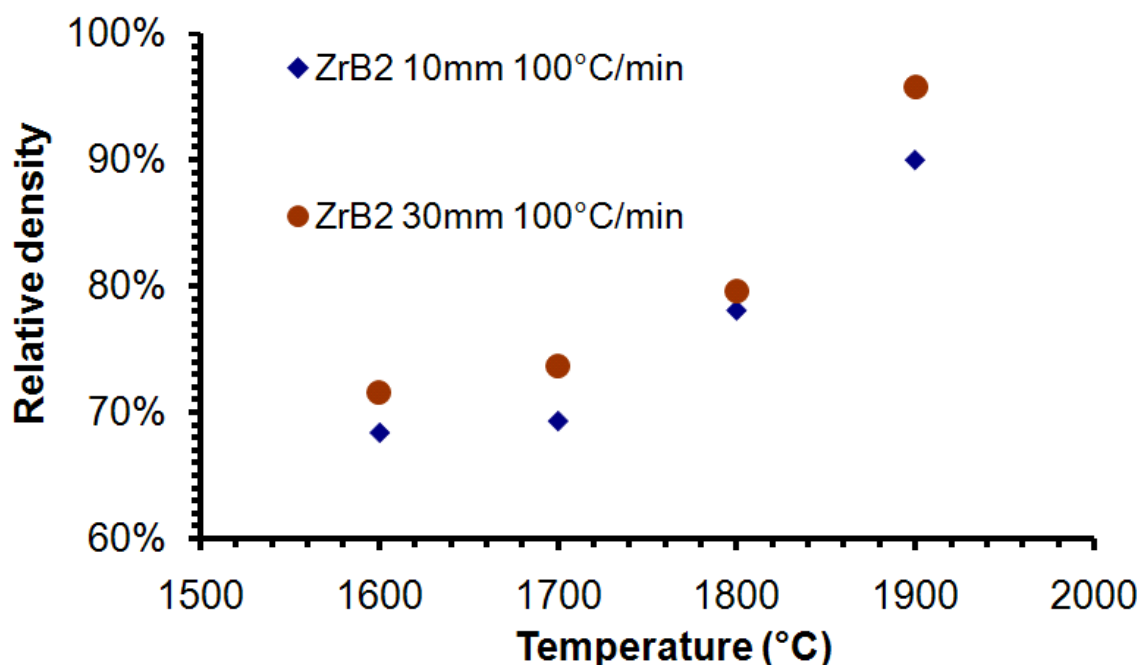


Fig 6.13. Comparison of density from 10mm and 30mm die ZrB₂ samples.

The increased density of 30mm dies indicated more sintering, associated with more diffusion and thus higher temperature. The difference between the microstructures of surface and core did not occur in the 30mm samples and were more homogenous.

6.1.5 Summary for SPS sintering of ZrB₂

These experiments inferred that significant reaction sintering occurred due to the graphite foil and highly reducing conditions in the SPS. This was because of the evidence of a reaction from 1700°C where the densification trajectory increases at 1650°C. The sintering mechanism suggested that the applied pressure, high heating rate and reactive sintering resulted in early particle contact that minimized surface diffusion derived neck growth. The final stage of pore removal relied on oxide removal and control of the grain boundary diffusion. Consultation with literature suggested that both HP and SPS can coarsen by different mechanisms - SPS was excellent at oxide removal but gives significant energy to grain boundary migration microstructure, and vice versa to HP. Higher heating rates demonstrated that higher densities were achievable, but the grain boundary diffusion was rapid and overlapped with densification. The heating rates were restricted to 100°C/min to control microstructure, with minimum allowable

pressure for electrode contact at 40MPa. This was in anticipation of an investigation into pressureless sintering. These parameters were also favourable given later damage to the SPS that restricted processing conditions such as high heating rate or applied pressures. Densities between 30mm and 10mm samples allowed for upsizing of samples and this was required to build larger specimens for mechanical and aerothermal testing where density was controlled.

6.2 ZrB₂ powder-gel composite

The purpose of this section was to produce a composite of ZrB₂ using 5 mol% ZrC as the nanophase addition. This would involve integrating the ZrB₂ powder into the sol-gel procedure to ensure a surface coating of a Zr-O-C gel precursor. Referred to as a powder-gel, the first group of experiments investigated the sol-gel coating on ZrB₂ powder without sufficient PFA decomposition, and this gel was noted as Z5O (O = oxide) because below a particular threshold of carbon, only nano-oxides were found. The next logical step was to begin carbon additions in Z5C (C = carbide) series, first in the reduction of the oxide film on ZrB₂ surface, then for reduction of the total oxide (nanoparticle + surface film) composition. The morphology of the surface attachment of nanoparticles was briefly examined, followed by densification study of the powder-gel compact.

6.2.1 Carbon depleted powder-gel

The Z5O gel samples were unable to convert their gel component to ZrC due to carbon depletion. All Z5O gel samples can be considered as any ratio less than $<12\text{C}/\text{Zr}$ in gel. This was the approximate threshold where ZrC was not detectable by XRD in the powder-gel. This was caused by insufficient PFA or acid catalysis, and significant monomer loss described elsewhere. Carbon was required to reduce the ZrB₂ surface oxide film. The gel nanoparticle oxides also required carbon. The unique microstructure of oxide coated ZrB₂ can be observed in these samples shown by the TEM images in Fig 6.14(a)-(c). These Z5O samples are just after 550°C surfactant burnout and show exposed nanocrystals on the surface of ZrB₂ that are not obscured by carbon. This was likely caused by crystallization of zirconia. It shows the microstructure of the powder-gel as the carbon ratio is increased.

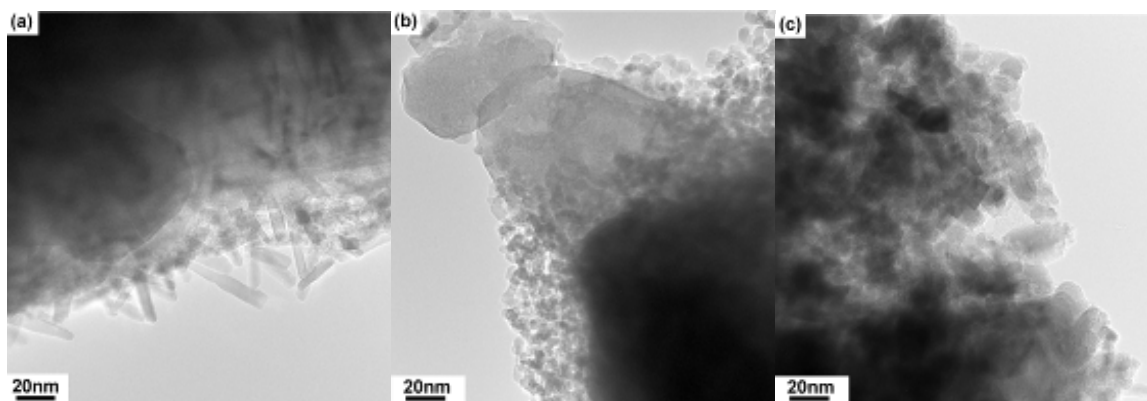


Fig 6.14. HR TEM images of 5 mol% Zr-O-C gel coating on ZrB_2 after 550°C treatment using (a) 4C/Zr gel (b) 6C/Zr gel (c) 10C/Zr gel

The deposited layer varies in thickness up to 100nm to the electron opaque region which was the ZrB_2 surface. Pertinent to remember was that the gel-based oxide at 550°C was a spherical-shaped tetragonal zirconia shown earlier in Fig 5.9 and later in Fig 6.19. Here in the powder-gel, at low levels of carbon, the crystals were unrestricted, could grow unrestrained and perhaps even heterogeneously from the oxide film on the ZrB_2 surface. Fig 6.15 shows the SEI surface of these oxide nanocrystals from the sol-gel coating after treatment at 1450°C. As PFA was added, the surface gel particles were surrounded by decomposed carbon, making crystal lattice fringes less visible and restricted in growth. It was difficult to observe the nanocrystals once the ratio reaches ~10C/Zr in Fig 6.14(c). This indicated that carbon played a role in preventing the oxides from coalescing or growing rapidly from the ZrB_2 surface. Additional growth occurred from 550°C to 1450°C depending on how much carbon was present, although this was not extensively characterized. Conservatively the crystals at 1450°C in Fig 6.15 were an order of magnitude larger than at 550°C in Fig 6.14(a). Only oxides were detected in XRD. These gel-derived oxides are distinct from the ZrB_2 oxide film shown later. While the initial surface adhesion may be due to gel shrinkage and oxidative etching of the ZrB_2 surface, some form of favoured or even epitaxial growth appears to occur from the gel-based oxide to the surface of ZrB_2 . This could mean that the oxide portion of the sol-gel nucleated heterogeneously from the oxide already present on the ZrB_2 surface. This indicated that the surface attachment did include gel-based-oxide to surface film oxide. Carbon could still envelope the oxide nanocrystals at 550°C.

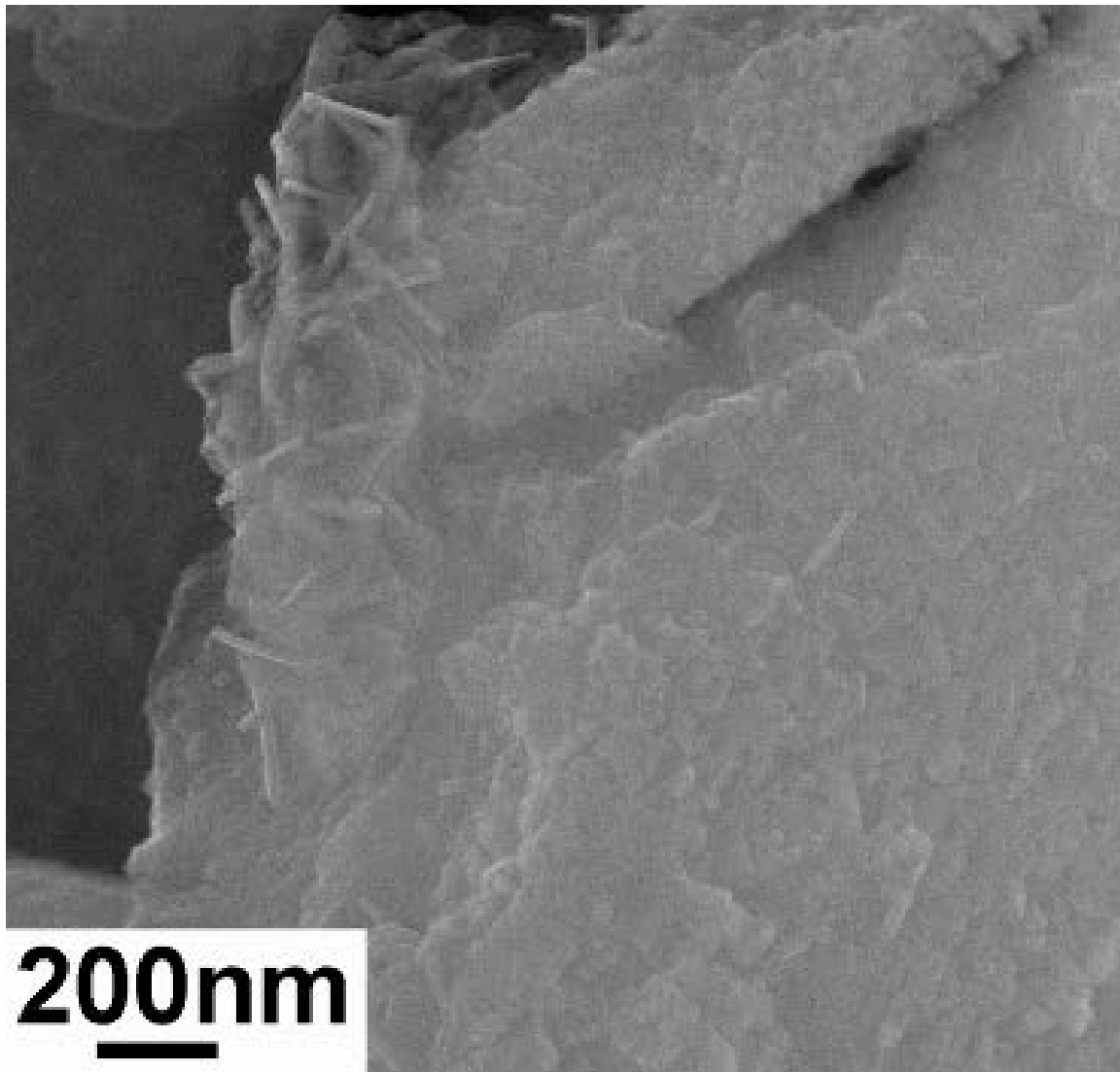


Fig 6.15. SEI of carbon depleted Z5O (4C/Zr) composed of ZrO_2 needle-like crystallites and other morphologies on the surface of ZrB_2 powders at 1450°C .

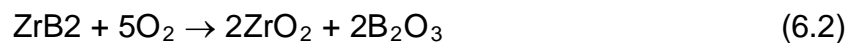
Knowing this, the first conclusion was that the Z5C samples could convert the oxide gel to ZrC if sufficient carbon was provided at 1450°C . Secondly, surface attachment was likely sufficient to prevent detachment of the nanoparticles. This coating process immediately illustrated the advantages of dispersion and coating by combining the nanoparticles synthesis with the powder preparation, rather than mixing the two powders conventionally.

6.2.2 Oxide film reduction

In a stoichiometric reaction, the gel required 3C/Zr for the carbothermal reduction of ZrO_2 , which followed the general equation:



However, furnace vacuum and oxygen partial pressure varied, and additional carbon was required to compensate for inefficiency in the reduction process. The same conditions affected the reduction of the oxide film on ZrB₂ as well. Therefore, the amount of oxide film on ZrB₂ was empirically determined. The oxidation of ZrB₂ was presumed to occur via the following decomposition³⁰⁴:



Therefore, there were two carbothermal reactions in the system – one to reduce the surface oxide films on ZrB₂ and one to convert the sol-gel oxides. To determine the approximate carbon requirements, a series of ZrB₂ powder-gels were designed as control samples, except the FA component was removed. Instead, carbon black was added to the sols in incremental quantities for each Z5O gel without going through the PFA-decomposition process. After treatments at 1450°C to determine how much carbon was required for ZrC formation, the XRD spectra can be shown in Fig 6.16. Additions of carbon black were commonly used to convert oxide films on ZrB₂ through conventional or HP sintering.^{169, 191} The gel coated ZrB₂ powders contained the surface oxide film from ZrB₂ and the oxide nanoparticle phase, both of which relied on the carbon black for reduction to carbide. It was a misconception to assume that PFA-based carbon would perform exactly the same as carbon black. However, these controls were designed to determine the minimum amount of carbon required to prevent oxide in the materials. If sufficient carbon was provided, this would logically result in only carbides and diborides after carbothermal reaction. Stoichiometrically this equated to the amount of carbon required to reduce all oxides in the system. The XRD results in Fig 6.16 denote 2 hour treatments at 1450°C in argon and shows that at a minimum of 6wt% carbon in the ZrB₂-gel system was required to suppress oxide formation. One aspect to note was the reported ZrC solubility of 4.5wt% into ZrB₂.³⁰⁵ While shifts in lattice parameter were noted, this solubility region did not appear in phase diagrams by Effenburg and Rogl et al.³⁸

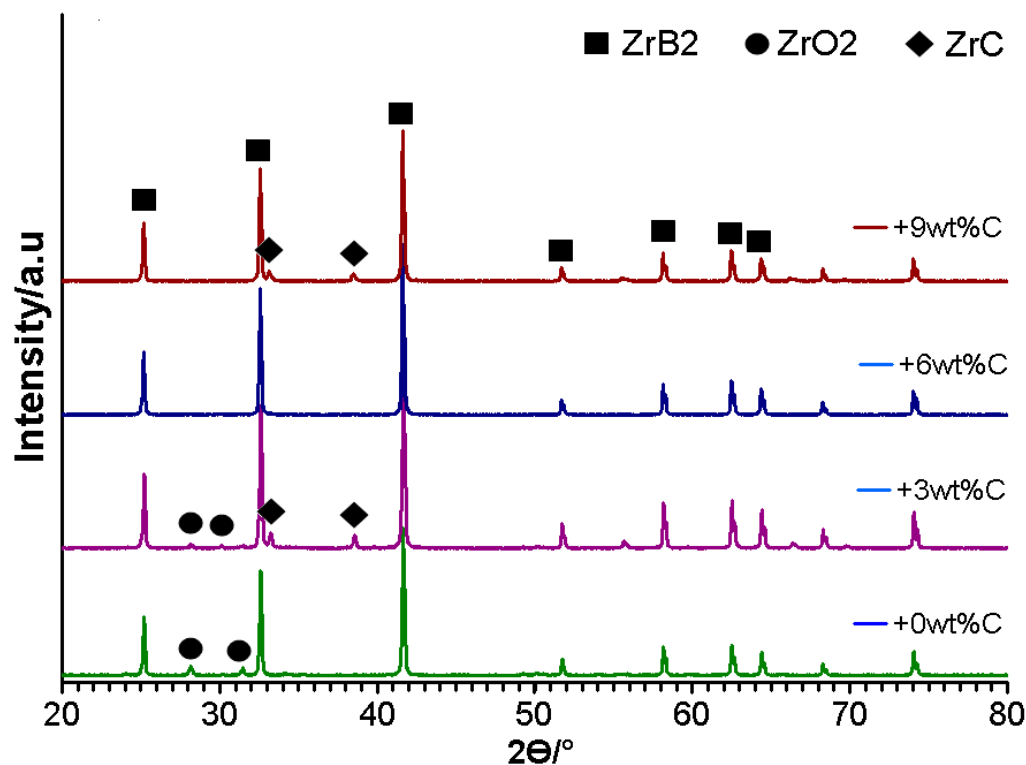


Fig 6.16. XRD of ZrB_2 -gel samples with increasing additions of carbon. The samples were heated at 1450°C for 2 hours in argon.

In reference to the uncertainty, all of the samples in Fig 6.16 used a precautionary 10 mol% gel additions in 90% ZrB_2 . At 10 mol% of ZrC some XRD quantification was deemed possible. This experiment provided a good starting point to calculate how much carbon was needed from the PFA decomposition for the powder-gel samples containing 95 mol% ZrB_2 and 5 mol% ZrC.

6.2.3 Carbon stoichiometry

The key challenge in controlling the composition of this powder-gel was the carbothermal reduction conditions. Insufficient carbon would result in oxides in the composite and excessive carbon would hinder the materials densification. Therefore understanding and controlling the amount of carbon in the PFA decomposition is critical. The PFA decomposes to nanoporous carbon.²⁷⁷ The amount of carbon was dictated by the decomposition of PFA, which was controlled by the degree of crosslink of FA monomer. Presumably, less crosslinking results in smaller oligomers which can evaporate at 550°C . The variable that could control how much carbon decomposes was the amount of acid

catalyst. A calibration graph of TG results is shown in Fig 6.17. This shows gels that had fixed starting amount of FA and increasing amounts of acid catalyst. More acid catalyst resulted in greater crosslinking, and thus more decomposed carbon after 550°C. This shows the amount of carbon retained in gels after decomposition. Two series are shown here; one with 5FA:Zr and one with 4FA:Zr – this is the initial FA/Zr molar ratio at the sol-gel stage. FA contains 5 carbon atoms per molecule. Thus the initial ratio of carbon is theoretically 20C for 4FA or 25C for 5FA. These were a hypothetical maximum (the other carbon sources such as solvent and surfactant are neglected) - in reality, complete crosslinking was not achievable and full decomposition to carbon was not possible under the current experimental conditions of a flowing nitrogen furnace.

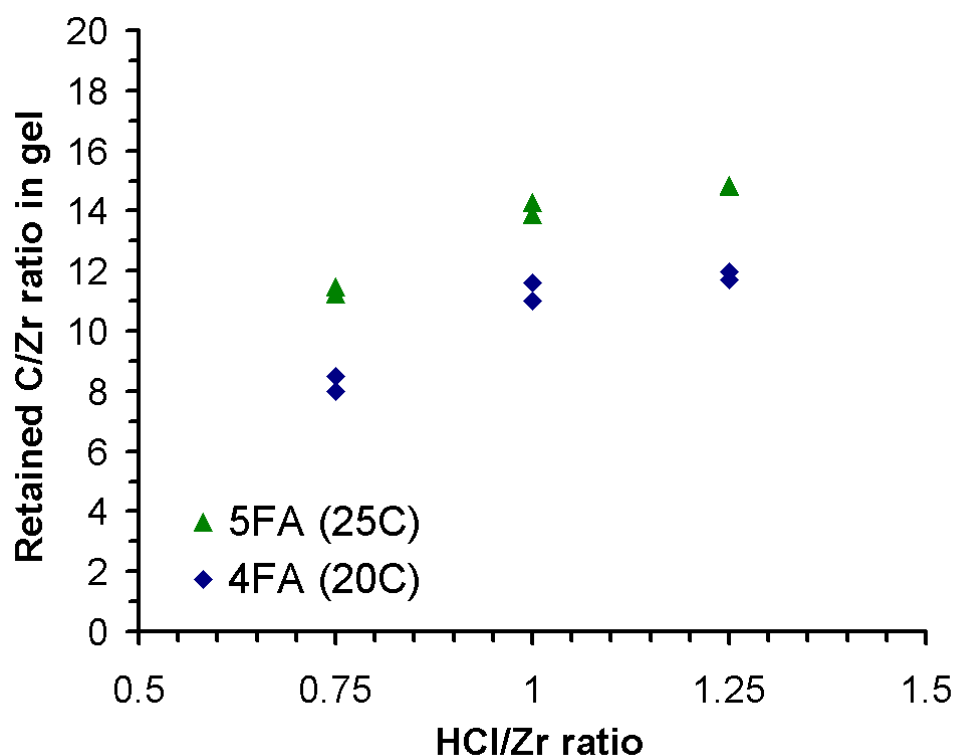


Fig 6.17. Retained carbon in gel compositions after 550°C with different acid catalyst additions.

The graph demonstrated that the degree of crosslinking could be varied by the acid catalyst. As more catalyst was added, more crosslinking could occur and more PFA was decomposed than evaporated. To further increase the carbon ratio, either more catalyst was added, or a new series with more initial FA was added. Since the curve eventually plateaus to a maximum achievable carbon

retention, it was more predictable to select a ratio at 1/1 HCl/Zr or higher as a standard error of 2wt% C is displayed in the data. The two major compositions discussed here were 1/5/1 and 1/4/1.25 Zr/FA/HCl, corresponding to gel compositions of 12C/Zr and 14C/Zr respectively. Both compositions selected for the ZrB₂ powder-gel were designed for 5 mol% gel (or 4.6wt % ZrC). These were referred to by their powder gel-zirconia carbon ratios Z5C_x (x =carbon ratio) in Table 6.1. The residual carbon for ZrB₂ was calculated by subtracting the carbon required for carbothermal reduction of the gel oxide nanoparticles. For example, 12/1 C/Zr ratio corresponds to 53.9 wt% C to ZrO₂ in the gel. Of this, 15.7wt% was consumed by the gel nanoparticles to form ZrC. The remaining 38.2% C was used by the ZrB₂ surface film. But this was 95% of the total mass, so the ratio to ZrB₂ is actually 4.76 wt% C to ZrB₂. This was slightly higher than reported surface film reductions in literature, but can be attributed to higher oxygen content in the furnace and lower reaction temperatures.^{197, 297}

Table 6.1: The division of allotted carbon between the gel and ZrB₂ powder. This is based on the planned 4.6wt% ZrC and 95.4wt% ZrB₂.

Sample	C/Zr (gel)	C/ZrO ₂ wt%	C wt% for gel	Residual	C wt% to ZrB ₂
Z5C12	12/1	53.9	15.7	38.2	4.76
Z5C14	14/1	58.2	14.3	43.9	5.88

The carbon calibration was tricky with PFA. Z5C12 resulted in 1 wt% unconverted oxide indicating insufficient carbon, whereas Z5C14 likely overshot yielding ZrC some residual carbon. In both cases, the assumed requirement of 6 wt% C to ZrB₂ alluded to by the series of calibrations in Fig 6.16 was not necessary. Less than 6 wt% carbon was required. This was probably because the total oxide content was lower, since those calibrations used 10 mol% gel. In the 5 mol% gels, less carbon was required to convert the oxides. The PFA coating may also be more efficient in reaction with the oxide than powder mixing of carbon black, thus less carbon was needed. Slow XRD scan speeds were required to detect the residual oxide phase. The results of Rietveld compositional analysis were displayed in Table 6.2. While this technique could not be used to quantify the

non-crystalline phases such as amorphous carbon, it was used to determine the progress of the conversion of ZrC. Three powder compositions were noted: Z5C12, Z5C14 and Z5C16. Z5C16 was provided to confirm the consistency of ZrC solubility in ZrB₂ and will not be discussed in detail. Table 6.2 reveals that from Z5C12 to Z5C16, despite increasing the amount of carbon and converting more zirconia, the amount of ZrC in the sintered composite never reaches the designed figure of 4.6wt%. The formation of ZrC can react with boron oxide to form ZrB₂ in this system, which may also be responsible for a lower content of ZrC than the designed value.¹⁹¹ A decrease in the a-axis and increase in the c-axis of composites was observed compared with a sintered control ZrB₂ specimen with values of $a = 3.1692 \text{ \AA}$ and $c = 3.5302 \text{ \AA}$. Lattice parameters for composites were $a = 3.1688 \text{ \AA}$ (Z5C12), 3.1678 \AA (Z5C14) and 3.1680 \AA (Z5C16). The lattice parameters for the c-axis were 3.5303 \AA (Z5C12), 3.5310 \AA (Z5C14/16). This may indicate solubility of ZrC/B₄C in ZrB₂ as previously reported.³⁸ The uncertainties in lattice parameters were $\pm 0.0001 \text{ \AA}$.

Table 6.2: XRD phase analyses for the three compositions of 5 mol% gel and 95 mol% ZrB₂ after 1450°C/2h (powder) and after SPS densification at 1800°C. A Z5C16 sample is also included for reference.

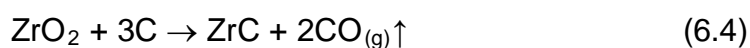
Powder-gel	ZrC (wt%)	ZrB ₂ (wt%)	ZrO ₂ (wt%)	B ₂ O ₃ (wt%)	B ₄ C (wt%)
Designed Composition	4.6	95.4	-	-	-
Z5C 12 powder	3.5	95.5	0.7	0.3	Trace
Z5C 12 (SPS-1800°C)	3.7	95.1	1.2	-	-
Z5C 14 powder	3.6	95.8	0.6	-	-
Z5C 14 (SPS-1800°C)	3.2	96.8	-	-	-
Z5C 16 powder	4.8	95.2	-	-	-
Z5C 16 (SPS-1800°C)	3.8	96.2	-	-	-

The lattice parameter for ZrC in the modified powder was 4.6706 \AA for Z5C12 and 4.6734 \AA for Z5C14 and 4.6769 \AA for Z5C16. Recall that ZrC is non-stoichiometric with a varying amount of carbon in the lattice. Despite significant quantities of

carbon, ZrC had substantial dissolved oxygen in the lattice, which meant full substitution of oxygen for carbon was never reached. This is despite sufficient carbon to reduce both ZrB₂ surface oxide films and the sol-gel oxide. This was probably due to oxygen partial pressure in the furnace. Oxide film on the nanoparticle surfaces noted earlier also indicated post-reaction oxidation. The lattice parameter of ZrC was observed to shift slightly during sintering, decreasing to 4.6685Å for Z5C12 and increasing for Z5C14 to 4.6743Å and increasing to 4.6769Å for Z5C16. The lattice parameter for oxygen free ZrC is 4.698Å.²⁹⁰ Z5C12 suggested carbon depletion from ZrC since the lattice parameter is shrinking, but also suggests that Z5C14 and Z5C16 contained residual carbon, since oxygen removal from ZrC continued during sintering.¹²⁹ It would suggest that more carbon might be beneficial in achieving ZrC_{0.99}. Nevertheless, a higher composition of carbon via PFA may completely remove dissolved oxygen in ZrC and convert ZrO₂, but would also result in residual carbon that could make densification difficult, as was found with Z5C14 and Z5C16. Leaving the incomplete formation of ZrC as an oxycarbide was actually beneficial in promoting reactive sintering during later SPS operations.

6.2.4 Empirical calculations

The amount of oxide film on ZrB₂ powder was determined by the above studies. The carbothermal reduction equations (6.3) and (6.4) can be used as a guide:⁵²



Because an additional ~6 wt% C is required per 100g ZrB₂, this indicates that the process produces a maximum ~7.0 wt% B₂O₃ and ~6.2 wt% ZrO₂. However, this is likely an overestimate because B₂O₃ can be removed by other means between 1450°C and 1800°C, such as volatilization to gas during sintering.

There are some limitations that were discovered from this method of controlling the amount of carbon. For comparison, Zhu et al consistently densified monolithic ZrB₂ to 99% density with only 1.7 wt% C at temperatures starting from 1900°C.¹⁶⁹ The present sol-gel coating process clearly causes significant oxide formation on

ZrB₂, which explains the high requirement of carbon. However, much of these variables depend on oxygen content, which was significantly related to processing. Mixing of solutions, treatment at 550°C without vacuum or poor vacuum conditions at 1450°C could all increase the amount of surface oxide film on ZrB₂. It should be noted that duplication of the PFA decomposition experiments resulted in a standard error of about 2 wt% C in the gel. This was likely caused by the experimental process itself through inconsistent evaporation of the FA monomers in air, during drying and in particular during the pyrolysis process at 550°C that decomposed PFA and the surfactant. The variation of carbon in the compositions may result in two different ZrB₂ composites, representing the two extremes – ZrC with residual ZrO₂ and porous ZrC microstructures with excess carbon. However, when only 5% gel is added to the ZrB₂ system, this error of residual carbon becomes negligible. Comparison to results by Mishra et al, who densified ZrB₂ through carbon additions, displayed a maximum density at between 3-5 wt% C.¹⁹⁷ Therefore, this current sol-gel route of using PFA as a variable carbon source needed to restrict the error to below 1 wt% C in order not to adversely affect final density. This would limit the gel to below a 15-20wt% addition, because at higher additions of gel, the reproducibility of the same amount of carbon may not be achievable. If a different carbon source with a more predictable and consistent decomposition was used in the sol-gel process, the control of carbon would be more easily achieved at higher gel additions. However, despite being a crude and empirical determination of carbon stoichiometry, it was clear that the technique employed in this work was adequate in suppressing the unwanted oxides in favour of ZrC and ZrB₂.

6.2.5 Surface morphology

Purchased ZrB₂ powders, 3-5 micron in size, contained substantial amounts of debris and impurities as shown in Fig 6.18(a) and (b). This could hinder identification of the sol-gel nanocrystals. The as-received powders were pre-fired under the same conditions as the sol-gel reduction at 1450°C to eliminate any artefacts for comparison in Fig 6.18(c) and (d). In Fig 6.16(c), steps are observed along with a slight surface charging, probably indicating surface oxide film. Fig 6.18(d) shows a remarkable amount of step growths that are also displayed

concentric around small round particles, which could be from impurities of Fe or Zr in the powder.

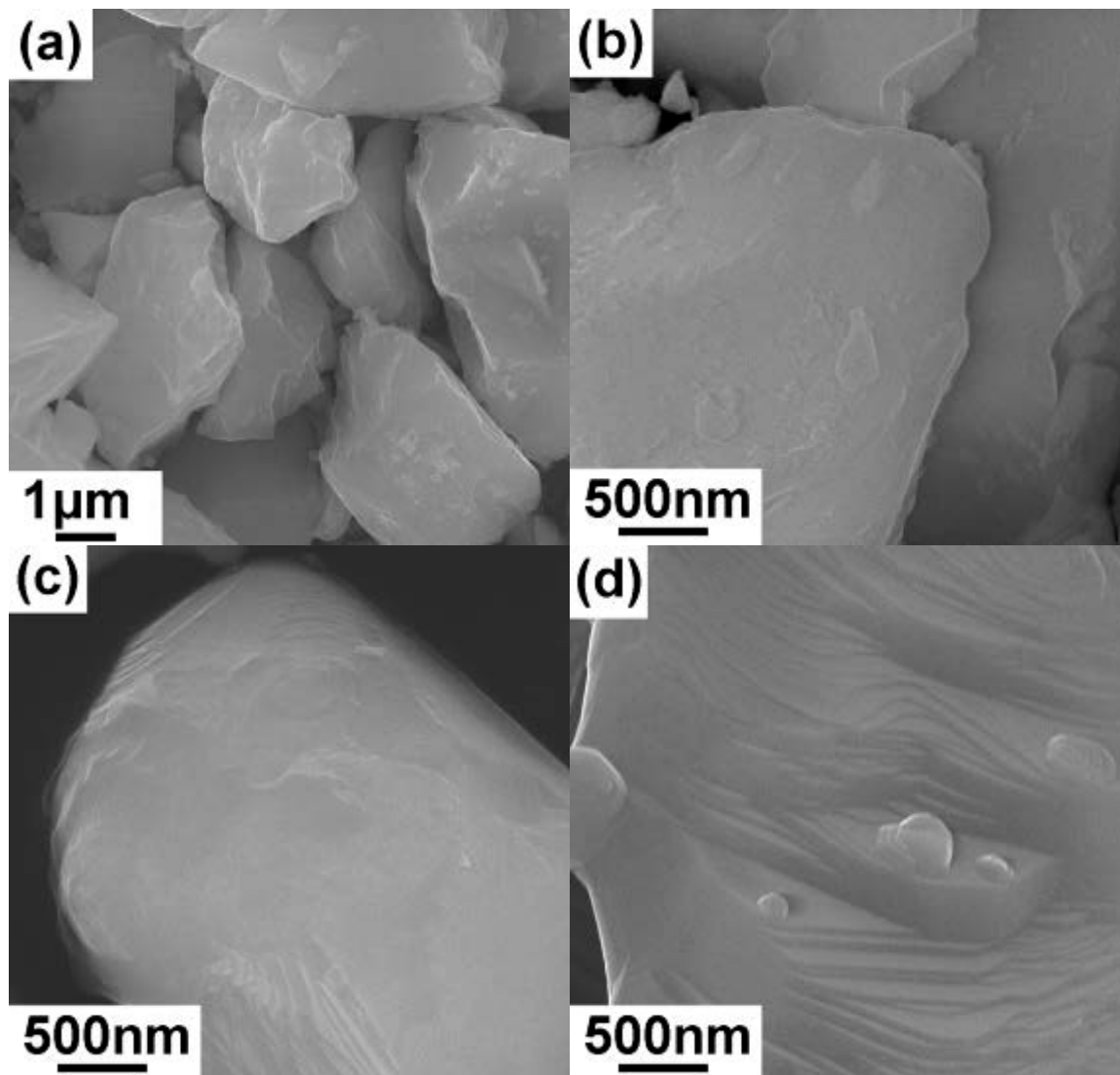


Fig 6.18. SEM images of ZrB_2 powder as purchased **(a)** and **(b)**, and after 1450°C treatment **(c)** and **(d)** for comparison.

TEM imaging best illustrated the microstructure of the stand-alone gel. The gel after 550°C treatment resulted in 4nm ZrO_2 particles distributed in a carbon matrix in Fig 6.19(a). The nanoparticles agglomerated and reacted at 1450°C with the adjacent carbon. The ZrC formed after firing at 1450°C were presented as nanocrystalline with a thin carbon coating in Fig 6.19(b). Note that the ZrC nanoparticles shows a particular crystallite shape, appearing to favour hexagon-appearing (111) likely due to close-packed trigonal symmetry yielding hexagons

for small crystal TEM bright field cross-sections. Fig 6.19(b) may have originally been 20 separate nanoparticles before reactive sintering. These formations were the result of necking of adjacent particles from their high surface energy. These formations could be found on the surface of powder-gel ZrB₂ and assisted in identification. Other ways of identifying nanosize ZrC was visibility under electron microscopy without conductive coating due to its superior electrical conductivity over ZrO₂. Their SEM microstructures are shown in Fig 6.20. It was presumed that the nanosize polygonal phases (marked with white arrows in Fig 6.20) on the surface of 2-4 micron ZrB₂ particles must be ZrC. While the gel could form micron size ZrC agglomerates, none were found, due to the innate surface attachment reported earlier that prevented large clusters. The residual carbon was likely responsible for some of the fine grainy surface textures as these samples were not conductively coated.

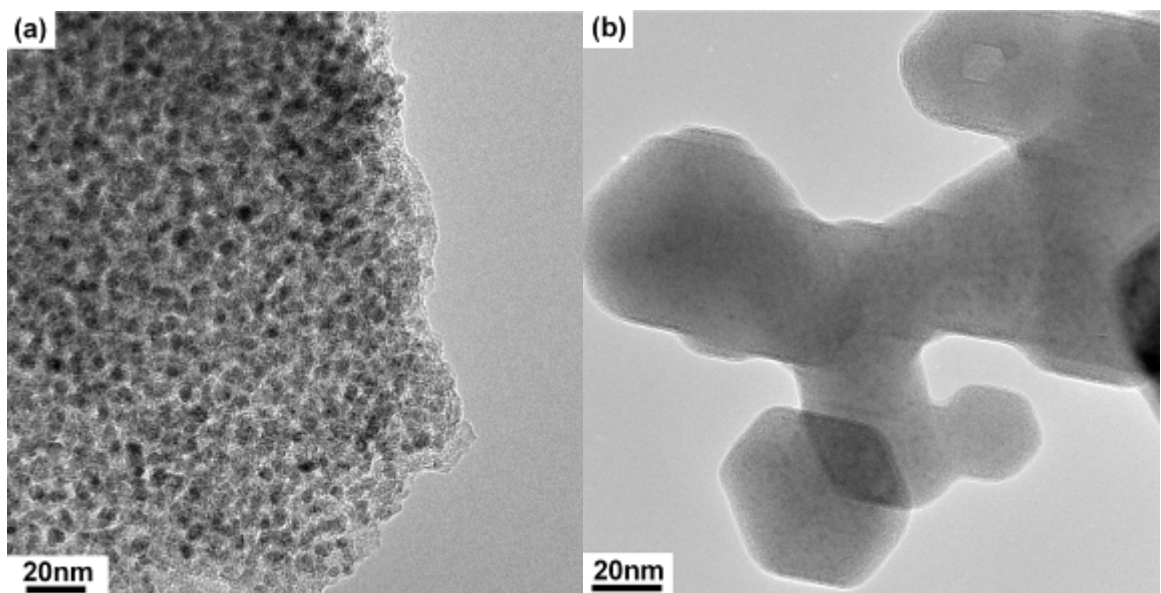


Fig 6.19. (a) Sol-gel ZrO₂-C composition of a 3.5C/Zr ratio after 550°C treatment **(b)** Early morphology and partial sintering of ZrC nanoparticles in the sample after 1450°C.

The coating on Z5C12 powder appeared to be intimate and it also sticks other ZrB₂ particles together in Fig 6.20(a). This agglomeration was still beneficial to the final microstructure provided ZrC was still nanocrystalline, thinly coated and intergranular. Examination of the surface at a higher magnification shows evenly spaced crystals (Fig 6.20(b)), with some electron-transparent flaky material around the surface that was presumably residual carbon.

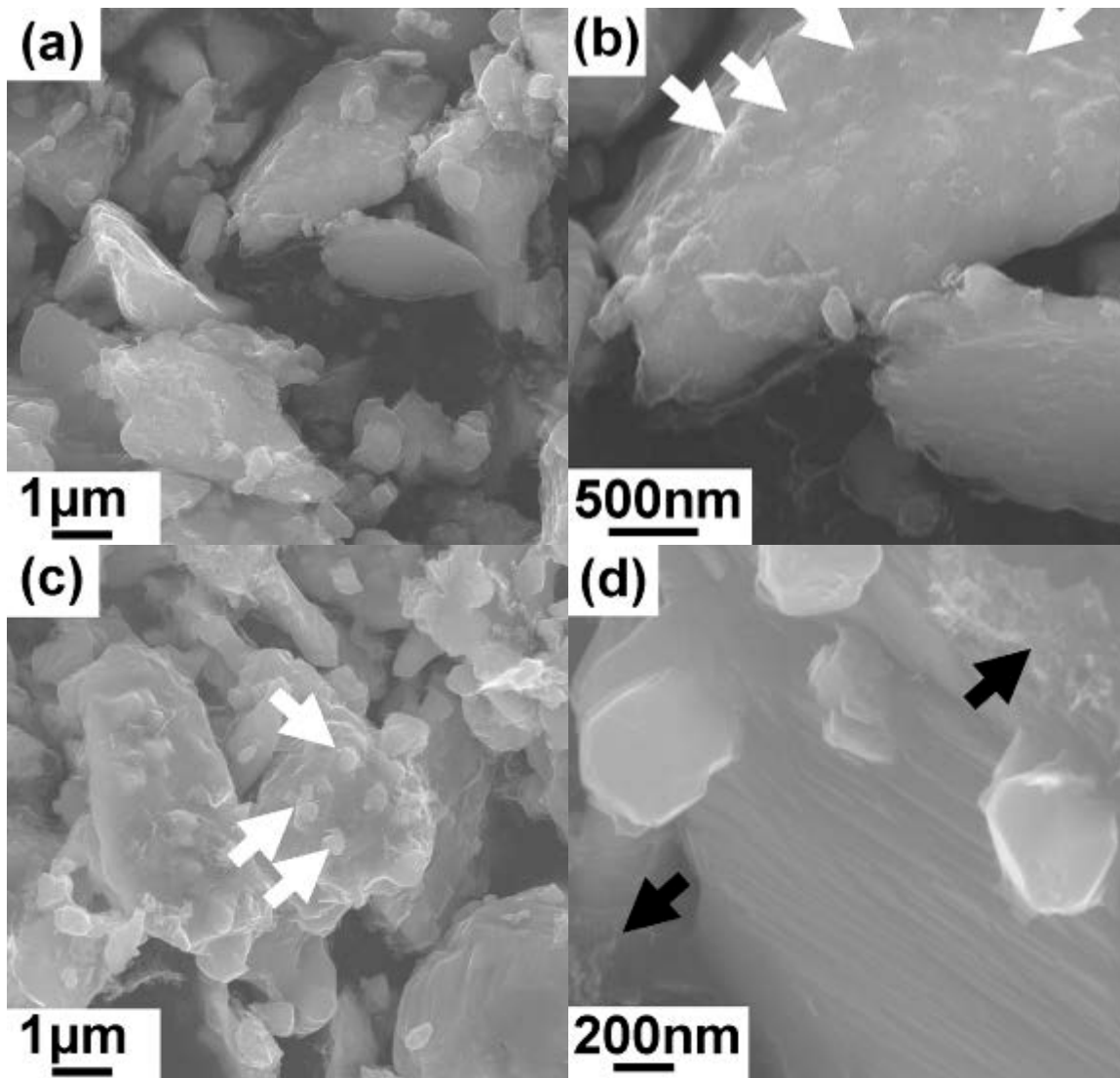


Fig 6.20. SEI images of ZrB_2 -ZrC powder after treatment at 1450°C. **(a)** Z5C12; **(b)** Z5C12 showing nanoparticles on the ZrB_2 surface (marked with white arrows), **(c)** Z5C14 powder with nanoparticles (marked with white arrows) **(d)** Z5C14 at high magnification, with residual carbon (marked with black arrows)

On Z5C14 powders, this carbon was observed more frequently between particles. Fig 6.20(d), provided an excellent example of residual carbon (marked with black arrows) and the intimacy of the nanoparticle mixture with ZrB_2 . The two ZrC crystals in Fig 6.20(d) shows a crystal geometry that matched the “hexagonal shape” previously discussed in the TEM images in Fig 6.19 (b). The positions of the crystals on the powder surface represented an ideal grain-microstructure refinement – hard carbides that could pin the moving grain boundary. Fig 6.20(c) demonstrated that each ZrB_2 particle had several nanoparticles on the surface

(marked with white arrows). It was apparent that the sol-gel process could coat a thin layer of Zr-O-C composition at ~100nm thickness. Nanocrystalline ZrC was thus well mixed without milling with ZrB₂ after heat treatment and could be used for subsequent composite formation. This type of surface attachment of nanosize ZrC would be superior to powder mixing as it prevented nanoparticle agglomeration, excessive oxygen uptake and phase separation. There were several possible causes for the surface attachment of ZrC. The shrinkage of the gel into or on surface defects or concave regions was a possibility. There was also possible bonding between the sol-gel oxides and the surface oxide film of ZrB₂. However, these would form in pre-reduction processes. In the reducing environment at elevated temperature, the reduction of zirconia and boria must result in a composition change. While most of the boria had clearly not favoured boron carbide to form via carbothermal reduction, it may have been converted to ZrB₂ through reaction with ZrC. The zirconia in a carbon rich environment would become ZrC. This indicated that there were likely two types of ZrC at 1450°C, namely the microstructure derived from the surface film on ZrB₂ and that from the ZrO₂ in the gel. The amount of surface film derived ZrC would be dependent on its solubility in ZrB₂, but from stoichiometry and quantification discussed previously, the system was above the solubility limit. It was known from previous research that the PFA decomposed carbon provides a graphene-like phase bonding the carbide crystals, such that the carbon-carbide possessed an elastic modulus.¹⁶⁵ Another possibility was direct ZrC-ZrC necking from the thin carbide on the surface of ZrB₂ to a nanoparticle carbide displayed in Fig 6.20(d). A further possibility was the reported epitaxy between ZrB₂ basal and ZrC close packed (111) planes, which would denote the surface in Fig 6.20(c) to be ZrB₂ rather than a thin ZrC layer.³⁸

6.3 Densification of ZrB₂-nc-ZrC

Once the correct carbon-zirconia stoichiometry was achieved on the ZrB₂ surface, the nanocomposite powders were densified by SPS. This section investigated whether densification could be assisted by a particle coating of nanosize or nanocrystalline (nc-)ZrC. From the examination of ZrB₂ sintering, there were several questions to address. It was possible that the carbothermal reactive

sintering trajectory could be used to sinter this composite at a lower temperature, since it was known that the significant densification could occur. This could be achieved if a greater extent of reaction occurred through additions of zirconium oxide or oxycarbide, and a higher diffusion rate offered by solubility of ZrC in ZrB₂. The heating rate yielded a short duration of non-densifying surface diffusion and evaporation-condensation mechanisms. But most importantly, the presence of surface nanoparticles reduced densification requirements. The major objective of this section was to understand the advantages of the powder-gel processing in forming homogenous UHTC composites, including processing temperature and microstructural control.

6.3.1 Composites of ZrC in ZrB₂

The densification behaviour of Z5C12 and Z5C14 powder-gels were practically the same, apart from Z5C12 registering residual oxide and Z5C14 yielding residual carbon as noted in Table 6.2. The majority of this section covered the Z5C12 sample. Both Z5C12 and Z5C14 at 1450°C had residual carbon, oxide and the carbide was an oxycarbide phase. Theoretically the presence of these oxides and oxycarbides could be used to assist in reactive sintering once the free energy change became favourable. This would contribute a chemical reaction driving force to facilitate lattice diffusion. The displacement rates above 1500°C were shown in Fig 6.21. Samples were heated at 100°C/min and 40MPa applied pressure matching the conditions as the control ZrB₂ samples. These graphs have been superimposed as the shrinkage from all four samples indicated where the most densification took place. The densifications rates were very different from the monolithic ZrB₂ control samples. In ZrB₂, the densification appeared to be assisted by carbothermal reduction, but only at the specific temperature of 1600°C and major densification associated with grain boundary contact was at 1800°C or higher. In Z5C12, the densification was continuous from 1350°C, indicating a large amount of activity occurring at this temperature. This was observed in all Z5C compositions. This activity demonstrated two respective peak densification rates at about 1600°C and 1800°C, but in this case, the densification rate at 1600°C was clearly higher than the densification at 1800°C. These were previously associated with reactive sintering of carbon with ZrB₂ surface oxides.

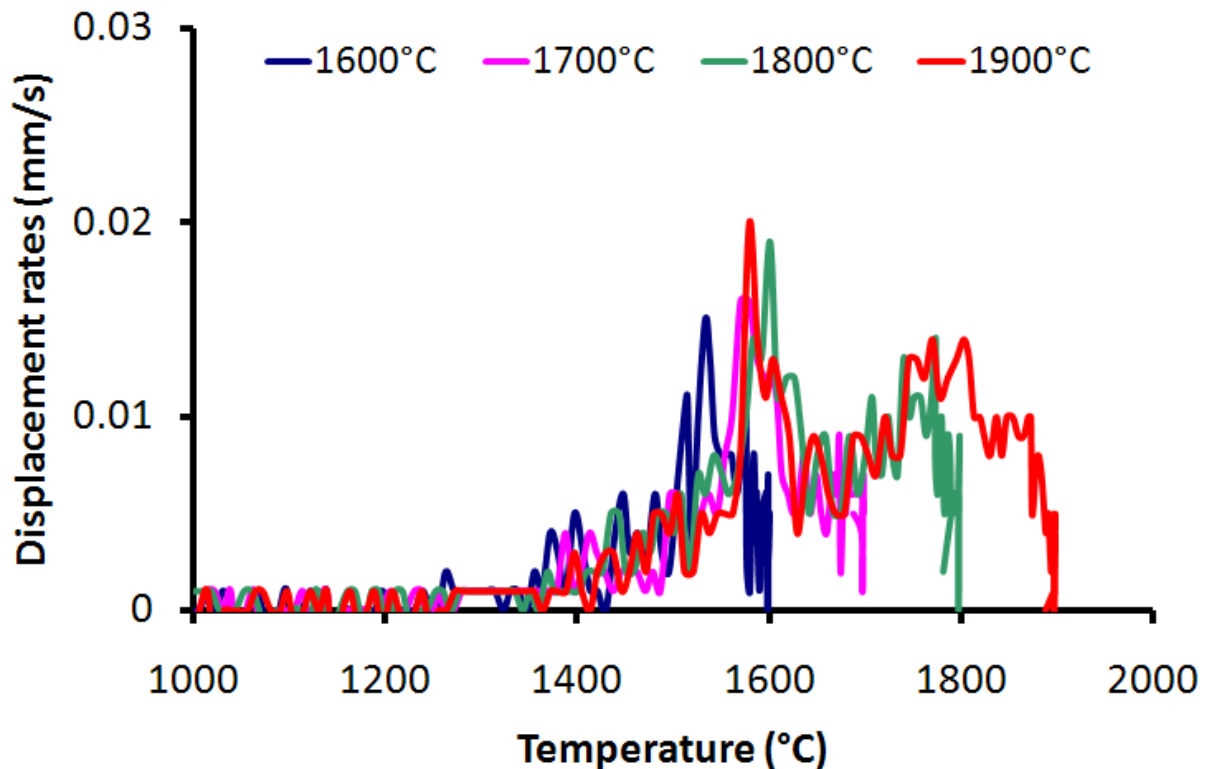


Fig 6.21. Displacement rates of Z5C12 powder-gel under SPS up to 1900°C

But it was likely that this was boosted by residual zirconia or zirconium oxycarbides (ZrO_xC_y). Note that in the monolithic sol-gel, 1350°C is approximately the temperature in Fig 5.7 where the formation of nanoparticle ZrC overcomes ZrO_2 as the major phase. In contrast, monolithic ZrB_2 had the major densification rate increase at 1800°C (Fig 6.8). The effect of the nanoparticle seeded surface on the reduction of surface area during densification was difficult to gauge without modelling. But any method to encourage diffusion assisted in densification. The solubility detected from Rietveld analysis of trace boron carbide and 1% ZrC in ZrB_2 likely contributed to diffusion. But the sol-gel coating of Zr_xO_yC/ZrO_2 likely contributed a larger chemical potential from the reaction in the powder-gel. Furthermore, the densification rate was a continuously increasing trajectory from the initiation at 1400°C, denoting less emphasis on the intrinsic ZrB_2 densification mechanisms. Inferred evidence of the above argument is the gas chamber pressure change, shown in Fig 6.22 over all four sintering isotherms from 1600°C to 1900°C for 5 minutes. While this could be associated with any gas discharge, the most likely explanation was the carbothermal reduction due to the temperatures of peak activity. In this system there are two oxide sources

available; the first was the nanoparticle addition through the sol-gel coating, which comprises of zirconium oxycarbide nanoparticles. The lattice parameters confirmed that the conversion was incomplete, and could now take place in the SPS. The second source was a remaining oxide film on the surface of ZrB_2 particles. Two distinct peaks were observed in Fig 6.22 (if the shoulder at 1400°C can be interpreted as a peak) and change in gradient shows possibly three reactions. Note that the heating rate was $100^\circ\text{C}/\text{min}$ and the gas exhaust represents a dynamic competition with the vacuum pump. Thus a peak of chamber pressure at 1600°C indicated a reaction that reached maximum activity a minute $\sim 50\text{-}100^\circ\text{C}$ earlier. The gas release in the first peak corresponding to 1250°C was likely due to the reaction of $0.6\text{wt}\%$ nano-zirconia from the surface residual of ZrB_2 . This corresponds to the earliest detected ZrC in the ZrO_2/C nanoparticle sol-gel from the XRD in Fig 5.7.

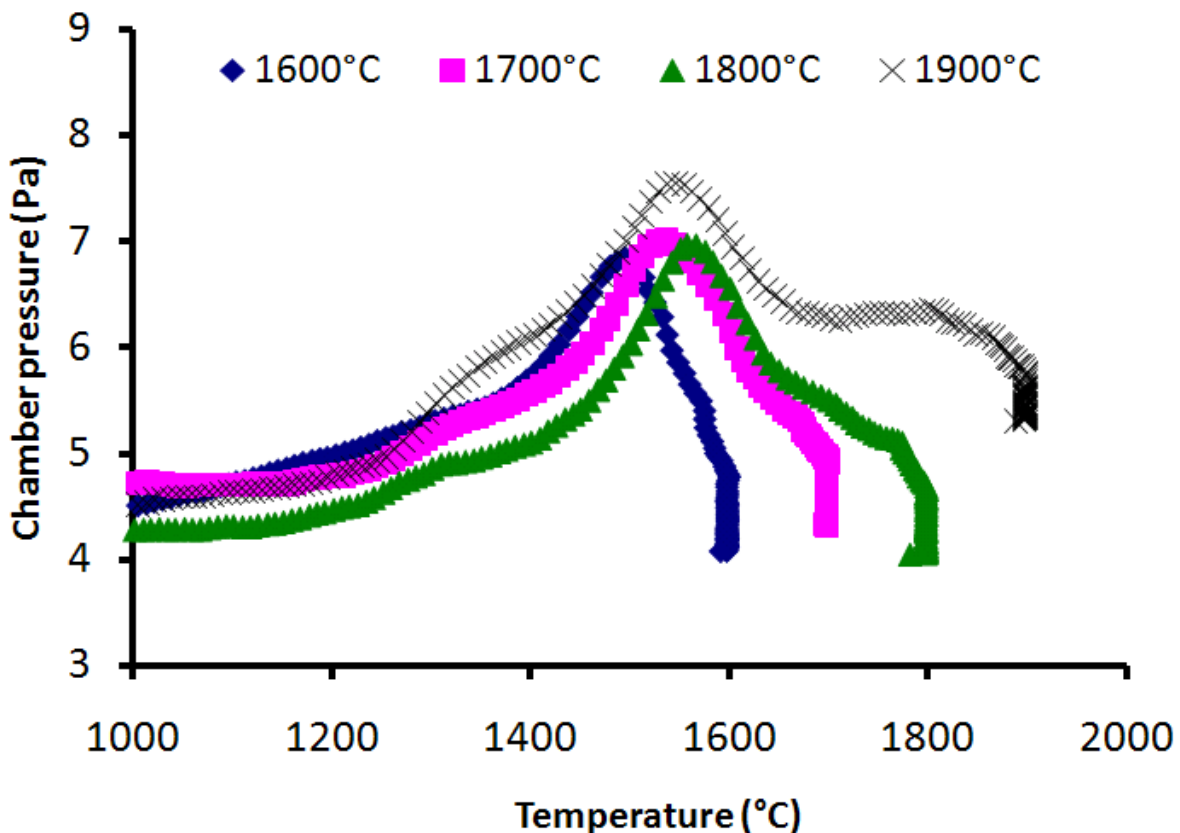


Fig 6.22. Change in chamber pressure during SPS sintering of Z5C14

The next favourable reaction was likely the conversion of the $3.6\text{ wt}\%$ zirconium oxycarbide nanocrystals to pure ZrC_{1-x} followed by any ZrB_2 surface films that contributed to the $0.6\text{wt}\%$ ZrO_2 . These reactions would have continued from

1250°C to 1600°C and released substantial $CO_{(g)}$, and Fig 6.22 demonstrates the vacuum recovered at 1650°C. In contrast, monolithic ZrB_2 has only a limited reaction sintering with chamber pressure increasing in Fig 6.7 from 1700°C and recovering at 1800°C. This was attributed to the graphite foil reacting with ZrB_2 surface oxide film. Studies have indicated that graphite is a poor diffusivity carbon source and the higher temperature for the reaction correlates with this. Reactive sintering likely caused surface activation and brought the grain boundaries together in a continuous sintering trajectory. Fig 6.23 shows the displacement change at 100°C/min to the specific isotherms at 1600°C to 1900°C respectively. It was known from ZrB_2 control samples that the densification from the grain boundary contact occurred from 1800°C (Fig 6.8). In using these nanoparticle carbides, two major displacement changes have occurred that corresponded to the two carbothermal reactions noted in Fig 6.21 and Fig 6.22. The isotherm at 1600°C indicates that substantial densification took place using the early carbothermal reduction, followed by another, slower sintering trajectory from the inflection at 1620°C. This inflection was not from the reduced heating rate approaching isotherm because it was found in the 1800°C and 1900°C samples as well.

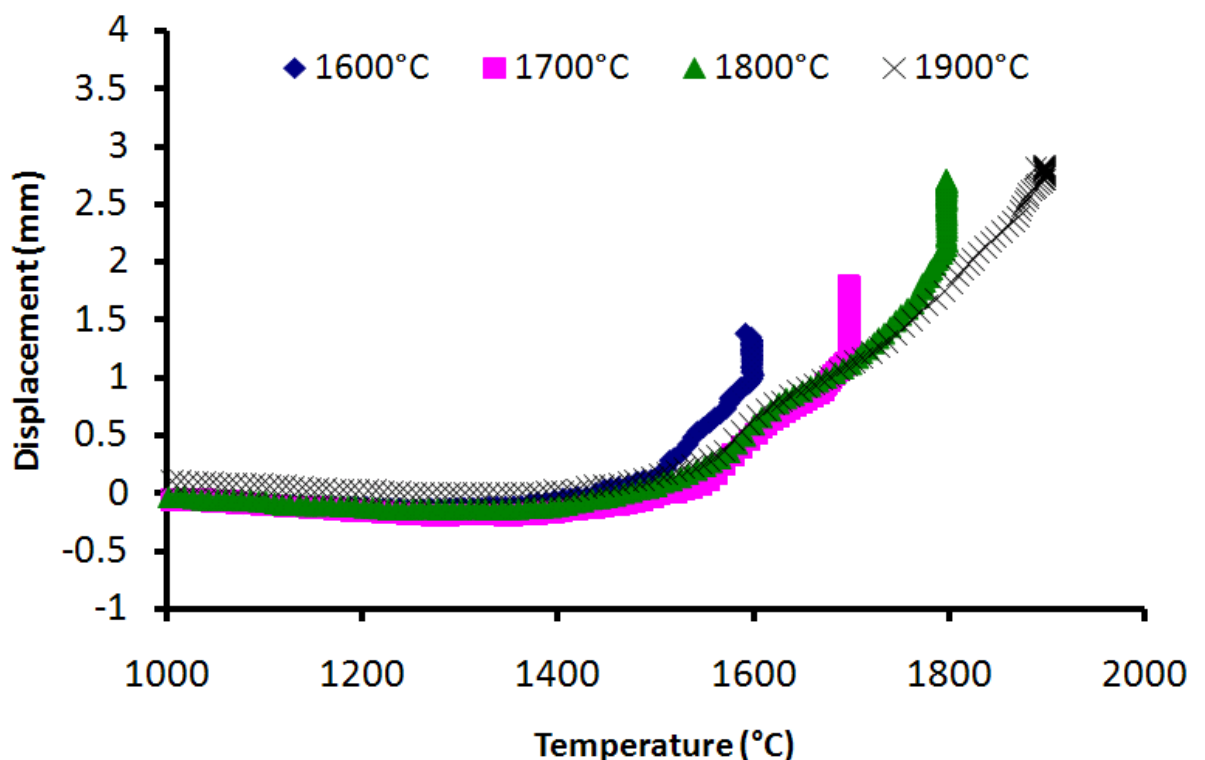


Fig 6.23. Displacement or sintering curves for the densification of Z5C12

This may correspond to the densification of the nanocrystalline phase of ZrC to micron-size particles. The contribution from ZrB_2 must lie within the 1800°C-1900°C region. After the inflection at 1620°C, these mechanisms of assisting densification continued to yield a constant densification rate from 1700°C. This likely limited the participation of the ZrB_2 grain boundary, resulting in a ZrB_2 powder size equivalent to the grain size. If reactive and nanoparticle assisted sintering occurred, then the density of these samples must have been consistently higher than the control samples.

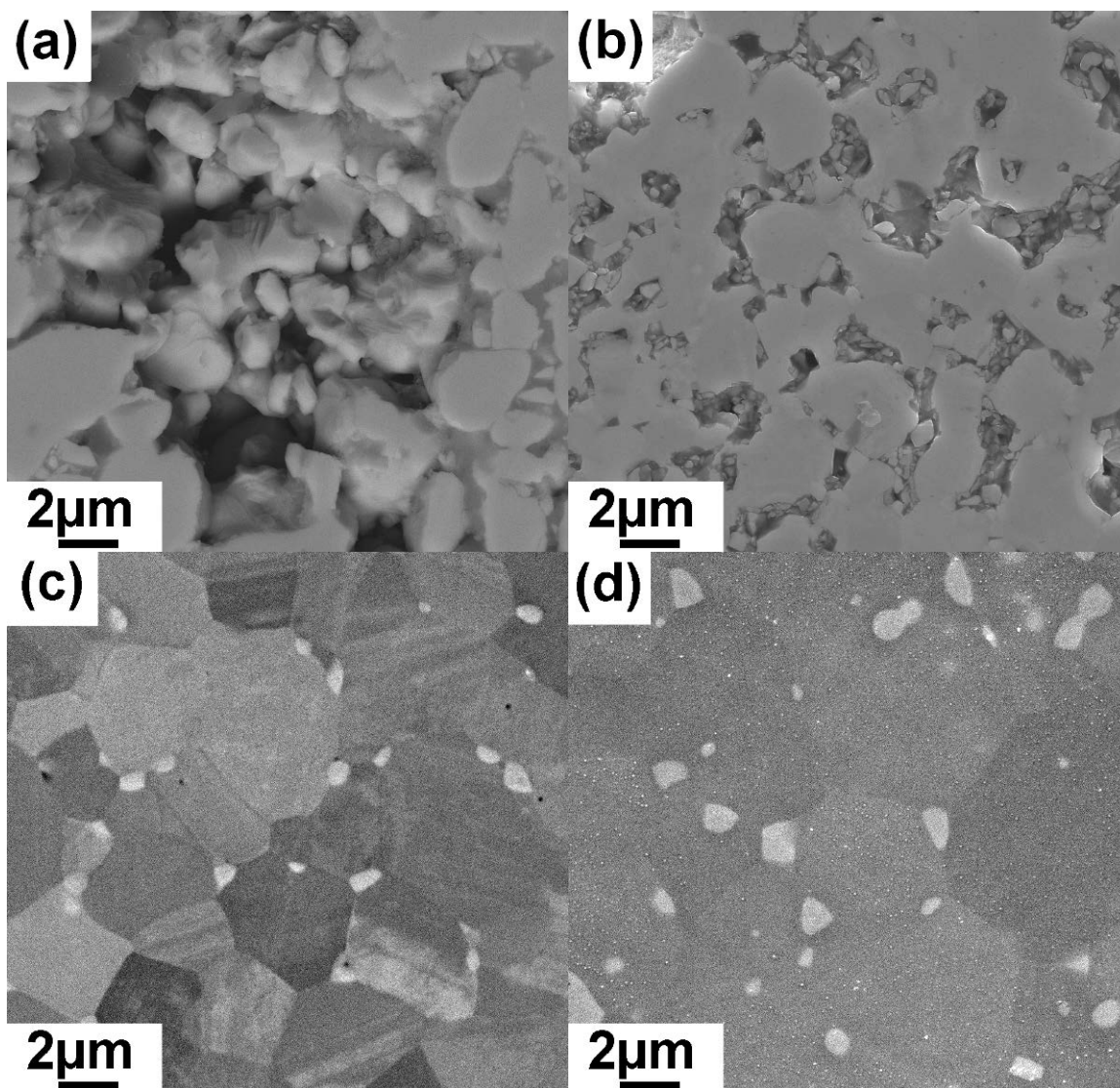


Fig 6.24. Densification of Z5C12 powders from (a) 1600°C in BSE (b) 1700°C in SEI (c) 1800°C in BSE (d) 1900°C in SEI at 100°C/min under 40MPa applied pressure.

Recall that the monolithic nc-ZrC are 50-80nm by TEM but in potentially micron size agglomerates. The conventional mixing of nc-ZrC and ZrB₂ later shows that ZrC grew to 1-10 μm . But in this case, nc-ZrC was more controlled, suggesting that attachment of the curvature of the ZrB₂ powder prevented large agglomerates. But coalescence already occurred, since at 1450°C the sol-gel derived ZrC were at ~200nm (Fig 6.20(a) and (b)) and ~500nm by 1600°C (Fig 6.24(a) and (b)) that shows the sintering microstructures. Fig 6.24 shows contact of ZrB₂ grains took place by 1700°C and coalescence of ZrC at 1800°C resulted in nearly full density. While the densification of ZrB₂ was assisted by the nanoparticle ZrC phase located at grain boundaries and triple points, substantial coalescence of ZrC up to micron size was likely a major contribution. Logically, from the powder-gel in Fig 6.20(c), it can be seen that several nano-size ZrC particles present on the ZrB₂ powder particle and their close proximity likely led to the coalescence of ZrC at elevated sintering temperatures. This coalescence must have included the grain boundary migration of ZrB₂ to reduce the total curvature of nanoparticle and substrate. Zener pinning was difficult to prove without further experiments. Solubility of ZrC in ZrB₂ likely implied that the grain boundary migration was not able to be pinned easily. However, the nanoparticles clearly formed a skeleton of intergranular pores that allowed for void removal and prevented boundary migration. The same evolution was demonstrated in Z5C14 samples over the same temperature range in Fig 6.25. However, the last stage of removing residual carbon was required, presumably by dissolution into the ZrB₂ matrix and Zr_xO_yC purification, since the XRD confirmed that all oxides were removed by 1800°C. Near full density was observed at 1900°C but this had the effect of coarsening the microstructure of the ZrC nanoparticles well into micron size. Pores were closed. The density of carbon was difficult to gauge, but both Z5C12 and Z5C14 were at least 98% by 1800°C. Due to depletion of carbon, Z5C12 yielded a residual 1% oxide by XRD in Table 6.2. In Z5C14, SEM and EDS confirmed residual carbon in pores and conversion of all zirconia. But identification of oxides was more difficult for Z5C12. TEM confirmed that some of the particles were oxide through diffraction and STEM EDS, and by stoichiometry in Table 6.2, this indicated that one in every four ZrC particles are actually ZrO₂ rather than ZrC in the sintered Z5C12. As noted, the sintering, densification

trajectory and microstructural evolution for both Z5C12 and Z5C14 were practically identical apart from the minor differences in microstructure.

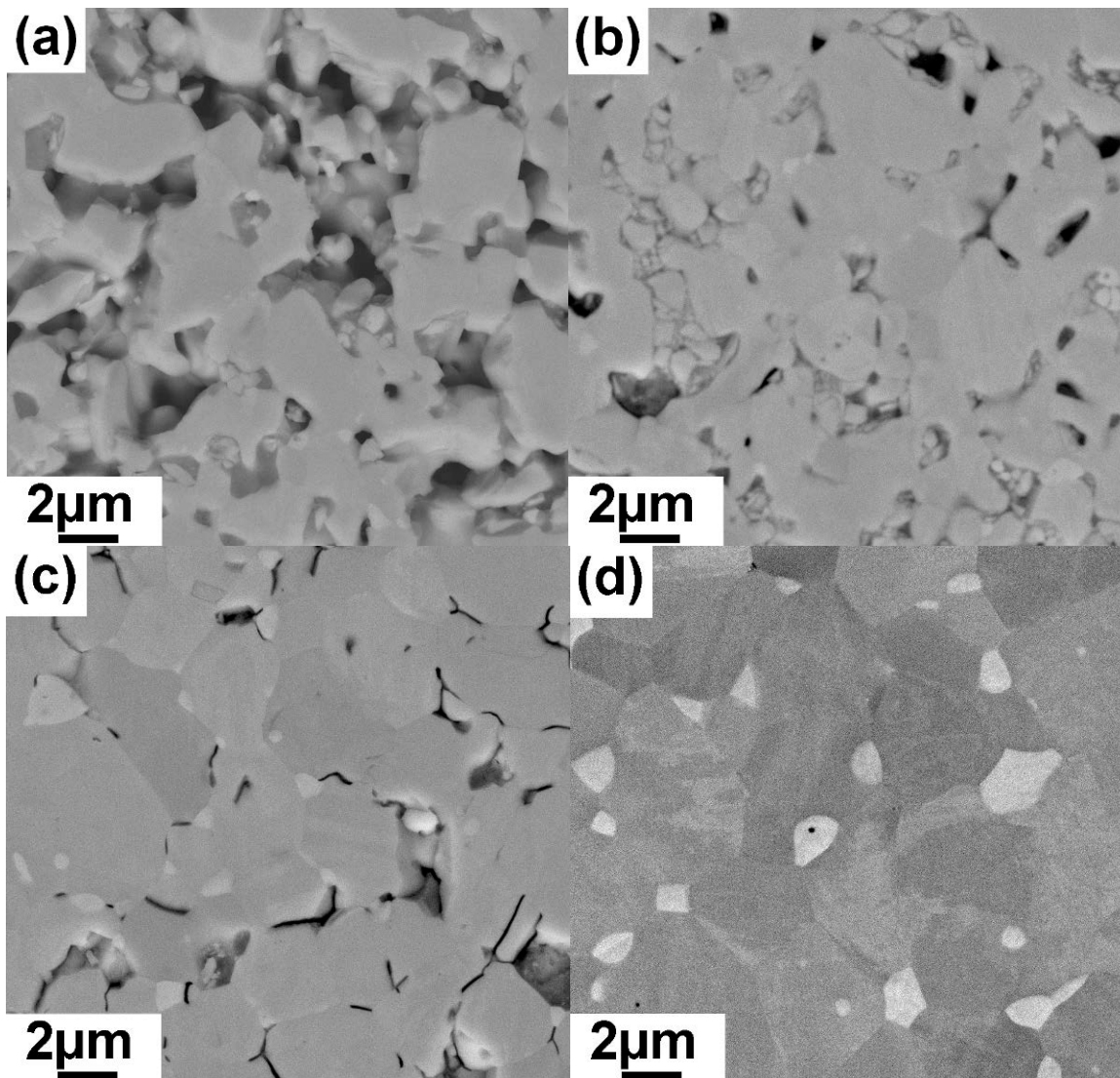


Fig 6.25. Densification of Z5C14 powders from (a) 1600°C (b) 1700°C, (c) 1800°C (d) 1900°C at 100°C/min under 40MPa applied pressure in BSE imaging.

The final density for Z5C14 was slightly lower from modest carbon contributions. The measured densities of the 10mm samples of ZrB_2 , Z5C12 and Z5C14 are shown in Fig 6.26. The densification route using powder-gel nanoparticles shows a lower temperature densification. This appeared to reduce the processing time at high temperatures that yield finer microstructures. The densification trajectory was also consistent with reported monolithic nano-ZrC densification that indicated

the inflection at 1700°C was from sol-gel ZrC.¹²⁹ This was likely due to the higher mass transport mechanisms of nanoparticles, solubility of B₄C and ZrC in ZrB₂ after 1450°C and carbothermal reduction diffusion assist that resulted in a large increase in densification trajectory from 1200°C-1600°C.

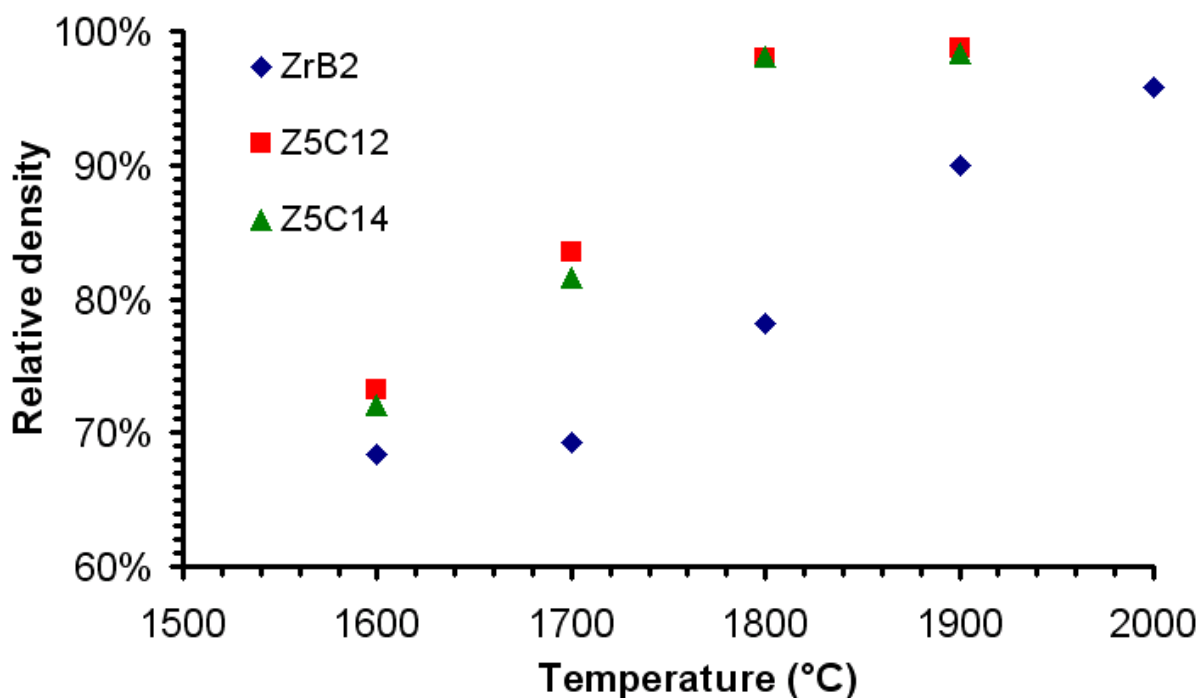


Fig 6.26. Density of all 10mm samples sintered from 1600-1900°C at 100°C/min under 40MPa applied pressure.

When heated to 1800°C in SPS, dense composites with a ZrC intergranular phase in a ZrB₂ matrix were produced from the modified ZrB₂ powder. The homogeneity of the composites is often unpublished in surface images, but this sol-gel mixture derived composite showed that even under low magnification in Fig 6.27 the dispersion was uniform. Due to the nature of wet-chemistry, when the gel infiltrated the powders and was ultrasonicated to prevent agglomerates, the coating was still even enough for homogenous nanoparticle dispersion. Apart from handfuls of powder where the sol-gel liquid did not infiltrate – such as moisture between powder particles – the coating was effective in its simplicity. The major processing hurdle was low temperature synthesis and good mixing without milling until heat treatment at 1450°C.

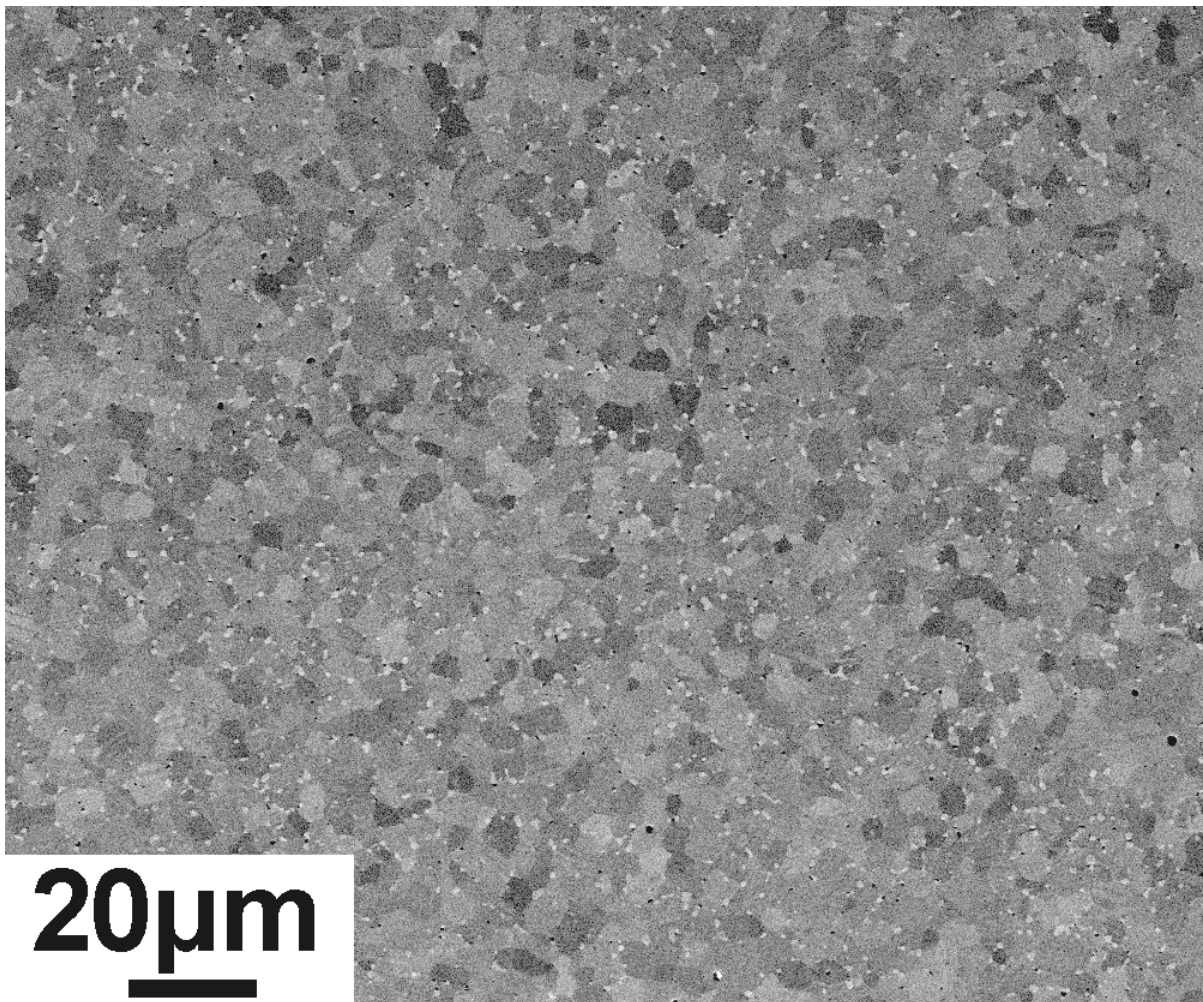


Fig 6.27. Dispersion of the sol-gel derived particles Z5C12 microstructure under low magnification BSE imaging.

At 1450°C surface attachment of ZrC nanoparticles on the ZrB_2 surface occurs. Once this occurred the powder-nanoparticle relationships were effectively static and ZrB_2 was always able to be found with attached nano-ZrC.

6.3.2 Conclusions of powder-gel densification

ZrB_2 -ZrC composites were produced using a specially modified ZrB_2 powder-gel using a nanosize ZrC sol-gel precursor. Homogenous particle reinforced ZrB_2 -5 mol% ZrC composites were densified at temperatures as low as 1800°C, although residual carbon required temperatures up to 1900°C to densify completely. However, the sintering trajectory substantially increased early densification compared to as-received ZrB_2 powders. From the chamber gas pressure, it was inferred that the 1300°C-1500°C carbothermal reduction reaction

contributed substantially to the system since the activation of surfaces at 1800°C in monolithic ZrB₂ were subsumed. This was confirmed by the high densification rate from 1350°C to 1600°C. It appeared that grain boundary diffusion of ZrB₂ did not significantly commence and the powder size was same as the grain size. The microstructure confirmed that use of the nano-ZrC precursor coating resulted in earlier contact of surfaces. It was likely that the higher diffusion kinetics were caused by solubility of ZrC, consumption of B₄C and ZrC, as well as carbothermal reduction from residual carbon. No evidence of plastic flow or deformation of the grains was observed, and densification under minimal conditions – particularly using minimum allowable pressure and heating rate – still allowed the future possibility of pressureless sintering.

6.4 Conclusions of sol-gel ZrC composites

The chapter indicated that using a nanocrystalline phase of ZrC from a sol-gel route had some remarkable advantages for processing. SPS appeared to be a technology that was not well understood, due to unknown current paths, sintering anomalies and diffusion contributions. But using a control ZrB₂ sample in SPS allowed for comparison of the effect of the nanoparticle addition. It appeared that the sol-gel zirconia plays a key role in interacting with the surface and producing a thin coating epitaxially to an oxide film. Control of carbon was critical to determine the microstructure and morphology of the powder-gel crystallites and transforming the oxide to carbide. This was achieved by using a varying amount of acid catalyst to control the polymerisation of PFA, which determined the magnitude of the PFA decomposition. Carbothermal reduction using the decomposed PFA-derived carbon was complete at 1450°C and prevented oxidation of ZrB₂. Through pyrolysis and carbothermal reduction, sol-gel derived nano-size ZrC particles were produced, which were attached to the surface of ZrB₂ particles. This attachment prevented excessive agglomeration and allowed their simple use in modifying the densification of ZrB₂ through mechanisms of reactive sintering via carbothermal reduction, diffusion assistance via ZrC/B₄C solubility and nanoparticle densification. Two future hopes in this system are pressureless sintering and nanocomposites. A further reduction of the gel concentration in the powder system may lead to a nano particle morphology in

the densified composite. Using the minimal parameters in SPS was useful in comparing this technology to applied research outcomes found in pressureless sintering techniques needed for more complex structures. The subsequent chapter explored the effect of dispersed ZrC under extreme environment conditions.

7. Materials extreme environment performance

This chapter investigated the structural stability of UHTC composites and whether the microstructure affected the resistance to oxidation. Successful completion resulted in understanding how small phase additions assist in materials performance under extreme conditions. The first aim was to understand the limits of the simulation facilities and the differences compared to the real environment (such as hypersonic flight). This was a reference environment, as the work here was not specifically designed for this purpose. The second hurdle was, broadly speaking, improving the performance of the materials. This was measured by several properties. Use of ZrB_2 already resulted in high thermal stability and mechanical strength, oxidation resistance and high thermal conductivity, which were key properties for materials to survive these environments.^{37, 40} These properties could be improved for composites of ZrB_2 , observed by material retention, reduced leading edge recession, geometric stability and properties of the protective oxide scale. Technical objectives were to simply improve performance. But the final outcome would be measured by whether this research was of use to define future directions for composites and the powder-gel process. There were also several features in the project that challenged conventional processing. Using 5% of a secondary phase was uncommon for UHTC composites. Impurities are in the order of 3-4 wt% and additives up to 10 vol%. Most are additions of 10-30 vol% of the secondary carbide phase.¹⁴ Most investigation has been on phase selection; there has been no investigation on the effect of homogeneity and microstructure in the ablative response of materials.

7.1 Microstructure and mechanical properties

A preliminary exploration of microstructure and mechanical properties was covered. Several other composites were made as controls for the experiments. Their density, microstructure and thus mechanical properties were relevant.

7.1.1 Powder-gel and powder-mixed composites

Several control ZrB_2 composites were developed in addition to the sol-gel based composites of ideal stoichiometry. Fig 7.1(a) recalled the homogenous

microstructure of Z5C14. The addition of further carbon ($C/Zr > 16$) of Z5C16 yielded the same microstructure in Fig 7.1(b), but resulted in intergranular residual carbon (by EDXS analysis). Depletion of carbon ($C/Zr < 10$) conversely yielded second phase oxide particles (the white phase in Fig 7.1(c)). These are referred to as Z5O, as all carbon ratios below ~ 10 yielded oxide.

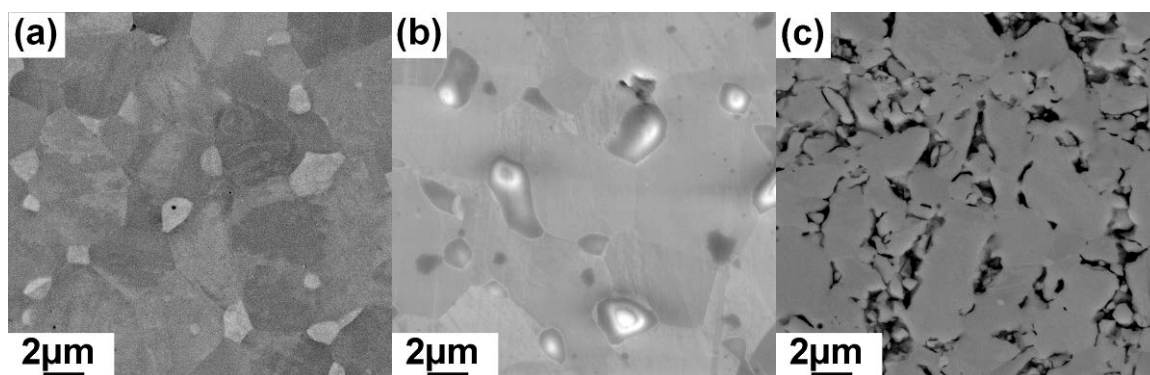


Fig 7.1. ZrB_2 powder-gels for oxidation testing (a) Z5C14 in BSE (b) Z5O in SEI. Note massive contrast correction from oxide charging/SEM damage on powder-gel Z5O. (c) Z5C16 in SEI showing their microstructures after $1900^\circ C/5min$ using the SPS.

These allowed for additional investigations. An excess of carbon (via PFA at the sol-gel stage) in Z5C16 investigated whether excess carbon and porosity affected the mechanical and aerothermal properties. The carbon depleted Z5O sample represented a typical 5 vol% or wt% thermally inferior phase (ZrO_2). It could also represent additives that yield glass or metal impurities. This impurity was also a poor thermal conductor and was technically a sensitive flaw. For example, a pore is a mechanical flaw due to stress concentrations, but here, an insulator interrupts the conduction of heat. The pertinent features of Z5O were the intergranular wetting angles representing possible melting of ZrO_2 and the charging steppes in Fig 7.1(b) that indicated low electrical conductivity of zirconia. The conventional powder mixing were designed as a comparison control; the ZrB_2 control was processed by SPS to $\sim 96\%$ relative density sufficient for closed pores by $1900^\circ C/5min$. However, the major comparison to the powder-gel was conventional powder mixing using the nanoparticle ZrC in Chapter 5. This involved a simple mole fraction of 95% ZrB_2 and 5%nc-ZrC mixed together and

conventionally ball milled known as ZrB_2 -5ZrCp (to distinguish between Z5O or Z5C-types) shown in Fig 7.2(b).

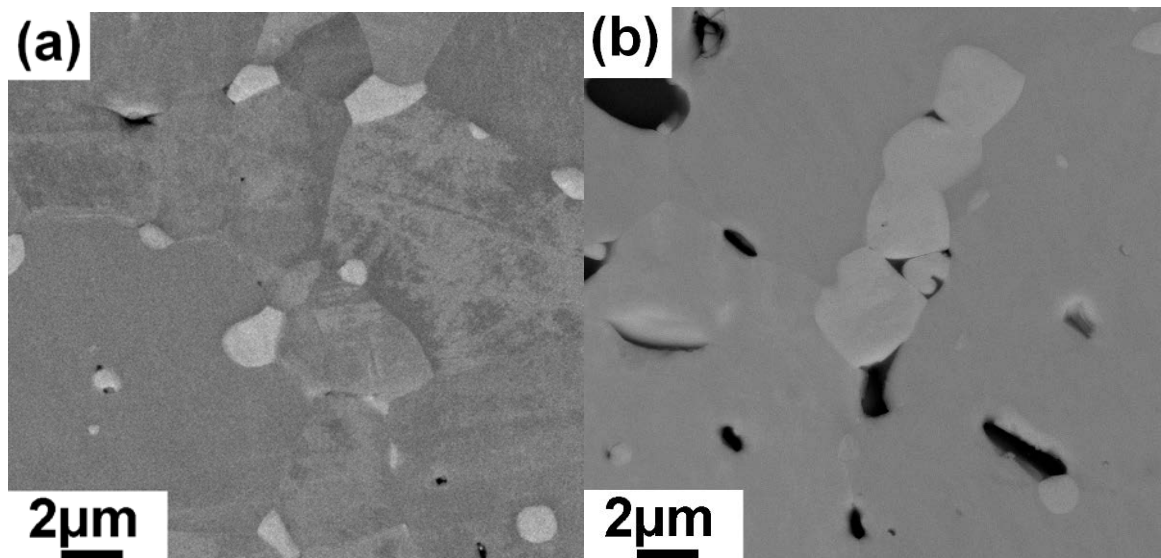


Fig 7.2. ZrB_2 composites in BSE (a) powder-gel Z5C14 (b) ZrB_2 -5%ZrCp 1900°C/5min at 100°C/min at 40MPa applied pressure.

The powder mixed composite also contained residual carbon attached to clusters of carbides, which was visible as large dark regions at least 1 micron in size, often with adjacent nanoparticle clusters, since the sol-gel ZrC yields residual carbon. Ball milling may have helped in distributing the nanoparticles to submicron clusters. This illustrated a key challenge in distributing nanoparticles by conventional method. Some nanoparticles remained isolated, but most formed agglomerates up to micron in size before sintering. However, during sintering all ZrC clearly coalesced, up to 10 microns in size. This means that there were key differences between ZrB_2 -5ZrCp and Z5C powder-gels. The coalescence of ZrC certainly occurred, but in isolated regions, not seeded the surface of the ZrB_2 , which likely caused the majority of the densification to take place at high temperature using the ZrB_2 boundary. Densities of above 97% were reached but the grain size of ZrB_2 -5%ZrCp was larger due to reliance upon the intrinsic ZrB_2 densification. Recall this was different to the powder-gel where most of the densification occurred from ~1300°C and thus the grain size was 3-5 times smaller. The dispersion must be emphasized. Both reactive sintering and nanoparticle coalescence occurred, but randomly without emphasis on the ZrB_2

powder surface. The homogeneity of the microstructure was about 5-10 times less based on the magnification required to replicate the same particle-grain distribution as Z5C series.

7.1.2 Mechanical properties

Fracture toughness was important for performance in the thermal shock of rapid heating and cooling, as it determined the strain response using pores and microcracks to compensate for internal stresses. Strength was related to the ability to withstand internal stresses from large temperature gradients during testing and to withstand thermal shock during heating and cooling. Hardness was also investigated to yield a gauge of strength for other compositions.

7.1.2.1 Fracture toughness

The fracture toughness was briefly examined between the control ZrB_2 and the powder-gel Z5C14. The ZrB_2 sample was densified at 2000°C to 96% relative density and was the only sample to suffer damage under the vibration and stresses of mechanical polishing. Z5C14 was densified to above 98% at 1900°C/5min.

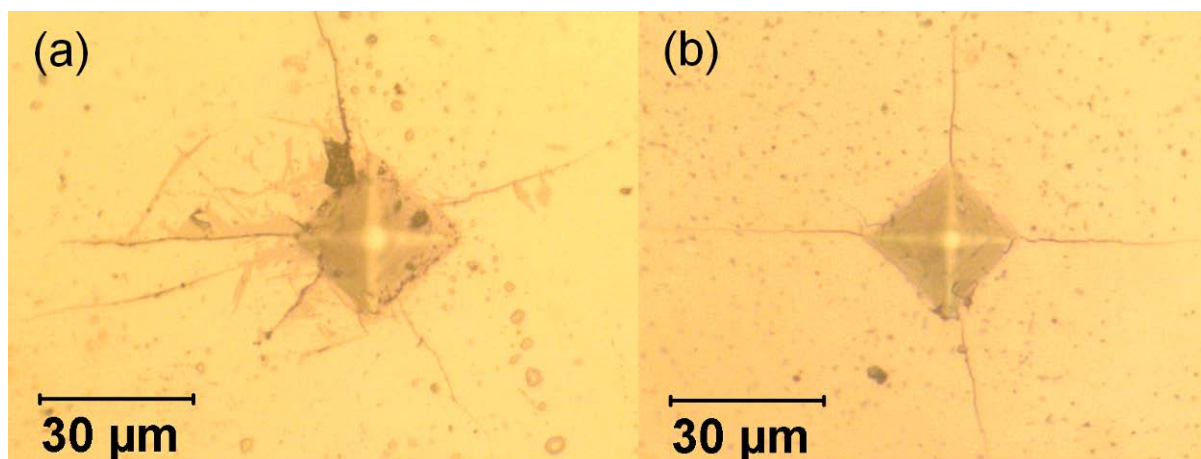


Fig 7.3. Comparison of fracture indentations into **(a)** ZrB_2 , and **(b)** Z5C14. Measured under a 1kg load.

It can be observed from the indentation images that the gel-dispersed ZrC was harder and denser, yielding a smaller indentation under the same load. Based

only on crack displacement width ($2c$), the control ZrB_2 yielded a K_{Ic} value of $3.6 \pm 0.3 \text{ MPa}\cdot\text{m}^{1/2}$ that was consistent with literature values. The powder-gel composite yielded a value of $4.1 \pm 0.3 \text{ MPa}\cdot\text{m}^{1/2}$. However, this value was more reliable than the K_{Ic} derived from the control sample. The powder-gel yielded consistent text-book indentation morphology. All powder mixed samples had sub-indentation cracks and additional radial cracks. Thus crack length did not include the subsidiary cracks that likely relieved the strain of the primary propagations. Furthermore, cracks emanated from below the indentation, which indicated that fracture began before the indentation was completed. No change in fracture mode was observed; all cracks appeared to be transgranular. Thus toughness mechanisms in the powder-gel composite were likely from the increased energy required to break dispersoids at the interface of ZrB_2 to ZrC and ZrC crack deflection. Both are shown in Fig 7.4 under compositional SEM imaging.

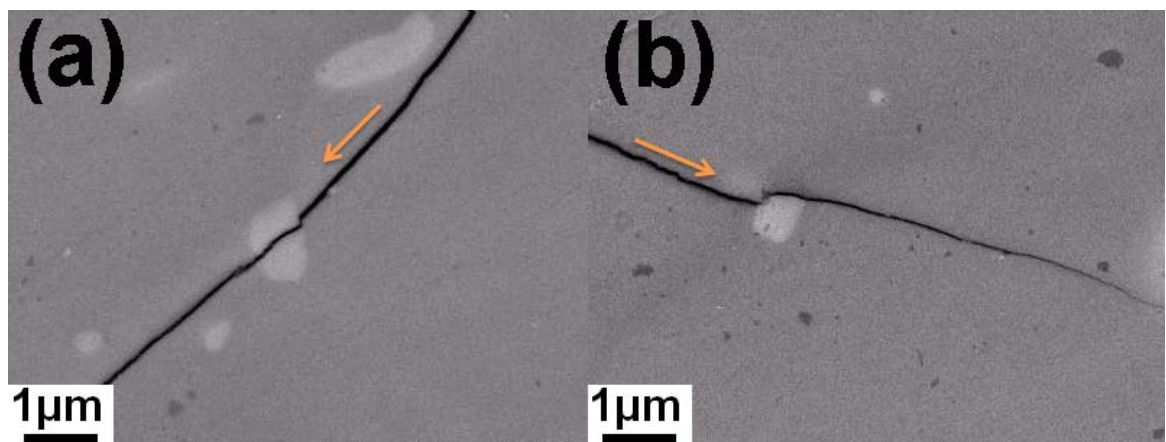


Fig 7.4. Examples of toughening mechanisms in Z5C14 composite. Crack propagation from the indentation was shown by the arrows.

It is possible that the higher density $\sim 2\%$ determined resistance to fracture. Generally, appreciable improvements in toughness require fibers or whiskers. In summary, changes in fracture toughness were probably negligible and difficult to quantify due to the differences in porosity and improper indentation morphology.

7.1.2.2 Indentation hardness and strength

It was likely that the addition of nanoparticles increased the strength because deformation was more difficult. Only two sets of samples were tested for flexural

strength, and the others were investigated by indentation. Fig 7.5(a) and (b) showed the engineering stress-strain curve data from the ZrB_2 control sample and composite respectively. The flexural strength of the powder-gel composite was about ~ 400 MPa and the modulus was derived to ~ 500 GPa as expected.^{24, 30, 306} Flexural strength was below literature values of about 500MPa for ZrB_2 composites.^{52, 70, 169, 297, 307-313} This was likely due to the tensile failure from residual porosity from carbon or partially graphitized regions of the sample. Z5C14 was also not designed for strength. The control sample was also shown in Fig 7.5(a), with an average strength of about 200MPa and a slightly lower modulus. However, while the composite Z5C14 was about 98%, the control ZrB_2 sample was actually only 96% relative density, and this may have contributed to the differences flexural strength. But the earlier microstructures suggest that both control ZrB_2 and Z5C14 can be compared because the difference of the intergranular phase is actually a micron size pore and a micron size particle. Both samples possessed the same indentation hardness noted later.

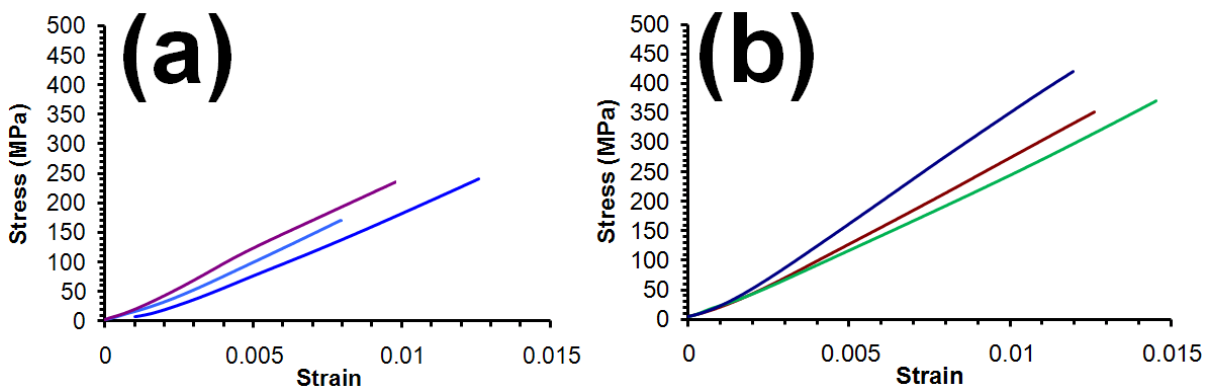


Fig 7.5. Stress-strain curves from flexural strength testing by 3-point bend of sample size 23mm x 5mm x 3mm bars using a span of 18mm. (a) ZrB_2 control, 96% relative density and (b) Z5C14, 98% relative density.

Hardness testing provided a quicker and less destructive guide to compare the relative strength between compositions without production of excessive materials. The strength can be approximated if necessary. Since hardness represents the resistance to plastic deformation, there is a relationship between the two defined by $H_v > 3\sigma$ for brittle ceramic materials without shear deformation ability.²⁵⁸⁻²⁵⁹ The data was relatively consistent with expected $H_v = 30\sim 40\sigma$ from literature for

hard (B_4C , SiC) ZrB_2 composites.^{52, 70, 169, 297, 307-313} However, this will not be explored here since the focus of processing was on oxidation performance rather than mechanical properties. Two control samples of ZrC and ZrB_2 were densified to as far as reasonably possible without significant grain growth. The control 100% ZrC and 100% ZrB_2 were listed at the top of Table 7.2; both were sintered at 2000°C. Grain growth was completely uncontrolled with nano-ZrC, which yielded 10 micron grains from an initial crystallite size of 80nm, and was expected difficulty in preparation of nanopowder compacts and controlling grain growth.^{60, 76, 314} The ZrB_2 30mm sample cut for aerothermal testing was sintered to a density of 96% and yielded a hardness of 15.8 ± 0.8 GPa, and this was softer than the 10mm sample because of a slightly lower density. ZrB_2 -ZrCp as expected did not perform to full potential despite having ZrC grains as it also had residual carbon and larger grain size. Given the size of the indentation ~ 30 microns (2a), no effect on hardness was expected unless the indenter impacted directly on a ZrC cluster, such as a cluster shown in Fig 7.2(b). In fact, it was more likely that porosity and residual carbon regions caused the lower hardness values to the comparison ZrB_2 30mm sample.

Table 7.2. Hardness of powder mixed composites including pure ZrC nanopowder. All were densified by SPS using a 5 minute peak temperature.

Sample/die	Processing	d	Hv (GPa)	Comments
nc-ZrC 10mm	2000°C/100°Cmin ⁻¹ /40MPa	97.2%	18.2±0.9	Grain growth
ZrB_2 10mm	2000°C/100°Cmin ⁻¹ /40MPa	96.0%	16.1±0.7	Grain growth
ZrB_2 30mm	1900°C/100°Cmin ⁻¹ /40MPa	95.6%	15.8±0.8	Match 10mm density
ZrB_2-ZrCp 30mm	5% nc-ZrC mix 1900°C/100°Cmin ⁻¹ /40MPa	97.5%	14.7±0.9	Residual carbon

The powder-gel composites were ranked in Table 7.3 by the amount of PFA-derived carbon. The Z5O had an intergranular phase substantially softer than the ZrB_2 -ZrC (Z5C) counterparts. Only one report of ZrB_2 - ZrO_2 was similar to this composition, which yielded 8wt% intergranular 2µm ZrO_2 and hardness of 17.6 ± 0.2 GPa at >99% density.²⁶¹ Wetting angles also suggested liquid phase sintering occurred. As PFA was increased above 12 in the gel, decomposed

carbon increases and more carbide was formed. Z5C12 yielded 3% carbide and 1% oxide particles, and thus a hardness of 19.5 ± 0.7 GPa. This does indicate the role of microstructure in determining hardness values, since a 30 micron (2a) indent would encounter a score of ZrC particles. It is likely that Z5C12 flexural strength testing would be consistent with literature values for ZrB_2 hard composites and better than Z5C14. It contained no oxides but had residual carbon, and as a result the hardness was drastically reduced to 15.8 ± 1.0 GPa, about the same as the ZrB_2 control. This may be because indentation tests a very small zone. Recalling the bulk 3-point flexural test noted that an additional 2% density, same grain size but replacing all pores with distributed ZrC made a significant difference to strength.

Table 7.3. Hardness of powder gel composites. All were densified by SPS using a 5 minute peak temperature at $100^\circ\text{C}/\text{min}$.

Sample/die	Processing	d	Hv (GPa)	Comments
Z5O 30mm	$1900^\circ\text{C}/100^\circ\text{Cmin}^{-1}/40\text{MPa}$	98.1%	14.0 ± 0.9	Oxide, liquid-phase sintering?
Z5C12 10mm	$1800^\circ\text{C}/100^\circ\text{Cmin}^{-1}/40\text{MPa}$	>98.5%	19.5 ± 0.7	Residual oxide
Z5C14 10mm	$1900^\circ\text{C}/100^\circ\text{Cmin}^{-1}/40\text{MPa}$	>99%	15.8 ± 1.0	Residual carbon
Z5C14 30mm	$1900^\circ\text{C}/100^\circ\text{Cmin}^{-1}/40\text{MPa}$	97.9%	15.7 ± 0.6	Match density & microstructure
Z5C16 30mm	$1900^\circ\text{C}/100^\circ\text{Cmin}^{-1}/40\text{MPa}$	97.0 ^a %	13.4 ± 0.6	Heavy residual carbon

When further PFA decomposition was added, at the cost of hardness and significant carbon inhomogeneity. The presence of significant ~ 3 wt% C yielded a hardness of 13.4 ± 0.6 GPa. Z5C16 density assumed all carbon graphitized to 3.2gcm^{-3} otherwise density is 93%. The similar densities ($\sim 97\%$) and hardness of the same sample (processed at different die size by temperature) were indicative of good control over the challenges in upscaling samples. Densities were kept consistent between all 30mm samples (noted in bold), as these were the samples tested under oxidation. Regarding designing for mechanical strength noted earlier, it would certainly be a preference to design for residual oxide rather than residual carbon. For high temperature aerospace structures, there was a solid performance history of carbon-based materials due to refractory stability and

good thermal conductivity. But the graphitization temperatures for resins like PFA are in the order of 2000°C-2500°C or more.^{144, 315-319} Even if graphitization occurred, mechanically graphite ($H_v \sim 0.66\text{GPa}$) was softer than zirconia ($H_v \sim 10\text{GPa}$) and decreasing strength from Z5C16 was very consistent with literature; Zhu et al reported H_v of $14.1 \pm 0.5\text{GPa}$ from 3.4wt% C residual carbon after densification of ZrB_2 at 1900°C.^{297, 312} Thus it should be emphasized that poor hardness/strength was because control of processing was biased toward leaving residual carbon rather than to optimize their mechanical strength by reacting with inferior phases. This was validated by later oxidation testing as the correct decision.

7.1.3 Summary

In comparing the densities it was likely that a significant amount of carbon may have been present as a residual impurity in these sintered coupons. This was the likely cause of modest hardness and mechanical strength. Upon densification, the carbon may have partially graphitized, but remained in the pores and may have weakened the grain boundary region. Because the ceramic fails at the point of flaw, a small amount of residual oxide may be better if designing for flexural strength. Nevertheless, it indicated that a dispersed particle phase in a composite can remarkably improve hardness and strength. Residual carbon was preferred for aerothermal performance over residual zirconia. Results were consistent with literature.

7.2 Aerothermal performance

Technical definitions of what constituted high temperature aerothermal performance included maintaining leading edge geometry and reducing material recession during exposure at ultra-high temperatures. Failure to maintain geometry constituted materials failure. Factors supporting stable geometry involved several intrinsic properties that assisted in understanding the multifaceted nature of ceramic ablation: thermal stability, thermal conductivity and fracture toughness. Thermal stability directly contributed to preventing liquid phase formation and collapse of geometry. Thermal conductivity distributed heat away, allowing passive cooling, reducing the dependence on thermal stability. Fracture toughness is desirable for all ceramics, as mechanism to accept strain

from thermal shock once strength is exceeded. But “resistance to oxidation” was particularly distinct from the other properties, as it significantly depended on materials processing control. Effectively, good resistance to oxidation implied the formation of a stable, dense and thin (since oxides are insulators) oxide scale that prevented or slowed the passage of oxygen to the underlying structure. This was dependent on microstructure and phase selection. This section evaluated the performance of these compositions and microstructures based on these properties.

7.2.1 Prediction, hypothesis and criteria

Ultimately, UHTCs are required to perform up to 3000°C in air. But tests at this extreme condition were not often reported due to limits in test facilities. Access to the facility at DSTO used an oxyacetylene torch similar to the setup by other reported literature.^{223, 228, 320} There was no agreed standard for this type of testing, and it was necessary to introduce a careful hypothesis, understand the testing method and the predict results to compare to the post-test data. Fig 7.6 mapped the questions and aspects that each sample investigated.

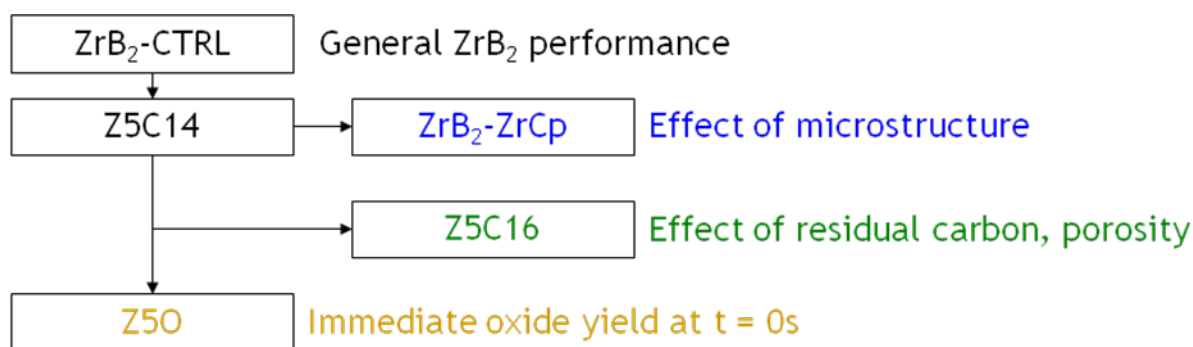


Fig 7.6. Samples and brief rationale for investigation

It was expected that ZrC would oxidize in preference or at a faster rate than ZrB₂. The major hypothesis was based around whether the viscosity of zirconia in liquid form or via densified oxide scale was sufficient to protect the underlying surface. This was determined by post-test microstructures. The other compositions investigated variations of this hypothesis statement. The design of these materials compromised several questions that aimed to increase the understanding of ablation of UHTCs unexplored at this temperature range.

The control test evaluated performance of ZrB_2 as the standard. The second goal was to understand the significance of the oxidation process. In the powder-gel samples, the question arose whether replacing the grain boundary 5% ZrC with 5% ZrO_2 would perform an immediate passivation of the surface. A substantial yield of ZrO_2 would be immediately available without the exothermic oxidation of ZrC that would raise the local temperature. The composite of 5% ZrC using the gel coating, also known as Z5C14 (with residual carbon), evaluated the improvements over the ZrB_2 standard, and addressed the question of whether a small carbide phase in a well dispersed microstructure could assist in (sacrificial) passivation at $3000^\circ C$ similar to SiC performance at $1500^\circ C$. The second powder-gel composites used an excess of carbon Z5C16 to effectively compare the effect of porosity and pre-graphitic carbon on the ablative performance. The last composite was powder mixed ZrB_2 -5ZrCp that effectively compared the effect of microstructure and homogeneity on the oxidation process, since the ZrC was not well distributed compared to Z5C14. Optical micrographs of all these samples are displayed in Fig 7.7.

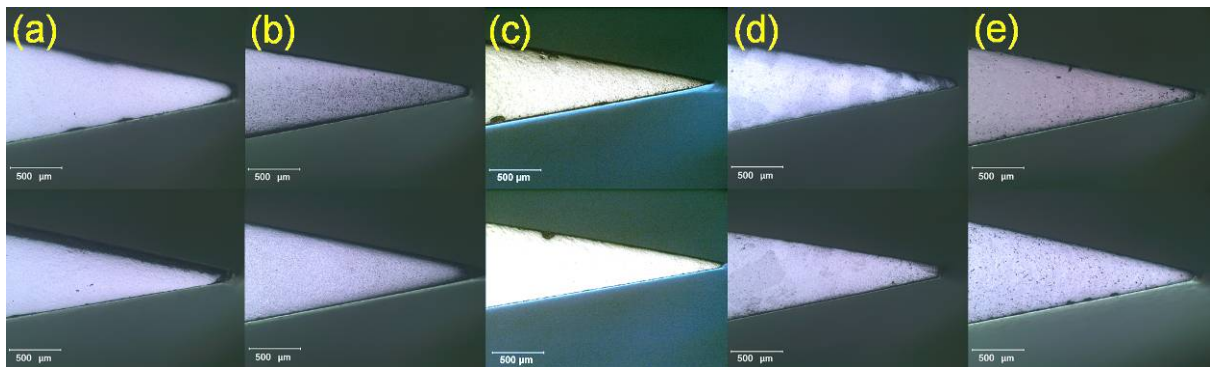


Fig 7.7. Pre-tested (a) ZrB_2 (b) ZrB_2 -5mol% ZrO_2 (Z5O) (c) ZrB_2 -5mol%ZrC (Z5C14) (d) ZrB_2 -5mol%ZrC plus carbon (Z5C16) (e) ZrB_2 -5%ZrCp powder mix.

Oxidation of ZrB_2 and ZrC phases takes place above $700^\circ C$ and $400^\circ C$ in air.³²¹⁻³²² Dense ZrB_2 had predictable specific heat, high thermal conductivity, high emissivity for cooling, and an adequate surface oxide scale that made it the leading candidate for these applications. Due to the majority of testing at below $2000^\circ C$ most have not actually tested for suitable compositions at the ultra-high temperature regime (i.e. above $3000^\circ C$) in open literature. While porous oxide scales were expected in all samples, the major question was whether it would

protect the underlying surface. This would depend on factors such as rate of formation of the oxide, thermal stability of the phase and thermal conductivity, which would determine if edge recession and geometry could be controlled.

7.2.2 Oxidation response of ZrB_2 at 3000°C

The facilities at DSTO included an oxyacetylene torch connected to a moving stage that was fixed during the test. The peak heat flux achievable was 10MWm^{-2} (1000Wcm^{-2}) with a peak temperature of 3400°C , although for uncertainty the minimum temperature 3000°C is cited here and through literature (as 3273K).^{223, 228, 320} This was verified by melting a standard of tantalum metal ($T_m \sim 3020^\circ\text{C}$), but the 3400°C temperature was measured by pyrometer. During the testing oxidation of ZrB_2 occurred as predicted with relatively stable leading edge geometry due to the high thermal conductivity that left only the tip at high temperature. The cross-section microstructure after 10s exposure was shown in the optical micrograph in Fig 7.8(a).

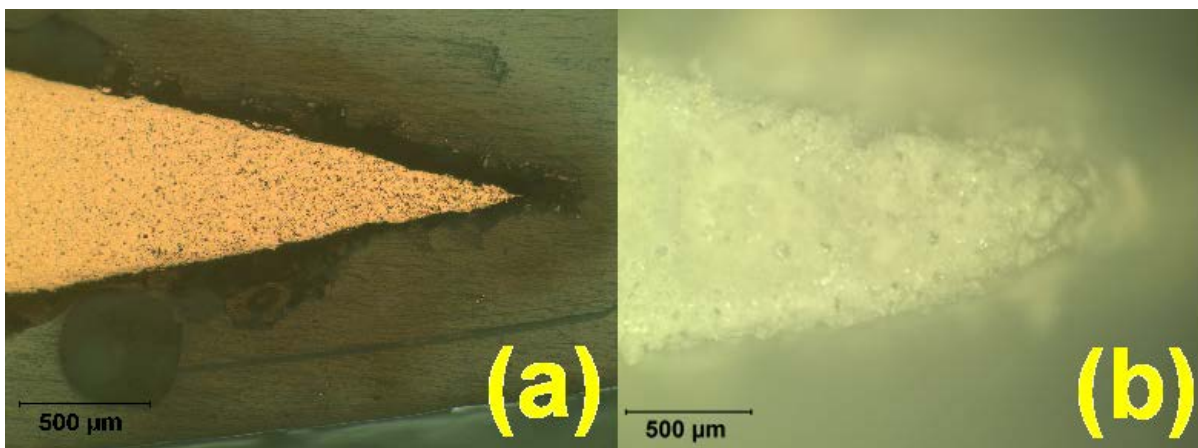


Fig. 7.8. Optical micrographs of ZrB_2 after exposure at 3000°C for 10s **(a)** showing the cut cross-section **(b)** surface morphology immediately after the test showing the white oxide scale coating the entire tip.

Fig 7.8(b) shows the tip immediately after the test with a layer from Fig 7.8(a) of oxidized material about $200\mu\text{m}$ thickness uniformly on all surfaces. The ceramic wedge was surrounded by a smoother epoxy mounting denoted by the glassy green. However, detachment in several regions downstream occurred on this

oxidized material, which was confirmed by XRD to be monoclinic zirconia. Further detachment of the oxide scale occurred during sample preparation for SEM.

The EDS analysis in Fig 7.9 showed the general morphology and composition of the zirconia scale. The oxygen and carbon K series EDS maps are attached in Fig 7.9 for reference. These can qualitatively define gradient concentrations of elements in the oxide scale and the epoxy boundary.

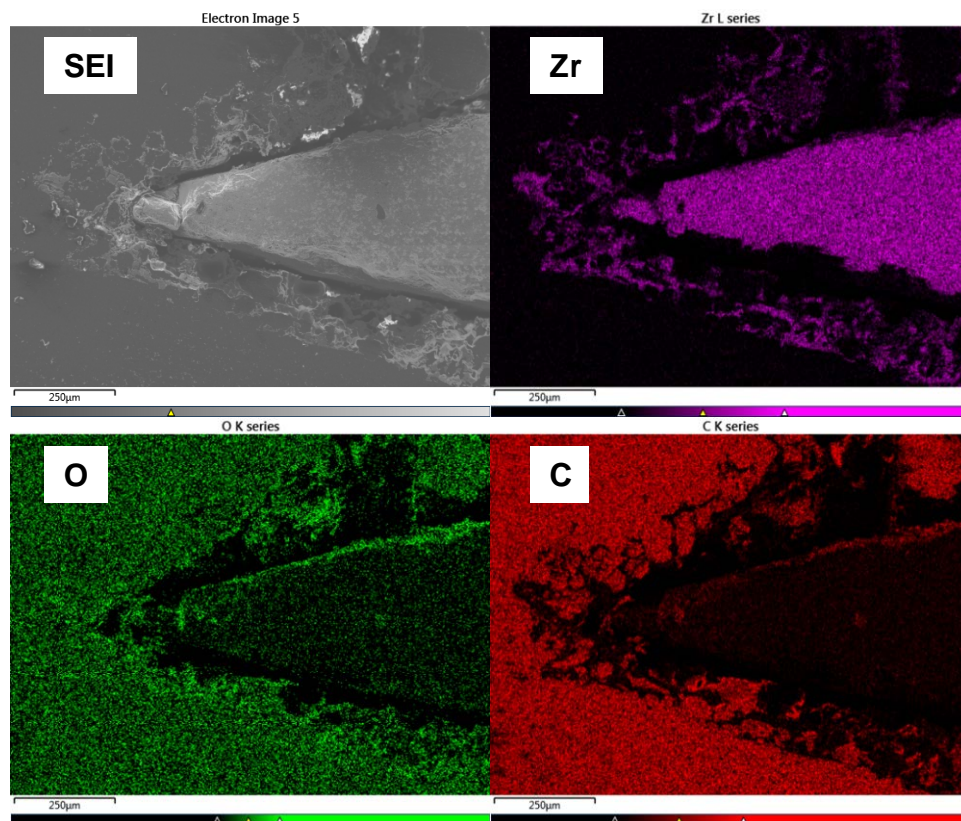
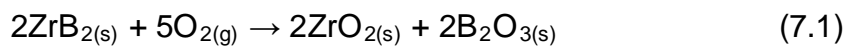


Fig. 7.9. SEM image and EDS analysis of ZrB_2 tip oxidized for 10s at $10MWm^{-2}$.

However, note that epoxy contains both C and O, and so Fig 7.9 does not actually show more oxide film on the upper surface, but the inclination of the sample. Boron was not detected at this magnification due to the low x-ray energy, detector absorption window and the saturation by other emitted x-rays, particularly at 15kV. The initial 1mm of the tip showed significant porosity and gaps in the Zr scale that clearly exposed the underlying surface to further oxidation. Both Fig 7.8(a) and 7.9 showed prominences and eruptions on the

surface, as well as non-uniformity in the surface film. The evolution of gas products was likely responsible for this morphology. The compounds of boron and oxygen as boric acid and boria only have thermal stabilities ranging from 450°C-510°C (depending on crystal structure) to a maximum of 1500°C where sublimation becomes thermodynamically favourable.^{14, 248} The SEI of the tip taken after testing in Fig 7.9 and the optical image of the tip in Fig 7.8(b) showed significant porosity that indicated that incomplete densification. If densification had occurred, oxygen would not have penetrated as far into the wedge, and surfaces would not be available for reaction. There was evidence that supported the production of gas products during the test. A gradient of porosity was observable, which decreased from the ceramic tip in Fig 7.8(a). At 3000°C, the reactions 7.1-7.3 were likely;



which could be described by the microstructure in Fig 7.8(a). It was possible that significant boria formed along the grain boundary, produced volatile gas products surging to the surface and caused the imperfections in the surface film. It appeared that the short duration of the test did not allow the formation of a stable zirconia film, and thus the catalytic activity of oxygen continuously fed reaction (7.1) within the first 2mm of the tip. This indicated that some grain boundary zirconia would also be present. It was likely that the evaporation of boria, as well as high thermal conductivity and radiative dissipation, contributed to the heat transfer away the tip during the test since geometry was maintained.

Formation of liquid phase during the testing was only observed after 180s. This was likely after significant oxidation occurred on the ZrB_2 grains. Note that reaction (7.1) was a significant mass gain (35%) that may counter any ablative or evaporative mass loss. Fig 7.10(a) showed the cross-section after 180s exposure to the oxyacetylene flame at 3000°C. It can be seen that the ceramic tip was surrounded by a thicker oxide scale of about 300µm, but in this region it appeared that significant detachment occurred. During sample preparation for

polishing and cutting, the epoxy was able to infiltrate in-between to the undamaged ZrB_2 surface. The evidence suggested that the permeation of oxygen was significantly reduced after the scale was established. The porosity gradient from the 10s exposure was notably absent in the 180s sample. Secondly, the oxide scale was denser. The third fact was that the formation of a liquid phase may have assisted in better sealing the surface against oxygen.

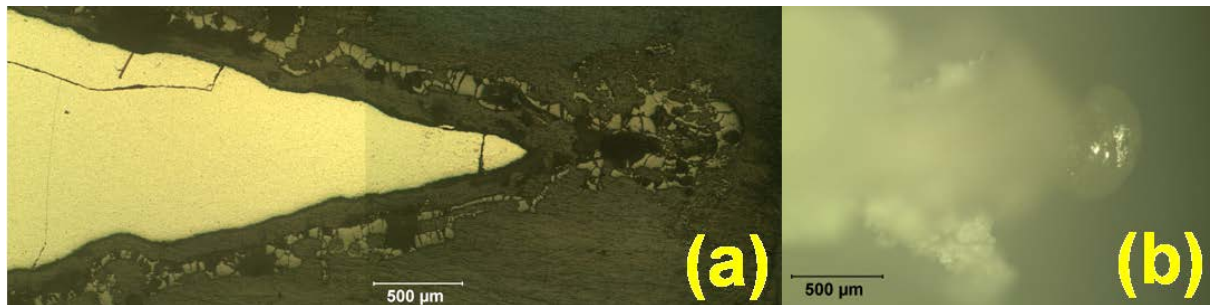


Fig 7.10. (a) ZrB_2 microstructure after 180s exposure and **(b)** tip immediately after testing at 3000°C.

Images taken immediately after the test in Fig 7.10(b) showed that melting had occurred on the tip due to the glassy appearance, wetting angle and curvature of the droplets. This may indicate that the following reaction occurred once an appreciable portion of the tip reached a temperature sufficient to start reaction 7.4 observed under several oxyacetylene methods that exceed 2500°C;^{144, 320, 323}



The term ‘appreciable’ portion was used because radiative heat losses were likely significant as reported by Monteverde and Sciti et al.^{221, 251} Thus the sample may be drastically cooler as the distance from the tip increased. If so, then liquid ZrO_2 likely solidified once it reaches cooler regions downstream of the tip. Three processes thus consume energy endothermically; boria sublimation, boria evaporation and the latent heat absorbed that was required to liquify zirconia. It was unknown from these two static 10s and 180s oxidation tests how much liquid ZrO_2 moved downstream and assisted in sealing the surface. The morphology of the tip supported the idea that liquid zirconia did not abruptly solidify at a fixed distance from the tip. If this was so, there would have been a buildup of ceramic

material representing the boundary region where the temperature dropped to below 2500°C. Densification may have also occurred to maintain the oxide layer. The continuous oxide scale may be possible because zirconia was an insulator and maintained a different thermal gradient. However, without modelling this was highly speculative. The process of liquid formation at the tip and solidification downstream could also be a part of a heat transfer process that kept the leading edge geometry relatively stable. The wedge was handled within a minute of cooling from 3000°C. The formation of amorphous glass was a possible outcome from the rapid cooling.

There are conclusions to be gained from the control ZrB_2 specimen. The detachment of the oxide scale on cooling was likely due to the different coefficients of thermal expansion (CTE) of ZrB_2 and ZrO_2 ; while in the same order of magnitude, ZrO_2 has twice the CTE of ZrB_2 .⁶¹ Solidification of ZrO_2 from liquid had three potential crystal structures, which could cause oxide scale fragmentation. Therefore all the observed microstructures are “frozen” with the incoherent oxide scale likely represented damage from cooling. In other words, the oxide scale was probably attached during the test. While ZrB_2 performed well in terms of leading edge stability, the oxide scale was mostly porous, non-uniform and detached on cooling. The cracks in Fig 7.10(a) were observed during cross-sectioning and polishing, and were not observed in other samples. This indicated that internal stresses made it more susceptible to damage. The source of the zirconia may have been a liquid-solid pool at the tip that formed when ZrB_2 completely oxidized. This may have been a superior diffusion boundary against oxygen over the porous oxide in cooler zones.³²⁰ Zirconia has thus formed in a temperature regime suitable for densification. However, the extent of the coverage of the oxide over the surface was not fully determined. The instinctive response from these microstructures would be the encouragement of a thicker oxide scale by providing an oxide source.

7.2.3 Z50 powder-gel (ZrB_2 -nc- ZrO_2) at 3000°C

Using the powder-gel process with the PFA component significantly removed resulted in a well dispersed oxide phase in ZrB_2 . This oxide phase was investigated to determine whether providing a source of zirconia would assist in

surface passivation without an exothermic ZrC oxidation. However, under the oxidation testing, the sample tip immediately formed a liquid and the tip receded a significant 440 μm within 10s. This was nearly 2% of its original length. The tip recession was shown below from an filtered camera capture in Fig 7.11(a) where $t = 1\text{s}$ and (b) where $t = 10\text{s}$.

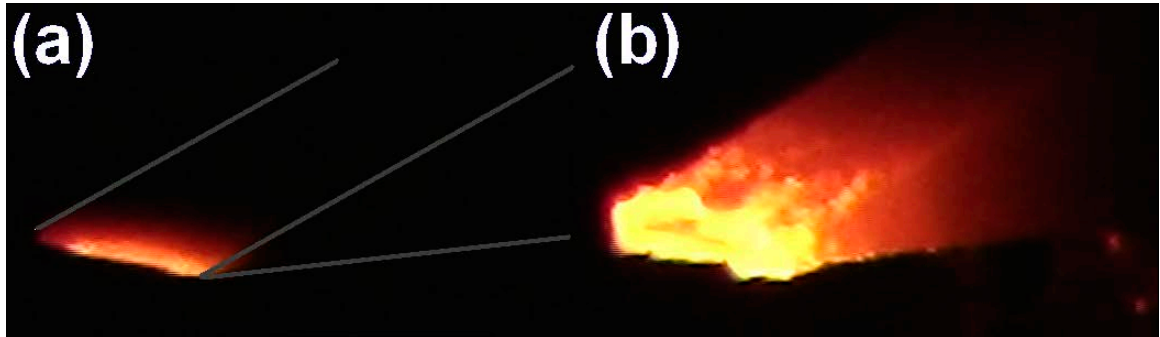


Fig 7.11. Filtered images of Z5O (powder-gel $\text{ZrB}_2\text{-5\%ZrO}_2$) tip oxidized at **(a)** $t = 1\text{s}$ with outline of the original geometry and **(b)** $t = 10\text{s}$ after recession.

The images were filtered from a small bandwidth of visible light, and the intensity of single color was an indication of temperature. The microstructure of the 5% oxide under the oxidation test within that 440 μm region could not be explored in detail. This was because same run at 180s showed no significant differences apart with tip recession measured at 450 μm from the starting position. This did suggest that the material stabilized at a particular distance, which must correspond to changed boundary conditions. It should be noted that the sample was still within the peak heat flux of 10MWm^{-2} . Fig 7.12 showed optical microscopy of the tip geometry after 180s exposure, which showed distinct tapering of the leading edge. The test results indicated that the recession was initially severe and then stabilized after 10s. The two recession distances from the combustion zone of 10s/180s were the same. Thus it was likely that the material composition could not tolerate the heat flux and receded to a position further away where conditions were less severe. The other alternative was that heat flux at both positions was the same, but the mechanism to prevent surface oxidation and recession took a significant time to activate. An oxide scale of thickness $\sim 200\mu\text{m}$ formed. Its formation likely contributed to the final stability of the geometry.



Fig 7.12. Tip of ZrO₂ sample after oxidation tests. SEI and EDS for atomic Zr on surface oxide shown from the circled region. Note the tapering of the ZrB₂ wedge, but the oxide coating that has a blunt tip ~ 1mm in width.

However, the recession was also matched by a mass gain of 0.35%, indicating that significant oxidation occurred. If the calibration was correct, then a possible explanation was that the thermal conductivity of the oxides at the grain boundary was too low, and the local temperature became higher than the melting point of ZrB₂/ZrO₂ because of the inability to transfer heat away from the tip. This would have caused the temperature to exceed 2500°C, causing reaction 7.4 to occur until a position was reached at 440µm from the origin where solidification of the grain boundary ZrO₂ could occur. The second possibility was that the grain boundary consisting of a surface zirconia film and zirconia micron-size particles simply melted and the composite flowed away from the heat source carrying ZrB₂ in a liquid zirconia flow. Both of these explanations result in recession of the tip.

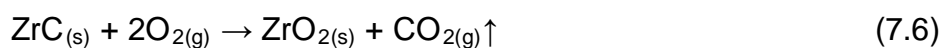
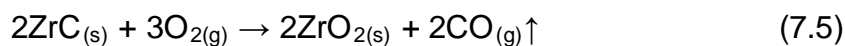
However, it was important to recall that this process was dynamic; filtered camera footage indicated that several seconds was required to establish steady state equilibrium of heat flux in and out of the wedge. In particular, radiative emission was a fourth power function of surface temperature. Thus the effect of insulating oxides could be inferred from the fact that emission rate was reduced because thermal conductivity was reduced by the oxides. A similar test between thermally insulating and conductive ceramics by Sciti et al reported similar results -

recession ceased once the process had reached thermal equilibrium and the heat flux in was balanced by the heat flux out, by which time the tip had melted and receded.²²¹ It was inadequate to simply state it was cooler 0.5mm downstream.

The presence of insulating oxide may also be inferred from the microstructure in Fig 7.12 due to the tip “tapering”. If the oxide built up more excessively on the tip rather than flowing or oxidizing downstream, a higher thermal load resulted on the surface oxide, and tapering of the tip occurred because the temperature was higher. As with the ZrB₂ sample, surface detachment occurred several millimetres downstream. The analysis of Z5O highlighted two key aspects of materials selection for extreme environments. The first is the sensitivity of thermal conductivity in phase selection and the prohibition of less refractory phases. Impurities found at the level of sintering additives ~ 5% can likely depreciate the performance of materials. This reduced their performance compared to pure compositions and resulted in immediate failure due to collapse of leading edge geometry.

7.2.4 Z5C14 powder-gel (ZrB₂-5%nc-ZrC)

The hypothesis was that this composite design would out-perform the others due to the controlled oxidation of ZrC, the formation of an immediate dense passivation scale of ZrO₂ and wetting from B₂O₃. The expected reactions included those of 7.1 to 7.4. But these would be superseded immediately by reaction 7.5 or 7.6;



as both these reactions were exothermic and favourable without significant applied energy since it can occur at RT. At 3000°C, ZrC was expected to be a good source of oxide. The reason why ZrC was usually avoided in UHTC composites was because the zirconia scale was porous and allows diffusion of oxygen through the scale, and eventually flaking off and exposing the substrate to further attack.^{61, 158, 321, 324} A third phase (e.g. SiC) is usually required to provide a phase to seal the pores at lower temperatures. However, there are differences

in these testing conditions, one of which was the higher temperature. In tests that approach 3000°C, zirconia may densify or form a viscous liquid and better seal the surface against oxygen diffusion.^{144, 325} Some promising liquid phase and densification of the oxide scale was observed in the ZrB₂ test. If assisted by distributed particles of ZrC, it may be able to establish an initially rapid oxide scale formation. This would ideally be followed by a slower steady-state parabolic weight gain compared to ZrB₂ because further oxidation was hindered. Fig 7.13(a) and (b) are filtered images of Z5C14 during testing. It showed the desirable features of control of the leading edge recession, stable geometry and a stable oxide scale.

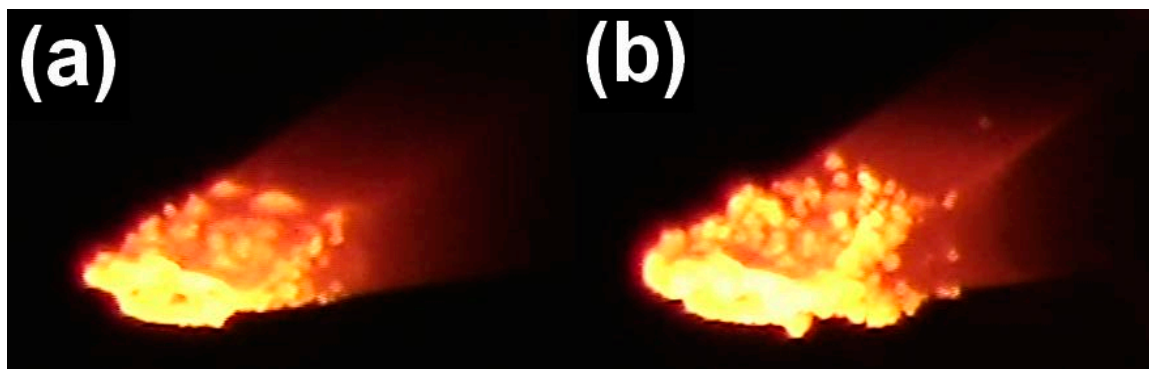


Fig 7.13. Filtered images of powder-gel composite ZrB₂-5ZrC tip oxidized at 3000°C **(a)** t = 10s and **(b)** t = 180s without recession and change in geometry.

The images in Fig 7.13 still suggest some challenges with the oxide scale. Later analysis indicated that the parabolic oxidation weight gain initially accelerated ahead of the ZrB₂ rate for the 10s sample. But at the 180s sample, this oxidation weight gain was below the weight gain of the ZrB₂ control at 180s. This was likely due to faster oxide scale formation and better sealing of ZrB₂ against further oxygen penetration as predicted. The edges in Fig 7.13 saw several humps on the surface could be surface gas pockets from reaction gases attempting to escape; these were prominently observed where the oxide scale was sufficiently dense or viscous.. Ideally, gases escape via a myriad of smaller pockets rather than a large coalesced bubble. This meant the oxide layer needed to be thick enough to prevent viscous flow, but not so thick as to cause large build-up of what are known as Bubble Burst Events.⁴⁶ This suggested that significant densification had been completed before trapped gases were removed, or the

viscosity of zirconia was high relative to the rate of gas evolution of reactions (7.2, 7.3, 7.5 and 7.6). Modelling was required to support temperature distributions across the surface. However, even in the filtered imaging, the temperature distribution was proportional to the distance from the tip at $t = 10\text{s}$. The distance from the surface oxide showed a temperature distribution as well, which suggested that the oxide trapped heat relative to the underlying conductive ZrB_2 wedge. This was tentatively supported by the temperature distribution of contours of visible light emitted from the wedge in Fig 7.13(b) that showed the convex boundary pointing toward the tip rather than away from it.

Fig 7.14 showed the initial tip at $t = 10\text{s}$ frozen after the test. Compositional EDS indicated the well defined limits of the leading edge geometry in both the C and O signals from the epoxy infiltration. The zirconia layer was excellent because it was uniform and thin, and was likely to trap less heat and prevent tapering of the leading edge.

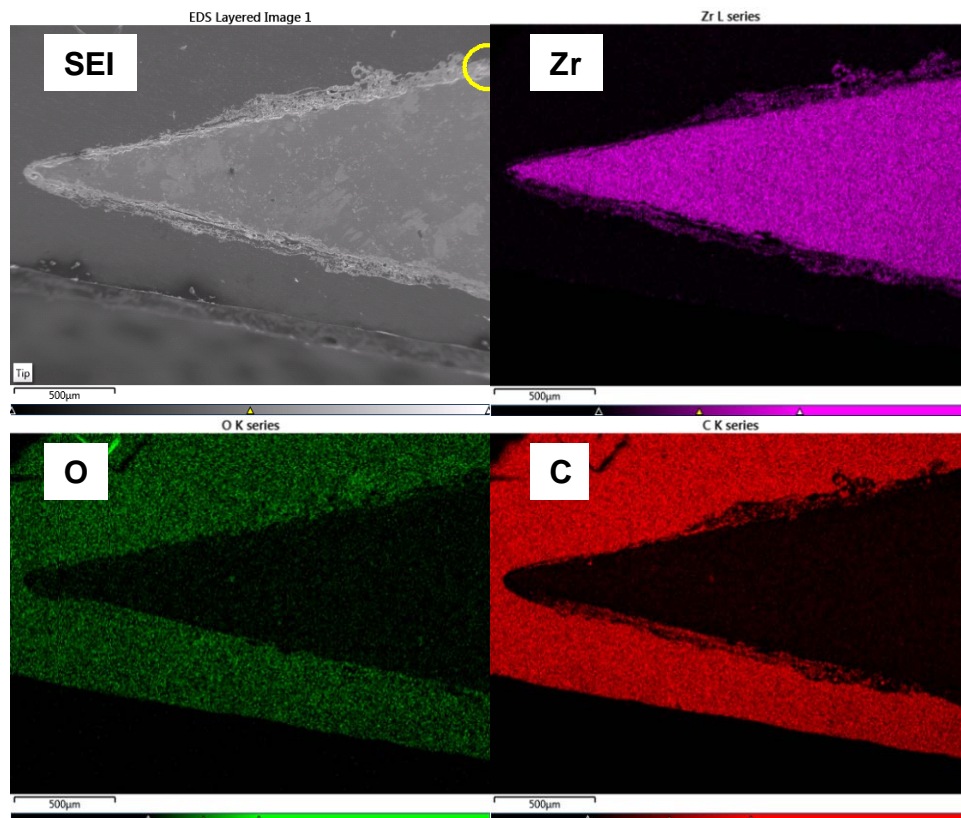


Fig 7.14. EDS analysis of Z5C14 tip oxidized for 10s at 10MWm^{-2} .

Prominences and eruptions downstream at $x > 1\text{mm}$ displacement from the tip indicated that gas evolution did disrupt the oxide layer stability. It was difficult to gauge whether the extensive oxide layer was formed by surface oxidation or simply by viscous flow of zirconia. Cooler regions downstream should have less zirconia in porous form. Hot regions should have dense “frozen” zirconia from solidification and more solid zirconia from oxide formation. But this is balanced by the flow of zirconia from hot to cold regions, as well as the fact that once zirconia formed on the hot zone, the underlying layer could be sealed against oxygen permeation. As long as the zirconia remained, further oxidation was unlikely. However the zirconia could be removed by thermal viscous flow (exposing the underlying surface) or through dissipation by evaporation or applied shear force. These described phenomena cannot be gauged. But it was clear the homogeneity of the sacrificial oxide phase lead to a thinner $<150\mu\text{m}$, more dense and uniform oxide layer at $t = 10\text{s}$ than control ZrB_2 . An analysis of the oxide layer confirmed that while superior to the ZrB_2 control specimen, some improvements could still be made. Fig 7.15 showed a higher magnification of the oxide layer at a downstream displacement of $x = 2\text{mm}$, highlighted by the circled region in Fig 7.14 of the leading edge. The O and C signal indicated the limit of the oxide layer by epoxy; the ZrB_2 substrate was at the bottom of the image because the higher oxygen signal corresponds to the zirconia film. The distinction between oxide layer and substrate was also clear in the SEI since the undamaged ZrB_2 was dense and polished, while the oxide is clearly porous and fragmented. The Zr signal denoted the oxide layer was under $150\mu\text{m}$ in thickness until it reached the oxygen in the epoxy, displayed in the C signal in the EDS. The C signal also showed that that the oxide layer had significant porosity due to the infiltration. The grain size in the oxide film in Fig 7.15 image showed fine grains $\sim 1\mu\text{m}$ at the interface between ZrB_2 and ZrO_2 , with larger grains $\sim 20\mu\text{m}$ on the top of the film. This correlated with the microstructure reported by Monteverde et al where above 2000°C zirconia can sinter upward in a globular shape.²¹⁵ But closer examination of the oxide layer pointed to evidence that indicated that the oxide scale was probably a liquid layer at some point. The larger grains at the surface suggested that the temperature was actually higher. This was consistent with ZrO_2 being an insulator and a poor conductor of heat. Heat dissipation occurs either by radiation or conduction to ZrB_2 .

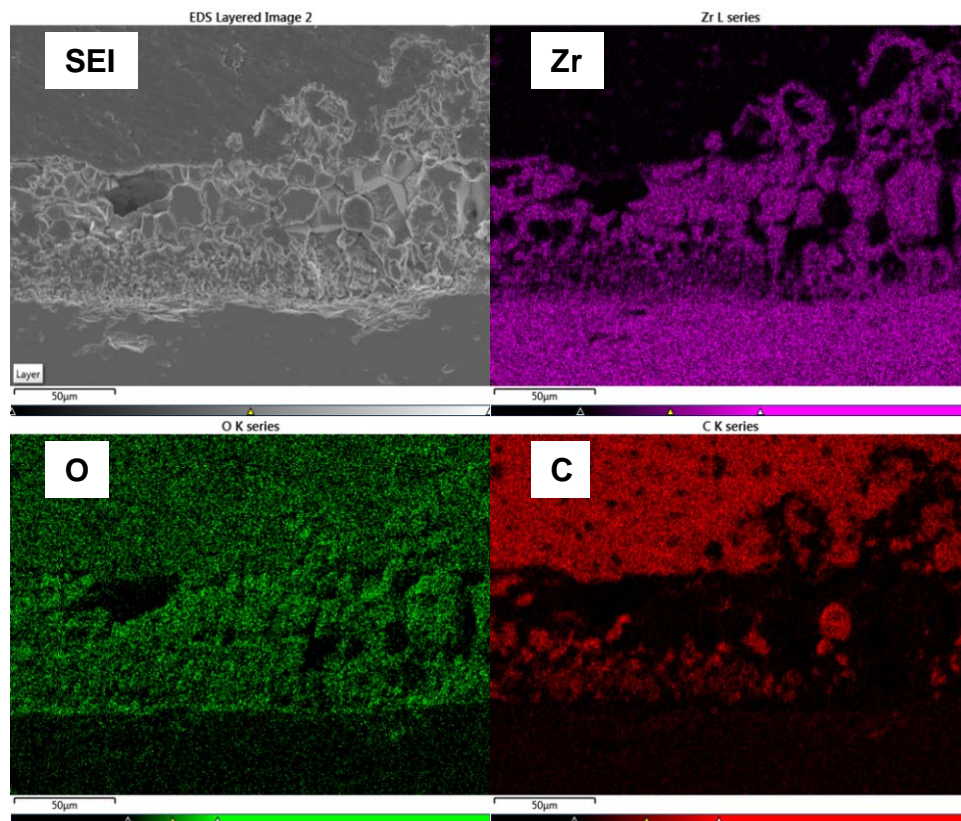


Fig 7.15. EDS of the surface oxide at downstream at $x = 2\text{mm}$

This explained the solidification microstructure because the smaller equiaxed grains are found at the interface, which must have cooled first. If this was a solidification microstructure, it suggested that the major contribution was cooling was conduction of heat into the substrate of higher ZrB_2 thermal conductivity rather than dissipation of heat from oxide radiation or convective cooling. This oxide morphology suggested that boria was liquefied or evaporated well within the surface film, moving upward to the surface where eruptions directed the zirconia film. These high angle shapes, particularly the morphology of the eruptions, would be consistent with a liquid layer rather than a solid oxide. The leading edge recession data for Z5C14 was the only unreliable data; it was reportedly 160 microns in the 10s exposure and only 30 microns in the 180s exposure time. Thus the recession data cannot be reliably used. However, the shallow parabolic weight gain was consistent with the predictions. The cross-section micrographs in Fig 7.16 indicated that the oxide layer was consistently

maintaining the leading edge symmetrically. The oxide layer was difficult to observe, particularly at $t = 10\text{s}$ due to the optically reflective ZrB_2 .

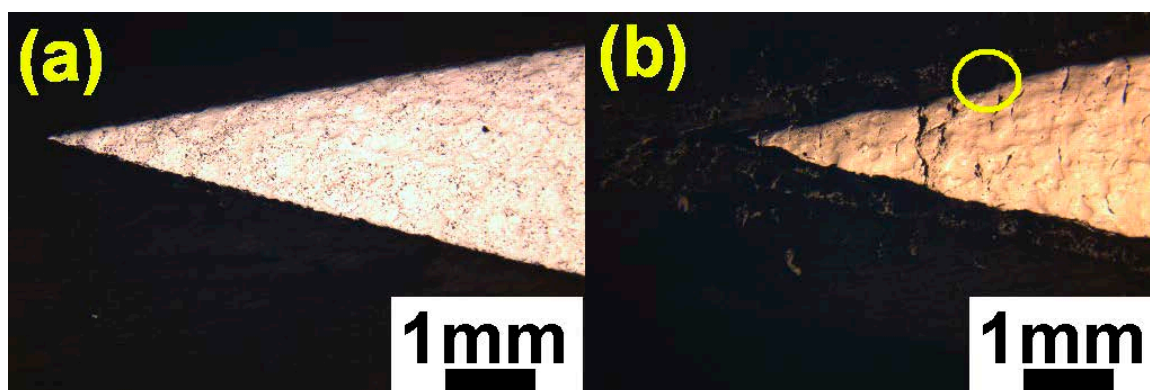


Fig 7.16. Leading edge geometry of Z5C14 after (a) $t = 10\text{s}$ (b) $t = 180\text{s}$

It appeared that performance was improved over the ZrB_2 control sample; the oxide layer was denser, slightly thicker and more adherent to the underlying surface. This was shown in Fig 7.17 (a) by the EDS Zr signal that denotes ZrO_2 encapsulating the original material. Fig 7.17(c) indicated that the source of matter at the tip may have also included liquid zirconia apparent from the wetting angles and glassy appearance after solidification. The morphology of the tip in Fig 7.17 (c) suggested that melt flow occurs away from the centreline, peeling back and symmetrically moving very slowly downstream. This indicated a very high viscosity or a low shear environment as expected. Even though the Z5C14 tip shown in solid color had maintained the general geometry, the cooled microstructure in Fig 7.17(b) did not appear to show a sealed surface. Cracking could have occurred during the cooling, or these could represent channels carved by jets of escaping gases. The large $100\mu\text{m}$ pores could have been caused by trapped gases. Porosity was still significant despite contributions from oxidation of ZrC . This indicated that diffusion continued through the zirconia. Comparative tests with SiC-ZrC indicated that the combination of SiO_2 from SiC and ZrO_2 from ZrB_2 could not seal the pores between intergranular zirconia and oxygen catalytic activity continued to build the oxide layer.²⁴²⁻²⁴⁴ It seemed unlikely that simply using the short-lived liquid B_2O_3 and ZrO_2 would have been sufficient to seal the Z5C14 surface. Similar events were observed in sealing the oxide layer at 2000°C in $\text{HfB}_2\text{-SiC}$, where a phase of HfSiO_4 forms as the stable but porous

layer because active oxidation of renders SiC ineffective after 1500°C.^{257, 326} To further improve the current composite, the zirconia layer from Z5C-series could still be improved by small tertiary additives of higher thermal stability, such as LaB₆, La₂O₃ and WC/W_xB_y to modify the oxide layer.^{158-159, 248} This could be done via a mixed sol-gel and distributed at the grain boundaries again.

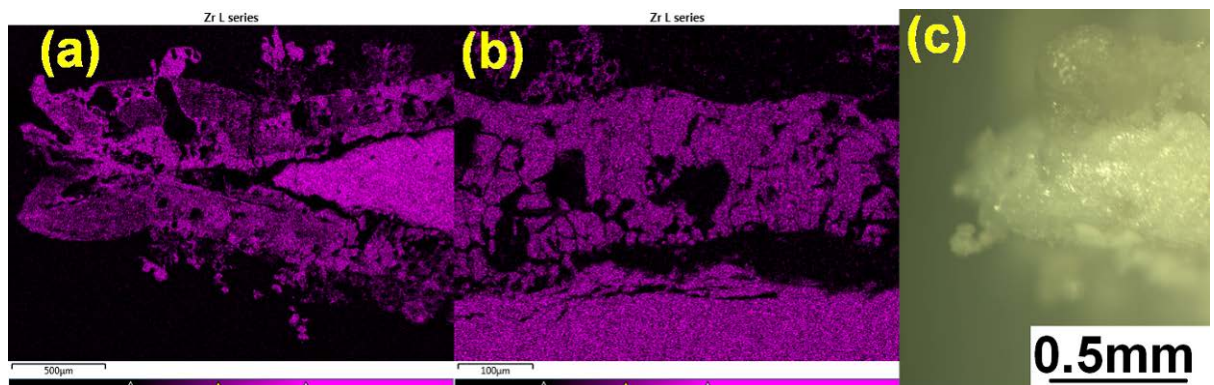


Fig 7.17. EDS analysis at 180s exposure of Zr in Z5C14 composite at (a) tip and oxide tip (b) surface film just before detachment (c) exposed tip under optical microscopy.

In summary, Z5C14 with distributed ZrC particles resulted in a more controlled oxidation after rapid build-up of the protective zirconia scale, resulting in consistent leading edge recession and geometric stability. It seemed likely that the protection was the result of a viscous liquid surface in hot regions with a reasonably dense oxide scale downstream. This composite was likely limited to the Ultra-High Temperature range, because zirconia densification is not available at low temperatures. The density and performance of the surface oxide could have improved density and wider temperature operation range by addition of oxide layer modifiers. These could be dispersed as homogeneously as ZrC.

7.2.5 Z5C16 powder-gel (88ZrB₂-4ZrC-8C)

This composition was the same as Z5C14 using 5% mol ZrC designed ratio but used excess carbon. This was defined by the sol-gel molar ratio as Z5C16. This was effectively a carbon rich porous version of the Z5C14 composite, except that due to protective carbon diffusion barriers on ZrC, no solubility was reported by

XRD. The carbon contributed to the lower density of the sample, similar to porous structures of ZrB_2 that used graphite additions.³²⁷ The approximate weight compositions by stoichiometry are thus 88% ZrB_2 -4% ZrC -8% C from the previous chapter of specimen compositions by Rietveld analysis. Such as excess of carbon, neglecting any densification of ZrC , corresponded to similar reported porosities of 6-10% by Mishra et al and Zhu et al.^{197, 297} Nevertheless, oxidation testing of this microstructure explored three pertinent questions. The first was the effect of carbon on the high temperature performance of the microstructure. The second was that high porosity should result in more oxidation due to higher surface catalytic activity from gas diffusion into these surfaces and third was the performance of the zirconia layer and whether it sealed against oxygen intrusion. The oxidation cross-sections are shown in Fig 7.18 for (a) $t = 10s$ and (b) $t = 180s$.

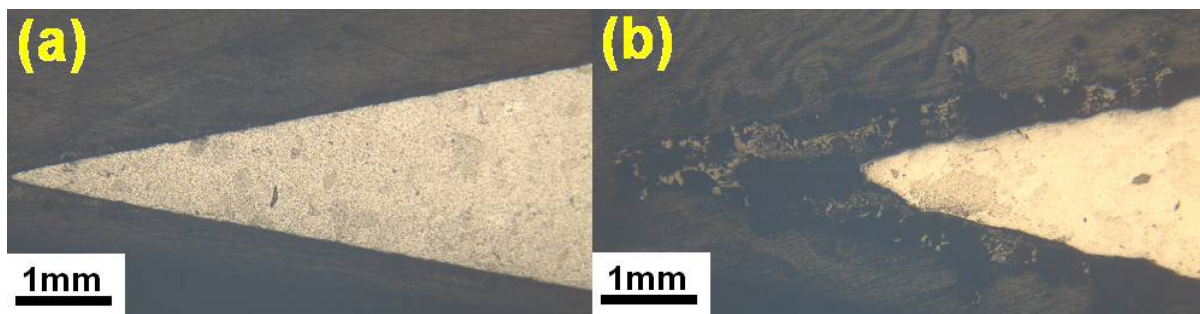


Fig 7.18. (a) Z5C16 exposed $t = 10s$ and (b) exposed $t = 180s$ oxidation.

Z5C14 and Z5C16 possessed the same microstructural distribution of ZrC , although Z5C16 does show regions of heavier carbon content from PFA-derived clusters. This was later compared to a powder-mixed sample that also had residual carbon and porosity, but had a coarser and less homogenous distribution of ZrC . There was very little difference from Z5C14 apart from a reduced performance in leading edge geometry. The outer oxide layer and inner ZrB_2 leading edge angles did not match. The oxide layer was slightly thicker in this specimen than Z5C14 but was of the same porosity. The leading 2mm oxidized edge was suggested that oxygen diffusion continued to attack the leading tip of ZrB_2 . This could eventually result in failure because of reduced thermal conductivity of the oxide tip past $t = 180s$. Apart from melted ZrO_2 , this sample had the highest leading edge recession. It also had the lowest mass gain, indicating oxidation weight gain of reactions 7.5 and 7.6 that formed zirconia were

actually countered by mass loss. This was explained by the porosity of the oxide layer, which resulted in oxidation mechanisms from the surfaces toward the centreline at an accelerated rate. It was also more rapid because the first ablated mass of Z5C16 was probably from the 8wt% C. Thus carbon oxidation was added to boron evaporation that was not present in other samples. The carbon contribution was technically a detriment because the leading edge was losing mass without absorbing energy and not using the mass efficiently to build the oxide layer. In fact, the oxidation of carbon was exothermic like reactions 7.5 and 7.6, but increased gas activity to the surface that probably reduced the performance of the oxide scale or layer. The undamaged ZrB_2 tip had actually tapered and truncated likely because the oxidation was more severe. However, it indicated that the distribution of submicron ZrC still allowed for the formation of stable oxide layer and some control of leading edge recession and geometry.

7.2.6 ZrB_2 -ZrC powder composite

The powder mixed sample was a control using the same composition as Z5C14, but mixed in ZrB_2 and ZrC powder form. As a powder mixture, the distribution of ZrC particles, particle size and ZrB_2 grain size was coarser up to about an order of magnitude. However, it effectively addressed the question of whether the oxidation and surface film formation was affected by microstructure. Intrinsicly, this was a recognition that the catalytic activity of oxygen was still a mass transfer and exchange reaction, and access to reactants depend on factors such as grain boundaries, surface diffusion and the particles that feed the passivation layer. Studies in corrosion have confirmed the role of microstructure in the homogeneity of the surface attack.³²⁸⁻³³⁰ If the hypothesis was correct about the powder mixed composite, it likely must suffer more oxidation or inhomogeneous oxidation compared to the powder-gel sample. Fig 7.19 shows the immediate oxidation response at $t = 10s$ with supporting EDS microstructures. The dynamic oxidation of this material was spectacularly different to the response of Z5C14. Large prominences and eruptions occurred on the surface, visible even under optical microscopy. The SEI clearly demonstrated evidence that first $100\mu m$ of the material suffered immediate oxidative damage.

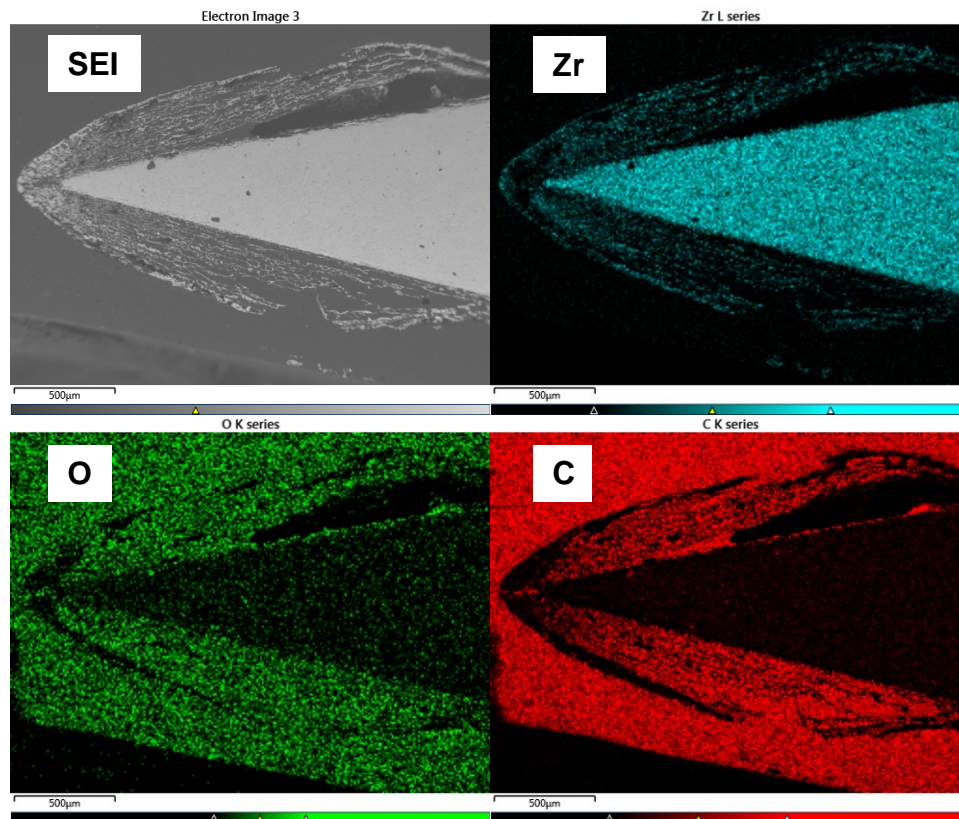


Fig 7.19. EDS analysis of $\text{ZrB}_2\text{-ZrCp}$ tip oxidized for 10s at 10MWm^{-2} .

The reaction began with a mixture of ZrC and ZrB_2 , respectively contributing zirconia and boria under these conditions. This oxidation product erupted from the tip and flowed downstream, with a corona that may correspond to the convective flow established by a temperature that was based on the combustion boundary layer. It was likely that this was a mixture of gaseous boria, carbon monoxide and droplets of liquid zirconia. Cooling occurred within a distance of 4mm from the tip; the eruptions could actually be traced to starting from the origin to about 500µm downstream in Fig 7.19, which suggested the whole region upstream was near the melting point of zirconia. It was important to note in the Zr EDS map that a taper of ZrB_2 was present at the tip at $t = 10\text{s}$ in Fig 7.19, heavily emphasized by the time $t = 180\text{s}$ in Fig 7.20. Tapering was already observed at $t = 10\text{s}$, which as previously noted indicated that surface oxide formation was too thick relative to the conductive substrate, trapping the heat. The tapering continued till $t = 180\text{s}$ and the leading edge geometry was lost, shown by the EDS and microscopy in Fig 7.20. When tapering occurred, more material melted

at the tip, further decreasing the conductive heat flux because zirconia was an insulator. However, the actual recession was less than $20\mu\text{m}$, which indicated that this specimen ironically had the best resistance to leading edge recession.

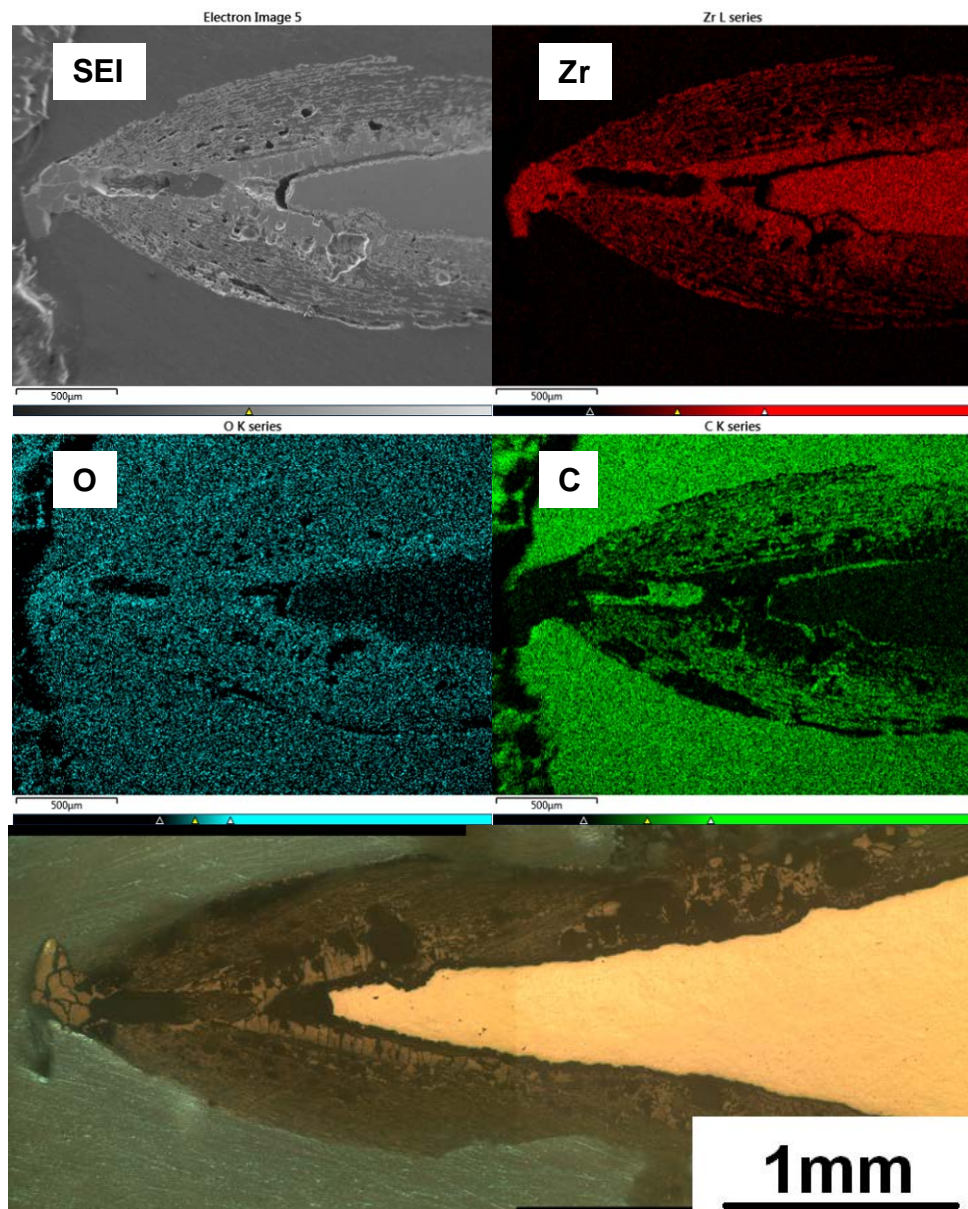


Fig 7.20. EDS analysis of $\text{ZrB}_2\text{-ZrCp}$ tip oxidized for 180s at 10MWm^{-2} and final microstructure by optical microscopy.

This illustrated the complexities of establishing a standard for ablative testing for structures. This may also represent why research toward using ZrC has been limited, since few efforts have been made to co-disperse or functionalize UHTC powder surfaces. Nanosize ZrC must still be made in the lab.

Downstream of the tip, the oxide layer at $t = 180\text{s}$ in the optical microscopy image in Fig 7.20 suggested that conditions were similar to those found in other ZrB_2 samples. However, it was probably assisted by deposition of material that precipitated from the oxyacetylene combustion corona. The oxide layer thickness and densities were comparable, although it should be noted that more oxide was present due to a deposition process after the zirconia cooled outside the combustion zone. The EDS and SEI images in Fig 7.21 show the oxide layer formation at $x = 4\text{mm}$ downstream.

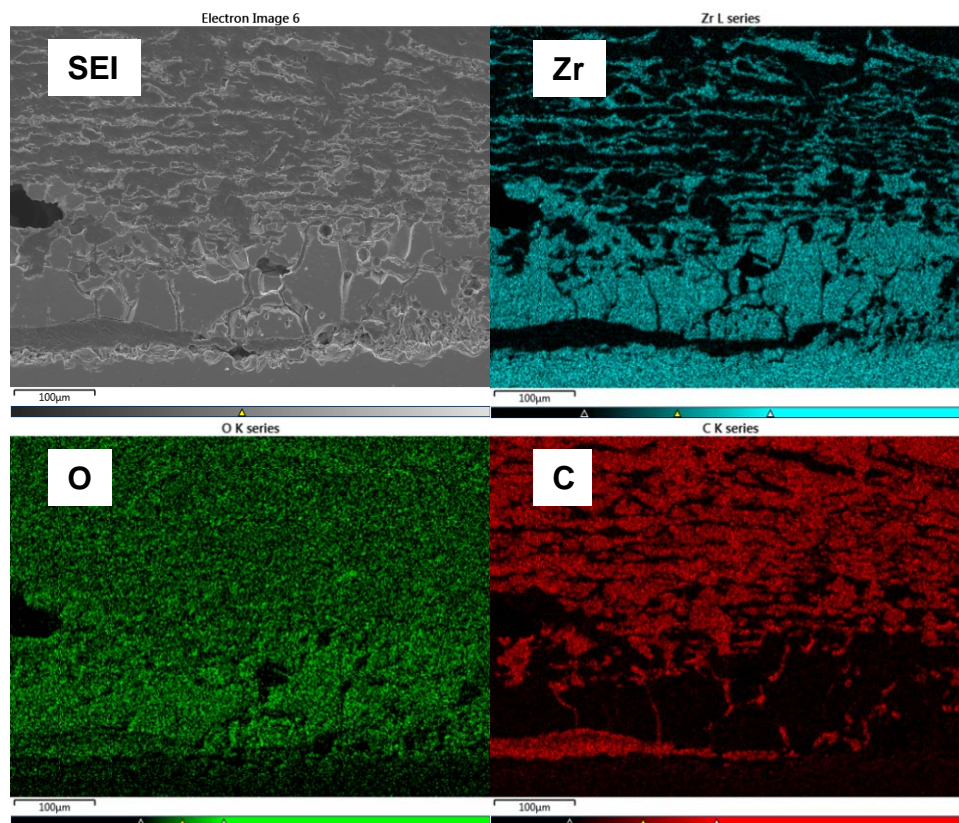


Fig 7.21. EDS analysis of $\text{ZrB}_2\text{-5ZrCp}$ layers oxidized for 180s at 10MWm^{-2} downstream 4mm from the tip.

Weight gain data (shown later in Fig 7.25) showed that the powder mixed sample initially had a low mass gain, indicating less oxidation. This is unlikely given the microstructures shown. The oxidation gain was likely compensated by material lost during the violent ejection. This is validated by the mass at $t = 180\text{s}$, which showed that the sample had the highest weight gain of all the samples, indicating that oxidation rate was both higher and at a higher rate than the control ZrB_2

behaviour. This would normally indicate in a conventional powder study that adding 5% ZrC nanoparticles was not good compared to the ZrB₂ control. This correlated well with previous literature on the disadvantage of adding ZrC to composites, all of which used powder mixing.^{61, 158, 321, 324} There are several explanations for this failure of leading edge geometry and it is derived from microstructure. Porosity can be eliminated as a reason; Z5C16 had higher porosity than this powder-mixed sample. This powder mixed sample also had less residual carbon than Z5C16. However, Z5C16 demonstrated a stable leading edge recession. Experimental conditions were consistent. Tapering proved that damage was not occurring from the direction of the heat source. Thus microstructure of the way the oxide layer formed were more likely explanations for the dynamic oxidation morphology. Thermodynamically, the reaction for oxidation of ZrC exothermic and a propagating reaction can occur easily under these conditions. But in Z5C14, ZrC was micron to submicron in size. As such, it was not unreasonable to assume that the reaction of 7.5 and 7.6 were dynamically smoother over time. This may be due to oxidation of a large number of small grains as opposed to a small number of large grains. The linear distance ablated in order to acquire sufficient oxide for the layer was much less. The availability of ZrC as oxygen diffused into the composite surface would be more consistent, and a thinner depth of oxygen diffusion was required to establish an oxide film. Thus this indicates that the microstructure of ZrC distribution plays some role in forming the oxide layer. Consider the powder mixed sample. It would have experienced sudden rises in temperature from oxidation of particularly large ZrC particles, forming a sudden mass of insulating zirconia which would likely trap the heat. The microstructure played its role here. Considering oxidation was also centripetal, the effective result was the creation of ZrO₂ particles in substantially large spheroids dispersed around the tip. In spheroid form, surface area was reduced, and this likely minimized the ability to remove the heat. Under real conditions of high shear environments, a spheroid of zirconia might flow downstream, increase its relative surface area and thus dissipate its heat to ZrB₂ by surface contact and provide surface passivation. In this case, perhaps no flow occurred. Energy was contained at the tip until regions violently boiled or were ejected, and were driven downstream through the boundary layer conditions created by the oxyacetylene combustion zone. The upper and lower surfaces

were probably attacked first, and this resulted in the excessive tapering as they were preferentially oxidized.

In this case, it opened the idea of a new understanding of “thermal” flaw sensitivity of UHTCs. This was noted in Z5O of the flaw of including impurities of insulating or thermally inferior phases, correlated by MoSi-S₃N₄ comparisons by Sciti et al.²⁵¹ But if the passivating phase was poorly distributed or inhomogeneous, the oxidation behaviour could be very different. This powder mixed sample suggested that the distribution affected the morphology of the oxide protective scale, the oxidation behaviour and leading edge stability.

7.2.7 Leading edge recessions and weight losses

This section summarized the data from the leading edge recessions that were observed in the individual microstructures. These were measured immediately after the test. Fig 7.25 summarises these weight changes concisely in one chart.

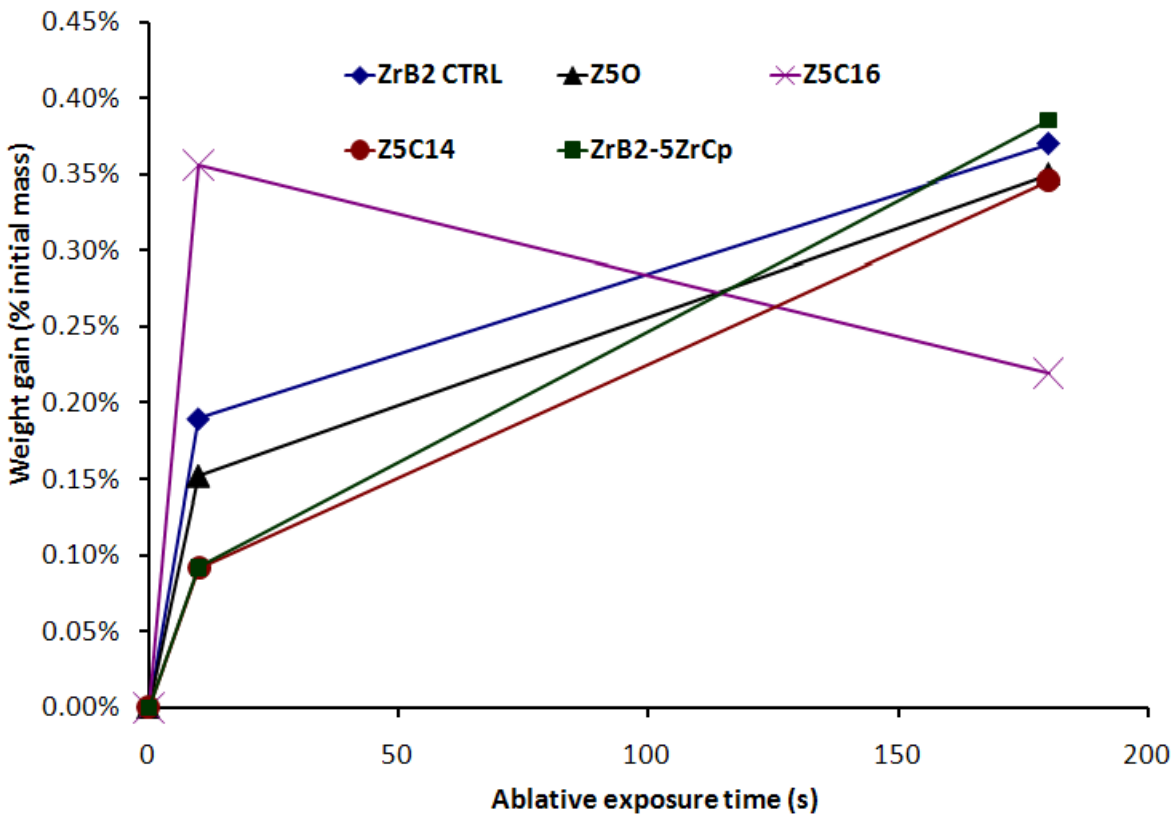


Fig 7.25. Weight gain as a percentage of initial mass, denoting that most of the composites (comprising 95% ZrB₂) modified the parabolic oxidation of ZrB₂.

General patterns emerged from this data. The general solution to ablation environments were to allow the material to oxidize and passivate, resulting in a parabolic weight gain. Sublimation or evaporation of a portion of this layer allowed for a heat-for-mass exchange. Passivation and heat dissipation reduce both oxygen diffusion and catalytic activity, and reduced the mass gain over time once an equilibrium was reached. The powder gel Z5C14 had the lowest weight gain over the others because oxidation of ZrC established a passivation layer quickly. Powder-gel Z5C16 resulted in a massive initial weight gain probably due to heavy oxygen access into the porous structure. Once the oxide layer was established, the weight gain was reduced for both Z5C series. Z5O showed lower weight gain than ZrB₂ due to the fact that ZrO₂ likely prevented oxygen from diffusing sufficiently in to access the ZrB₂ grain boundary. However, this did not reflect the failure of the material. Even neglecting the drastic difference in microstructure, ZrB₂-5ZrCp and Z5C14 had the same mass gain (formation of oxide) at 10s.

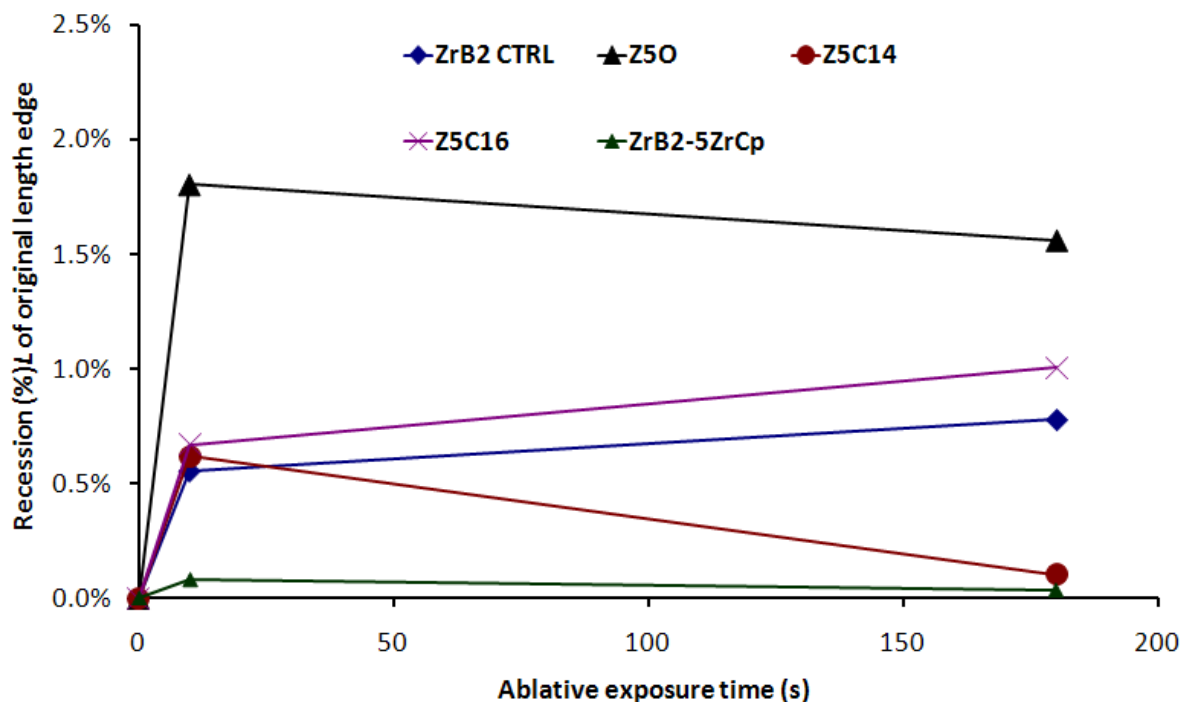


Fig 7.26. Leading edge recession lost (in % of the original length). This can appear parabolic because of increasing cross-section and mass moving away from the tip.

It was clear that it was used more effectively to protect the ZrB_2 surface, since the mass gain of Z5C14 at 180s was lower indicating less oxidation. The powder mixed ZrB_2 -5ZrCp also may have had low mass gain due to heavy ablation losses, but certainly the oxidation mass gain at 180s was higher due to the inability to establish an oxide layer. The loss of the leading edge was summarized in Fig 7.26. This cannot be considered even similar to “linear mass ablation rates”, which are found in the common perpendicular exposure of flat specimens to the oxidizing environment that assume semi-infinite solid calculations.^{243, 323, 325, 331-332} This is the disadvantage of leading edge testing. Modelling using increasing cross-section area starting from tip distance would be complex; this was emphasized by the apparently excellent result of ZrB_2 -5ZrCp (which had a tapered tip that did not recede). Z5O showed tip loss and then remarkable recovery, but does not describe the fact that the geometry became obtuse within 10s of exposure. Z5C14 data was not exact, but the edge recessions from microstructure were comparable to the ZrB_2 control and Z5C16. But leading edge recession does not account for the oxide layer, geometry and reaction processes. This was particularly true for the ZrB_2 -5%ZrCp. Thus leading edge recession should be taken as a guide to microstructural analysis.

7.3 Summary

The research demonstrated that only a small addition of ~5% ZrC was required to change the nature of the ablation/oxidation process and that the protective layer need only in the order of hundreds of microns in thickness to protect the substrate material. In terms of analysis of sharp leading edges, leading recession needed to be correlated with geometry. Weight loss was only indicative of reactions that took place, and should be interpreted only as static TGA accompanied by knowledge of basic processes. Both of these results are thus guides for deeper optical, microstructural and phase analysis of the material. ZrB_2 as a candidate for leading edge geometries under extreme environment conditions was re-validated. This research demonstrated that the effect of a 5% addition of an inferior phase of either lower thermal conductivity or lower thermal stability was disastrous to the oxidation performance. Thus residual carbon was likely better than residual oxide for this extreme environment performance. Using

ZrC as a gel-derived phase yielded the best result. A superior microstructure promoted better oxidation resistance, due to the more homogeneous build up of surface oxide formation. Thus using sol-gel to form powder-gel composites gives the significant ability to control the microstructure and the oxidation process.

8. Conclusions

This research program determined that HfC and ZrC in nanopowder form could be produced by a sol-gel process. Control of room temperature wet chemistry showed that an oxide and carbon precursor could be mixed at a nano-level to allow carbothermal reduction to occur at very short diffusion distances. The crystallite size could be controlled by the amount of residual carbon, which clearly affected whether agglomeration occurred. This did not affect the centripetal diffusion mechanism but did change the agglomeration behaviour. Composite powders could be designed at 1-micron level homogeneity due to control of the coating and agglomeration of ZrC on powder surfaces. Thus the inclusion of a ZrB_2 powder mixing step resulted in a uniform coating of nanoparticles. With appropriate control of the surface reaction of oxide and carbon precursors, this was able to perform the same carbothermal reduction on the surface of the powder without agglomeration of the nanocrystals of ZrC. This special powder was ideal for sintering well dispersed UHTC composites because of the change in surface curvature and the driving force of a chemical reaction. These composites were processed using minimal parameters by SPS sintering. This resulted in microstructures that had small ZrB_2 grain size and were reinforced with submicron ZrC at grain boundaries. Testing indicated that the composites possessed better mechanical properties than their powder mixed counterparts. During high temperature oxidation, the superior distribution of sacrificially oxidized ZrC particles resulted in a controlled ablation of geometry due to a protective oxide layer.

8.1 Outcomes of research

This research demonstrated that the production of nanopowders could be simplified and shifted away from difficult and costly air-sensitive synthesis. It investigated the well-studied carbothermal reduction system to fill a research gap – that nanoparticle oxide-carbon reactions had not been addressed since the advent of nanomaterials. This resulted in better understanding and control of oxide-carbon synthesis and more accurate prediction of the final product from ZrO_2 to ZrO_xC_y to ZrC. This work also emphasized that powder mixing can be

replaced by coatings (and co-dispersions), in order to reduce impurities that lead to detrimental performance of UHTC materials. The use of a surface seeded coating of nanoparticle ZrC changed the sintering mechanism. It used the higher surface area of the nanoparticles, not the surface curvature of ZrB_2 as the driving force for sintering. Deliberately incomplete reduction of ZrO_xC_y and residual ZrO_2 drove a chemical reaction to assist in completing the densification at lower temperature. This resulted in improved properties. Use of minimal parameters offered the chance for this work to be adopted for pressureless sintering, where complex shapes could be made. More importantly, the simplicity of this process could easily modify any powder preparation method, with potential improvements of lower energy cost and better microstructural control. Current focus of ceramic microstructural control is on processing variables. Hybrid sol-gels, wet chemistry and co-dispersion techniques were required only where functional or catalytic properties were required. But this technique may revive interest in preparing specialty powders that can overcome the limitations of powder mixing in UHTCs. Sol-gel carbides allow for a relatively easy surface modification to be applied to a ceramic industry dominated by conventional powders. Pre-modified powders with a second phase of nanocrystals are a possible future of ceramic powder vendors. This logical first question is neglected in most ceramic processing: whether it is possible to change these limiting starting materials. This technique may be extended to other nanopowders and fibers. While other institutions focused on modelling and determination of the optimum leading edge radius or the mechanisms of oxidation resistance, this research program focused on control of the processing and microstructure.³³³ But specifically, this program offered three fundamental changes in the approach of designing materials for extreme environments. First, carbides of ZrC and HfC can be used as long as temperatures are elevated to the UHT regime. Carbides apart from SiC had been avoided; this program demonstrated that these can be beneficial in a higher temperature regime. Secondly, only small amounts were required. Due to limits of powder mixing, large contributions of the second phase were reported, simply to ensure an adequate surface oxide layer was produced. It was definitively possible to use 5% additions by careful selection of the second phase and controlling the way the second phase was distributed. Thirdly and most

importantly: microstructure plays a key role in the thermal stability and oxidation performance of UHTCs in extreme environment conditions.

8.2 Future work

The potential for future directions and improvement are briefly highlighted. The nanoparticles could be improved by determining a method to disperse or co-disperse and prevent excessive agglomeration. Improved residual carbon control would be beneficial. The composite formation was inhibited by the higher than expected oxygen partial pressure. This resulted in residual oxide and residual carbon composition overshoot, which can be improved by better processing. It would also be desirable to form nanocomposites by dispersing the nanoparticles even finer, or dispersing less (e.g. 2%) into the microstructure and prevent their coalescence. For applied research or manufacturing, pressureless sintering would be the next logical choice of study to open up the field of complex shaping of UHTCs. Future investigations into the oxidation testing will explore oxide layer modification. These third phases that are added already show promise even in cruder powder mixed methods by assisting in densification and preventing regions of detachment of the oxide layer on cooling that was common to all composite samples.^{158-159, 248-249} While the density of the surface layer is emphasized, compensating for a change in crystal structure in the oxide may also be relevant, given that all tested materials had zirconia detachment on cooling. But the advantage of this powder-gel process was the exact control over microstructure. For example, if WO_2 was the chosen modifier, future work might create Z5C14 with 1 in 4 substituted ZrC particles with WC (via a mixed sol-gel), or thinly coated WC (via pre-treatment) on ZrB_2 grains before forming Z5C14. Thus sol-gel offers the ability to truly dictate the oxidation behaviour because of good control over intergranular particles, grain boundary area and thus surface diffusion. Extension of testing time would extrapolate the behaviour of the oxide layer performance. Future work would also require modelling, with more data regarding the actual temperature and temperature distribution being essential. Carbides oxidize well before their thermal stability are challenged. Finally, if the project moves toward applied research in materials for hypersonic flight, access

to arc-jet or plasma torch in wind tunnels would be more ideal in determining composite behaviour in more realistic conditions.

8.3 Publications

The research project has produced two publications in an ERA A-class journal and a new journal in this field. Their current citations are in press:

Caen Ang, Tim Williams, Aaron Seeber, Huanting Wang, Yi-Bing Cheng, (2013) *Synthesis and evolution of zirconium carbide via sol-gel route: features of nanoparticle oxide-carbon reactions*, Journal of the American Ceramic Society, ISSN 1551-2916, DOI 10.1111/jace.12260 released 19 March 2013.⁶⁰

Caen Ang, Aaron Seeber, Kun Wang, Yi-Bing Cheng, (2013), *Modification of ZrB₂ powders by a sol-gel ZrC precursor – a new approach for ultra high temperature ceramic composites*, Journal of the Asian Ceramic Societies, June 2013.

There are publications are pending if support and facilities can be found: *“Densification and properties of ZrB₂-5%ZrC composite powder by sol-gel method”* (Chapter 6), *“Effect of phase selection and porosity in ZrB₂-5%ZrC sharp hot structure composites oxidized at 3000°C”* (Chapter 7) and *“Effect of thermal stability and microstructure in ZrB₂-5%ZrC leading edge composites oxidized at 3000°C”* using the ZrCp and Z5C14 (Chapter 7).

This list does not include unplanned, speculated publications with co-authors.

8.4 Facility acknowledgements

This research acknowledges the support received from three and a half years of the Australian Postgraduate Award of the Australian Government. The use of facilities within the Monash Centre for Electron Microscopy (MCEM) and CSIRO Process Science and Engineering increased the research output of this thesis. This research used equipment funded by Australian Research Council grant(s) RIEFP 99 and ARC CoE for Design in Light Metals. A special thanks to Chris

Wood and Sonya Slater for arranging time on DSTO facilities at Fisherman's Bend.

9. References

1. G. Effenberg, Ilyenko, Svitlana (ed.). , "Rogl, Peter: Boron – Carbon – Hafnium," *SpringerMaterials - The Landolt-Börnstein Database, Springer-Verlag Berlin Heidelberg* (2009).
2. D. Ghosh and G. Subhash, "Chapter 3.3 - Recent Progress in Zr(Hf)B₂ Based Ultrahigh Temperature Ceramics," pp. 267-299. in *Handbook of Advanced Ceramics (Second Edition)*. Edited by S. Shigeyuki. Academic Press, Oxford, 2013.
3. D. Sciti, L. Silvestroni, L. Mercatelli, J.-L. Sans, and E. Sani, "Suitability of ultra-refractory diboride ceramics as absorbers for solar energy applications," *Sol Energy Mater Sol Cells*, 109[0] 8-16 (2013).
4. M. W. Bird, R. P. Aune, F. Yu, P. F. Becher, and K. W. White, "Creep behavior of a zirconium diboride–silicon carbide composite," *J Eur Ceram Soc*, 33[13-14] 2407-2420 (2013).
5. N. Chandra, M. Sharma, D. K. Singh, and S. S. Amritphale, "Synthesis of nano-TiC powder using titanium gel precursor and carbon particles," *Mater Lett*, 63[12] 1051-1053 (2009).
6. M. Dollé, D. Gosset, C. Bogicevic, F. Karolak, D. Simeone, and G. Baldinozzi, "Synthesis of nanosized zirconium carbide by a sol-gel route," *J Eur Ceram Soc*, 27[4] 2061-2067 (2007).
7. Y. Yan, Z. Huang, X. Liu, and D. Jiang, "Carbothermal synthesis of ultra-fine zirconium carbide powders using inorganic precursors via sol–gel method," *J Sol-Gel Sci Technol*, 44[1] 81-85 (2007).
8. S. Venugopal, A. Paul, B. Vaidhyanathan, J. Binner, A. Heaton, and P. Brown, "Nano-Crystalline Ultra High Temperature HfB₂ and HfC Powders and Coatings using a Sol-Gel Approach," pp. 151-159. in *Advanced Ceramic Coatings and Materials for Extreme Environments*. John Wiley & Sons, Inc., 2011.
9. Q. Li, S. Dong, Z. Wang, P. He, H. Zhou, J. Yang, B. Wu, and J. Hu, "Fabrication and Properties of 3-D Cf/SiC–ZrC Composites, Using ZrC Precursor and Polycarbosilane," *J Am Ceram Soc*, 95[4] 1216-1219 (2012).
10. Y. Wang, X. Zhu, L. Zhang, and L. Cheng, "Reaction kinetics and ablation properties of C/C–ZrC composites fabricated by reactive melt infiltration," *Ceram Int*, 37[4] 1277-1283 (2011).
11. J. She, Y. Zhan, M. Pang, C. Li, and W. Yang, "In situ synthesized (ZrB₂+ZrC) hybrid short fibers reinforced Zr matrix composites for nuclear applications," *Int J Refract Met Hard Mater*, 29[3] 401-404 (2011).
12. S. R. Levine, E. J. Opila, M. C. Halbig, J. D. Kiser, M. Singh, and J. A. Salem, "Evaluation of ultra-high temperature ceramics for aer propulsion use," *J Eur Ceram Soc*, 22[14–15] 2757-2767 (2002).
13. F. Monteverde and A. Bellosi, "Oxidation of ZrB₂-based ceramics in dry air," *J Electrochem Soc*, 150[11] B552-B559 (2003).
14. W. G. Fahrenholtz and G. E. Hilmas, "Oxidation of ultra-high temperature transition metal diboride ceramics," *International Materials Reviews* 57[1] 61-72 (2012).
15. C. R. Wang, J. M. Yang, and W. Hoffman, "Thermal stability of refractory carbide/boride composites," *Mater Chem Phys*, 74[3] 272-281 (2002).

16. C. Bartuli, T. Valente, and M. Tului, "Plasma spray deposition and high temperature characterization of ZrB₂-SiC protective coatings," *Surf Coat Technol*, 155[2-3] 260-273 (2002).
17. J. Han, P. Hu, X. Zhang, and S. Meng, "Oxidation behavior of zirconium diboride-silicon carbide at 1800 °C," *Scr Mater*, 57[9] 825-828 (2007).
18. S. Meng, C. Liu, G. Liu, G. Bai, C. Xu, and W. Xie, "Mechanisms of material failure for fast heating up at the center of ultra high temperature ceramic," *Solid State Sci*, 12[4] 527-531 (2010).
19. D. Alfano, L. Scatteia, F. Monteverde, E. Bêche, and M. Balat-Pichelin, "Microstructural characterization of ZrB₂-SiC based UHTC tested in the MESOX plasma facility," *J Eur Ceram Soc*, 30[11] 2345-2355 (2010).
20. R. Borrelli, A. Riccio, D. Tescione, R. Gardi, and G. Marino, "Thermostructural behaviour of an UHTC made nose cap of a reentry vehicle," *Acta Astronaut*, 65[3-4] 442-456 (2009).
21. F. Monteverde, A. Bellosi, and L. Scatteia, "Processing and properties of ultra-high temperature ceramics for space applications," *Mater Sci Eng, A*, 485[1-2] 415-421 (2008).
22. R. Savino, M. De Stefano Fumo, D. Paterna, and M. Serpico, "Aerothermodynamic study of UHTC-based thermal protection systems," *Aerosp Sci Technol*, 9[2] 151-160 (2005).
23. E. Dugan, N. Diaz, S. Kuras, S. Keshavmurthy, and I. Maya, "Conceptual Design of a Vapor Core Reactor Rocket Engine for Space Propulsion." in Contractor Report, Lewis Research Centre Contract NAS3-26314. 1996.
24. S.-Q. Guo, Y. Kagawa, T. Nishimura, and H. Tanaka, "Pressureless sintering and physical properties of ZrB₂-based composites with ZrSi₂ additive," *Scr Mater*, 58[7] 579-582 (2008).
25. Q. Qu, J. Han, W. Han, X. Zhang, and C. Hong, "In situ synthesis mechanism and characterization of ZrB₂-ZrC-SiC ultra high-temperature ceramics," *Mater Chem Phys*, 110[2-3] 216-221 (2008).
26. C. Hu, Y. Sakka, H. Tanaka, T. Nishimura, S. Guo, and S. Grasso, "Microstructure and properties of ZrB₂-SiC composites prepared by spark plasma sintering using TaSi₂ as sintering additive," *J Eur Ceram Soc*, 30[12] 2625-2631 (2010).
27. D. Sciti, S. Guicciardi, and M. Nygren, "Densification and Mechanical Behavior of HfC and HfB₂ Fabricated by Spark Plasma Sintering," *J Am Ceram Soc*, 91[5] 1433-1440 (2008).
28. D. Sciti, L. Silvestroni, and M. Nygren, "Spark plasma sintering of Zr- and Hf-borides with decreasing amounts of MoSi₂ as sintering aid," *J Eur Ceram Soc*, 28[6] 1287-1296 (2008).
29. U. Anselmi-Tamburini, Y. Kodera, M. Gasch, C. Unuvar, Z. Munir, M. Ohyanagi, and S. Johnson, "Synthesis and characterization of dense ultra-high temperature thermal protection materials produced by field activation through spark plasma sintering (SPS): I. Hafnium Diboride," *J Mater Sci*, 41[10] 3097-3104 (2006).
30. D. Sciti, F. Monteverde, S. Guicciardi, G. Pezzotti, and A. Bellosi, "Microstructure and mechanical properties of ZrB₂-MoSi₂ ceramic composites produced by different sintering techniques," *Materials Science and Engineering: A*, 434[1-2] 303-309 (2006).

31. M. Pastor, "Metallic borides: preparation of solid bodies," pp. 457–493. in Boron and Refractory Borides. Edited by V. I. Matkovich. Springer-Verlag, New York (1977), New York 1977.
32. R. Teghil, A. Santagata, M. Zaccagnino, S. M. Barinov, V. Marotta, and G. De Maria, "Hafnium carbide hard coatings produced by pulsed laser ablation and deposition," *Surface and Coatings Technology*, 151-152 531-533 (2002).
33. K. G. K. Warriar and G. M. Anilkumar, "Densification of mullite-SiC nanocomposite sol-gel precursors by pressureless sintering," *Mater Chem Phys*, 67[1-3] 263-266 (2001).
34. L. Shi, H. Zhao, Y. Yan, Z. Li, and C. Tang, "Synthesis and characterization of submicron silicon carbide powders with silicon and phenolic resin," *Powder Technol*, 169[2] 71-76 (2006).
35. J. R. Groza and A. Zavaliangos, "Sintering activation by external electrical field," *Mater Sci Eng, A*, 287[2] 171-177 (2000).
36. R. Licheri, R. Orrù, C. Musa, A. M. Locci, and G. Cao, "Consolidation via spark plasma sintering of HfB₂/SiC and HfB₂/HfC/SiC composite powders obtained by self-propagating high-temperature synthesis," *Journal of Alloys and Compounds*, 478[1-2] 572-578 (2009).
37. H. O. Pierson, "Carbides of Group IV: Titanium, Zirconium, and Hafnium Carbides," pp. 55-80. in Handbook of Refractory Carbides and Nitrides. William Andrew/Noyes Publishing, Westwood, NJ, 1996.
38. G. Effenberg, Ilyenko, Svitlana (ed.). , "Rogl, Peter: Boron – Carbon – Zirconium," *SpringerMaterials - The Landolt-Börnstein Database*, Springer-Verlag Berlin Heidelberg (2009).
39. H. Bittermann and P. Rogl, "Critical assessment and thermodynamic calculation of the binary system hafnium-carbon (Hf-C)," *Journal of Phase Equilibria*, 18[4] 344-356 (1997).
40. A. W. Weimer(editor), "Carbide, Nitride and Boride Materials Synthesis and Processing " *Chapman & Hall* 639, Tables A631, B631, C631 & D631 (1997).
41. M. Nagao, Y. Sacho, T. Sato, T. Matsukawa, S. Kanemaru, and J. Itoh, "Fabrication of Polycrystalline Silicon Field Emitter Arrays with Hafnium Carbide Coating for Thin-Film-Transistor Controlled Field Emission Displays," *Japanese Journal of Applied Physics*, 43[6B] 3919-3922 (2004).
42. L. Baca and N. Stelzer, "Adapting of sol-gel process for preparation of TiB₂ powder from low-cost precursors," *J Eur Ceram Soc*, 28[5] 907-911 (2008).
43. G. Vasudevamurthy, T. W. Knight, E. Roberts, and T. M. Adams, "Laboratory production of zirconium carbide compacts for use in inert matrix fuels," *J Nucl Mater*, 374[1-2] 241-247 (2008).
44. C. Liu, B. Liu, Y. Shao, Z. Li, and C. Tang, "Preparation and Characterization of Zirconium Carbide Coating on Coated Fuel Particles," *J Am Ceram Soc*, 90[11] 3690-3693 (2007).
45. C. R. F. Azevedo, "Selection of fuel cladding material for nuclear fission reactors," *Eng Fail Anal*, 18[8] 1943-1962 (2011).
46. B. Pierrat, M. Balat-Pichelin, L. Silvestroni, and D. Sciti, "High temperature oxidation of ZrC–20%MoSi₂ in air for future solar receivers," *Sol Energy Mater Sol Cells*, 95[8] 2228-2237 (2011).

47. R. J. Irving and I. G. Worsley, "The oxidation of titanium diboride and zirconium diboride at high temperatures," *Journal of the Less Common Metals*, 16[2] 103-112 (1968).
48. P. Lefort, A. Maitre, and P. Tristant, "Influence of the grain size on the reactivity of TiO₂/C mixtures," *J Alloys Compd*, 302[1-2] 287-298 (2000).
49. A. Maitre and P. Lefort, "Solid state reaction of zirconia with carbon," *Solid State Ionics*, 104[1-2] 109-122 (1997).
50. R. Ebrahimi-Kahrizsangi and E. Amini-Kahrizsangi, "Zirconia carbothermal reduction: Non-isothermal kinetics," *Int J Refract Met Hard Mater*, 27[3] 637-641 (2009).
51. Y.-C. Woo, H.-J. Kang, and D. J. Kim, "Formation of TiC particle during carbothermal reduction of TiO₂," *J Eur Ceram Soc*, 27[2-3] 719-722 (2007).
52. W. G. Fahrenholtz, G. E. Hilmas, I. G. Talmy, and J. A. Zaykoski, "Refractory Diborides of Zirconium and Hafnium," *J Am Ceram Soc*, 90[5] 1347-1364 (2007).
53. L. Chen, Y. Gu, Z. Yang, L. Shi, J. Ma, and Y. Qian, "Preparation and some properties of nanocrystalline ZrB₂ powders," *Scr Mater*, 50[7] 959-961 (2004).
54. T. Tsuchida and S. Yamamoto, "MA-SHS and SPS of ZrB₂-ZrC composites," *Solid State Ionics*, 172[1-4] 215-216 (2004).
55. T. Tsuchida and S. Yamamoto, "Mechanical activation assisted self-propagating high-temperature synthesis of ZrC and ZrB₂ in air from Zr/B/C powder mixtures," *J Eur Ceram Soc*, 24[1] 45-51 (2004).
56. X. Ren, H. Miao, and Z. Peng, "A review of cemented carbides for rock drilling: An old but still tough challenge in geo-engineering," *Int J Refract Met Hard Mater*, 39 61-77 (2013).
57. F. J. J. Van Loo, W. Wakelkamp, G. F. Bastin, and R. Metselaar, "Diffusion of carbon in TiC and ZrC," *Solid State Ionics*, 32/33 824-832 (1989).
58. G. Leclercq, K. Kamal, J. F. Lamonier, L. Feigenbaum, P. Malfroy, and L. Leclercq, "Treatment of bulk Group VI transition metal carbides with hydrogen and oxygen," *Appl Catal, A*, 121[2] 169-190 (1995).
59. C. H. Prescott, "The Equilibrium between Zirconium oxide and Carbon and their Reaction Products at Incandescent Temperatures," *J Am Chem Soc*, 48[10] 2534-2550 (1926).
60. C. Ang, T. Williams, A. Seeber, H. Wang, and Y.-B. Cheng, "Synthesis and Evolution of Zirconium Carbide via Sol-Gel Route: Features of Nanoparticle Oxide-Carbon Reactions," *J Am Ceram Soc*, 96[4] 1099-1106 (2013).
61. M. M. Opeka, I. G. Talmy, E. J. Wuchina, J. A. Zaykoski, and S. J. Causey, "Mechanical, Thermal, and Oxidation Properties of Refractory Hafnium and zirconium Compounds," *J Eur Ceram Soc*, 19[13-14] 2405-2414 (1999).
62. S. Hampshire, "Ceramic processing and sintering : M. N. Rahaman Marcel Dekker, 1995, Materials Engineering Series, Vol. 10, ISBN 08247-9573-3, 770 pp, \$195 (\$69.75 for five or more copies for classroom use only)," *Mater Des*, 17[1] 55-56 (1996).
63. A. G. Lanin, E. V. Marchev, and S. A. Pritchin, "Non-isothermal sintering parameters and their influence on the structure and properties of zirconium carbide," *Ceram Int*, 17[5] 301-307 (1991).

64. M. N. Rahaman, "Ceramic Processing and Sintering [Electronic Resource] / M.N.Rahaman." in New York. M. Dekker, 2003.
65. R. Telle, L. S. Sigl, and K. Takagi, "Boride-Based Hard Materials," pp. 802-945. in Handbook of Ceramic Hard Materials. Edited by R. Prof. Dr. Ralf, 2008.
66. F. Monteverde, A. Bellosi, and S. Guicciardi, "Processing and properties of zirconium diboride-based composites," *J Eur Ceram Soc*, 22[3] 279-288 (2002).
67. X. Sun, W. Han, Q. Liu, P. Hu, and C. Hong, "ZrB₂-ceramic toughened by refractory metal Nb prepared by hot-pressing," *Mater Des*, 31[9] 4427-4431 (2010).
68. X. Zhang, L. Xu, S. Du, C. Liu, J. Han, and W. Han, "Spark plasma sintering and hot pressing of ZrB₂-SiC_W ultra-high temperature ceramics," *J Alloys Compd*, 466[1-2] 241-245 (2008).
69. S. R. Levine, E. J. Opila, M. C. Halbig, J. D. Kiser, M. Singh, and J. A. Salem, "Evaluation of ultra-high temperature ceramics for aeropropulsion use," *J Eur Ceram Soc*, 22[14-15] 2757-2767 (2002).
70. A. L. Chamberlain, W. G. Fahrenholtz, and G. E. Hilmas, "Reactive hot pressing of zirconium diboride," *J Eur Ceram Soc*, 29[16] 3401-3408 (2009).
71. C. Nachiappan, L. Rangaraj, C. Divakar, and V. Jayaram, "Synthesis and Densification of Monolithic Zirconium Carbide by Reactive Hot Pressing," *J Am Ceram Soc*, 93[5] 1341-1346 (2010).
72. I. G. Talmy, J. A. Zaykoski, and M. M. Opeka, "Synthesis, processing and properties of TaC-TaB₂-C ceramics," *J Eur Ceram Soc*, 30[11] 2253-2263 (2010).
73. J.-X. Liu, Y.-M. Kan, and G.-J. Zhang, "Pressureless Sintering of Tantalum Carbide Ceramics without Additives," *J Am Ceram Soc*, 93[2] 370-373 (2010).
74. J.-X. Liu, Y.-M. Kan, and G.-J. Zhang, "Synthesis of Ultra-Fine Hafnium Carbide Powder and its Pressureless Sintering," *J Am Ceram Soc*, 93[4] 980-986 (2010).
75. J. Y. Xiang, S. C. Liu, W. T. Hu, Y. Zhang, C. K. Chen, P. Wang, J. L. He, D. L. Yu, B. Xu, Y. F. Lu, Y. J. Tian, and Z. Y. Liu, "Mechanochemically activated synthesis of zirconium carbide nanoparticles at room temperature: A simple route to prepare nanoparticles of transition metal carbides," *J Eur Ceram Soc*, 31[8] 1491-1496 (2011).
76. A. Mukhopadhyay and B. Basu, "Consolidation–microstructure–property relationships in bulk nanoceramics and ceramic nanocomposites: a review" *Int Mater Rev*, 52[5] 257-288 (2007).
77. J. Binner and B. Vaidyanathan, "Processing of bulk nanostructured ceramics," *J Eur Ceram Soc*, 28[7] 1329-1339 (2008).
78. X. Zhang, Y. Hou, P. Hu, W. Han, and J. Luo, "Dispersion and co-dispersion of ZrB₂ and SiC nanopowders in ethanol," *Ceram Int*, 38[4] 2733-2741 (2012).
79. K. Nogi, M. Naito, and T. Yokoyama, "Chapter 3 - Characteristics and behavior of nanoparticles and its dispersion systems," pp. 113-176. in Nanoparticle Technology Handbook (Second Edition). Edited by K. Nogi, M. Naito, and T. Yokoyama. Elsevier, Amsterdam, 2012.

80. D. Jianxin, Z. Hui, W. Ze, L. Yunsong, and Z. Jun, "Friction and wear behaviors of WC/Co cemented carbide tool materials with different WC grain sizes at temperatures up to 600°C," *Int J Refract Met Hard Mater*, 31 196-204 (2012).
81. R. Porat, "Cemented carbide from micron size to nano size," *Met Powder Rep*, 53[2] 40 (1998).
82. X. Shi, H. Yang, G. Shao, X. Duan, and Z. Xiong, "Nanoindentation study of ultrafine WC–10Co cemented carbide," *Mater Charact*, 59[4] 374-379 (2008).
83. J. Xiong, Z. Guo, M. Yang, W. Wan, and G. Dong, "Tool life and wear of WC–TiC–Co ultrafine cemented carbide during dry cutting of AISI H13 steel," *Ceram Int*, 39[1] 337-346 (2013).
84. C. Xu, X. Ai, and C. Huang, "Research and development of rare-earth cemented carbides," *Int J Refract Met Hard Mater*, 19[3] 159-168 (2001).
85. C. M. Fernandes and A. M. R. Senos, "Cemented carbide phase diagrams: A review," *Int J Refract Met Hard Mater*, 29[4] 405-418 (2011).
86. C. Suryanarayana and N. Al-Aqeeli, "Mechanically alloyed nanocomposites," *Prog Mater Sci*, 58[4] 383-502 (2013).
87. Y. Ozaki and R. H. Zee, "High temperature diffusion of hafnium in tungsten and a tungsten-hafnium carbide alloy," *Scripta Metallurgica et Materialia*, 30[10] 1263-1267 (1994).
88. A. Luo, J. J. Park, D. L. Jacobson, B. H. Tsao, and M. L. Ramalingam, "High-temperature tensile properties of molybdenum and a molybdenum-0.5%hafnium carbide alloy," *Scripta Metallurgica et Materialia*, 29[6] 729-732 (1993).
89. X. S. Fan, Z. G. Yang, C. Zhang, Y. D. Zhang, and H. Q. Che, "Evaluation of vanadium carbide coatings on AISI H13 obtained by thermo-reactive deposition/diffusion technique," *Surf Coat Technol*, 205[2] 641-646 (2010).
90. M. Tului, S. Lionetti, G. Pulci, E. Rocca, T. Valente, and G. Marino, "Effects of heat treatments on oxidation resistance and mechanical properties of ultra high temperature ceramic coatings," *Surf Coat Technol*, 202[18] 4394-4398 (2008).
91. J. M. Arroyo, A. E. Diniz, and M. S. F. de Lima, "Cemented carbide surface modifications using laser treatment and its effects on hard coating adhesion," *Surf Coat Technol*, 204[15] 2410-2416 (2010).
92. C.-M. Lin, H.-L. Tsai, and C. Yang, "Effects of microstructure and properties on parameter optimization of boron carbide coatings prepared using a vacuum plasma-spraying process," *Surf Coat Technol*, 206[10] 2673-2681 (2012).
93. M. Watanabe, M. Komatsu, and S. Kuroda, "Multilayered WC–Co/Cu coatings by warm spray deposition," *Surf Coat Technol*, 205[23–24] 5358-5368 (2011).
94. B. C. Schulz, B. Wang, R. A. Morris, D. Butts, and G. B. Thompson, "Influence of hafnium carbide on vacuum plasma spray processed tantalum carbide microstructures," *J Eur Ceram Soc*, 33[6] 1219-1224 (2013).
95. E. Rayón, V. Bonache, M. D. Salvador, J. J. Roa, and E. Sánchez, "Hardness and Young's modulus distributions in atmospheric plasma sprayed WC–Co coatings using nanoindentation," *Surf Coat Technol*, 205[17–18] 4192-4197 (2011).

96. S. Dosta, M. Couto, and J. M. Guilemany, "Cold spray deposition of a WC-25Co cermet onto Al7075-T6 and carbon steel substrates," *Acta Mater*, 61[2] 643-652 (2013).
97. N. S. Lim, S. Das, S. Y. Park, M. C. Kim, and C. G. Park, "Fabrication and microstructural characterization of nano-structured WC/Co coatings," *Surf Coat Technol*, 205[2] 430-435 (2010).
98. M. Xie, S. Zhang, and M. Li, "Comparative Investigation on HVOF Sprayed Carbide-based Coatings," *Appl Surf Sci*, 273 799-805 (2013).
99. A. R. Choudhury, T. Ezz, S. Chatterjee, and L. Li, "Microstructure and tribological behaviour of nano-structured metal matrix composite boride coatings synthesized by combined laser and sol-gel technology," *Surf Coat Technol*, 202[13] 2817-2829 (2008).
100. W. Sun, X. Xiong, B.-y. Huang, G.-d. Li, H.-b. Zhang, Z.-k. Chen, and X.-L. Zheng, "ZrC ablation protective coating for carbon/carbon composites," *Carbon*, 47[14] 3368-3371 (2009).
101. W. Sun, X. Xiong, B. Y. Huang, G. D. Li, H. B. Zhang, P. Xiao, Z. K. Chen, and X. L. Zheng, "Preparation of ZrC nano-particles reinforced amorphous carbon composite coating by atmospheric pressure chemical vapor deposition," *Appl Surf Sci*, 255[16] 7142-7146 (2009).
102. G. F. Hurley, J. D. Katz, and P. D. Shalek, "Prealloyed catalyst for growing silicon carbide whiskers : (United States Department of Energy, USA) GB 2186 208 A (12 August 1987)," *Composites*, 19[4] 331 (1988).
103. R. C. Mehrotra, "Synthesis and reactions of metal alkoxides," *J Non-Cryst Solids*, 100[1-3] 1-15 (1988).
104. D. R. Ulrich, "Prospects of sol-gel processes," *J Non-Cryst Solids*, 100[1-3] 174-193 (1988).
105. R. Koc, "Kinetics and phase evolution during carbothermal synthesis of titanium carbide from carbon-coated titania powder," *J Eur Ceram Soc*, 17[11] 1309-1315 (1997).
106. P. Gibot and C. Vix-Guterl, "TiO₂ and [TiO₂/[beta]-SiC] microtubes prepared from an original process," *J Eur Ceram Soc*, 27[5] 2195-2201 (2007).
107. H. Preiss, L.-M. Berger, and M. Braun, "Formation of black glasses and silicon carbide from binary carbonaceous/silica hydrogels," *Carbon*, 33[12] 1739-1746 (1995).
108. V. Raman, G. Bhatia, A. K. Mishra, S. Bhardwaj, and K. N. Sood, "Synthesis of silicon carbide nanofibers from pitch blended with sol-gel derived silica," *Mater Lett*, 60[29-30] 3906-3911 (2006).
109. D. Sarkar, M. Chu, S.-J. Cho, Y. Il Kim, and B. Basu, "Synthesis and Morphological Analysis of Titanium Carbide Nanopowder," *J Am Ceram Soc*, 92[12] 2877-2882 (2009).
110. Y. Wang, H. He, Y. Cao, and H. Tang, "Growth of crystalline SiC film free of cavities by heating PS/silica sol-gel coatings on Si (111) substrate," *Mater Lett*, 57[5-6] 1179-1183 (2003).
111. C. R. Rambo, J. Cao, O. Rusina, and H. Sieber, "Manufacturing of biomorphic (Si, Ti, Zr)-carbide ceramics by sol-gel processing," *Carbon*, 43[6] 1174-1183 (2005).
112. J. M. C. Pavón, E. V. Alonso, M. T. S. Cordero, A. G. d. Torres, and J. M. López-Cepero, "Use of spectroscopic techniques for the chemical analysis of biomorphic silicon carbide ceramics," *Anal Chim Acta*, 528[1] 129-134 (2005).

113. Q. Wang, D. Wang, G. Jin, Y. Wang, and X. Guo, "Biomorphic SiC from lotus root," *Particuology*, 7[3] 199-203 (2009).
114. Y.-Y. Wang, G.-Q. Jin, and X.-Y. Guo, "Growth of ZSM-5 coating on biomorphic porous silicon carbide derived from durra," *Microporous Mesoporous Mater*, 118[1-3] 302-306 (2009).
115. Y. Gotoh, K. Fujimura, M. Koike, Y. Ohkoshi, M. Nagura, K. Akamatsu, and S. Deki, "Synthesis of titanium carbide from a composite of TiO₂ nanoparticles/methyl cellulose by carbothermal reduction," *Mater Res Bull*, 36[13-14] 2263-2275 (2001).
116. Y. Zheng, Y. Zheng, L.-X. Lin, J. Ni, and K.-M. Wei, "Synthesis of a novel mesoporous silicon carbide with a thorn-ball-like shape," *Scr Mater*, 55[10] 883-886 (2006).
117. K.-Z. Li, J. Wei, H.-J. Li, Z.-J. Li, D.-S. Hou, and Y.-L. Zhang, "Photoluminescence of hexagonal-shaped SiC nanowires prepared by sol-gel process," *Materials Science and Engineering: A*, 460-461 233-237 (2007).
118. C. Yan, R. Liu, Y. Cao, C. Zhang, and D. Zhang, "Synthesis of zirconium carbide powders using chitosan as carbon source," *Ceram Int*, 39[3] 3409-3412 (2013).
119. I. Hasegawa, Y. Fukuda, and M. Kajiwara, "Inorganic-organic hybrid route to synthesis of ZrC and Si-Zr-C fibres," *Ceram Int*, 25[6] 523-527 (1999).
120. I. Hasegawa, T. Nakamura, and M. Kajiwara, "Synthesis of continuous silicon carbide-titanium carbide hybrid fibers through sol-gel processing," *Materials Research Bulletin*, 31[7] 869-875 (1996).
121. K. Xia, C. Lu, and Y. Yang, "Preparation of anti-oxidative SiC/SiO₂ coating on carbon fibers from vinyltriethoxysilane by sol-gel method," *Appl Surf Sci*, 265[0] 603-609 (2013).
122. G.-Q. Jin and X.-Y. Guo, "Synthesis and characterization of mesoporous silicon carbide," *Microporous Mesoporous Mater*, 60[1-3] 207-212 (2003).
123. K. Wang, Y.-B. Cheng, and H. Wang, "A New Route of Forming Silicon Carbide Nanostructures with Controlled Morphologies," *Key Eng Mater*, 403 149-152 (2009).
124. J. Zhong, S. Liang, C. Xu, H. Wang, and Y.-B. Cheng, "Meso/micro-porosity and phase separation in TiO₂/SiO₂/C nanocomposites," *Microporous and Mesoporous Materials* 150[0] 25-31 (2012).
125. R. González, R. Martínez, and P. Ortiz, "Polymerization of furfuryl alcohol with trifluoroacetic acid, 2. The formation of difurfuryl ether," *Die Makromolekulare Chemie, Rapid Communications*, 13[11] 517-523 (1992).
126. C. de Almeida Filho and A. J. G. Zarbin, "Hollow porous carbon microspheres obtained by the pyrolysis of TiO₂/poly(furfuryl alcohol) composite precursors," *Carbon*, 44[14] 2869-2876 (2006).
127. A. J. G. Zarbin, R. Bertholdo, and M. A. F. C. Oliveira, "Preparation, characterization and pyrolysis of poly(furfuryl alcohol)/porous silica glass nanocomposites: novel route to carbon template," *Carbon*, 40[13] 2413-2422 (2002).
128. C.-A. Wang and M. D. Sacks, "Processing of nanocrystalline hafnium carbide powders," pp. 33-41. in 27th International Cocoa Beach Conference on Advanced Ceramics and Composites: A. Edited by W. M. Kriven and H.-T. Lin. The American Ceramic Society, Westerville, OH, 2004.

129. M. D. Sacks, C.-A. Wang, Z. Yang, and A. Jain, "Carbothermal reduction synthesis of nanocrystalline zirconium carbide and hafnium carbide powders using solution-derived precursors," *Journal of Materials Science*, 39[19] 6057-6066 (2004).
130. A. Maitre, D. Tetard, and P. Lefort, "Role of some technological parameters during carburizing titanium dioxide," *J Eur Ceram Soc*, 20[1] 15-22 (2000).
131. C. Yan, R. Liu, Y. Cao, C. Zhang, and D. Zhang, "Carbothermal Synthesis of Submicrometer Zirconium Carbide from Polyzirconoxane and Phenolic Resin by the Facile One-Pot Reaction," *J Am Ceram Soc*, 95[11] 3366–3369 (2012).
132. H. Preiss, L.-M. Berger, and D. Schultze, "Studies on the Carbothermal Preparation of Titanium Carbide from Different Gel Precursors," *J Eur Ceram Soc*, 19[2] 195-206 (1999).
133. B. Matović, B. Babić, D. Bučevac, M. Čebela, V. Maksimović, J. Pantić, and M. Miljković, "Synthesis and characterization of hafnium carbide fine powders," *Ceram Int*, 39[1] 719-723 (2013).
134. H. Preiss, L.-M. Berger, and K. Szulzewsky, "Thermal treatment of binary carbonaceous/ zirconia gels and formation of Zr(C,O,N) solid solutions," *Carbon*, 34[1] 109-119 (1996).
135. S. Y. Park and B. I. Lee, "Reaction sintering of gel derived ceramic composites," *J Non-Cryst Solids*, 100[1–3] 345-351 (1988).
136. H. Wang, X. Chen, B. Gao, J. Wang, Y. Wang, S. Chen, and Y. Gou, "Synthesis and characterization of a novel precursor-derived ZrC/ZrB₂ ultra-high-temperature ceramic composite," *Appl Organomet Chem*, 27[2] 79-84 (2012).
137. D. Ghosh, G. Subhash, R. Radhakrishnan, and T. S. Sudarshan, "Scratch-induced microplasticity and microcracking in zirconium diboride-silicon carbide composite," *Acta Mater*, 56[13] 3011-3022 (2008).
138. I. Hasegawa, Y. Fukuda, and M. Kajiwara, "An improved procedure for fabricating SiO₂-TiO₂-phenolic resin hybrid fibers as precursors for long Si-Ti-C fibers by sol-gel processing," *J Eur Ceram Soc*, 17[12] 1467-1473 (1997).
139. G. W. Meng, Z. Cui, L. D. Zhang, and F. Phillipp, "Growth and characterization of nanostructured [beta]-SiC via carbothermal reduction of SiO₂ xerogels containing carbon nanoparticles," *J Cryst Growth*, 209[4] 801-806 (2000).
140. V. Revankar, V. Lakhota, and V. Hlavacek, "Material Characterization of Chemical Vapor Deposited TiB₂ Fibers," pp. 1086-1094. in Proceedings of the 15th Annual Conference on Composites and Advanced Ceramic Materials: Ceramic Engineering and Science Proceedings. John Wiley & Sons, Inc., 2008.
141. S. Motojima and H. Iwanaga, "Preparation of micro-coiled TiC fibers by metal impurity-activated chemical vapor deposition," *Materials Science and Engineering: B*, 34[2–3] 159-163 (1995).
142. L. M. Manocha and S. M. Manocha, "Studies on solution-derived ceramic coatings for oxidation protection of carbon-carbon composites," *Carbon*, 33[4] 435-440 (1995).
143. R. Gadiou, S. Serverin, P. Gibot, and C. Vix-Guterl, "The synthesis of SiC and TiC protective coatings for carbon fibers by the reactive replica process," *J Eur Ceram Soc*, 28[11] 2265-2274 (2008).

144. S. Xuetao, L. Kezhi, L. Hejun, D. Hongying, C. Weifeng, and L. Fengtao, "Microstructure and ablation properties of zirconium carbide doped carbon/carbon composites," *Carbon*, 48[2] 344-351 (2010).
145. F. Goutier, G. Trolliard, S. Valette, A. Maître, and C. Estournes, "Role of impurities on the spark plasma sintering of ZrCx-ZrB2 composites," *J Eur Ceram Soc*, 28[3] 671-678 (2008).
146. T. Tsuchida and S. Yamamoto, "MA-SHS and SPS of ZrB2-ZrC composites," *Solid State Ionics*, 172[1-4] 215-216 (2004).
147. T. Tsuchida and S. Yamamoto, "Spark plasma sintering of ZrB2-ZrC powder mixtures synthesized by MA-SHS in air," *J Mater Sci*, 42[3] 772-778 (2007).
148. Q. Liu, W. Han, and J. Han, "Influence of SiCnp content on the microstructure and mechanical properties of ZrB2-SiC nanocomposite," *Scr Mater*, 63[6] 581-584 (2010).
149. Q. Liu, W. Han, and P. Hu, "Microstructure and mechanical properties of ZrB2-SiC nanocomposite ceramic," *Scr Mater*, 61[7] 690-692 (2009).
150. Q. Liu, W. Han, X. Zhang, S. Wang, and J. Han, "Microstructure and mechanical properties of ZrB2-SiC composites," *Mater Lett*, 63[15] 1323-1325 (2009).
151. M. Cao, S. Wang, and W. Han, "Influence of nanosized SiC particle on the fracture toughness of ZrB2-based nanocomposite ceramic," *Materials Science and Engineering: A*, 527[12] 2925-2928 (2010).
152. S. Zhu, W. G. Fahrenholtz, and G. E. Hilmas, "Influence of silicon carbide particle size on the microstructure and mechanical properties of zirconium diboride-silicon carbide ceramics," *J Eur Ceram Soc*, 27[4] 2077-2083 (2007).
153. X. Zhang, L. Xu, W. Han, L. Weng, J. Han, and S. Du, "Microstructure and properties of silicon carbide whisker reinforced zirconium diboride ultra-high temperature ceramics," *Solid State Sci*, 11[1] 156-161 (2009).
154. X. Zhang, L. Xu, S. Du, W. Han, and J. Han, "Crack-healing behavior of zirconium diboride composite reinforced with silicon carbide whiskers," *Scr Mater*, 59[11] 1222-1225 (2008).
155. A. Rezaie, W. G. Fahrenholtz, and G. E. Hilmas, "Evolution of structure during the oxidation of zirconium diboride-silicon carbide in air up to 1500 °C," *J Eur Ceram Soc*, 27[6] 2495-2501 (2007).
156. R. Gao, G. Min, H. Yu, S.-q. Zheng, Q. Lu, J. Han, and W. Wang, "Fabrication and oxidation behavior of LaB6-ZrB2 composites," *Ceram Int*, 31[1] 15-19 (2005).
157. S. Otani, T. Aizawa, and N. Kieda, "Solid solution ranges of zirconium diboride with other refractory diborides: HfB2, TiB2, TaB2, NbB2, VB2 and CrB2," *J Alloys Compd*, 475[1-2] 273-275 (2009).
158. L. Zhao, D. Jia, X. Duan, Z. Yang, and Y. Zhou, "Improved Oxidation Resistance of Zirconium Carbide at 1500°C by Lanthanum Hexaboride Additions," *J Am Ceram Soc*, 94[11] 3648-3650 (2011).
159. X.-h. Zhang, P. Hu, J.-c. Han, L. Xu, and S.-h. Meng, "The addition of lanthanum hexaboride to zirconium diboride for improved oxidation resistance," *Scr Mater*, 57[11] 1036-1039 (2007).
160. F. Yang, X. Zhang, J. Han, and S. Du, "Processing and mechanical properties of short carbon fibers toughened zirconium diboride-based ceramics," *Mater Des*, 29[9] 1817-1820 (2008).

161. D. Sciti, S. Guicciardi, and L. Silvestroni, "SiC chopped fibers reinforced ZrB₂: Effect of the sintering aid," *Scr Mater*, 64[8] 769-772 (2011).
162. L. Silvestroni, D. Sciti, C. Melandri, and S. Guicciardi, "Toughened ZrB₂-based ceramics through SiC whisker or SiC chopped fiber additions," *J Eur Ceram Soc*, 30[11] 2155-2164 (2010).
163. N. Gupta, A. Mukhopadhyay, K. Pavani, and B. Basu, "Spark plasma sintering of novel ZrB₂-SiC-TiSi₂ composites with better mechanical properties," *Materials Science and Engineering: A*, 534 111-118 (2012).
164. L. Xu, C. Huang, H. Liu, B. Zou, H. Zhu, G. Zhao, and J. Wang, "Study on in-situ synthesis of ZrB₂ whiskers in ZrB₂-ZrC matrix powder for ceramic cutting tools," *Int J Refract Met Hard Mater*, 37 98-105 (2013).
165. J. Zhong, S. Liang, K. Wang, H. Wang, T. Williams, H. Huang, and Y.-B. Cheng, "Synthesis of Mesoporous Carbon-Bonded TiC/SiC Composites by Direct Carbothermal Reduction of Sol-Gel Derived Monolithic Precursor," *J Am Ceram Soc*, 94[11] 4025-4031 (2011).
166. J. Chen, Z. Huang, and X. Liu, "The co-dispersion of silicon carbide with nano-C and B₄C in aqueous ethanol solution," *Mater Chem Phys*, 109[2-3] 194-198 (2008).
167. Y. X. Huang, A. M. R. Senos, and J. L. Baptista, "Preparation of an aluminium titanate-25 vol% mullite composite by sintering of gel-coated powders," *J Eur Ceram Soc*, 17[10] 1239-1246 (1997).
168. M. C. Wu, M. K. Hsieh, C. W. Yen, Y. C. Huang, W. T. Huang, and W. F. Su, "Low sintering BaNd₂Ti₄O₁₂ microwave ceramics prepared by CuO thin layer coated powder," *J Eur Ceram Soc*, 27[8-9] 2835-2839 (2007).
169. S. Zhu, W. G. Fahrenholtz, G. E. Hilmas, and S. C. Zhang, "Pressureless sintering of carbon-coated zirconium diboride powders," *Materials Science and Engineering: A*, 459[1-2] 167-171 (2007).
170. T. Zhu, L. Xu, X. Zhang, W. Han, P. Hu, and L. Weng, "Densification, microstructure and mechanical properties of ZrB₂-SiCw ceramic composites," *J Eur Ceram Soc*, 29[13] 2893-2901 (2009).
171. J. Gao, H. Xiao, and H. Du, "Effect of Y₂O₃ addition on ammono sol-gel synthesis and sintering of Si₃N₄-SiC nanocomposite powder," *Ceram Int*, 29[6] 655-661 (2003).
172. S. Kawano, J. Takahashi, and S. Shimada, "The preparation and spark plasma sintering of silicon nitride-based materials coated with nano-sized TiN," *J Eur Ceram Soc*, 24[2] 309-312 (2004).
173. Z. Tatli and D. P. Thompson, "Densification behaviour of oxide-coated silicon nitride powders," *Mater Lett*, 59[14-15] 1897-1901 (2005).
174. E. Yarrapareddy and R. Kovacevic, "Synthesis and characterization of laser-based direct metal deposited nano-particles reinforced surface coatings for industrial slurry erosion applications," *Surf Coat Technol*, 202[10] 1951-1965 (2008).
175. J. R. Groza and A. Zavaliangos, "Sintering activation by external electrical field," *Materials Science and Engineering: A*, 287[2] 171-177 (2000).
176. Y. Zhou, K. Hirao, Y. Yamauchi, and S. Kanzaki, "Effects of heating rate and particle size on pulse electric current sintering of alumina," *Scr Mater*, 48[12] 1631-1636 (2003).
177. M. Tokita, "Development of Large-Size Ceramic/Metal Bulk FGM Fabricated by Spark Plasma Sintering," *Mater Sci Forum*, 308-311 83-88 (1999).

178. K. R. Anderson, J. R. Groza, M. Fendorf, and C. J. Echer, "Surface oxide debonding in field assisted powder sintering," *Materials Science and Engineering: A*, 270[2] 278-282 (1999).
179. M. Demuynck, J.-P. Erauw, O. Van der Biest, F. Delannay, and F. Cambier, "Densification of alumina by SPS and HP: A comparative study," *J Eur Ceram Soc*, 32[9] 1957-1964 (2012).
180. L. Gao, X. Jin, H. Kawaoka, T. Sekino, and K. Niihara, "Microstructure and mechanical properties of SiC–mullite nanocomposite prepared by spark plasma sintering," *Materials Science and Engineering: A*, 334[1–2] 262-266 (2002).
181. F. Meng, Z. Fu, J. Zhang, H. Wang, W. Wang, Y. Wang, R. Todd, and Q. Zhang, "Study on the structure and properties of fine-grained alumina fast sintered with high heating rate," *Mater Res Bull*, 43[12] 3521-3528 (2008).
182. F. Meng, F. Zhang, W. Huang, Y. Yang, M. Guo, X. Jiang, and Z. Tian, "Fabrication of ultrafine-grained alumina ceramics by two different fast sintering methods," *Ceram Int*, 37[6] 1973-1977 (2011).
183. V. Y. Kodash, J. R. Groza, G. Aldica, M. S. Toprak, S. Li, and M. Mamoun, "Field-activated sintering of skutterudites," *Scr Mater*, 57[6] 509-511 (2007).
184. V. Y. Kodash, J. R. Groza, K. C. Cho, B. R. Klotz, and R. J. Dowding, "Field-assisted sintering of Ni nanopowders," *Materials Science and Engineering: A*, 385[1-2] 367-371 (2004).
185. F. Monteverde, "Ultra-high temperature HfB₂-SiC ceramics consolidated by hot-pressing and spark plasma sintering," *J Alloys Compd*, 428[1-2] 197-205 (2007).
186. F. Monteverde, C. Melandri, and S. Guicciardi, "Microstructure and mechanical properties of an HfB₂ + 30 vol.% SiC composite consolidated by spark plasma sintering," *Mater Chem Phys*, 100[2-3] 513-519 (2006).
187. D. M. Hulbert, D. Jiang, D. V. Dudina, and A. K. Mukherjee, "The synthesis and consolidation of hard materials by spark plasma sintering," *Int J Refract Met Hard Mater*, 27[2] 367-375 (2009).
188. L. Cheng, Z. Xie, G. Liu, W. Liu, and W. Xue, "Densification and mechanical properties of TiC by SPS-effects of holding time, sintering temperature and pressure condition," *J Eur Ceram Soc*, 32[12] 3399-3406 (2012).
189. R. Licheri, R. Orrù, C. Musa, and G. Cao, "Combination of SHS and SPS Techniques for fabrication of fully dense ZrB₂-ZrC-SiC composites," *Mater Lett*, 62[3] 432-435 (2008).
190. I. Akin, M. Hotta, F. C. Sahin, O. Yucel, G. Goller, and T. Goto, "Microstructure and densification of ZrB₂-SiC composites prepared by spark plasma sintering," *J Eur Ceram Soc*, 29[11] 2379-2385 (2009).
191. S. K. Mishra and S. K. Das, "Sintering and microstructural behaviour of SHS produced zirconium diboride powder with the addition of C and TiC," *Mater Lett*, 59[27] 3467-3470 (2005).
192. T. Tsuchida and T. Kakuta, "Fabrication of SPS compacts from NbC-NbB₂ powder mixtures synthesized by the MA-SHS in air process," *J Alloys Compd*, 415[1-2] 156-161 (2006).
193. S. Ran, O. Van der Biest, and J. Vleugels, "ZrB₂-SiC composites prepared by reactive pulsed electric current sintering," *J Eur Ceram Soc*, 30[12] 2633-2642 (2010).

194. A. Zavaliangos, J. Zhang, M. Krammer, and J. R. Groza, "Temperature evolution during field activated sintering," *Materials Science and Engineering: A*, 379[1-2] 218-228 (2004).
195. K. Vanmeensel, A. Laptev, J. Hennicke, J. Vleugels, and O. Van der Biest, "Modelling of the temperature distribution during field assisted sintering," *Acta Mater*, 53[16] 4379-4388 (2005).
196. M. Omori, "Sintering, consolidation, reaction and crystal growth by the spark plasma system (SPS)," *Materials Science and Engineering: A*, 287[2] 183-188 (2000).
197. S. K. Mishra and L. C. Pathak, "Effect of carbon and titanium carbide on sintering behaviour of zirconium diboride," *J Alloys Compd*, 465[1-2] 547-555 (2008).
198. T. Oku, "Chapter 33 - Carbon/Carbon Composites and Their Properties," pp. 523-544. in *Carbon Alloys*. Edited by Y. Ei-ichi, I. Michio, K. Katsumi, E. Morinobu, O. Asao, and T. Yasuhiro. Elsevier Science, Oxford, 2003.
199. H. Heidari, H. Alamdari, D. Dubé, and R. Schulz, "Interaction of molten aluminum with porous TiB₂-based ceramics containing Ti-Fe additives," *J Eur Ceram Soc*, 32[4] 937-945 (2012).
200. J. D. Anderson, "Hypersonic and High Temperature Gas Dynamics," 2nd Edition ed. American Institute of Aeronautics and Astronautics: Blacksburg, Virginia, (2006).
201. J. H. Allen, "The aerodynamic heating of atmosphere entry vehicles - a review," *Paper for Symposium on Fundamental Phenomena in Hypersonic Flow*, NACA TM X-54, 056 1125-1140 (1964).
202. J. P. Rybak and R. Churchill, "Progress in reentry communications," *IEEE Trans Aerosp Electron Syst*, 7[5] 879-894 (1971).
203. R. Haoui, "Physico-chemical state of the air at the stagnation point during the atmospheric reentry of a spacecraft," *Acta Astronaut*, 68[11-12] 1660-1668 (2011).
204. C. J. Maiden and C. S. Pierre, "Some measurements of the physical properties of the plasma sheath around hypersonic projectiles," *Planet Space Sci*, 6 196-206 (1961).
205. J. H. Allen and A. J. E. Jr, "A Study of the Motion and Aerodynamic Heating of Ballistic Missiles Entering the Earth's Atmosphere at High Supersonic Speeds." NACA Technical Report 1381," *Forty-Fourth Annual Report of the NACA* 1125-1140 (1958).
206. J. H. Allen and A. J. E. Jr, "A study of the motion and aerodynamic heating of missiles entering the earth's atmosphere at high supersonic speeds," *NACA TN4047 (Oct 1957)* 1125-1140 (1957).
207. J. J. Bertin and R. M. Cummings, "Fifty years of hypersonics: where we've been, where we're going," *Prog Aerosp Sci*, 39[6-7] 511-536 (2003).
208. S. P. Schneider, "Hypersonic laminar-turbulent transition on circular cones and scramjet forebodies," *Prog Aerosp Sci*, 40[1-2] 1-50 (2004).
209. J. Salute, J. Buff, and D. Rasky, "SHARP-B2: Flight Test Objectives, Project Implementation and Initial Results." in 2nd Annual Conference on Composites, Materials and Structures. United States Advanced Ceramics Association, Cocoa Beach, FL, United States, 2001.
210. S. Kumar, J. Kushwaha, S. Mondal, A. Kumar, R. K. Jain, and G. Rohini Devi, "Fabrication and ablation testing of 4D C/C composite at 10MW/m²

- heat flux under a plasma arc heater," *Materials Science and Engineering: A*, 566 102-111 (2013).
211. M. Auweter-Kurtz, G. Hilfer, H. Habiger, K. Yamawaki, T. Yoshinaka, and H. D. Speckmann, "Investigation of oxidation protected C/C heat shield material in different plasma wind tunnels," *Acta Astronaut*, 45[2] 93-108 (1999).
212. J. L. Shideler, G. L. Webb, and C. M. Pittman, "Verification Tests of Durable Thermal Protection System Concepts," *Journal of Spacecraft*, 22[6] 598 (1984).
213. V. V. Verbinski, D. G. Costello, and H. L. Moody, "Bremsstrahlung-activation ablation gauge for tungsten nosetip ablation during atmospheric reentry," *Nucl Instrum Methods*, 133[1] 131-136 (1976).
214. S. S. Penner and D. B. Olfe, "Chapter 7 - Ablation during re-entry," pp. 415-474. in *Radiation and Reentry*. Academic Press, 1968.
215. F. Monteverde, R. Savino, and M. De Stefano Fumo, "Dynamic oxidation of ultra-high temperature ZrB₂-SiC under high enthalpy supersonic flows," *Corros Sci*, 53[3] 922-929 (2011).
216. S. M. Johnson, M. Gasch, J. W. Lawson, M. I. Gusman, and M. M. Stackpole, "Recent Developments in Ultra High Temperature Ceramics at NASA Ames." in 16th AIAA/DLR/DGLR International Space Planes and Hypersonic Systems and Technologies Conference, Vol. HYTASP-4: Materials & Structures. Bremen, Germany, 2009.
217. Z.-G. Zhang and L. Jun-feng, "Sharp-leading-edge test conducted on Minuteman III," pp. 47. in *Aviation Week and Space Technology*, Vol. 153. 2000.
218. K.-Z. Li, X.-T. Shen, H.-J. Li, S.-Y. Zhang, T. Feng, and L.-L. Zhang, "Ablation of the carbon/carbon composite nozzle-throats in a small solid rocket motor," *Carbon*, 49[4] 1208-1215 (2011).
219. S. Schmidt, S. Beyer, H. Knabe, H. Immich, R. Meistring, and A. Gessler, "Advanced ceramic matrix composite materials for current and future propulsion technology applications," *Acta Astronaut*, 55[3-9] 409-420 (2004).
220. R. Savino, M. De Stefano Fumo, D. Paterna, A. Di Maso, and F. Monteverde, "Arc-jet testing of ultra-high-temperature-ceramics," *Aerosp Sci Technol*, 14[3] 178-187 (2010).
221. D. Sciti, R. Savino, and L. Silvestroni, "Aerothermal behaviour of a SiC fibre-reinforced ZrB₂ sharp component in supersonic regime," *J Eur Ceram Soc*, 32[8] 1837-1845 (2012).
222. L. Wei, X. Yang, W. Song, M. Yan, and C. Zhao-hui, "Ablation behavior of three-dimensional braided C/SiC composites by oxyacetylene torch under different environments," *Ceram Int*, 39[1] 463-468 (2013).
223. A. Paul, S. Venugopal, J. G. P. Binner, B. Vaidhyanathan, A. C. J. Heaton, and P. M. Brown, "UHTC-carbon fibre composites: Preparation, oxyacetylene torch testing and characterisation," *J Eur Ceram Soc*, 33[2] 423-432 (2013).
224. B. Yan, Z. Chen, J. Zhu, J. Zhang, and Y. Jiang, "Effects of ablation at different regions in three-dimensional orthogonal C/SiC composites ablated by oxyacetylene torch at 1800°C," *J Mater Process Technol*, 209[7] 3438-3443 (2009).

225. D. Fang, Z. Chen, Y. Song, and Z. Sun, "Morphology and microstructure of 2.5 dimension C/SiC composites ablated by oxyacetylene torch," *Ceram Int*, 35[3] 1249-1253 (2009).
226. A. N. Hayhurst and D. B. Kittelson, "The positive and negative ions in oxyacetylene flames," *Combust Flame*, 31[0] 37-51 (1978).
227. V. J. Hall-Roberts, A. N. Hayhurst, D. E. Knight, and S. G. Taylor, "The origin of soot in flames: is the nucleus an ion?," *Combust Flame*, 120[4] 578-584 (2000).
228. F. Zuo, L. Cheng, L. Xiang, L. Zhang, and L. Li, "Ablative property of laminated ZrB₂-SiC ceramics under oxyacetylene torch," *Ceram Int*, 39[4] 4627-4631 (2012).
229. P. A. Williams, R. Sakidja, J. H. Perepezko, and P. Ritt, "Oxidation of ZrB₂-SiC ultra-high temperature composites over a wide range of SiC content," *J Eur Ceram Soc*, 32[14] 3875-3883 (2012).
230. D. Sciti and L. Silvestroni, "Processing, sintering and oxidation behavior of SiC fibers reinforced ZrB₂ composites," *J Eur Ceram Soc*, 32[9] 1933-1940 (2012).
231. J. L. Neuringer, "Derivation of shape change equations for asymmetrically heated ablating reentry vehicles," *Int J Eng Sci*, 11[4] 451-457 (1973).
232. M. Sibulkin and E. A. Dennar, "Radiating boundary layers at planetary entry velocities," *Int J Heat Mass Transfer*, 15[4] 619-635 (1972).
233. J. S. Evans and P. W. Huber, "Prediction of Reentry Plasma-Sheath Properties," *Proceedings of the NASA Conference on Communicating Through Plasmas of Atmospheric Entry and Rocket Exhaust*, NASA SP-52 7-22 (1964).
234. M. C. Ellis and P. W. Huber, "Real Gas Flow Conditions about Hypersonic Vehicles," *Reentry Dynamics, Part 11: Proceedings of the Conference on Physics of the Solar System and Reentry Dynamics* 120-154 (1962).
235. D. Alfano, L. Scatteia, F. Monteverde, E. Bêche, and M. Balat-Pichelin, "Microstructural characterization of ZrB₂-SiC based UHTC tested in the MESOX plasma facility," *J Eur Ceram Soc*, 30[11] 2345-2355 (2010).
236. X. Zhang, P. Hu, J. Han, and S. Meng, "Ablation behavior of ZrB₂-SiC ultra high temperature ceramics under simulated atmospheric re-entry conditions," *Compos Sci Technol*, 68[7-8] 1718-1726 (2008).
237. F. Monteverde and R. Savino, "Stability of ultra-high-temperature ZrB₂-SiC ceramics under simulated atmospheric re-entry conditions," *J Eur Ceram Soc*, 27[16] 4797-4805 (2007).
238. Y. D. Blum, J. Marschall, D. Hui, and S. Young, "Thick Protective UHTC Coatings for SiC-Based Structures: Process Establishment," *J Am Ceram Soc*, 91[5] 1453-1460 (2008).
239. W.-B. Han, P. Hu, X.-H. Zhang, J.-C. Han, and S.-H. Meng, "High-Temperature Oxidation at 1900°C of ZrB₂-xSiC Ultrahigh-Temperature Ceramic Composites," *J Am Ceram Soc*, 91[10] 3328-3334 (2008).
240. J. Zou, G.-J. Zhang, C.-F. Hu, T. Nishimura, Y. Sakka, J. Vleugels, and O. Van der Biest, "Strong ZrB₂-SiC-WC Ceramics at 1600°C," *J Am Ceram Soc*, 95[3] 874-878 (2012).
241. L. Zhao, D. Jia, X. Duan, Z. Yang, and Y. Zhou, "Oxidation of ZrC-30 vol% SiC composite in air from low to ultrahigh temperature," *J Eur Ceram Soc*, 32[4] 947-954 (2012).

242. J. Xie, K. Li, H. Li, Q. Fu, and L. Guo, "Ablation behavior and mechanism of C/C–ZrC–SiC composites under an oxyacetylene torch at 3000°C," *Ceram Int*, 39[4] 4171-4178 (2013).
243. Z. Li, H. Li, S. Zhang, and K. Li, "Microstructure and ablation behaviors of integer felt reinforced C/C–SiC–ZrC composites prepared by a two-step method," *Ceram Int*, 38[4] 3419-3425 (2012).
244. Z. Q. Li, H. J. Li, W. Li, J. Wang, S. Y. Zhang, and J. Guo, "Preparation and ablation properties of ZrC–SiC coating for carbon/carbon composites by solid phase infiltration," *Appl Surf Sci*, 258[1] 565-571 (2011).
245. D. Gao, Y. Zhang, C. Xu, Y. Song, and X. Shi, "Atomic oxygen adsorption and its effect on the oxidation behaviour of ZrB₂–ZrC–SiC in air," *Mater Chem Phys*, 126[1–2] 156-161 (2011).
246. M. Ramacciotti, C. Journeau, F. Sudreau, and G. Cognet, "Viscosity models for corium melts," *Nucl Eng Des*, 204[1–3] 377-389 (2001).
247. F. Sudreau and G. Cognet, "Corium viscosity modelling above liquidus temperature," *Nucl Eng Des*, 178[3] 269-277 (1997).
248. C. M. Carney, T. A. Parthasarathy, and M. K. Cinibulk, "Oxidation Resistance of Hafnium Diboride Ceramics with Additions of Silicon Carbide and Tungsten Boride or Tungsten Carbide," *J Am Ceram Soc*, 94[8] 2600-2607 (2011).
249. L. Zhao, D. Jia, X. Duan, Z. Yang, and Y. Zhou, "Improved Oxidation Resistance of Zirconium Carbide at 1500°C by Lanthanum Hexaboride Additions," *J Am Ceram Soc*, 94[11] 3648-3650 (2011).
250. T. A. Parthasarathy, M. D. Petry, M. K. Cinibulk, T. Mathur, and M. R. Gruber, "Thermal and Oxidation Response of UHTC Leading Edge Samples Exposed to Simulated Hypersonic Flight Conditions," *J Am Ceram Soc*, 96[3] 907-915 (2013).
251. F. Monteverde and R. Savino, "ZrB₂–SiC Sharp Leading Edges in High Enthalpy Supersonic Flows," *J Am Ceram Soc*, 95[7] 2282-2289 (2012).
252. D. Bradley and F. C. (editor), "Metal alkoxides," *Progress in Inorganic Chemistry*, Interscience Publishers, 2 303-309 (1960).
253. D. Bradley, R. Mehrotra, and W. Wardlaw, "330 Hafnium Alkoxides," *J Chem Soc*, 1953 1634 - 1636 (1953).
254. A. Larbot, T. Hours, P. Bergez, J. Charpin, and L. Cot, "Study of sol-gel transition during hafnium alkoxide hydrolysis," *J Non-Cryst Solids*, 147-148 85-91 (1992).
255. E. L. Corral, A. A. Ayala, and R. E. Loehman, "Evaluation of Oxidation Protection Testing Methods on Ultra-High Temperature Ceramic Coatings for Carbon-Carbon Oxidation Resistance," pp. 359-370. in *Mechanical Properties and Performance of Engineering Ceramics and Composites III*. John Wiley & Sons, Inc., 2009.
256. E. L. Corral and L. S. Walker, "Improved ablation resistance of C–C composites using zirconium diboride and boron carbide," *J Eur Ceram Soc*, 30[11] 2357-2364 (2010).
257. C. M. Carney, T. A. Parthasarathy, and M. K. Cinibulk, "Separating Test Artifacts from Material Behavior in the Oxidation Studies of HfB₂–SiC at 2000°C and Above," *Int J Appl Ceram Technol*, 10[2] 293-300 (2013).
258. P. Zhang, S. X. Li, and Z. F. Zhang, "General relationship between strength and hardness," *Materials Science and Engineering: A*, 529 62-73 (2011).

259. I. Brooks, P. Lin, G. Palumbo, G. D. Hibbard, and U. Erb, "Analysis of hardness–tensile strength relationships for electroformed nanocrystalline materials," *Materials Science and Engineering: A*, 491[1–2] 412-419 (2008).
260. G. R. Anstis, P. Chantikul, B. R. Lawn, and D. B. Marshall, "A Critical Evaluation of Indentation Techniques for Measuring Fracture Toughness: I, Direct Crack Measurements," *J Am Ceram Soc*, 64[9] 533-538 (1981).
261. V. Zamora, A. L. Ortiz, F. Guiberteau, and M. Nygren, "In situ formation of ZrB₂–ZrO₂ ultra-high-temperature ceramic composites from high-energy ball-milled ZrB₂ powders," *J Alloys Compd*, 518[0] 38-43 (2012).
262. K. Wang, Y.-B. Cheng, and H. Wang, "Growth of SiC Whiskers by Carbothermal Reduction of Mesoporous Silica-Carbon Composites Infiltrated With SiC Nuclei," *J Aust Ceram Soc*, 45[1] 2009 (2009).
263. K. Wang, H. Wang, and Y.-B. Cheng, "Synthesis of nanostructured silicon carbide spheres from mesoporous C–SiO₂ nanocomposites," *Chem Commun*, 46[2] 303 (2010).
264. J. Zhong, S. Liang, J. Zhao, W. D. Wu, W. Liu, H. Wang, X. D. Chen, and Y.-B. Cheng, "Formation of novel mesoporous TiC microspheres through a sol–gel and carbothermal reduction process," *J Eur Ceram Soc*, 32[12] 3407-3414 (2012).
265. J. Zhong, S. Liang, C. Xu, H. Wang, and Y.-B. Cheng, "Meso/micro-porosity and phase separation in TiO₂/SiO₂/C nanocomposites," *Microporous Mesoporous Mater*, 150[0] 25-31 (2012).
266. D. C. Bradley and C. E. Holloway, "Nuclear magnetic resonance and cryoscopic studies on some alkoxides of titanium, zirconium, and hafnium," *J Chem Soc A* 1316-1319 (1968).
267. S. Martin, "Production of high purity metal powder from metal alkoxide." in, Vol. 1995-252511. Edited by USPTO. H.C. Starck, GmbH & Co., KG, 1995.
268. P. Blanc, A. Larbot, J. Palmeri, M. Lopez, and L. Cot, "Hafnia ceramic nanofiltration membranes. Part I: Preparation and characterization," *J Membr Sci*, 149[2] 151-161 (1998).
269. "JCPDS-International Centre for Diffraction Data." in Powder Diffraction File Card No 65-2906 JCPDS-International Centre for Diffraction Data, Newtown Square, PA, 2002.
270. P. G. Cotter and J. A. Kohn, "Industrial Diamond Substitutes: I, Physical and X-Ray Study of Hafnium Carbide," *J Am Ceram Soc*, 37[9] 415-420 (1954).
271. A. N. Kornilov, N. V. Chelovskaya, V. I. Zhelankin, and G. P. Shveikin, "Enthalpies of formation of hafnium carbides," *The Journal of Chemical Thermodynamics*, 9[7] 629-642 (1977).
272. R. Koc and J. S. Folmer, "Carbothermal synthesis of titanium carbide using ultrafine titania powders," *J Mater Sci*, 32[12] 3101-3111 (1997).
273. R. Koc, "Kinetics and phase evolution during carbothermal synthesis of titanium carbide from ultrafine titania/carbon mixture," *Journal of Materials Science*, 33[4] 1049-1055 (1998).
274. R. Koc and J. S. Folmer, "Synthesis of Submicrometer Titanium Carbide Powders," *Journal of the American Ceramic Society*, 80[4] 952-956 (1997).
275. R. Koc, "Kinetics and Phase Evolution During Carbothermal Synthesis of Titanium Carbide," pp. 703-711. in Proceedings of the 21st Annual Conference on Composites, Advanced Ceramics, Materials, and

- Structures—B: Ceramic Engineering and Science Proceedings. John Wiley & Sons, Inc., 2008.
276. T. Hirasaki, T. Meguro, T. Wakihara, J. Tatami, and K. Komeya, "Effect of ultrasonic irradiation in the polymerization of furfuryl alcohol, with ethylene glycol as a pore-forming agent, on the microstructure of the derived carbons," *Carbon*, 46[12] 1630-1630 (2008).
277. C. L. Burket, R. Rajagopalan, A. P. Marencic, K. Dronvajjala, and H. C. Foley, "Genesis of porosity in polyfurfuryl alcohol derived nanoporous carbon," *Carbon*, 44[14] 2957-2963 (2006).
278. J. Yao, H. Wang, J. Liu, K.-Y. Chan, L. Zhang, and N. Xu, "Preparation of colloidal microporous carbon spheres from furfuryl alcohol," *Carbon*, 43[8] 1709-1715 (2005).
279. J. C. Groen, L. A. A. Peffer, and J. Pérez-Ramírez, "Pore size determination in modified micro- and mesoporous materials. Pitfalls and limitations in gas adsorption data analysis," *Microporous Mesoporous Mater*, 60[1-3] 1-17 (2003).
280. A. C. Ferrari, "Raman spectroscopy of graphene and graphite: Disorder, electron-phonon coupling, doping and nonadiabatic effects," *Solid State Communications*, 143[1-2] 47-57 (2007).
281. S. Urbonaitė, L. Hålldahl, and G. Svensson, "Raman spectroscopy studies of carbide derived carbons," *Carbon*, 46[14] 1942-1947 (2008).
282. A. C. Ferrari, J. C. Meyer, V. Scardaci, C. Casiraghi, M. Lazzeri, F. Mauri, S. Piscanec, D. Jiang, K. S. Novoselov, S. Roth, and A. K. Geim, "Raman Spectrum of Graphene and Graphene Layers," *Phys Rev Lett*, 97[18] 187401 (2006).
283. C. L. Burket, R. Rajagopalan, and H. C. Foley, "Overcoming the barrier to graphitization in a polymer-derived nanoporous carbon," *Carbon*, 46[3] 501-510 (2008).
284. Z. Wang, X. Zhang, X. Liu, M. Lv, K. Yang, and J. Meng, "Co-gelation synthesis of porous graphitic carbons with high surface area and their applications," *Carbon*, 49[1] 161-169 (2011).
285. M. Lei, H. Z. Zhao, H. Yang, B. Song, and W. H. Tang, "Synthesis of transition metal carbide nanoparticles through melamine and metal oxides," *Journal of the European Ceramic Society*, 28[8] 1671-1677 (2008).
286. J. Luo, Z. Guo, Y. Gao, and T. Lin, "Synthesis of nanosized tungsten carbide from phenol formaldehyde resin coated precursors," *Rare Metals*, 27[2] 201-204 (2008).
287. R. Koc and S. K. Kodambaka, "Tungsten carbide (WC) synthesis from novel precursors," *J Eur Ceram Soc*, 20[11] 1859-1869 (2000).
288. R. Guinebrière, A. Dager, A. Lecomte, and H. Vesteghem, "Tetragonal zirconia powders from the zirconium n-propoxide-acetylacetone-water-isopropanol system," *J Non-Cryst Solids*, 147-148 542-547 (1992).
289. T. Kidchob, L. Malfatti, F. Serra, P. Falcaro, S. Enzo, and P. Innocenzi, "Hafnia sol-gel films synthesized from HfCl₄: Changes of structure and properties with the firing temperature," *Journal of Sol-Gel Science and Technology* 42[1] 89-93 (2007).
290. S. K. Sarker, A. D. Miller, and J. I. Mueller, "Solubility of Oxygen in ZrC," *Journal of the American Ceramic Society*, 55[12] 628-630 (1972).
291. M. Gendre, A. Maître, and G. Trolliard, "Synthesis of zirconium oxycarbide (ZrC_xO_y) powders: Influence of stoichiometry on densification kinetics

- during spark plasma sintering and on mechanical properties," *J Eur Ceram Soc*, 31[13] 2377-2385 (2011).
292. I. Pócsik, M. Hundhausen, M. Koós, and L. Ley, "Origin of the D peak in the Raman spectrum of microcrystalline graphite," *J Non-Cryst Solids*, 227–230 1083-1086 (1998).
293. G. Compagnini, O. Puglisi, and G. Foti, "Raman spectra of virgin and damaged graphite edge planes," *Carbon*, 35[12] 1793-1797 (1997).
294. L. M. Malard, M. A. Pimenta, G. Dresselhaus, and M. S. Dresselhaus, "Raman spectroscopy in graphene," *Phys Rep*, 473[5–6] 51-87 (2009).
295. J. Li, J.-T. Xia, H.-B. Liu, J.-L. He, and J.-H. Zhang, "Nanoporous carbon synthesized from sol–gel template for adsorbing gibberellic acid in aqueous solution," *Mater Sci Eng, C*, 31[7] 1313-1319 (2011).
296. C. Balzer, T. Wildhage, S. Braxmeier, G. Reichenauer, and J. P. Olivier, "Deformation of Porous Carbons upon Adsorption," *Langmuir*, 27[6] 2553-2560 (2011).
297. S. Zhu, W. G. Fahrenholtz, G. E. Hilmas, and S. C. Zhang, "Pressureless Sintering of Zirconium Diboride Using Boron Carbide and Carbon Additions," *J Am Ceram Soc*, 90[11] 3660-3663 (2007).
298. S. Baik and P. F. Becher, "Effect of Oxygen Contamination on Densification of TiB₂," *J Am Ceram Soc*, 70[8] 527-530 (1987).
299. C. B. Finch, P. F. Becher, P. Angelini, S. Baik, C. E. Bamberger, and J. Brynestad, "Effect of impurities on the densification of submicrometer titanium diboride powder," *Advanced Ceramic Materials*, 1[1] 50-54 (1986).
300. M. A. Kuzenkova and P. S. Kislyi, "Grain growth in zirconium diboride during sintering," *Powder Metall Met Ceram*, 5[1] 10-13 (1966).
301. M. F. Yan, U. Chowdhry, and R. M. Cannon, "Conditions for Discontinuous Grain Growth with Pore Entrapment or Pore Coarsening," *Journal of the American Ceramic Society Bulletin*, 57[3] 316 (1978).
302. M. F. Yan, "Microstructural Control in the Processing of Electronic Ceramics," *Materials Science and Engineering*, 48 53-72 (1981).
303. D.-W. Lee, S.-M. Jin, J.-H. Yu, and H.-M. Lee, "Synthesis of Ultrafine ZrC Powders by Novel Reduction Process," *Materials Transactions*, 51[12] 2266-2268 (2010).
304. W. G. Fahrenholtz and G. E. Hilmas, "Oxidation of ultra-high temperature transition metal diboride ceramics," *Int Mater Rev*, 57[1] 61-72 (2012).
305. A. E. McHale, "Volume X: Borides, Carbides and Nitrides," Vol. 10. The American Ceramic Society, Westerville, OH, (1994).
306. H. Wang, D. Chen, C.-A. Wang, R. Zhang, and D. Fang, "Preparation and characterization of high-toughness ZrB₂/Mo composites by hot-pressing process," *Int J Refract Met Hard Mater*, 27[6] 1024-1026 (2009).
307. F. Monteverde, "The addition of SiC particles into a MoSi₂-doped ZrB₂ matrix: Effects on densification, microstructure and thermo-physical properties," *Mater Chem Phys*, 113[2–3] 626-633 (2009).
308. F. Monteverde and A. Bellosi, "Effect of the addition of silicon nitride on sintering behaviour and microstructure of zirconium diboride," *Scr Mater*, 46[3] 223-228 (2002).
309. F. Monteverde, S. Guicciardi, and A. Bellosi, "Advances in microstructure and mechanical properties of zirconium diboride based ceramics," *Materials Science and Engineering: A*, 346[1-2] 310-319 (2003).

310. D. Sciti, F. Monteverde, S. Guicciardi, G. Pezzotti, and A. Bellosi, "Microstructure and mechanical properties of ZrB₂-MoSi₂ ceramic composites produced by different sintering techniques," *Materials Science and Engineering: A*, 434[1-2] 303-309 (2006).
311. J. J. Meléndez-Martínez, A. Domínguez-Rodríguez, F. Monteverde, C. Melandri, and G. de Portu, "Characterisation and high temperature mechanical properties of zirconium boride-based materials," *J Eur Ceram Soc*, 22[14-15] 2543-2549 (2002).
312. W. Zhi, W. Zhanjun, and S. Guodong, "Fabrication, mechanical properties and thermal shock resistance of a ZrB₂-graphite ceramic," *Int J Refract Met Hard Mater*, 29[3] 351-355 (2011).
313. J. Zou, G.-J. Zhang, and Y.-M. Kan, "Pressureless densification and mechanical properties of hafnium diboride doped with B₄C: From solid state sintering to liquid phase sintering," *J Eur Ceram Soc*, 30[12] 2699-2705 (2010).
314. A. V. Sergueeva, D. M. Hulbert, N. A. Mara, and A. K. Mukherjee, "Chapter 3 - Mechanical Properties of Nanocomposite Materials," pp. 127-172. in *Frontiers of Nanoscience*, Vol. 1. Edited by W. Gerhard. Elsevier, 2009.
315. E. Fitzer, "The future of carbon-carbon composites," *Carbon*, 25[2] 163-190 (1987).
316. G. Rellick, "Densification efficiency of carbon-carbon composites," *Carbon*, 28[4] 589-594 (1990).
317. J. Economy, H. Jung, and T. Gogeva, "A one-step process for fabrication of carbon-carbon composites," *Carbon*, 30[1] 81-85 (1992).
318. K. Christ and K. J. Hüttinger, "Carbon-fiber-reinforced carbon composites fabricated with mesophase pitch," *Carbon*, 31[5] 731-750 (1993).
319. T. Windhorst and G. Blount, "Carbon-carbon composites: a summary of recent developments and applications," *Mater Des*, 18[1] 11-15 (1997).
320. A. Paul, J. G. P. Binner, B. Vaidhyanathan, A. C. J. Heaton, and P. M. Brown, "Oxyacetylene torch testing and microstructural characterization of tantalum carbide," *Journal of Microscopy*, 250[2] 122-129 (2013).
321. D. Gozzi, G. Guzzardi, M. Montozzi, and P. L. Cignini, "Kinetics of high temperature oxidation of refractory carbides," *Solid State Ionics*, 101-103[Part 2] 1243-1250 (1997).
322. C.-M. Chen, L. T. Zhang, W. C. Zhou, Z. Z. Hao, Y. J. Jiang, and S. L. Yang, "Microstructure, mechanical performance and oxidation mechanism of boride in situ composites," *Compos Sci Technol*, 61[7] 971-975 (2001).
323. Z. Li, H. Li, W. Li, J. Wang, S. Zhang, and J. Guo, "Preparation and ablation properties of ZrC-SiC coating for carbon/carbon composites by solid phase infiltration," *Appl Surf Sci*, 258[1] 565-571 (2011).
324. D. Gozzi, M. Montozzi, and P. L. Cignini, "Oxidation kinetics of refractory carbides at low oxygen partial pressures," *Solid State Ionics*, 123[1-4] 11-18 (1999).
325. Z. Chen, W. P. Wu, Z. F. Chen, X. N. Cong, and J. L. Qiu, "Microstructural characterization on ZrC doped carbon/carbon composites," *Ceram Int*, 38[1] 761-767 (2012).
326. F. Monteverde and A. Bellosi, "The resistance to oxidation of an HfB₂-SiC composite," *J Eur Ceram Soc*, 25[7] 1025-1031 (2005).

327. G. Liu, S. Meng, J. An, S. Sun, and X. Ding, "The evaluation of reliability for zirconium diboride composite with additives of graphite," *Int J Refract Met Hard Mater*, 27[5] 868-871 (2009).
328. M. Alizadeh and S. Bordbar, "The influence of microstructure on the protective properties of the corrosion product layer generated on the welded API X70 steel in chloride solution," *Corros Sci*, 70[0] 170-179 (2013).
329. S. Bordbar, M. Alizadeh, and S. H. Hashemi, "Effects of microstructure alteration on corrosion behavior of welded joint in API X70 pipeline steel," *Mater Des*, 45 597-604 (2013).
330. D. A. López, W. H. Schreiner, S. R. de Sánchez, and S. N. Simison, "The influence of carbon steel microstructure on corrosion layers: An XPS and SEM characterization," *Appl Surf Sci*, 207[1-4] 69-85 (2003).
331. J. E. Chappelow and V. L. Sharpton, "Atmospheric variations and meteorite production on Mars," *Icarus*, 184[2] 424-435 (2006).
332. X. Li, J. Shi, G. Zhang, H. Zhang, Q. Guo, and L. Liu, "Effect of ZrB₂ on the ablation properties of carbon composites," *Mater Lett*, 60[7] 892-896 (2006).
333. X. Jin, R. He, X. Zhang, and P. Hu, "Ablation behavior of ZrB₂-SiC sharp leading edges," *J Alloys Compd*, 566 125-130 (2013).